Histone Ubiquitination by the DNA Damage Response is Required for Efficient DNA Replication in Unperturbed S-Phase

---

Dissertation

zur

Erlangung der naturwissenschaftlichen Doktorwürde
(Dr. sc. nat.)

vorgelegt der

Mathematisch-naturwissenschaftlichen Fakultät

der

Universität Zürich

von

Jonas Schmid

von

Niedermuhlern BE

Promotionskommission:

Prof. Dr. Massimo Lopes (Vorsitz und Leitung der Dissertation)
Prof. Dr. Lorenza Penengo
Prof. Dr. Matthias Altmeyer
PD Dr. Pavel Janscak
Prof. Dr. Jiri Lukas

Zürich, 2018

The capacity to blunder slightly is the real marvel of DNA. Without this special attribute, we would still be anaerobic bacteria and there would be no music.

Lewis Thomas, The Lives of a Cell

Table of Contents

1. Zusammenfassung

Unser Genom umfasst annähernd 3 Milliarden Basenpaare und enthält mehr als 19'000 Gene, welche den Bauplan für den gesamten menschlichen Körper mit all seinen zellulären Prozessen festlegen. Es ist deshalb nicht überraschend, dass die Verdopplung dieser riesigen Informationsmenge innerhalb eines einzigen Zellzyklus ein enorme Herausforderung mit zahlreichen Schwierigkeiten darstellt.

Während einer normalen S-Phase, trifft die Replikationsmaschinerie auf unzählige Hindernisse. Dazu gehören durch Chemikalien verursachte DNA Schäden, aber auch schwer zu replizierende Sequenzen. Beides führt zum sog. Replikationsstress, das heisst einer Verlangsamung oder Pausieren des Replikationsprozesses, oft verbunden mit eine strukturelle Umformung der Replikationsgabel - wobei die Replikationsgabel aktiv von einer dreiarmigen in eine vierarmige Struktur überführt wird. Dieser Prozess fördert die zelluläre Replikationsstresstoleranz und die DNA-Reparatur während der Replikation. Die exakte und schadensfreie Replikation der DNA ist von grösster Wichtigkeit für den Erhalt der genetischen Information und verhindert daher frühzeitige Alterung sowie die Entstehung von Krebs. Demzufolge sind während der menschlichen Evolution zahlreiche komplexe Mechanismen entstanden, die unseren Zellen helfen mit Replikationsstress umzugehen und beschädigte DNA Stränge zu reparieren.

Einer dieser Mechanismen nennt sich DNA Damage Response (DDR), eine Signalkaskade aus verschieden Kinasen und Ubiquitin-Ligasen. Diese Enzyme modifizieren das Chromatin in der Umgebung von DNA-Doppelstrangbrüchen und bewirken so die Akkumulation von Reparaturproteinen an der Schadensstelle. Homozygote Mutationen in bestimmten DDR Genen verursachen schwere Erbkrankheiten, gekennzeichnet durch Empfindlichkeit gegenüber Röntgenstrahlung, ein erhöhtes Krebsrisiko, Immunschwäche und neurologische Fehlbildungen. Auch Träger von heterozygoten Mutationen in diesen Genen zeigen ein deutlich erhöhtes Risiko für Brust- und andere Krebsarten.

Ein zentrales Enzym der DDR ist die Ubiquitin-Ligase RNF168, welche Ubiquitinketten an den N-terminalen Bereich der Histon-Varianten H2A/H2AX in der Nähe von Doppelstrangbrüchen konjugiert. Diese Ketten dienen ihrerseits als Andockungsstelle für die Reparaturenzyme 53BP1 und BRCA1. In dieser Arbeit präsentiere ich unsere Beobachtung, dass die Ubiquitinierung von Histon H2A/H2AX durch RNF168 notwendig ist um eine effiziente DNA Replikation zu garantieren. Wir zeigen, dass RNF168 an aktiven Replikationsgabeln in der Zelle akkumuliert und dass seine Enzymaktivität benötigt wird, um blockierte Replikationsgabeln neu zu starten und so vor nukleolytischem Abbau zu schützen. Ausserdem demonstrieren wir, dass strukturell umgeformte Replikationsgabeln vollständig chromatinisiert sind und somit von RNF168 modifiziert werden können. Da auch andere Proteine der DDR dieselbe Replikationsfunktion wie RNF168 zeigen, proponieren wir die Prozessierung von umgeformte Replikationsgabeln als alternative Funktion der klassische DDR Enzyme, die damit entscheidend zur Stabilität der genetischen Information in unseren Zellen beitragen.

Weitere Kapitel meiner Doktorarbeit enthalten Beobachtungen zur Funktion verschiedener Ubiquitinketten und diverser anderer DNA Reparaturenzyme während der Replikation.

Diese Arbeit unterstreicht die bemerkenswerte strukturelle Ähnlichkeit zwischen DNA Doppelstrangbrüchen und umgeformten Replikationsgabeln und zeigt, dass in beiden Fällen ähnliche Signal- und Reparaturkaskaden an deren Auflösung und Reparatur beteiligt sind.

2. Summary

Our genome contains approximately 3 billion base pairs that encode more than 19.000 genes specifying the blueprint for all cellular processes and the entire structure of the human body. It is thus hardly surprising that copying this vast amount of information during a single cell cycle is a gigantic undertaking and subject to innumerable challenges.

During any normal S-phase, our replicative machinery is confronted with countless obstacles that originate from both intracellular and extracellular sources such as genotoxic agents or difficult to replicate DNA sequences. Such replication stress can induce the slowing and stalling of the replisome, which triggers the remodeling of replication forks into four-way junctions. This process, termed fork reversal, has recently emerged as a mechanism for promoting DNA damage tolerance and repair during replication. Accurate and damage-free DNA replication and the repair of injuries to the genome is vital to safeguard genetic information thereby preventing premature aging and the development of cellular malignancies. Consequently, human cells have evolved many intricate signaling and repair networks for the resolution of replicative stress and the repair of damaged or broken DNA.

One such pathway is the ubiquitin (Ub) dependent DNA damage response (DDR), a cascade of kinases and ubiquitin ligases that modify chromatin at sites of DNA double-strand breaks (DSBs) and thereby regulate the recruitment of repair factors. Biallelic mutations in certain DDR genes underlie severe congenital syndromes characterized by sensitivity to X-rays, cancer predisposition, immunodeficiency, neurological abnormalities and defective DNA DSB repair. Additionally, people carrying mono-allelic mutations in the same genes show an elevated prevalence of breast and other cancers, but whether this solely reflects DNA repair defects is still elusive.

A central factor of the DDR pathway is the E3 ubiquitin ligase RNF168 that assembles Ub chains on the N-terminal tail of histone variants H2A and H2AX, which subsequently serve as a docking site for the downstream repair factors 53BP1 and BRCA1. In this thesis, I present our finding that RNF168 mediated poly-ubiquitination of histones H2A is also essential for efficient DNA replication in unperturbed S-phase. We show that RNF168 localizes to a subset of active replication factories in cells devoid of detectable DNA double-strand breaks. We further establish that RNF168-induced ubiquitination activity towards H2A K13/15 is necessary for the restart of replication forks that reverse at difficult to replicate DNA sequences and for their protection against Mre11 dependent degradation. In addition, we demonstrate for the first time the nucleosomal organization of reversed replication forks, which is consistent with our finding that the replication function of RNF168 requires H2A ubiquitination. This novel function of RNF168 is shared with key DDR proteins including ATM, RNF8 and 53BP1. We therefore propose that double-stranded ends at reversed forks are modified and processed by classical DDR factors, pointing towards an alternative role of this pathway in preventing genome instability and human disease.

In further chapters, I present observations on the role of different Ub chains and several additional DSB repair factors during normal and perturbed DNA replication.

This thesis highlights the remarkable structural similarities between DNA DSBs and the double-stranded ends at the regressed arm of reversed replication forks and addresses how these two different intermediates are recognized and processed by the same set of cellular factors.

3. Introduction

3.1. Genome Instability

In 2011 Douglas Hanahan and Robert Weinberg defined genome instability and mutation as an enabling characteristic of cancer in their highly influential paper *Hallmarks of cancer: the next generation* (Hanahan & Weinberg 2011). This appreciation of the central role of genome instability for cancerogenesis and cancer therapy builds on a long history of research. It's intellectual roots date back to the work of Theodor Boveri at the beginning of the 20th century (Jeggo et al. 2015). Today cancer is understood as a disease of our genes, brought about by the accumulation of DNA changes over time (Hoeijmakers 2001). However, the inherent genomic instability of cancers has also been recognized as an Achilles heel of the disease and is an important entry point for modern therapeutic approaches (O'Connor 2015). In this subchapter, I will discuss both the causes of genome instability in human cells and its consequences for the aging process and the development of cancer.

3.1.1. Causes of genome instability

During the heydays of atomic energy research in the 1930s and 40s it became evident that mutagenic agents such as ionizing radiation and ultraviolet light are able to cause damage to the genetic material of human cells (Friedberg 2008). Since then many DNA damaging agents and processes have been discovered that either change the sequence of the DNA directly or alter it by affecting the cellular processes of DNA replication and repair (Lord & Ashworth 2012). The causes of genome instability can be broadly divided by their origin as exogenous and endogenous. Both types will be discussed separately below, even though there is always a certain mechanistic cross-talk between these two categories.

3.1.1.1. Exogenous

The international agency for research on cancer (IARC) currently lists 120 substances that are mutagenic and carcinogenic to humans and an additional 81 that are probably carcinogenic (IARC 2012). Hence, the scope of this subchapter is not to discuss all of these agents individually but rather to highlight certain important classes of DNA damaging agents.

One of the first exogenous sources of DNA damage was already postulated in 1775 by the English surgeon Percival Pott – almost two hundred years before the discovery of the DNA double helix. Pott observed a strikingly high incidence of scrotum cancers in chimney sweeps and proposed a link to their frequent exposure to soot. This marked the first recorded evidence for an environmental cause of cancer. Only in the 1950s however it became fully appreciated that exposure to certain chemical substances can increase the DNA mutation rate (Jeggo et al. 2015). Chemical analyses in the second half of the 20th century eventually identified several different polyaromatic hydrocarbons (PAHs) as the carcinogenic agents in chimney-soot (IARC Working Group on the Evaluation of Carcinogenic Risks to Humans 2010). Various PAHs including benzo[*a*]pyrene, one of the major carcinogens in tobacco smoke, have been shown to form DNA adducts leading to an increased cancer risk (Perera et al. 2005; Pfeifer et al. 2002).

The chemical modification of DNA bases by reactive chemicals such as PAHs is summarized under the term alkylation. The resulting DNA adducts can interfere with replication fork progression, which explains part of their mutagenic activity. Alkylating agents are divided into two large categories.

Monofunctional alkylating agents carry a single active moiety that can only modify single bases. Several of these compounds like alkylsulphonates or temozolomide are currently used as cancer chemotherapeutics. The second category are bifunctional alkylating agents, which have two reactive sites and can therfore crosslink DNA with proteins. Alternatively, they can crosslink two DNA bases within the same strand (intra-strand crosslink) or on opposing DNA strands (inter-strand crosslink). Inter-strand crosslinks pose a particularly sever obstacle for replication. Not surprisingly, inter-strand crosslinking agents like mitomycin C or cisplatin have become prominent chemotherapeutic drugs (Helleday et al. 2008).

Another important class of DNA damaging agents are antimetabolites that interfere with the metabolism of nucleotides and DNA synthesis itself. A prominent example of this substance class is aphidicolin (APH), an antibiotic produced by the mold *Cephalosporium aphidicola* (Bucknall et al. 1973). APH is a potent DNA polymerase inhibitor commonly employed in academic research but it has also been considered for cancer therapy (Michaelis et al. 2001; Zellweger et al. 2015). Hydroxyurea (HU) is another important antimetabolite used both in cancer research and therapy. It functions as an inhibitor of ribonucleotide reductase, an enzyme catalysing a rate-limiting step in deoxyribonucleotide synthesis, and thereby impairs DNA synthesis and repair (Madaan et al. 2012). It is commonly employed in cell culture experiments to block DNA replication and synchronize cells but it also has a long and continued history as an anti-cancer drug (Singh & Xu 2016). In addition, HU generates oxidative stress which is likely to contribute to its cytostatic activity (Somyajit et al. 2017) and may explain its vigorous induction of the ATR-mediated replication checkpoint not observed upon APH treatment (Zellweger et al. 2015).

Topoisomerase inhibitors are a class of DNA damaging agents that list among the most effective and most widely used drugs in modern cancer therapy. Topoisomerases are vital enzymes that counteract DNA supercoiling and entanglements through distinct enzymatic activities and thereby release torsional stress (Pommier et al. 2016). The cytotoxic activity of topoisomerase inhibitors does not stem from classical enzymatic inhibition, but rather is a consequence of trapping topoisomerases on the DNA, which ultimately results in the formation of DNA double strand breaks. Camptothecin (CPT) derivatives are inhibitors of topoisomerase 1 (Top1) and form an important group of chemotherapeutics used in the treatment of a diverse set of cancers including gastrointestinal tumours, brain malignancies, sarcomas and ovarian cancer. Furthermore, the topoisomerase 2 (Top2) inhibitors etoposide (ETP) and doxorubicin (DOX) are potent chemotherapeutic drugs that are widely used in cancer treatment (Pommier 2013).

Electromagnetic waves such as ionizing radiation or ultraviolet (UV) light represent the archetype of DNA damaging agents, whose cancer causing potential has been recognized since the early days of the atomic age (Friedberg 2008). Radiation elicits its genotoxic activity through the generation of DNA damaging radicals either by ionizing water molecules or through the direct ionization of atoms within the DNA itself. It has been estimated that 1 Gy of ionizing radiation can generate close to 1’000 DNA single strand breaks (SSBs) and 35 double strand breaks (DSBs) per cell, making it highly cytotoxic. Due to its remarkable cytotoxicity, radiotherapy is a very important tool in the clinical management of cancer and may be responsible for almost 40% of curative interventions (O’Connor 2015). Exposure of DNA to UV light causes bulky photoproducts such as cyclobutane pyrimidine dimers that pose severe problems during replication and can be highly mutagenic. This is especially problematic since UV is a

spectral component of normal sunlight. A single day in the sun can therefore lead to the formation of up to 10^5 photoproducts in each of the exposed skin keratinocytes (Hoeijmakers 2001; Hoeijmakers 2009).

3.1.1.2. Endogenous

Although the relative importance of exogenous and endogenous factors for cancerogenesis in different organ systems remains a matter of debate (Tomasetti & Vogelstein 2015; Wu et al. 2016) modern sequencing techniques have recently highlighted the remarkable abundance and diversity of endogenous DNA damage (Alexandrov et al. 2013).

A classical cause of endogenous mutational processes is the inactivation of DNA repair pathways, which is commonly found in hereditary forms of cancer (Tubbs & Nussenzweig 2017). A prime example of this is Lynch syndrome, a cancer predisposition syndrome caused by inactivating germline mutations in DNA mismatch repair (MMR) genes. The MMR pathway is responsible for the recognition and correction of non-Watson-Crick base pairs and strand misalignments that arise during normal DNA replication. Defects in the MMR process lead to a hypermutation phenotype and a strongly increased risk for tumorigenesis, most prominently the development of colon cancers (Jiricny 2013; Peña-Diaz & Rasmussen 2016). Hereditary breast and ovarian cancer (HBOC) is another prominent cancer predisposition syndrome caused by mutations in the breast cancer susceptibility genes BRCA1 and BRCA2, who's diverse functions in genome protection will be discussed in later chapters (Roy et al. 2012).

One of the most common causes of single-base mutations in the human genome is the spontaneous deamination of 5' methylcytosine, resulting in C:G>T:A substitutions at methylated CpG dinucleotides. CpG sites mutate at a highly-elevated rate compared to other types of dinucleotides. Consequently, their frequency in the human genome is four times lower than expected by chance. Furthermore, C:G to T:A substitutions account for 25% of somatic mutations found in the tumour suppressor gene TP53 and may thus be an important driver of cancerogenesis (Olivier et al. 2010; Tubbs & Nussenzweig 2017).

Interestingly, by-products of normal cellular metabolism can exert considerable mutagenic activity. Various metabolic pathways in our cells produce reactive oxygen species that can induce DNA lesions like the conversion of guanine to 8-oxoguanine. 8-oxoguanine can mispair with adenine resulting in G to T transversions (Tubbs & Nussenzweig 2017). Another important example are the by-products of lipid peroxidation such as acrolein and corontaldehyde that list among the most well-characterized sources of ICLs in nature (Deans & West 2011). Acetaldehyde is a chemical that may be viewed as a combination of an exogenous and endogenous DNA damaging agent. It is a mutagenic metabolite of ethanol and is considered to mediate the carcinogenic activity of alcohol consumption, a habit that accounts for almost 6% of cancer related deaths world-wide (Guillén-Mancina et al. 2018).

The normal replicative process and the consequences of replicative stress are further major drivers of mutation and carcinogenesis is (Técher et al. 2017). These processes are a central focus of this thesis and will be discussed in a separate chapter.

3.1.2. Consequences of genome instability

Genome instability can have severe consequences for our wellbeing. Most importantly it drives the process of aging and the development of cancer (López-Otín et al. 2013; Jeggo et al. 2015), both of which will be discussed in this subchapter. From a superficial point of view cancerogenesis and ageing appear to be fundamentally different phenomena. Cancer cells can be viewed as hyperactive, harbouring advantageous mutations allowing for rapid proliferation, while aged cells are hypoactive and accumulate disadvantageous mutations that ultimately prohibit active proliferation. Nonetheless, the two phenomena are driven by many of the same underling processes. Both originate due to the time-dependent accumulation of damage in cells and organs of which genome instability is a major driver (Hoeijmakers 2009; Aunan et al. 2017).

For cancerogenesis the most important consequence of genome instability and mutation is the loss of tumour-suppressor genes and the activation of oncogenes that can trigger uncontrolled proliferation. This in turn promotes replicative stress that further aggravates genetic damage in the cell (Hoeijmakers 2009). These processes are counteracted by DNA damage response (DDR) signalling that promotes DNA repair and prevents the proliferation of damaged cells through activation of apoptosis and checkpoint arrest. Only by inactivating DDR signalling can the cells accumulate persistent genomic instability and reach full malignant transformation (*Figure 1*)(Jeggo et al. 2015).

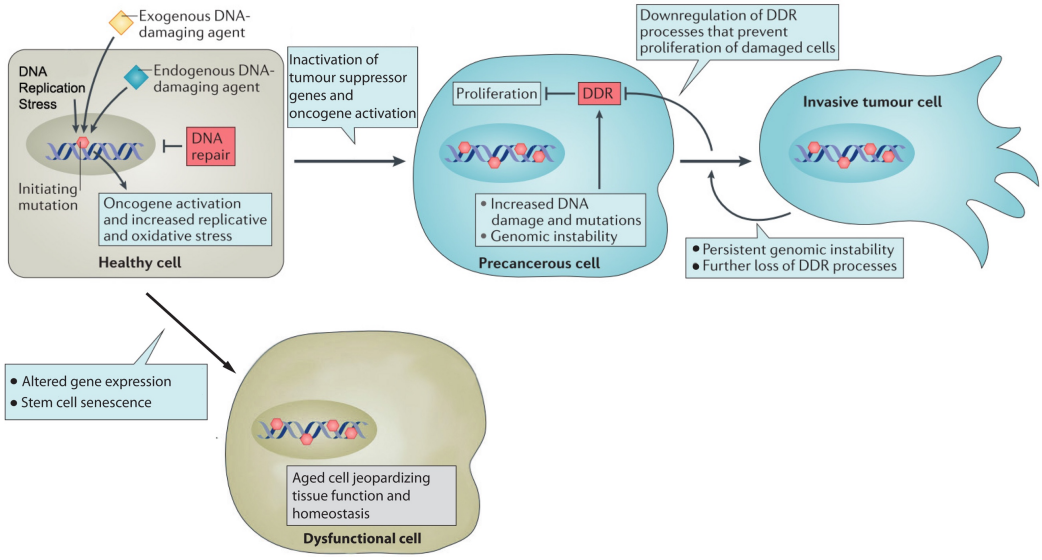

Figure 1: Genome instability in cancerogenesis and aging (Modified from Jeggo et al. 2015)
Genome instability is a driving force of cancerogenesis and aging. Genetic alterations brought about by diverse means can promote uncontrolled proliferation and invasiveness of tumour cells. At the same time, mutational processes can cause altered gene expression and stem cell senescence that jeopardize the function and homeostasis of aging tissues.

Like in cancer, genome instability has been widely accepted as a hallmark of aging (López-Otín et al. 2013) even though the gravity and universality of its involvement remain a matter of debate (Moskalev et al. 2013). An important indication for the connection between genome instability and aging is the fact that prominent human progeria diseases such as Werner syndrome, Cockayne syndrome and ataxia telangiectasia are caused by mutations in DNA repair genes (Burtner & Kennedy 2010). Age

related accumulation of genetic changes causes stochastic deregulation of gene expression among neighbouring cells, which can jeopardize tissue function (Aunan et al. 2017). Furthermore, it has been suggested that DNA damage can cause the senescence of stem cells and thereby affect tissue homeostasis. Whether this process plays a critical role during the normal aging process is however still a matter of debate (Jones & Rando 2011).

3.2. Ubiquitination

Ubiquitin is a small (76 amino acid) polypeptide that can be covalently conjugated via its c-terminal glycine residue (G) to mostly lysine residues (K) on target proteins. Protein ubiquitination is a crucial post-translational modification (PTM) utilized to control protein function and interactions, thereby regulating a plethora of different cellular processes. It plays essential roles in the regulation of both the DNA damage response and DNA replication and thus has a major impact on genome stability (Smeenk & Mailand 2016)

3.2.1. Writing and erasing the Ub code

Ubiquitination is a multistep process (*Figure 2*) involving ubiquitin activating enzymes (E1s), ubiquitin conjugating enzymes (E2s) and ubiquitin ligases (E3s). During the initial step of ubiquitination, Ub is activated in an ATP-dependent manner by forming a thioster bond with an E1 activation enzyme (Husnjak & Dikic 2012). Next, Ub gets transferred onto an E2 enzyme, again forming a thioester intermediate. In many cases the E2 appears to regulate the specific type of Ub mark assembled on the substrate, ultimately determining the consequences of ubiquitylation for the modified target (Ye & Rape 2009). The actual transfer of Ub onto the final substrate is mediated by an E3 ligase. E3 ligases simultaneously bind to the target protein and to an E2 enzyme thioesterified with ubiquitin. By bringing together E2 and substrate they mediate the specificity of the ubiquitination reaction. There are two distinct enzymatic ways by which E3 ligases can transfer ubiquitin molecules onto a target protein. RING domain and U-box containing E3s mediate a direct transfer of Ub from the E2 onto the substrate, whereas in HECT and RBR E3s a covalent E3-Ub thioester intermediate is formed (Kulathu & Komander 2012; Komander & Rape 2012).

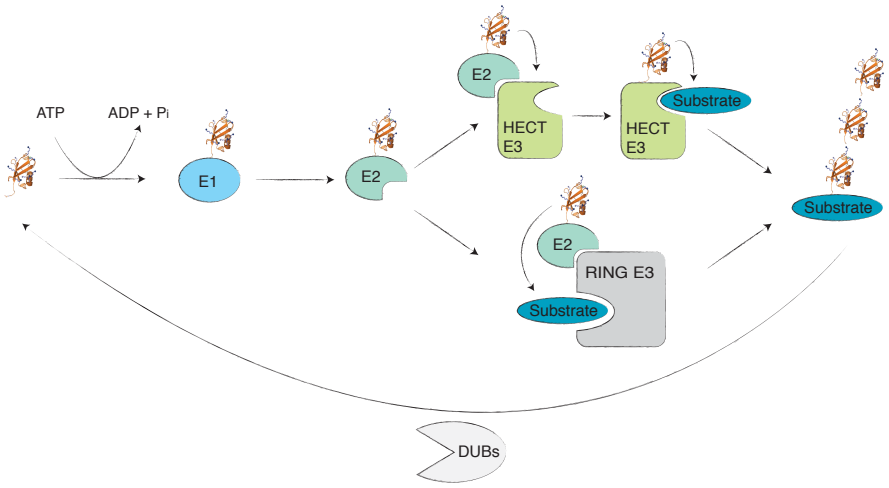

Figure 2: Writing and erasing the ubiquitin code (based on Komander and Rape, 2012)
Ubiquitination is brought about by a multistep process involving ubiquitin activating enzymes (E1s), ubiquitin conjugating enzymes (E2s) and ubiquitin ligases (E3s). More than 100 distinct deubiquitinating enzymes (DUBs) can remove Ub from its substrates and thereby ensure the reversibility of the ubiquitin code.

Ubiquitination can only confer a meaningful cellular signal if it is spatially and temporally restricted. Ub signals should only be present when they are required and must be removed when this is no longer the case. In human cells, more than 100 specialized deubiquitinating enzymes (DUBs) can remove Ub from its substrates and thereby ensure the reversibility of the ubiquitin code (Komander & Rape 2012; Kulathu & Komander 2012).

3.2.2. Types and recognition of ubiquitin marks

Ubiquitin can be conjugated as a single entity to one or multiple sites of a target protein leading to mono- or multi mono-ubiquitination. However, the versatility of ubiquitin for the regulation of cellular processes stems from its ability to form eight structurally distinct chain types. Ubiquitin molecules in a chain can be linked through one of their seven lysine residues (K6, K11, K27, K29, K33, K48 and K63) or via their N-terminal methionine (M1) (Deshaies & Joazeiro 2009; Husnjak & Dikic 2012; Komander & Rape 2012). All different linkage types have been found to coexist in vivo (P. Xu et al. 2009). K48- and K63-linked chains are the most prevalent chain types in human cells and they are also the most extensively studied. K48-linked poly-ubiquitin chains have been found to target proteins for degradation by the 26S proteasome. In contrast K63-linked chains play a non-proteolytic role in diverse signalling pathways such as NF-κβ signalling, the Interleukin-1 and Toll-like receptor pathways and most prominently in the response to DNA damage (Chen & Sun 2009). Our knowledge about the functional consequences of the remaining ubiquitin chain types (K6, K11, K27, K29, K33 and M1) is much more limited. Of these so called atypical chains both K6 and K27 have been implicated in the maintenance of genome stability. The BRCA1-BARD1 complex, a heterodimeric RING E3 ligase involved in DNA repair, has been reported to assemble K6-linked chains on itself and on Histone H2A. This activity was suggested to play a role during DNA replication and repair, however its precise functional consequences have not yet been firmly established (Morris & Solomon 2004; Kalb et al. 2014). K27

chains in turn have been found to be assembled by the E3 ligase RNF168 on histone H2As upon DNA double strand break formation and are strictly required for proper DNA damage response activation (Gatti et al. 2015).

Comparable to the recognition of other PTMs, the diverse types of Ub marks in human cells are recognized by a large variety of ubiquitin-binding domains (UBDs) or ubiquitin receptors that carry at least one UBD. Proteins binding to ubiquitin marks on specific factors or to certain chain types via their UBD can translate these signals into activation of appropriate biochemical cascades within the cell. UBDs are structurally diverse motives that can be divided into several subfamilies. They all share the characteristic of non-covalent binding to ubiquitin signals, however the mechanisms by which they recognize specific Ub marks can vary tremendously (Husnjak & Dikic 2012).

3.3. DNA double strand break repair

DNA double strand breaks (DSBs) represent one of the most cytotoxic lesions that can occur in our genome. If left unrepaired, they affect the content and organization of genetic information in a way that can lead to cell death and cancerogenesis. To counteract the formation and persistence of such dangerous DNA lesions, cells have evolved a diverse set of signalling and repair pathways. One of the most prominent of these is the ubiquitin dependent DNA damage response (DDR) (Smeenk & Mailand 2016)

3.3.1. The ubiquitin dependent DNA damage response

DNA double strand break formation elicits a complex chromatin response driven by post-translational modifications of histones and histone-binding proteins and prominently involves non-proteolytic ubiquitin chains (*Figure 3*). These modifications trigger an extensive build-up of repair factors on chromatin segments flanking the lesion. Such protein accumulations can be visualized by fluorescence microscopy and are commonly called nuclear repair foci (Lukas et al. 2011).

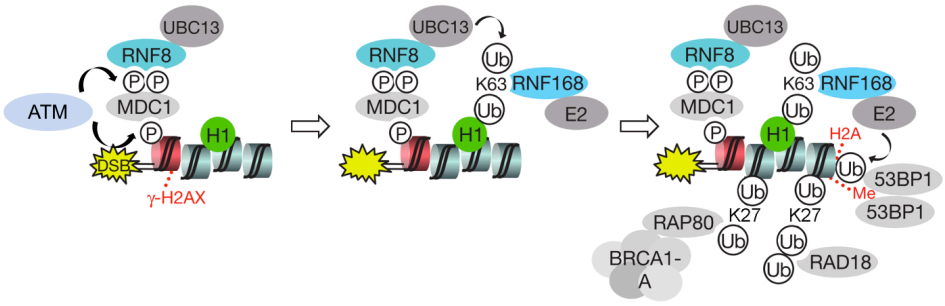

Figure 3: The Ub dependent signaling response to DNA double strand breaks (Modified from Thorslund et al., 2015) Upon DSB formation the serine/threonine kinase ATM phosphorylates histone H2AX. This in turn promotes the recruitment of the scaffold protein MDC1, which serves as a docking platform for RNF8. RNF8 together with its E2 UBC13 subsequently targets linker histone H1 by K63 ubiquitin chains. Ubiquitinated H1 then serves as a recruitment signal for RNF168 and a yet unidentified E2 ligase. Together they ubiquitinate H2A type histones on K13 and K15, which constitutes a docking site for downstream repair factors such as 53BP1 and BRCA1.

The multi protein complex MRN (MRE11/RAD50/NBS1) functions as an initial DSB sensor for the Ub dependent DDR. It subsequently recruits the serine/threonine kinase ATM (ataxia telangiectasia

mutated) through NBS1 and stimulates its activity by a yet poorly understood mechanism. ATM is a member of the phosphatidylinositol 3-kinase-like kinase (PIKK) family that are responsible for the activation of an intricate DNA damage response network. One of the most critical ATM dependent events is the phosphorylation of histone variant H2AX on S139 in its C-terminal tail. The phosphorylated form of H2AX (γH2AX), serves as a DNA damage mark and provides a binding platform for the scaffold protein MDC1 (mediator of DNA damage checkpoint) (Al-Hakim et al. 2010; Blackford & Jackson 2017). Upon its recruitment to the break site, MDC1 gets phosphorylated by ATM at multiple positions. This provides docking sites for the E3 ligase RNF8, which binds phosphorylated MDC1 via its FHA domain (Smeenk & Mailand 2016). RNF8, in conjunction with the E2 conjugating enzyme UBC13, was shown to assemble K63-linked chains on H1-type linker histones but remains inactive towards core histones. H1 ubiquitination then promotes the recruitment of RNF168 to the site of DSBs (Thorslund et al. 2015). A recent study has however suggested that the putative polycomb group protein L3MBTL2, rather than H1, serves as the ubiquitination target of RNF8 and as the recruitment platform for RNF168 (Nowsheen et al. 2018). Together with a yet unidentified E2 enzyme, RNF168 assembles K27 linked Ub chains on core histones H2A and H2A.X (Gatti et al. 2015). This RNF168 mediated Ub mark constitutes a recruitment platform for downstream DDR factors, most prominently BRCA1 (Breast Cancer 1) and 53BP1 (p53 Binding Protein). BRCA1 and 53BP1 promote the activation of distinct pathways ultimately resulting in the repair of the DNA break (Doil et al. 2009; Al-Hakim et al. 2010; Smeenk & Mailand 2016).

Excessive spreading of DNA-damage-induced chromatin ubiquitination can have deleterious effects including the unscheduled transcriptional silencing of nearby genes and the sequestration of important genome caretakers. Human cells have evolved several counter mechanisms to prevent such problems. The three DUBs, BRCC36, OTUB1 and USP3, have been shown to limit the accumulation of DSB induced chromatin ubiquitination (Nicassio et al. 2007; Shao et al. 2009; Nakada et al. 2010). In addition, the two E3 ligases TRIP12 and UBR5 strictly regulate the amount of RNF168 in the nucleus and thereby prevent excessive spreading of histone ubiquitination away from break sites (Gudjonsson et al. 2012).

3.3.2. Double strand break repair pathways

Human cells possess two main repair pathways, i.e. non-homologous end joining (NHEJ) and homologous recombination (HR), alongside several sub-pathways not discussed here, to mend DNA double strand breaks. Non-homologous end joining repairs DNA breaks by blunt end ligation and requires little or no sequence homology, allowing it to occur throughout the cell cycle. Due to its template independent nature, the pathway is commonly viewed as error prone, even though it is probably accurate in most cases (Hustedt & Durocher 2017; Ranjha et al. 2018). Homologous recombination requires a sister or homologous chromatid as a template for repair and thus mainly occurs in late S and G2 phase when such templates are available (Ceccaldi et al. 2016). The following two subchapters will discuss both pathways and their regulation in more detail.

3.3.2.1. Nonhomologous end joining

Double strand breaks forming during interphase are rapidly bound and protected by the heterodimeric complex Ku70/Ku80 (Ku). The Ku heterodimer then recruits and activates DNA-PKc, a phosphoinositide 3-kinase-related kinase (PIKK). Together Ku and DNA-PKc constitute the DNA-PK holoenzyme that promotes DNA-end tethering via NHEJ (Blackford & Jackson 2017). The repair of blunt ended DSB does not require DNA-PKc activity. Instead it entirely relies on XRCC4 and potentially PAXX for the bridging

of the two DNA ends and on DNA ligase IV for the ligation step. During the repair of non-blunt ended breaks, DNA-PKc recruits and activates the endonuclease Artemis, which subsequently clips off 5' and 3' overhangs. This trimming creates DNA end structures that can be joined by a complex consisting of XRCC4 and Ligase IV. In the case of 5' overhangs the ligation is additionally stimulated by XLF and PAXX (Chang et al. 2017).

The ubiquitin dependent DNA damage response plays a central role in regulating the NHEJ pathway. During the G1 cell cycle phase, 53BP1 blocks homologous recombination repair via the ATM dependent recruitment of its binding partners PTIP and RIF1. 53BP1 forms a complex with RIF1 and REV7 that counteracts the recruitment of the central HR factor BRCA1. It thereby inhibits DNA end resection and thus promotes repair through NHEJ. PTIP, the other binding partner, recruits Artemis to the break site, which further fosters NHEJ repair. In G1, the anaphase-promoting complex (APC/C) ubiquitinates CtIP, an end resection factor involved in HR repair. CtIP is thereby targeted for proteasomal degradation and HR repair blocked in this cell cycle phase (*Figure 4*) (Schwertman et al. 2016). Interestingly, RNF8 was shown to modify Ku80 with K48 linked ubiquitin chains and loss of RNF8 profoundly impairs the efficiency of NHEJ repair. It has thus been suggested that RNF8 is involved in the removal of Ku from DSB ends (Feng & Chen 2012).

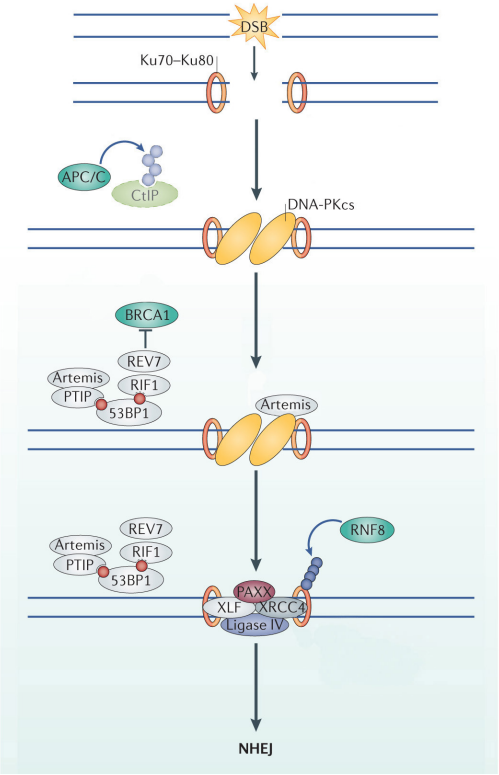

Figure 4: Nonhomologous end joing (Modified from Schwertman et al., 2016)
DSBs formed in interphase are rapidly bound and protected by the heterodimeric Ku complex. This leads to the recruitment of DNA-PKc in conjunction with the endonuclease Artemis. Artemis is then activated through DNA-PKc and trims overhangs at the break site. 53BP1 and its two interactors RIF1 and PTIP prevent BRCA1 binding and promote Artemis recruitment to the break site, thereby channelling the repair into the NHEJ pathway. The actual ligation is achieved through the XRCC4-Ligase IV complex which can be assisted by PAXX and/or XLF depending on the precise structure of the break. During G1 the APC/C complex targets CtIP for proteasomal degradation and thereby prevents HR repair in this cell cycle phase. The E3 ligase RNF8 assembles K48 linked Ub chains on Ku80, which promotes the removal of the Ku complex from the break ends and is necessary for efficient NHEJ repair.

3.3.2.2. Homologous recombination

In contrast to NHEJ, homologous recombination repair requires a homologous sequence as a template. This enables the HR machinery to restore the entire genetic information around the break site resulting in highly accurate repair. In most cases the sister chromatid is employed to retrieve the missing sequences. This restricts HR to cell cycle stages when such a repair template is physically available, which is only the case during the S- and G2-phase (Ranjha et al. 2018; Kowalczykowski 2015). To prevent this mechanism from running awry it must be tightly regulated. A critical process for the regulation of DSB repair is DNA end resection, which likely dictates pathway choice between NHEJ and HR. The initial phase of end resection in HR is performed by the structure specific endonuclease MRE11, a component of the MRN (MRE11/RAD50/NBS1) complex, in conjunction with CtIP. During this so-called “end clipping”, only a relatively small number of nucleotides is degraded. The second phase of processing consists of extensive resection, which is carried out by the combined actions of helicases and nucleases including DNA2, BLM, WRN, CtIP and EXO1. This generates long stretches of single stranded DNA (ssDNA) at the break ends, committing the cells to the HR repair pathway (Ceccaldi et al. 2016). Upon S-Phase entry, end resection is increasingly promoted by the activity of cyclin-dependent kinases (CDKs), especially CDK1. The CDK dependent phosphorylation of NBS1 and CtIP stimulates the end processing activity of the MRN complex. Additionally, CtIP phosphorylation on Ser327 allows it to be bound by BRCA1, which counteracts 53BP1 recruitment to the break site and possibly further stimulates end resection. In addition, BRCA1 is recruited to RNF168-ubiquitinated chromatin as a part of the BRCA1-A complex. CDK activity also fosters long range resection through phosphorylation of the EXO1 nuclease. ssDNA stretches produced in the resection process are initially bound by the single strand binding protein RPA. BRCA1, BRCA2 and PALB2 then promote the replacement of RPA by the recombinase RAD51, which undertakes homology search and strand invasion on a suitable template (Schwertman et al. 2016; Hustedt & Durocher 2017). Once the template has been invaded, DNA synthesis sets in to copy the genetic information that has been lost due to DSB formation. This is followed by dissolution of the ensuing structures, which results either in a crossover between the sister chromatids or a crossover-free repair of the break, depending on the precise dissolution process (*Figure 5*) (Kowalczykowski 2015).

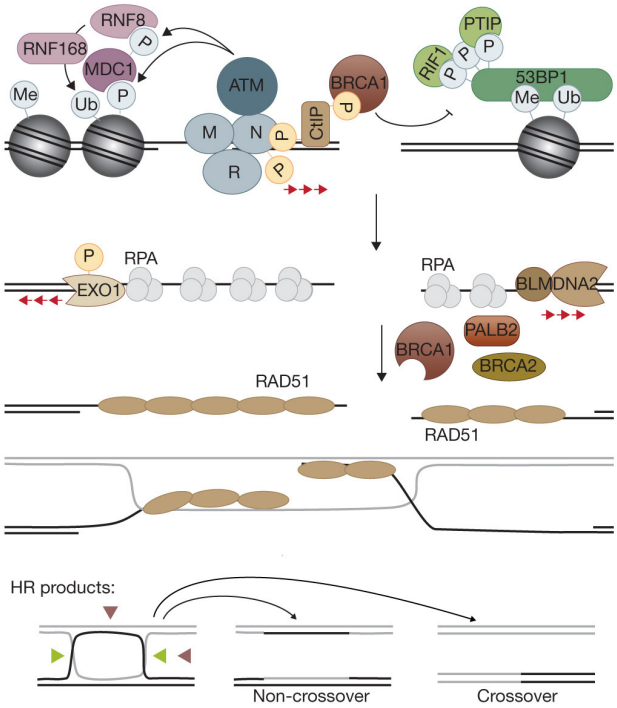

Figure 5: Homologous recombination (Modified from Husted & Durocher 2017)
The critical regulatory node to decide whether DSBs are repaired through NHEJ or HR is DNA end resection. This in turn is tightly regulated by the rising activity of CDKs during S-Phase. CDK dependent phosphorylation of NBS1 and CtIP stimulates end resection and promotes the recruitment of BRCA1. BRCA1 then counteracts 53BP1 binding to the break site and further promotes end resection. Long range resection is achieved through the combined actions of DNA2/BLM and EXO1, which is also stimulated via CDK dependent phosphorylation events. BRCA1, BRCA2 and PALB2 assist the replacement of RPA on ssDNA by RAD51. The recombinase RAD51 then performs homology search and strand invasion, which is followed by DNA synthesis. The resulting structures can be dissolved via different processes that either result in a crossover between sister

3.3.3. Ataxia telangiectasia

As highlighted above, the DNA damage response and the various pathways employed in DNA repair are of crucial importance for organismal well-being and long-term survival. A plethora of distinct human congenital syndromes have been identified that are caused by mutations in genes involved in the cellular response to DNA damage and its repair. Even though they tend to have pleomorphic and sometimes complicated manifestations, DNA repair disorders are often partial phenocopies of each other. They can thus be classified into an overarching syndrome that is characterized by sensitivity to X-rays, cancer predisposition, immunodeficiency, neurological abnormalities and defective DNA DSB repair, or XCIND syndrome for short. Cell lines derived from such patients represent a valuable research tool to decipher the mechanistic roles of individual DNA damage response components (Kerzendorfer & Driscoll 2009; Nahas & Gatti 2009).

A prime example of a human DNA damage response deficiency syndrome is ataxia telangiectasia (AT), also known as Louis-Bar syndrome. AT is a rare disease with a prevalence of approximately 1:88.000. Its name is derived from the cerebellar ataxia, a lack of voluntary coordination of muscle movement, and the ocular and cutaneous telangiectasia, visible dilated blood vessels in the eyes and skin, that are present in many but not all patients. The clinical symptoms of AT patients can be quite diverse and may include progressive cerebellar degeneration, telangiectasia, radiation sensitivity, premature aging, immunodeficiency, poor growth, gonadal atrophy and a marked cancer predisposition, especially cancers of lymphoid origin. Cells derived from AT patients show a strong sensitivity to ionizing radiation, chromosomal instability, defective DSB repair and premature senescence (Teive et al. 2015; Rothblum-Oviatt et al. 2016). In 1988, it was discovered that the defective gene causing AT is located on chromosome 11q22-23 (Gatti et al. 1988) and soon after the gene was identified as the ATM kinase

(Savitsky et al. 1995), a crucial factor of the ubiquitin dependent DNA damage response introduced in previous chapters. Whether the complex symptoms in AT patients are mainly a consequence of faulty DSB repair, or whether they also reflect defects in other processes is yet unclear.

3.3.4. RIDDLE syndrome

In 2007, a novel human immunodeficiency disorder named RIDDLE syndrome was described for the first time. RIDDLE is characterized by radiosensitivity, immunodeficiency, dysmorphic features and learning difficulties. Additional symptoms can include ataxia, telangiectasia, elevated alpha-fetoprotein levels and pulmonary failure. These symptoms are strikingly similar to those observed in ataxia-telangiectasia patients and several other XCIND syndromes such as the Nijmegen breakage syndrome (NBS) and radiosensitive severe combined immunodeficiency (RS-SCID). In addition, cells derived from RIDDLE patients show hypersensitivity to ionizing radiation and exhibit defective DSB repair foci formation. All of these factors indicated that RIDDLE may be caused by mutations in an unknown DSB repair protein (Stewart, Stankovic, Byrd, Wechsler, Miller, Huissoon, Drayson, West, Elledge & A. M. R. Taylor 2007; Devgan et al. 2011). Subsequent studies showed that the protein mutated in RIDDLE syndrome is RNF168, the central E3 ligase of the ubiquitin dependent DNA damage (Doil et al., 2009; Pinato et al., 2009; Stewart et al., 2009). RIDDLE is a strikingly rare syndrome with only four patients identified up to now, whose clinical phenotype is quite varied (Pietrucha et al. 2017). As for AT, it is not yet clear whether the full set of symptoms observed in RIDDLE patients can solely be attributed to defects in DSB repair, or if the deregulation of other processes is also responsible.

Interestingly, a study in eastern Finland found heterozygous truncations in the RNF168 gene to be quite prevalent in the investigated population. Furthermore, these recessive RIDDLE syndrome alleles showed a borderline association with hereditary breast cancer**,** highlighting the central role of RNF168 in genome stability maintenance (Mantere et al. 2017).

3.4. Principles of mammalian DNA replication

3.4.1. General concepts:

DNA replication is a fundamental requirement for cell division and the transmission of genetic information to the next generation, making it essential for the existence of all forms of life on earth. It is thus nor surprising that the fundamental principles of replication are highly conserved among all organisms of the three kingdoms (Burgers & Kunkel 2017). However, there are considerable differences in replication regulation as well as in the complexity of replication factors even among different eukaryotes. Eukaryotic cells control the replication of their genomes by precise and stringent regulatory mechanisms that ensure accurate and fast genome duplication and safeguard genomic stability. DNA replication is tightly monitored and closely coupled to cell cycle progression. This ensures that the genome is replicated exactly once per cell cycle, and that the replicative process is completed before the cell undergoes mitosis. Eukaryotic genomes can be of considerable size, sometimes far exceeding a billion base pairs (bp), and are generally structured into multiple chromosomes. During human development, our cells need to duplicate their large and discontinuous genomes billions of times to give rise to the 4×10^{13} copies of DNA present in an adult body. To do this in an efficient way, initiation of DNA replication takes place at multiple sites along the chromosomes, termed replication origins. This makes it possible for multiple replisomes to copy the genome in parallel. Cells can ration

their limited resources for replication by synchronously firing specially clustered sets of origins and wait until a certain number of forks fuse before additional origins are activated. Mammalian cells split their genome into approximately 5.000 units of simultaneously firing replication clusters, so called replication domains that harbour up to 30.000 origins (Kelly & Brown 2000; Branzei & Foiani 2010; Rivera-Mulia & Gilbert 2016; Fragkos et al. 2015). In certain organisms like the budding yeast *Saccharomyces cerevisiae*, replication origins are strictly defined by consensus sequences. In humans on the other hand, DNA sequence requirements for replication origins are more relaxed and origin determination is overall based on DNA secondary structures, chromatin organization and specific epigenetic marks (Boulos et al. 2015). The replicative process can broadly be divided into three consecutive stages: Initiation, elongation and termination. The following subchapters will discuss each stage of the replication process in mammalian cells separately, even though they are closely intertwined and not strictly separate from each other.

3.4.2. Initiation of replication

Replication initiation in eukaryotes is a highly-regulated process that is organised into two separate steps, replication *origin licensing* and *origin firing*. Origin licensing is tightly restricted to late mitosis and the early G1-phase of the cell cycle, to prevent rereplication of the genome. It begins with the binding of the six-subunit AAA+ ATPase origin recognition complex (ORC) at thousands of future replication origins along the genome. The ORC subsequently recruits CDC6 and CDC10-dependent transcript 1 (CDT1) to the future origin site. As a last step of the licensing process, these three factors promote the chromatin loading of the six-subunit mini-chromosome maintenance helicase complex (MCM2–7). Together ORC, CDC6, CDT1 and MCM2-7 constitute the pre-replicative complex (preRC). Origins that are licensed during G1 remain dormant until the cell is entering S-phase, during which the licensing of new origins is strictly inhibited (Arias & Walter 2007; Fragkos et al. 2015). Higher eukaryotes employ two main mechanisms to prevent origin licensing during S-phase, both of which act on CDT1. The CDT1 protein can get removed from the cell through ubiquitin-mediated proteasomal degradation or it can be bound by the inhibitory protein Geminin (McGarry & Kirschner 1998; Wohlschlegel et al. 2000; Nishitani et al. 2006). Origin firing, the second step in the initiation process, occurs throughout S-phase when previously licensed preRCs are bound by further initiation factors and the MCM2-7 helicase complex is activated. This is set in motion by the combined activity of DBF4-dependent kinase (DDK) and cyclin-dependent kinases (CDKs). The key event during origin firing is the phosphorylation and subsequent recruitment of CDC45 and the GINS complex to MCM2–7. The resulting 11-subunit complex encircles the parental DNA and is termed CMG helicase. Upon DDK and CDK dependent phosphorylation of the double hexametric MCM2-7 complex, it spits into two separate hexamers that begin with the unwinding of the DNA double strand. This establishes two sister replication forks that move away from the origin in opposite directions while copying the genetic information stored on the parental DNA duplex. Importantly, the CMG helicase must remain stably associated with the replication fork (RF) during the entire replicative process, no matter what obstacles are encountered. If it falls off, it cannot be reloaded during the same cell cycle, since MCM2-7 recruitment can no longer occur once the cell has entered S-phase (Labib et al. 2000; Arias & Walter 2007; Fragkos et al. 2015).

3.4.3. Elongation

DNA duplication is accomplished by the replisome, a multi-protein apparatus, which is stably associated with active replication forks (RFs). The CMG replication complex represents the functional core, around which the replicative machinery is assembled. The replisome includes multiple DNA and RNA polymerases with distinct functions (polymerase-α, polymerase-ε and polymerase-δ) as well as several polymerase accessory factors such as the clamp loader replication factor C (RFC) and the proliferating cell nuclear antigen (PCNA). Further important components include the checkpoint mediator Claspin and the Tim1/Tipin complex, required for RF pausing (Christiano et al. 2003; Gotter et al. 2007; Branzei & Foiani 2010; Errico & Costanzo 2012; Snedeker et al. 2017). The unwinding of the parental DNA duplex by the CMG helicase generates single stranded DNA, which is instantly coated by replication protein A (RPA). This provides sites for priming by DNA polymerase-α (Pol-α or primase). Pol-α first synthetizes a short RNA primer of approximately 10 ribonucleotides which is subsequently extended by approximately 30 deoxy-ribonucleotides. RFC recognizes these RNA/DNA primers, displaces Pol-α and in turn loads PCNA. PCNA then functions as a recruitment and processivity factor for the main replicative DNA polymerases (Pol-δ and Pol-ε), which elongate the primer and thereby copy the parental DNA duplex (Maga & Hübscher 2003; Arias & Walter 2007; Burgers & Kunkel 2017). Due to the underling chemistry of DNA synthesis, new nucleotides can only be added to the 3' OH-end of a nascent strand. The antiparallel structure of the DNA helix thus forces replication to proceed in a semi-discontinuous manner. On the leading strand, Pol-ε can travel in the same direction as the CMG helicase and incoming DNA nucleotides are continuously added to the initial primer. On the opposing lagging strand however, new RNA primers need to be synthesized by Pol-α and subsequently elongated by Pol-δ throughout the entire replication process. This leads to the formation of discontinuous Okazaki fragments and the exposure of single-stranded DNA stretches at the RF, which are immediately bound and protected by RPA. After their formation, Okazaki fragments are processed and subsequently ligated to the previous fragment with the help of FEN1, Dna2 helicase, RNase H, Pol-δ and DNA ligase I (Ligase) (Balakrishnan & Bambara 2013; Branzei & Foiani 2010). Cohesins link the newly formed sister chromatids after the replisome has passed through (*Figure 6*) (Snedeker et al. 2017).

Parental DNA duplex separation by replicative helicases leads to the accumulation of positive torsional stress. This can induce supercoiling of the parental strand ahead of the RF and lead to the formation of precatenanes, an intertwining of the two replicated strands behind the fork. Type IB (TOP1) and type II (TOP2) topoisomerases remove supercoils ahead of the replication fork, which is instrumental for efficient progression of the replisome. Precatenanes do not affect replication fork progression per se. However, once replication is completed they are automatically converted into catenanes, interlocked regions between the newly replicated sister chromatids. Catenanes pose a problem during mitosis when chromosomes need to be separated. Thus the cell continuously removes precatenanes through the specialised actions of TOP2 (Schvartzman & Stasiak 2004; Branzei & Foiani 2010).

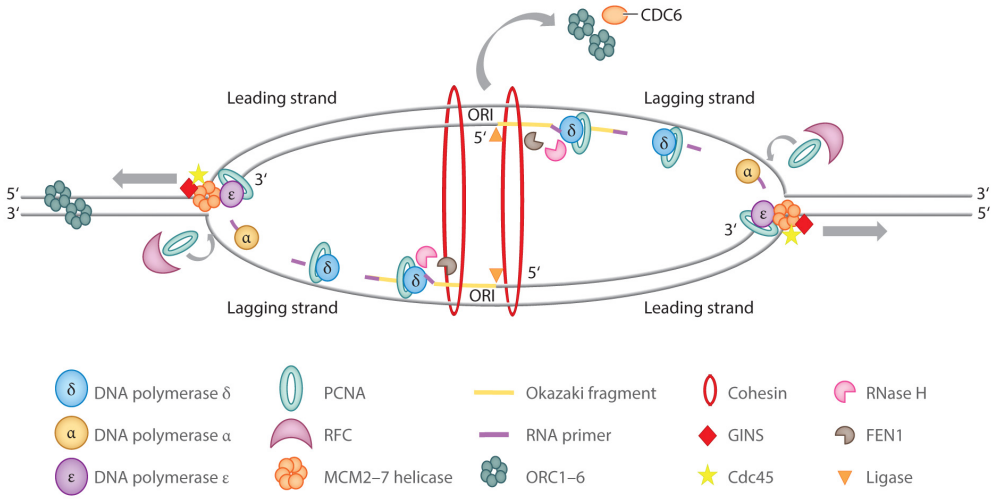

Figure 6: Elongation (Snedeker et al. 2017)
Upon origin firing the ORC complex and CDC6 dissociate from the origin and the CMG helicase starts to unwind the parental DNA duplex in a bidirectional fashion. The CMG replication complex now forms the core of the multi protein replicative machinery. Pol-α synthesizes RNA primers on the newly formed single stranded DNA that serve as a start point for the replicative polymerases δ and ε. The leading strand is assembled in a continuous manner through the activity of Pol-ε. The lagging strand is synthesized as discontinuous Okazaki fragments, generated by the combined actions of Pol-α and Pol-δ. It is subsequently processed by FEN1, RNase H and DNA ligase 1 to complete synthesis. PCNA serves as a recruitment and processivity factor for the main replicative DNA polymerases and is loaded onto the DNA by RFC. The newly formed sister chromatids are linked by cohesins after the replication fork has passed through.

For a long time, it was assumed that DNA synthesis on the leading and lagging strand must be tightly coordinated to avoid the formation of large single stranded gaps on the nascent strands. Recent evidence however indicated that the leading- and lagging-strand polymerases within a single replisome can assume individually changing rates of synthesis interspersed with complete pauses. This suggests that the two polymerases are not coordinated and that DNA replication on the leading- and lagging-strand proceeds in a kinetically discontinuous manner (Graham et al. 2017).

3.4.4. Replication termination

If the elongation process goes on for sufficient time, converging replication forks coming from adjacent origins will eventually meet and fuse in a process called replication termination. Our current understanding of the eukaryotic termination process is still incomplete. Nonetheless, several general concepts have emerged in recent years. At least in the model organism Saccharomyces cerevisiae, termination preferentially occurs at specific termination regions containing fork pausing elements, but it is not clear whether this holds true for other eukaryotes as well (Fachinetti et al. 2010). Replication termination is widely believed to consist of at least four, not necessarily consecutive, steps. During the first step, termed dissolution, the last stretch of the parental DNA duplex between the converging forks is unwound and the two replisomes come into direct contact. The dissolution step is followed by ligation, during which residual single stranded gaps are filled in and the two nascent daughter strands are ligated to each other. Ligation is accompanied by simultaneous decatenation, a process by which left over catenanes between the daughter chromosomes are removed. As a final step, the replisome gets disassembled and removed from the DNA (Dewar et al. 2015). Studies in budding yeast and

Xenopus egg extract have shown that replisome disassembly is initiated by ubiquitination of the CMG helicase on its MCM7 subunit by the E3 ligase complex SCF^{Dia2}. Ubiquitinated CMG is then recognized and rapidly disassembled by the segregase CDC48/p97 (Maric et al. 2014; Moreno et al. 2014).

3.5. Replication stress

As mentioned in previous chapters, the normal replicative process and the consequences of replication stress are major drivers of mutation and genome instability in human cells (Técher et al. 2017). Due to its prominent role in carcinogenesis replication stress has even been proposed as a separate hallmark of cancer (Macheret & Halazonetis 2015).

During any normal S-Phase the replicative machinery is confronted with countless obstacles that originate from both intracellular and extracellular sources (*Figure 7*). Troubles of this kind are often summarized under the term replication stress and are widely regarded as a substantial challenge to genome stability and cell survival. Despite extensive research efforts in this field, no single unifying definition of replication stress has been established thus far and there is no clear set of cellular markers that explicitly characterize it (Zeman & Cimprich 2014). In this thesis, replication stress will be defined as the transient slowing or stalling of overall DNA synthesis and individual replication forks.

3.5.1. Causes of replication stress

Replication forks are frequently challenged by unrepaired DNA lesions on the parental duplex, which can act as physical barriers for the replicative machinery (Zeman & Cimprich 2014; Berti & Vindigni 2016). Such lesions are caused by diverse environmental or endogenous DNA damaging agents that have been extensively discussed in previous chapters. This chapter focuses instead on replicative stress caused by processes that are inherent to DNA replication itself.

Even though the replicative polymerases Pol-δ and Pol-ε are highly accurate at base pairing, they are surprisingly poor when it comes to discriminating between deoxy-ribonucleotides (dNTPs) and ribonucleotides (rNTPs). This leads to a strikingly high rate of ribonucleotide misincorporation into nascent DNA. Ribonucleotides on the template strand can induce replication stress by stalling the replicative polymerases. Furthermore, they carry the risk of being converted into single stranded DNA nicks by TOP1 (Dalgaard 2012; Zeman & Cimprich 2014). Collisions between the replisome and the DNA transcription machinery are a further prominent source of replication stress (García-Muse & Aguilera 2016; Hamperl & Cimprich 2016; Merrikh 2017). Such events have been proposed to cause chromosome instability at sites of very long human genes (Helmrich et al. 2011) as well as at highly transcribed regions replicated early in S-phase (Barlow et al. 2013). Several essential components of the replicative machinery, precursors (i.e. nucleotides) and histone proteins can become limiting during DNA replication. These shortages can slow-down replication forks and thus cause replication stress. It has been proposed that this plays an important role during early oncogenesis when uncontrolled activation of factors regulating cell proliferation causes a depletion of cellular nucleotides. This may lead to replication impairment, contributing to genome instability and cellular transformation (Bester et al. 2011; Zeman & Cimprich 2014).

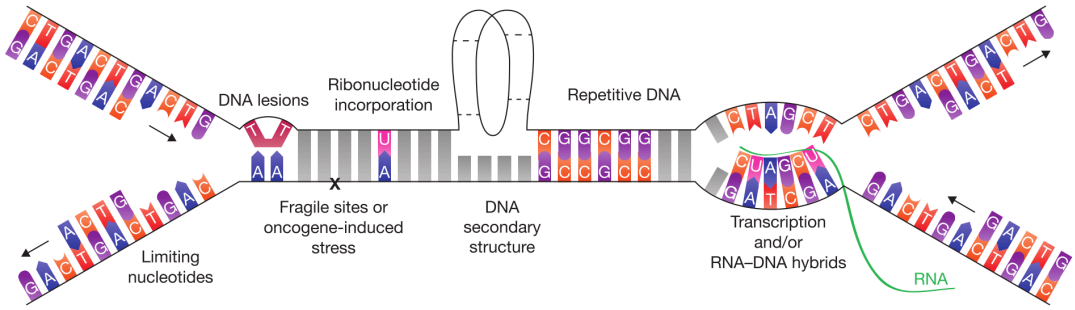

Figure 7: Causes of replication stress (modified from Zeman & Cimprich, 2014)
DNA replication stress originates from various causes. Replication forks can be challenged by unrepaired DNA lesions, or misincorporated ribonucleotides on the template strand and there can be collisions between replication and transcription at certain cites in the genome. Furthermore, nucleotides and other essential factors for replication can become limiting under specific circumstances. Inherently difficult to replicate DNA structures such as repetitive sequences or unusual DNA conformations are another important source of replication stress.

An important source of replication stress are repetitive DNA sequences that make up between 50 and 70% of the human genome. Certain repetitive elements can be inherently difficult to replicate. Palindromic sequence repeats may for example form secondary structures that can lead to fork stalling and breakage. Replication forks also tend to slow at GC-rich repetitive sequences, which has been attributed to G-quadruplex formation at these sites. It is thus not surprising that an increasing number of diseases such as Chorea Huntington and Friedrich Ataxia are correlated with genetic changes in repetitive sequences (Padeken et al. 2015). Another, overlapping class of difficult to replicate sequences are DNA stretches that can assume non-canonical B-DNA conformations. This includes regions forming triplex DNA, hairpins, cruciform, left handed Z-DNA and the above mentioned G-quadruplexes that can all serve as roadblocks for replication (Técher et al. 2017). Importantly, extended stretches of trinucleotide repeats that assume triplex conformation have been found to induce replication fork stalling and remodelling in vivo. This was shown using a plasmid based replication systems (Follonier et al. 2013), also employed in this thesis.

3.5.2. The cellular replication stress response:

Replicative stress, independently of its source, usually causes the formation of single-stranded DNA stretches of varying length. This can be attributed to an uncoupling of the replisomes helicase activity after stalling of the replicative polymerases and to the nucleolytic processing of various types of DNA lesions. The newly exposed ssDNA is quickly bound and protected by the single-strand binding protein RPA (Byun et al. 2005). RPA coated ssDNA that lies adjacent to newly replicated double-stranded DNA constitutes a recruitment signal for a diverse set of replication-stress-response factors. One of the first factors that gets recruited to these sites is ATRIP, a protein that is stably associated with the apical DNA replication stress response kinase ATR (ATM and Rad3-related). ATR recruitment to RPA coated ssDNA via ATRIP is not sufficient for its full activation but requires further activator proteins such as TopBP1 and ETAA1. Once ATR is activated, it phosphorylates numerous downstream substrates that help the cell to resolve problems at the fork and faithfully resume DNA replication (Zeman & Cimprich 2014; Bass et al. 2016; Haahr et al. 2016; Blackford & Jackson 2017). The ATR signalling process is highly

complex and has only been partially understood, despite almost two decades of research. One of the most important ATR targets under conditions of replication stress is the effector checkpoint kinase CHK1. Upon ATR dependent activation, CHK1 phosphorylates the phosphatase Cdc25a, which marks it for proteasomal degradation. Since Cdc25a is a crucial activator of both Cyclin E-Cdk2 and Cyclin B-Cdk1, its degradation supresses cell cycle progression and the firing of new origins, thereby providing additional time for the cell to resolve problems at the fork (Yazinski & Zou 2016). The suppression of origin firing is also crucial to prevent global exhaustion of rate limiting replication regulators and repair factors, which would lead to catastrophic genome disruptions (Toledo et al. 2017). Another important activity of the ATR pathway is to limit replication fork collapse by restraining fork processing enzymes such as SMARCAL1. Unrestrained SMARCAL1 activity can produce fork configurations that are targeted and cleaved by the SLX4/MUS81 nuclease complex. Furthermore, ATR regulates the availability of deoxy-ribonucleotides in the cell by promoting an increase in the cellular pool of the ribonucleotide reductase subunit RRM2 (Blackford & Jackson 2017). ATR and the closely related ATM kinase phosphorylate many of the same substrates and thus engage in considerable cross-talk. The most prominent of these shared targets is histone variant H2AX, which can be phosphorylated on serine 139 (γH2AX). γH2AX thus represents a general marker for replication stress and DNA damage (Técher et al. 2017).

3.6. Replication fork reversal

Replication fork reversal is a key protective mechanism for fork stabilization under replicative stress. It is achieved by transforming an active replication fork into a four-way junction through partial reannealing of the parental DNA duplex and simultaneous displacement and annealing of the two newly synthesized strands into a fourth, regressed arm (Neelsen & Lopes 2015). This process has recently emerged as an evolutionary conserved response to diverse types of replication stress, including DNA damaging agents (Zellweger et al. 2015; which is part of this thesis), oncogene activation (Neelsen et al. 2013) and difficult to replicate DNA sequences (Follonier et al. 2013). Despite its crucial role in genome stability maintenance, the precise mechanistic processes and signalling cascades governing the reversal and subsequent restart of replication forks are only partially understood (Quinet et al. 2017). The following subchapters will summarize the current state of knowledge and try to indicate important gaps in our understanding of the fork reversal pathway.

3.6.1. Mechanisms of reversal

The different factors and exact mechanistic steps necessary for the formation of reversed forks are still mostly elusive, even though several key players have been identified (*Figure 8*). The two SNF-2 family translocases SMARCAL1 and ZRANB3 have recently been shown to mediate the transition from active to reversed replication forks. SMARCAL1 has been shown to assist in the reversal of replication forks with extensive ssDNA gaps in Xenopus laevis egg extract under conditions of mild genotoxic stress (Kolinjivadi et al. 2017). Furthermore, SMARCAL1 promotes fork reversal in hydroxyurea treated human breast cancer cells, which depends on its ability to bind RPA (Taglialatela et al. 2017). However, SMARCAL1 is also recruited to replication forks in the absence of genotoxic treatments (Dungrawala et al. 2015) and has been suggested to play an important role in the resolution of endogenous replication stress (Poole & Cortez 2017). The ZRANB3 translocase was shown to regulate fork speed, replication fork reversal and chromosome integrity upon treatment with genotoxic substances in human cells. To

elicit its fork reversal activity under stress conditions, ZRANB3 needs to be recruited to replication forks via binding to poly-ubiquitinated PCNA (Vujanovic et al. 2017). Interestingly, HLTF, one of the E3 ligases contributing to the poly-ubiquitination of PCNA, possesses DNA translocase activity and has also been directly implicated in fork slowing and reversal in human cells (Kile et al. 2015). The human recombinase RAD51 is required for reversing uncoupled replication forks upon genotoxic stress, pointing to a hitherto unappreciated role of homologous recombination factors in fork remodelling (Zellweger et al. 2015). In contrast to classical HR repair, RAD51 mediated fork reversal neither depends on the presence of BRCA2 nor on the formation of a stable RAD51 nucleofilament (Mijic et al. 2017). The reason for this discrepancy may be that RAD51 fork reversal activity requires no extensive homology search, since the different arms of the replication fork are in such close proximity (Quinet et al. 2017). The 3'-5' DNA helicase FBH1, a known interactor of RAD51 (Masuda-Ozawa et al. 2013), was also shown to promote fork reversal in human cells (Fugger et al. 2015). It has thus been speculated that FBH1 may assist RAD51 in the fork remodelling process (Neelsen & Lopes 2015). It is still unclear whether the currently known fork reversal factors show functional interactions or if they are each required for the remodelling of distinct structures, arising from different sources of replication stress (Quinet et al. 2017).

Upon certain genotoxic treatments reversed replication forks are observed at a frequency of up to 35% of total forks in human cells (Ray Chaudhuri et al. 2012). However, these structures also make up 3-6% of replication forks at any given time during unperturbed S-phase (Zellweger et al. 2015), where they most likely arise due to endogenous obstacles such as the presence of repetitive DNA sequences (Follonier et al. 2013). Considering that between 50 and 70% of the human genome consist of repetitive sequences, one may expect that most replication forks will at some point assume a reversed conformation in the course of a full S-Phase.

3.6.2. Protection and Restart

Once formed, reversed replication forks display a double stranded DNA end on their fourth regressed arm, which can become a substrate for nucleolytic attacks (*Figure 8*). Recent discoveries are implicating central homologous recombination factors in the protection of these structures. It was found that in absence of BRCA1/2, stalled forks are extensively degraded in a manner that depends on the endonuclease activity of MRE11 (Schlacher et al. 2011; Schlacher et al. 2012). This emerging role of the BRCA proteins can be functionally uncoupled from their established activities in HR repair and was shown to be a leading cause of chemo sensitivity in BRCA2-deficient tumours (Ray Chaudhuri et al. 2016). Several recent studies have identified the regressed arm of reversed replication forks as the entry point for MRE11 dependent fork degradation (Mijic et al. 2017; Taglialatela et al. 2017; Lemaçon et al. 2017; Kolinjivadi et al. 2017). Furthermore, it was found that CtiP initiates MRE11 dependent degradation of reversed forks in BRCA2-deficient cells and that the degradation is subsequently extended by the EXO1 nuclease (Lemaçon et al. 2017). This sequence of events is clearly reminiscent of the resection process known from HR repair.

Currently, two separate mechanisms are known to mediate the restart of reversed replication forks in human cells (*Figure 8*). The first pathway relies on the ATP-dependent helicase RECQ1, which binds to reversed forks and pushes them back into an active conformation via its branch migration activity. Under conditions of replication stress and DNA damage, the RECQ1 helicase is transiently inhibited by

PARP1 dependent parylation. Eventual repair of DNA damage and alleviation of replication stress lead to the local inactivation of PARP1, which releases RECQ1 from its inhibition and permits fork restart by branch migration (Berti et al. 2013). The second restart pathway is restrained in its activity by the binding of RECQ1 to reversed forks. This pathway depends on the unwinding and partial resection of the regressed arm via the combined actions of the Werner syndrome helicase WRN and the helicase-nuclease DNA2 (Thangavel et al. 2015). The precise mechanism downstream of this resection process is not yet understood but has been speculated to include the activity of unidentified branch migration factors or RAD51 mediated HR dependent restart (Neelsen & Lopes 2015).

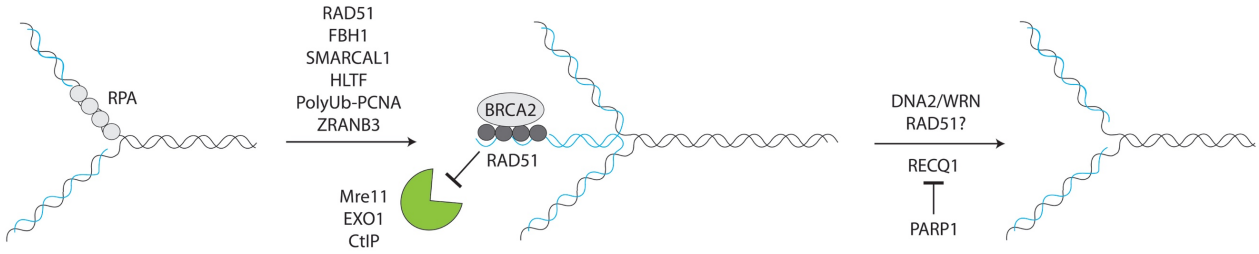

Figure 8: Replication fork reversal, protection and restart (based on Neelsen & Lopes, 2015 and Quinet et al. 2017)
Uncoupling of replication forks upon replicative stress exposes ssDNA at the junction, which is rapidly bound by RPA. This promotes the recruitment of fork remodeling factors, including multiple translocases and recombinases that may act together in different combinations depending on the source of replicative stress in the cell. Once the forks are brought into the reversed state, a BRCA2 dependent RAD51 filament forms on the regressed arm. This filament protects the forks against extensive nucleolytic degradation of newly synthesized DNA. Reversed forks can be restarted either via RECQ1 mediated branch migration or through a process that involves partial resection of the regressed arm by WRN and DNA2.

3.6.3. Comparing reversed forks to DNA double strand breaks

Recent advances in the field have made it clear to the careful observer that reversed replication forks bare a certain resemblance to DNA double strand breaks both in structure and in the mechanisms of their resolution (Quinet et al. 2017). The two structures both present a double stranded DNA end that can serve as a substrate for nucleolytic degradation. Strikingly, the very same nucleases, ie. MRE11, EXO1 and DNA2, are active in both scenarios. Furthermore, the central HR factors BRCA2 and RAD51 are involved in the resolution of reversed forks in a process that mirrors their function in double strand break repair. Both structures can also be resolved in an HR independent way, which is achieved by NHEJ for DSBs and via branch migration in the case of reversed forks.

Whether the processing and resolution is regulated by similar signalling pathways in both cases is yet unclear. Interestingly, 53BP1, one of the main downstream effectors of the ubiquitin dependent DNA damage response, has recently been implicated in the restart of replication forks stalled by genotoxic treatments in avian cells (Xu et al. 2017). In addition, it was shown that 53BP1 protects stalled replication forks against DNA2 dependent degradation in yeast cells defective of Mec1, the yeast homologue of ATR (Villa et al. 2018). This hints at a potential regulatory role of the ubiquitin dependent DNA damage response in the protection and restart of reversed replication forks. In my PhD work I have investigated the role of several DNA damage signalling factors in the protection and restart of replication forks stalling at repetitive DNA sequences during unperturbed replication. I have found that

the central DDR factors ATM, RNF8, RNF168 and 53BP1 prevent reversed fork accumulation and subsequent resection at difficult to replicate sequences throughout the human genome. Furthermore, I have shown for the first time that chromatin is regularly assembled on the regressed arm of reversed replication forks. This provides an attractive target for the E3 ligase RNF168, whose role in fork protection depends on its ability to ubiquitinate H2a type histones.

4. Histone ubiquitination by the DNA damage response is required for efficient DNA replication in unperturbed S-phase (Schmid et al.)

This chapter consists of the manuscript Schmid et al. accepted for publication in Molecular Cell at the time of writing.

Jonas A. Schmid[1], Matteo Berti[1], Franziska Walser[1], Maria Chiara Raso[1], Fabian Schmid[1], Jana Krietsch[1], Henriette Stoy[1], Katharina Zwicky[1], Sebastian Ursich[1], Raimundo Freire[2], Massimo Lopes[1*] and Lorenza Penengo[1,3*]

[1]Institute of Molecular Cancer Research, University of Zurich, 8057 Zurich, Switzerland; [2]Unidad de Investigación, Hospital Universitario de Canarias, Instituto de Tecnologías Biomédicas, Ofra s/n, La Cuesta, La Laguna, Tenerife, Spain. [3]Lead contact. [*]Correspondence: penengo@imcr.uzh.ch (LP), lopes@imcr.uzh.ch (ML)

Summary

Chromatin ubiquitination by the ubiquitin ligase RNF168 is critical to regulate the DNA damage response (DDR). DDR deficiencies lead to cancer-prone syndromes, but whether this reflects DNA repair defects is still elusive. We identified key factors of the RNF168 pathway as essential mediators of efficient DNA replication in unperturbed S-phase. We found that loss of RNF168 leads to reduced replication fork progression and to reversed fork accumulation, particularly evident at repetitive sequences stalling replication. Slow fork progression depends on MRE11-dependent degradation of reversed forks, implicating RNF168 in reversed fork protection and restart. Consistent with regular nucleosomal organization of reversed forks, the replication function of RNF168 requires H2A ubiquitination. As this novel function is shared with the key DDR players ATM, gH2A.X, RNF8 and 53BP1, we propose that double-stranded ends at reversed forks engage classical DDR factors, suggesting an alternative function of this pathway in preventing genome instability and human disease.

Keywords: RNF168, RNF8, 53BP1, ATM, RIDDLE syndrome, ataxia telangiectasia, chromatin ubiquitination, H2AK15Ub, fork reversal, genome stability

Introduction

Maintenance of genome stability is an active process within the cells, which copes with the huge number of DNA lesions arising both from exogenous (i.e. genotoxic drugs and irradiation) and endogenous (i.e. DNA replication) sources. Ubiquitin (Ub) mediated post-translational modifications play essential roles in this process, finely regulating both the DNA damage response (DDR) and DNA replication (Smeenk and Mailand, 2016). A paradigmatic example of the ubiquitination signaling role is represented by the pathway activated by DNA double-strand breaks (DSBs) (Smeenk and Mailand, 2016). Upon DSB formation, the histone variant H2A.X is phosphorylated by the ATM kinase leading to

the recruitment of the ubiquitinating pair RNF8/UBC13, which promotes K63-linked ubiquitination (Huen et al., 2007; Kolas et al., 2007; Mailand et al., 2007; Nowsheen et al., 2018; Thorslund et al., 2015; Wang and Elledge, 2007). These ubiquitinating events allow the recruitment of the Ub ligase RNF168 to damaged chromosomes, where it targets histones H2A and H2A.X, in a UbK27- dependent manner (Gatti et al., 2015). Remarkably, RNF168 generates a highly specific mark on chromatin, by modifying the N-terminal site of H2As on K13 and K15 (Gatti et al., 2012; Mattiroli et al., 2012), referred as H2AK13/15Ub. Ubiquitinated H2As represent the docking site for additional factors, such as 53BP1 and the BRCA1 complex, which activate downstream events to repair damaged DNA by promoting either non- homologous end joining (NHEJ) or homologous recombination (HR), respectively.

RNF168's activity and the H2AK13/15Ub histone mark are at the hub of the DDR pathway, and their key role has been clearly demonstrated by the identification of germline mutations in the RNF168 gene as the cause of a combined disorder called RIDDLE syndrome, characterized by radiosensitivity, immunodeficiency, microcephaly, growth retardation and cancer predisposition (Devgan et al., 2011; Pietrucha et al., 2017; Stewart et al., 2009). Similarly, mutations in the apical kinase ATM are associated with the human syndrome Ataxia telangiectasia, which combines neurological defects with immunosuppression and elevated cancer risk. Knockout mouse models for all genes in this pathway are compatible with life, but display different combinations of phenotypes, such as abnormal development, infertility, immunodeficiencies, premature aging and/or cancer predisposition (Specks et al., 2015). Overall, while immunodeficiency and radiosensitivity are clearly linked to the DSB response defect, the molecular mechanisms underlying the other defects are currently unknown.

Recent work has investigated the role of classical DSB processing and signaling factors in response to replication stress. HR factors have long been known to mediate specialized pathways of replication fork restart, although this was long assumed to involve collapse of stalled forks into DSBs (Petermann and Helleday, 2010). Moreover, DSB processing factors – such as the MRE11 nuclease – were found to regulate ssDNA accumulation on replication intermediates (Hashimoto et al., 2010). The BRCA genes – key HR factors and tumor suppressors (Roy et al., 2011) – were shown to limit this MRE11-dependent fork resection, preventing extensive degradation of newly synthesized DNA (Schlacher et al., 2011). This alternative function of these crucial HR factors can be genetically uncoupled from their classical role in DSB repair and was recently reported to underlie the exquisite chemosensitivity observed in BRCA2-defective tumors (Ray Chaudhuri et al., 2016; Schlacher et al., 2011). Differently from DSB processing and repair, the relevance of the DSB signaling pathway in DNA replication has not yet been thoroughly investigated. Large 53BP1 foci in G1-phase – described as "53BP1 nuclear bodies" – arise as a consequence of increased replication stress in the previous S-phase, via mitotic processing of residual replication intermediates into DSBs. Recently, Rad9/53BP1 was shown in yeast to protect stalled forks from degradation (Villa et al., 2018) and to modulate in mammals checkpoint signaling and stalled fork restart (Her et al., 2018; Xu et al., 2017). However, these observations were made upon exogenous genotoxic treatments, and a potential role of DSB signaling factors in unperturbed replication has not been investigated to date.

Replication fork remodeling into four-way junctions – also known as replication fork reversal – has recently emerged as a global response to a variety of conditions of replication stress, such as oncogene activation and treatment with multiple genotoxins (Neelsen et al., 2013; Ray Chaudhuri et al., 2012; Zellweger et al., 2015). Intriguingly repetitive sequences prone to form secondary structures are also

sufficient to induce frequent fork reversal, even in the absence of genetic or chemical perturbations (Follonier et al., 2013a). This transaction was proposed to limit fork progression under unfavorable conditions, thereby preventing breakage of replicating chromosomes (Neelsen and Lopes, 2015). However, the regressed arm of reversed forks was also recently shown to act as necessary entry points for fork degradation in BRCA-defective cells (Lemacon et al., 2017; Mijic et al., 2017; Taglialatela et al., 2017). The striking structural similarity between the double-stranded end of regressed arms and DSBs raises the intriguing possibility that DSB processing factors modulate stability and restart of transiently stalled forks, while they are remodeled into four-way junctions. However, whether these alternative double-stranded ends could also be recognized and modulated by classical DSB signaling pathways has remained elusive.

Here we show that RNF168 and other factors of the DDR cascade are recruited to replication factories and promote efficient replication fork progression during unperturbed S-phase, by preventing reversed fork accumulation at difficult-to-replicate sequences and their processing by MRE11 nuclease. This alternative function of the DDR pathway requires RNF168-dependent ubiquitination of H2A, suggesting that modifications of chromatin – which we found regularly assembled on the regressed arms – promote efficient restart of endogenously formed reversed forks and allow continuous fork progression. This novel activity of the DDR pathway may provide alternative molecular explanations to the complex phenotypes associated with DDR defects in animal models and human cancer-prone syndromes.

Results

RNF168 localizes at replication factories in unperturbed conditions

Although RNF168 activity has been extensively studied in the context of DSB signaling, not much is known about its function during unperturbed proliferation. We thought to retrieve some information from its subcellular localization in undamaged cells: while RNF168 is rapidly recruited to DDR foci upon induction of DSBs, showing an evident punctuate staining, its distribution in unperturbed conditions is more heterogeneous within the cell population. However, using a U2OS Flp-In T-REx system expressing FLAG-RNF168 to obtain controlled and detectable expression of RNF168, we noted that in a subpopulation of cells undergoing DNA replication RNF168 partially co-localizes with replication factories marked by PCNA foci (Figure 1A). We thus investigated a possible association between RNF168 and PCNA by performing co-immunoprecipitation and GST pull-down experiments. Both biochemical approaches clearly showed that PCNA and RNF168 interact in cells (Figure 1B). To further substantiate this observation, we set up a proximity ligation assay (PLA) between RNF168 and PCNA, using both wild-type FLAG-RNF168 and a mutant form (referred as UBD), which carries inactivating point mutations in the three Ub binding domains UMI, MIU1 and MIU2 (Penengo et al., 2006; Pinato et al., 2011). The UBD mutant is unable to bind ubiquitinated proteins and hence does not properly localize to chromatin (Figure 1C) (Pinato et al., 2011). PLA analysis shows that RNF168 can be found in close proximity to PCNA, while the UBD does not show any significant association (Figure 1D). Moreover, to determine whether RNF168/PCNA interaction occurs in a specific cell cycle phase, we labelled cells with 5- ethynyl-2'-deoxyuridine (EdU) to clearly mark DNA synthesis, and we analyzed them by quantitative image- based cytometry (QIBC) (Gudjonsson et al., 2012). This allowed us to determine that the interaction between RNF168 and PCNA, measured by PLA, mainly occurs during

late S-phase (Figures 1E, 1F and S1). Using a similar experimental setting, we found that the cell cycle distribution of the histone modification H2A-K15Ub, specifically generated by RNF168, correlates with the distribution of PLA signal obtained for RNF168/PCNA (Figures 1G and 1H), indicating that RNF168 is active on chromatin in this specific cell cycle phase. Altogether these data suggest a potential role of RNF168 in DNA replication during unperturbed S-phase.

RNF168 is required for proper DNA replication in unperturbed conditions

To test this hypothesis, we asked whether depletion of RNF168 has an impact on DNA synthesis, by measuring EdU incorporation in S-phase using flow-cytometric analysis (FACS). We found that U2OS shRNF168 cells show a marked reduction in the rate of EdU incorporation upon RNF168 downregulation (doxycycline addition), indicating impaired DNA synthesis (Figures 2A, S1A and S1B). We next used the DNA fiber spreading assay (Jackson and Pombo, 1998) to investigate the effect of RNF168 depletion on replication fork progression at single-molecule level. Strikingly, we found an approximately 40% reduction in fork speed in unperturbed RNF168-deficient cells, using either shRNA- or siRNA-mediated downregulation with different target sequences (Figure 2B). This reduction in fork speed involved the full population of replication forks and was also visible upon shorter labeling times, albeit less pronounced (Figure S2C). We next assessed whether this reduced fork speed reflected frequent fork pausing, analyzing forks diverging from the same replication origin. While in control cells these forks move at similar rates (sister fork ration close to 1), RNF168 depletion led to marked sister fork asymmetry, indicating an increased frequency of fork stalling upon RNF168 inactivation (Figure 2C). Interestingly, these effects on DNA replication were not accompanied by detectable global DDR activation, as revealed by overall nuclear levels of H2A.X phosphorylation (gH2A.X, Figure 2A, right panel) and by canonical markers of checkpoint activation (KAP1-, CHK1- and RPA-phosphorylation; Figure 2D). To further exclude that this reduction in DNA synthesis upon RNF168 depletion is due to increased DNA damage, we performed a DNA comet assay comparing RNF168-proficient with -deficient cells. The two cell populations did not differ significantly, while cells treated with the DNA damaging agent camptothecin (CPT) expectedly show a remarkable accumulation of chromosomal breaks (Figures 2E and S2D). These data strongly suggest that the delayed fork progression observed in RNF168-defective cells does not reflect detectable accumulation of endogenous DNA damage and global DDR signaling. To confirm the effect of RNF168 loss on replication fork progression in another system, we used fibroblasts derived from a RIDDLE syndrome patient (RIDDLE cells) (Stewart et al., 2007) – which contain inactivating mutations of the RNF168 gene in both alleles – and the same cells complemented with HA-RNF168 as a reference (Stewart et al., 2009). Importantly, both the reduced EdU incorporation rate and the slow-down in fork speed as displayed by DNA fiber track length are recapitulated in this experimental system and are suppressed by exogenous RNF168 expression (Figures 2F and S2E).

Unperturbed RNF168-deficient cells display elevated fork reversal, which is required for the observed fork slowing

Recent evidence in human cells suggests that replication forks are frequently undergoing remodeling into four- way junctions (namely reversed forks), upon various types of exogenous replication stress or at endogenous difficult-to-replicate loci (Follonier et al., 2013b; Neelsen and Lopes, 2015; Zellweger et al., 2015). Intriguingly, the regressed arm at these structures exposes a double-stranded DNA end,

which strikingly resembles a DSB and may thus implicate the function of DSB-responding factors. To test the hypothesis that replication fork remodeling underlies the involvement of DDR factors in unperturbed replication, we employed an established EM protocol to stabilize and visualize in vivo the architecture of replication intermediates, in presence or absence of RNF168. Strikingly, RNF168-deficient cells reproducibly showed a ~3-fold increased accumulation of reversed forks during unperturbed replication, compared to RNF168-proficient cells (Figures 3A and S3A- D; Table S1A), suggesting that RNF168 affects the dynamics of these remodeled replication intermediates. Reversed forks are transient intermediates and their accumulation upon genotoxic treatments depends on the balance between promoting activities – such as the central recombinase RAD51 or the dsDNA translocases SMARCAL1 and ZRANB3 – and restart/resolution factors, such as the RECQ1 helicase, which is negatively regulated by PARP1-dependent PARylation ((Berti et al., 2013; Neelsen and Lopes, 2015) and references therein). Importantly, we found that preventing fork reversal by depleting either RAD51 or SMARCAL1 in RNF168-deficient cells completely restored normal rates of fork progression during unperturbed S-phase (Figures 3B-C and S3E-F), while depletion of ZRANB3 – reportedly dispensable for endogenous levels of fork reversal (Vujanovic et al., 2017) – did not recapitulate the same effect (Figures 3D and S3G). Analogously, PARP inhibition restored efficient fork progression in RNF168-defective cells in a RECQ1-dependent manner (Figures 3E and S3H). Remarkably, PARP inhibition in RIDDLE cells also fully rescued efficient fork progression to the levels observed upon RNF168 complementation (Figures 3F and S3I). Altogether, these results indicate that replication fork reversal is a prerequisite for the defective fork progression observed upon RNF168 inactivation and suggest a potential role for RNF168 in promoting reversed fork restart. Furthermore, as RAD51 is strictly required for DSB repair, the suppression of fork slowing upon RAD51 inactivation strongly argues against accumulation of endogenous DSBs as the underlying mechanism of reduced fork progression in RNF168-defective cells. Along with the data in Figure 2D-E, this evidence further supports a DSB- independent role for RNF168 during unperturbed S-phase.

Upstream and downstream DDR factors are epistatic to RNF168 for its replication function

If the function of RNF168 in replication fork progression and remodeling truly reflects the formation of a double- stranded end at regressed arms, we reckoned that depletion of other DDR factors should result in similar defects. To address this point, we used various systems to target different DDR factors, alone or in combination with RNF168 depletion. First, we used shRNA inducible U2OS cells to test the contribution of RNF8 – which acts upstream of RNF168 in the DDR pathway – to unperturbed DNA replication. We found that, like RNF168, RNF8 depletion leads to a reduced rate of DNA synthesis - measured by EdU incorporation (Figure S4A) - and of replication fork progression (Figure 4A). Importantly, co-depletion of RNF8 and RNF168 did not lead to any further reduction in fork speed, suggesting that, in analogy to the DSB response, the two factors are epistatic. We obtained remarkably similar results in 53BP1 knockout U2OS cells, which displayed a reduced rate of DNA synthesis (Figure S4B) and fork progression that was not further exacerbated by concomitant RNF168 depletion (Figure 4B). Finally, we analyzed the contribution of ATM, the apical kinase of the DSB signaling pathway, responsible for RNF8/RNF168 recruitment at DSBs. We tested fork progression in U2OS shRNF168 cells optionally treated with the ATM inhibitor KU55933 and/or doxycycline, to conditionally downregulate RNF168. In parallel, we analyzed fork progression in AT (ataxia telangiectasia) patient cells (AT22iJE-T), which carry inactivating mutations in the ATM gene, and in their complemented counterpart (Savitsky

et al., 1995; Ziv et al., 1997). In both systems, we observed that ATM activity is required for efficient DNA replication: both pharmacological inhibition and genetic inactivation lead to reduced DNA fork progression during unperturbed S-phase, which is again epistatic to the effects observed upon RNF168 inactivation (Figure 4C and 4D). Moreover, similarly to the effects reported in RNF168-deficient cells (Figure 3A), our EM analysis revealed a 2.5-3.5 fold accumulation of reversed forks in RNF8- and 53BP1-deficient U2OS cells, as well as upon ATM inhibition (Figure 4E and Table S1B-D). Importantly, BRCA1 depletion had only a marginal effect on replication fork progression, which was not epistatic to RNF168 depletion (Figure S4C), suggesting that RNF168 role in replication is independent of the downstream HR pathway.

Although these data clearly indicate that the ATM/RNF8/RNF168/53BP1 signaling pathway is required for efficient DNA replication and for reversed fork turnover in unperturbed S-phase, we were puzzled by the absence of detectable checkpoint activation under these conditions (Figures 2A and 2D). We thus carefully monitored H2A.X phosphorylation throughout the cell cycle by QIBC analysis and found that cells in middle and late S-phase do show detectable gH2A.X foci even in the absence of exogenous treatments (Figures 4F and S4D). This gH2A.X signal is specific, since cells expressing the non-phosphorylatable version of histone H2A.X (namely H2A.X-S139A) did not show any reactivity with the phospho-specific antibody (see Figure S4E). Furthermore, this endogenous gH2A.X signal is largely reduced upon treatment with both ATR and ATM inhibitors (Figure 4F). Thus, despite undetectable global DDR activation (Figure 2A-2D), local ATR/ATM- mediated H2A.X phosphorylation detectably increases during cell cycle progression, reaching a peak in late S-phase and correlating with other marks of activation of the DDR cascade (Figures 1E and 1H). Accordingly, blocking this signaling cascade downstream by RNF168 depletion did not affect global H2A.X phosphorylation, but induced local accumulation of gH2A.X in these endogenous foci (Figures 2A, 4F, 4G and S4F). Similar conclusions could be drawn by iPOND (Sirbu et al., 2013), by which we found detectable levels H2A.X phosphorylation directly at replication forks, which were increased upon RNF168 depletion (Figure 4H). Finally, we tested whether the impairment of endogenous H2A.X phosphorylation resulted into similar replication phenotypes to those observed upon other DDR defects. Using untransformed RPE-1 cells expressing either wild-type H2A.X or its phosphorylation mutant (S139A; Figure S4E), we found that – similarly to all other tested DDR defects (Figure 4A-D) – defective H2A.X phosphorylation leads to accumulation of reversed forks and impaired replication fork progression, and that the latter defect is epistatic to ATM inhibition (Figures 4I and 4L; Table S1E). Altogether, these results suggest that, despite undetectable global activation of the DDR, local H2A.X phosphorylation during unperturbed S-phase engages classical DDR factors in controlling fork remodelling and promoting efficient fork progression.

Reduced fork speed upon RNF168 depletion depends on nucleolytic processing

Although fork reversal was proposed to assist fork integrity and restart upon replication stress (Neelsen and Lopes, 2015), it was also recently shown to trigger MRE11-dependent degradation of stalled forks under certain genetic perturbations, which mediates the chemosensitivity of BRCA-defective cells (Lemacon et al., 2017; Mijic et al., 2017; Ray Chaudhuri et al., 2016). We thus tested whether MRE11-dependent degradation is also implicated in the defects in fork progression and architecture observed upon interference with the DDR pathway. Using mirin as a well-characterized inhibitor of MRE11 nuclease activity at replication forks (Schlacher et al., 2011), we found that MRE11 inhibition significantly restored replication fork progression in all tested systems of RNF168-, RNF8-, 53BP1-,

ATM-, gH2A.X-depletion/inactivation conditions (Figure 5A-F). These data suggest that the fork slowing observed in all these conditions reflects increased MRE11 activity or accessibility to de-protected forks, leading to nucleolytic processing of newly synthesized DNA. In light of the limited processivity reported for cellular nucleases, the reduced track length observed upon DDR inactivation is unlikely to purely reflect degradation of nascent DNA. In fact, it may also result from impaired DNA synthesis while forks are engaged in unscheduled processing, ultimately leading to temporary fork stalling and consequently a reduced net rate of fork progression. Moreover, the partial rescue of fork speed observed upon mirin treatment might reflect the redundant action of nucleases other than MRE11 (Lemacon et al., 2017) at replication forks destabilized by inactivation of the DDR pathway. As reported (Mijic et al., 2017), mirin treatment per se did not affect the frequency of reversed forks. Surprisingly – and differently from what was reported at hydroxyurea-stalled forks upon BRCA defects (Lemacon et al., 2017; Mijic et al., 2017) – mirin treatment in unperturbed RNF8-, RNF168- or 53BP1-defective cells invariably lead to further marked accumulation of reversed forks (Figures 5G and S5A-B; Table S1A-C). Both in presence and absence of mirin, reversed forks accumulating upon RNF8, RNF168 or 53BP1 inactivation frequently exposed extended ssDNA stretches, further suggesting that inactivation of the DDR pathway promotes deregulated regressed arm resection in unperturbed conditions (Figures 5G and S5A-B).

It is seemingly counterintuitive that inhibiting MRE11 activity rescues fork speed, but leads to further accumulation of reversed forks, upon inactivation of various DDR factors. However, it is important to note that DNA fiber spreading measures the rate of fork progression over a distance, while EM analysis provides snapshots of the most persisting intermediates along the path of active forks (Vindigni and Lopes, 2017). As discussed above, MRE11-dependent degradation of transiently reversed forks may counteract DNA synthesis under conditions of defective DDR, leading to slow fork progression as a net effect. Impairing this degradation would prevent fork backtracking and promote continued fork progression via resection-independent restart of reversed forks. However, the overload and/or the intrinsic slowness of this restart mechanism upon MRE11 inhibition may force forks to spend a higher fraction of time in the reversed state, explaining our EM observations. In agreement with this scenario, inactivation of RECQ1 promotes reversed fork processing and leads to reversed fork accumulation in unperturbed conditions, albeit only slightly affecting the rate of fork progression (Thangavel et al., 2015; Zellweger et al., 2015). The marked accumulation of reversed forks observed by inactivation of MRE11 and the DDR pathway is particularly striking, considering that these cells are not exposed to exogenous sources of genotoxic stress. This suggests that the RNF168 pathway is essential to counteract regressed arm resection and to provide efficient restart of endogenously reversed forks, preventing their accumulation during unperturbed S-phase.

RNF168-dependent histone H2A ubiquitination is required for efficient DNA replication

A key event of the DSB signaling pathway is the ubiquitination of histone H2A on the N-terminal site K13/K15 promoted by RNF168 (Gatti et al., 2012; Mattiroli et al., 2012), which is required for the activation of the downstream signaling cascade, being directly recognized by 53BP1 (Fradet-Turcotte et al., 2013). Hence, we asked whether this histone mark is also essential for RNF168 function in DNA replication. To address this point, we took advantage of a single point mutation in RNF168 (R57D), which maintains the ubiquitinating capability but specifically impairs the ubiquitination of histone H2A (Mattiroli et al., 2012). We generated Flp-In T-REx U2OS stable cell lines expressing FLAG-RNF168 wild-type, UBD and R57D – all designed to be resistant to siRNAs targeting endogenous RNF168 – confirmed

that they had normal cell cycle progression and used them to perform complementation experiments (Figure S6A-C). We were able to restore efficient fork progression in siRNF168 depleted cells by expressing wild-type RNF168, but neither with UBD nor with R57D mutants, clearly indicating that not only the proper localization of RNF168, but also its specific activity towards histone H2A are required to mediate efficient fork progression during unperturbed S-phase (Figure 6A).

Regular nucleosome deposition occurs on regressed arms

Next, we reasoned that if the RNF168-mediated ubiquitination of H2A is required for the efficient DNA replication, via controlled restart of reversed forks, we would expect its targets (i.e. nucleosomes) to be present on the fourth, regressed arms of these intermediates. To address this important point, we performed in vivo psoralen crosslinking, coupled to EM analysis in denaturing conditions. As psoralen only intercalates in linker DNA between nucleosomes, this analysis reveals the nucleosomal organization of replicating molecules as a string of single-stranded bubbles separated by psoralen crosslinks, while non-chromatinized DNA (e.g. mitochondrial DNA, Figure S6D) appears as uniformly crosslinked DNA (Lucchini and Sogo, 1995). To verify that reversed forks could be confidently identified by denaturing EM analysis, we analyzed two different conditions of reversed fork accumulation – i.e. RNF168 depletion and topoisomerase I poisoning by CPT (Ray Chaudhuri et al., 2012) – and confirmed that their frequency was very similar in standard (native) and denaturing EM analysis (Figure S6E). We then carefully inspected the appearance of the identified regressed arms and noticed that single-stranded bubbles could be readily detected on all reversed replication forks found (Figure 6B), and had standard size (~150 bp per nucleosome) and periodicity as detected on parental and replicated DNA (Figures 6C, S6F and S6G). These data strongly suggest that, despite their transient nature, regressed arms are readily chromatinized and display standard nucleosomal organization, thereby offering targets for DDR-mediated modifications.

RNF168-deficient cells show defects in replicating repetitive sequences and accumulate chromosomal abnormalities in mitosis

Taken altogether, the replication defects described above upon inactivation of RNF168 and other DDR factors could be explained by a role of these proteins in replicating genomic regions that are intrinsically difficult to replicate and are thus particularly prone to fork reversal. Repetitive sequences – that are notably abundant in the human genome – are known to induce replication fork slowing (Neil et al., 2017). Recently, expanded GAA/TTC sequences – which are linked to the etiology of the neurodegenerative syndrome Friedreich's Ataxia – were shown to undergo frequent fork reversal under unperturbed conditions, by bidimensional electrophoresis (2D gels) and EM analysis of chromatinized, SV40-based plasmids (Follonier et al., 2013a) (Follonier and Lopes, 2014). Transfecting this plasmid system in U2OS shRNF168 cells, we verified that control plasmids were replicated with similar efficiency in presence or absence of RNF168 (Figure S7A). However, when the transfected plasmids contained expanded GAA/TTC regions, additional signals were readily detected by 2D gels, such as a spot on the Y arc due to fork pausing at repeats, a "X-spot" corresponding to triplex-mediated post-replicative junctions and a spike signal – departing from the pausing spot and reaching just above the X-spot – which was shown to be highly enriched in forks reversed at the repetitive sequence (Figure 7A) (Follonier et al., 2013a). Strikingly, by accurate quantification of 2D gels (Figure S7B) in two independent experiments, we reproducibly observed that the signal corresponding to reversed forks

was specifically increased upon conditional RNF168 depletion (Figure 7A and S7C). Along with the data in Figure 3A, these results strongly suggest that RNF168 is required to prevent reversed fork accumulation at endogenous difficult-to-replicate regions, presumably by promoting effective reversed fork restart. In line with these replication problems, we observed that prolonged (1 week) RNF168 depletion in U2OS shRNF168 cells, as well as permanent RNF168 inactivation in RIDDLE cells, are associated with increased chromosome abnormalities in mitosis, mostly visible as regions of decondensed chromatin along metaphase chromatids (Figure 7B and S7D-F). The effect is exacerbated when DNA replication is challenged by treating cells with low dose of aphidicolin (Aph, Figure 7C). Similar observations have been reported upon other genetic perturbations increasing endogenous replication stress and bona fide reflect genomic regions where replication is not complete upon entry into mitosis (Bhowmick and Hickson, 2017; Mankouri et al., 2013).

Discussion

We provide here several lines of evidence that well-established DDR factors of the RNF168 pathway play a crucial role to assist the replication process, in the absence of any exogenous genotoxic stress. A link between this pathway and endogenous replication stress was proposed while describing 53BP1 nuclear bodies, as these G1 phase-specific nuclear accumulations of 53BP1 were linked to unresolved replication stress inherited from the previous S-phase. However, these structures were suggested to arise via mitotic processing of these residual intermediates into DSBs, invoking the classical function of this pathway in DSB signaling and repair (Lukas et al., 2011). Similarly, Rad9/53BP1 – along with its antagonistic partner BRCA1 – was also recently involved in mechanisms of stalled fork processing and restart upon genotoxic treatments (Her et al., 2018; Villa et al., 2018; Xu et al., 2017), but a potential role of DSB signaling factors at replication forks during unperturbed S-phase has remained unexplored. We now show that these factors are required for efficient replication fork progression even in the absence of exogenous stress and detectable DNA breakage or DSB signaling, identifying a new crucial role for this pathway, in addition to its established role in the DSB response. Four important lines of evidence support a specific role for the RNF168-associated DDR pathway during unperturbed replication, independently of DSB formation: 1) RNF168 co-localizes and physically interacts with PCNA at a subset of replication factories in unperturbed conditions, which are not associated with detectable DDR activation or physical evidence of DNA breaks; 2) the replication function of RNF168 requires specific ubiquitination of histone H2A (H2AK15Ub), which is indeed cytologically detectable during unperturbed S-phase; 3) even though global DDR activation is undetectable in unperturbed S-phase, local ATR/ATM-dependent H2A.X phosphorylation can be monitored – especially in late S-phase - and plays a key role upstream of RNF168 activation in mediating efficient replication fork progression; 4) RNF168 is required to limit the accumulation of unusual replication intermediates at a prototype of difficult-to-replicate regions, i.e. expanded GAA repeats, previously shown to induce transient fork slowing and remodeling.

These findings are reminiscent of the surprising evidence that key DNA repair factors – such as BRCA factors and Fanconi anemia proteins – play a genetically separable role in replication fork protection, which emerged as a key determinant of the chemosensitivity observed in BRCA-defective tumors (Ray Chaudhuri et al., 2016; Schlacher et al., 2012). Several groups reported that this clinically relevant, unscheduled nucleolytic degradation observed in BRCA-defective cancer cells is triggered by the remodeling of stalled forks into four way junctions (Lemacon et al., 2017; Mijic et al., 2017; Quinet et

al., 2017; Taglialatela et al., 2017). Analogously, Tel1 – the yeast ATM ortholog – was recently reported to protect forks reversed upon Topoisomerase I inhibition from degradation (Menin et al., 2018). Remarkably, using multiple genetic tools to interfere with replication fork remodeling (i.e. PARP inhibition and RAD51, SMARCAL1 or RECQ1 depletion), we found that also the surprising defects observed during unperturbed replication upon inactivation of RNF168 strictly depend on replication fork reversal. In light of the striking similarity between DSBs and double-stranded ends exposed at regressed arms, we propose that, besides DSB processing, also DSB signaling factors are recruited to replication forks, as a consequence of their frequent remodeling, participating in modulating stability and restart of transiently stalled forks.

An important implication of our EM observations is that, even during unperturbed S-phase, a surprisingly high number of replication forks undergo reversal, imposing efficient fork restart mechanisms to prevent massive accumulation of reversed forks. This is consistent with the effects on fork progression and architecture reported for PARG inactivation, which is expected to shift the equilibrium of stalled forks towards a reversed state and result in their defective restart (Ray Chaudhuri et al., 2015). Several chromosomal regions have been identified as “difficult-to-replicate”, be it because of their repetitive nature, their propensity to form secondary structures and/or their active transcription (Glover et al., 2017; Neil et al., 2017). Difficult-to-replicate regions tend to be replicated towards the end of S-phase (Glover et al., 2017) and it is interesting to note that all marks of recruitment/activation of the RNF168 pathway (local gH2A.X, RNF168/PCNA proximity and H2AK15Ub) are also enriched in late S-phase. However, repetitive DNA represents up to 50% of all human genome, which may explain why almost the entire population of replication forks seems to experience delayed progression upon inactivation of the DDR pathway during the labelling time of a standard fiber spreading experiment. It is likely that a large fraction of replication forks frequently undergoes transient remodeling and requires an active DDR pathway to efficiently drive fork protection and restart. In that respect, RNF168 activation may consistently occur at replication forks, but the associated marks may become cytologically detectable only at chromosomal locations where fork pausing and reversal is less transient, i.e. at endogenous difficult-to-replicate regions, and/or where they inherently cluster, e.g. at condensed heterochromatic regions.

Another important implication of our data is that frequent, albeit transient, accumulation of double-stranded end during fork remodeling implies an intrinsic risk of DDR activation, posing very similar issues to those extensively characterized at telomeres (Maciejowski and de Lange, 2017). However, even in genetic conditions that prevent a rapid turnover of reversed forks and thus lead to their accumulation and processing, we observed no detectable evidence of global DDR activation. It will be an interesting avenue of future research to clarify whether, similarly to telomeres, active mechanisms have evolved to finely control DDR activation from these endogenous DNA ends, which are associated with every unperturbed S-phase and which certainly exceed telomeres in numbers. It is very likely that, despite the involvement of several classical DSB signaling factors in replication fork transactions, the DDR pathway may have specific mechanisms of signal amplification/limitation while playing its key role in unperturbed replication, in order to avoid interference with cell cycle progression. As shown here, detection of local and transient DDR activation during fork remodeling requires refined experimental conditions than those extensively characterized in response to DSBs.

How is the DDR pathway modulating the restart of reversed forks, limiting their accumulation? Our EM evidence suggests that inactivation of this pathway shifts the equilibrium of transiently stalled forks towards a reversed state and promotes nucleolytic processing of regressed arms, which at least partially limit accumulation of these structures in DDR-defective cells. As reversed fork restart was also showed to occur via both nucleolytic and non-nucleolytic pathways (Berti et al., 2013; Thangavel et al., 2015), it is tempting to speculate that recruitment of these factors to the DNA end at regressed arms may limit access to nucleases. This may be achieved by direct protection of the end and/or by promoting an alternative pathway of reversed fork restart – e.g. via RECQ1-dependent branch migration – which does not implicate DNA end resection. Alternatively and in analogy with its role in HR-mediated DSB repair (Smeenk and Mailand, 2016), RNF168- dependent chromatin ubiquitination may finely control regressed arm resection and promote RAD51-mediated fork protection and restoration mechanisms. Indeed, besides the well-established competition of 53BP1 and BRCA1 for DSB repair mechanism (Bunting et al., 2010), our data highlight the importance of ubiquitin- dependent 53BP1 functional recruitment in finely regulating the productive outcome of the recombination process, most likely by limiting unscheduled double-stranded end processing (Ochs et al., 2016). It will be important to explore specific protein partners of DDR factors during unperturbed S-phase, to gain mechanistic insight into the alternative function of these factors in replication.

The observation that regressed arms readily assemble nucleosomes is important and unexpected for structures that are inherently meant to be transient, as effective processing of these arms during fork restart would need nucleosome eviction. However, we reckon that nucleosome deposition on all DNA branches at the replication fork is passively accomplished, as it would be mechanistically difficult for the nucleosome deposition apparatus to distinguish regressed arms from standard replicated duplexes. Moreover, it would also be risky for the cells to have non-chromatinized DNA in proximity to paused replication forks, as this would increase the risk of unscheduled nucleolytic processing and chromosomal rearrangements. In fact, the evidence that nucleosomes are deposited on regressed arms – which were recently identified as entry points for fork degradation – suggests that histone modifications may be crucial determinant for the necessary equilibrium between DNA synthesis and degradation which assists efficient fork pausing and restart. This is in keeping with growing evidence that histone methylases – such as MLL3/4 – and chromatin remodelers – such as CHD4 – play critical roles in modulating fork accessibility by active nucleases, such as MRE11 (Ray Chaudhuri et al., 2016). It will be a challenging, but crucial task for future research to establish methods to specifically isolate and analyze the dynamic composition of nascent chromatin at regressed arms. Besides assessing the direct binding of DSB processing and signaling factors, such experiments promise to reveal the complex cellular apparatus, as well as epigenetic modifications, modulating reversed fork stability and restart. These studies may significantly help to shed light on mechanisms of genome instability during cellular proliferation and on patient-specific responses to chemotherapeutic treatments interfering with replication.

Overall, this work directly involves key DDR factors in the molecular mechanisms promoting efficient replication during unperturbed conditions. Some of the phenotypes associated with inactivation of these factors – such as immunodeficiency and radiosensitivity – are clearly linked to their role in the DSB response (Jackson and Bartek, 2009). However, it is tempting to speculate that other phenotypes associated with DDR inactivation at cellular levels – i.e. chromosomal instability – or in specific DDR-

defective animal models and patients may also reflect the alternative role in unperturbed replication that we propose here for this signaling cascade.

Acknowledgments

We are grateful to G. Stewart, J. Lukas, S. Jackson, N. Mailand, D. Durocher and Y. Shiloh for providing valuable cell lines, to M. Altmeyer and F. Teloni for support with QIBC studies, and to K. Mutreja for assistance with the comet assays and to R. Zellweger for assistance with electron microscopy. We thank M. S. Walser, M. Gatti and all members of the Lopes and the Penengo labs for technical assistance and helpful discussions. We thank J. Lukas and M. Altmeyer for useful suggestions on the project. We thank the Center for Microscopy and Image Analysis of the University of Zurich for technical assistance with electron microscopy and imaging analysis. This work was supported by the SNF grant 31003A_169959, the ERC Consolidator Grant 617102 and the Swiss Cancer League grant KFS-3967-08-2016 to M.L., by the SNF grant 31003A_166370, the Helmut Horten grant and the Novartis grant (#17A039) to L.P. M.B. is supported by a postdoctoral fellowship from the European Union's Horizon 2020 research and innovation programme (Marie Skłodowska-Curie grant agreement 704817).

Author contributions

J.A.S. performed and analyzed all EM, FACS, DNA fibers experiments, comet assays and immunofluorescence studies of gH2A.X; M.B. and F.W. performed additional immunofluorescence, QIBC and PLA; M.C.R. performed metaphase spreads; J.K. and F.S. assisted with biochemical studies; H.S. and K.Z. performed 2D gels; S.U. assisted with EM analysis; R.F. generated antibodies; M.L. and L.P. designed the experiments and wrote the manuscript, assisted by J.A.S.

Declaration of Interests

We declare no conflicts of interest.

References

Berti, M., Ray Chaudhuri, A., Thangavel, S., Gomathinayagam, S., Kenig, S., Vujanovic, M., Odreman, F., Glatter, T., Graziano, S., Mendoza-Maldonado, R., et al. (2013). Human RECQ1 promotes restart of replication forks reversed by DNA topoisomerase I inhibition. Nat Struct Mol Biol 20, 347-354.

Bhowmick, R., and Hickson, I.D. (2017). The "enemies within": regions of the genome that are inherently difficult to replicate. F1000Res 6, 666.

Bunting, S.F., Callen, E., Wong, N., Chen, H.T., Polato, F., Gunn, A., Bothmer, A., Feldhahn, N., Fernandez-Capetillo, O., Cao, L., et al. (2010). 53BP1 inhibits homologous recombination in Brca1-deficient cells by blocking resection of DNA breaks. Cell 141, 243-254.

Devgan, S.S., Sanal, O., Doil, C., Nakamura, K., Nahas, S.A., Pettijohn, K., Bartek, J., Lukas, C., Lukas, J., and Gatti, R.A. (2011). Homozygous deficiency of ubiquitin-ligase ring-finger protein RNF168 mimics the radiosensitivity syndrome of ataxia-telangiectasia. Cell Death Differ 18, 1500-1506.

Follonier, C., and Lopes, M. (2014). Combined bidimensional electrophoresis and electron microscopy to study specific plasmid DNA replication intermediates in human cells. Methods Mol Biol 1094, 209-219.

Follonier, C., Oehler, J., Herrador, R., and Lopes, M. (2013a). Friedreich's ataxia-associated GAA repeats induce replication-fork reversal and unusual molecular junctions. Nat Struct Mol Biol 20, 486- 494.

Follonier, S., Escapa, I.F., Fonseca, P.M., Henes, B., Panke, S., Zinn, M., and Prieto, M.A. (2013b). New insights on the reorganization of gene transcription in Pseudomonas putida KT2440 at elevated pressure. Microb Cell Fact 12, 30.

Fradet-Turcotte, A., Canny, M.D., Escribano-Diaz, C., Orthwein, A., Leung, C.C., Huang, H., Landry, M.C., Kitevski-LeBlanc, J., Noordermeer, S.M., Sicheri, F., et al. (2013). 53BP1 is a reader of the DNA- damage-induced H2A Lys 15 ubiquitin mark. Nature 499, 50-54.

Gatti, M., Pinato, S., Maiolica, A., Rocchio, F., Prato, M.G., Aebersold, R., and Penengo, L. (2015). RNF168 promotes noncanonical K27 ubiquitination to signal DNA damage. Cell Rep 10, 226-238.

Gatti, M., Pinato, S., Maspero, E., Soffientini, P., Polo, S., and Penengo, L. (2012). A novel ubiquitin mark at the N-terminal tail of histone H2As targeted by RNF168 ubiquitin ligase. Cell Cycle 11, 2538- 2544.

Glover, T.W., Wilson, T.E., and Arlt, M.F. (2017). Fragile sites in cancer: more than meets the eye. Nat Rev Cancer 17, 489-501.

Gudjonsson, T., Altmeyer, M., Savic, V., Toledo, L., Dinant, C., Grofte, M., Bartkova, J., Poulsen, M., Oka, Y., Bekker-Jensen, S., et al. (2012). TRIP12 and UBR5 suppress spreading of chromatin ubiquitylation at damaged chromosomes. Cell 150, 697-709.

Hashimoto, Y., Ray Chaudhuri, A., Lopes, M., and Costanzo, V. (2010). Rad51 protects nascent DNA from Mre11-dependent degradation and promotes continuous DNA synthesis. Nat Struct Mol Biol 17, 1305-1311.

Her, J., Ray, C., Altshuler, J., Zheng, H., and Bunting, S.F. (2018). 53BP1 Mediates ATR-Chk1 Signaling and Protects Replication Forks under Conditions of Replication Stress. Mol Cell Biol 38.

Huen, M.S., Grant, R., Manke, I., Minn, K., Yu, X., Yaffe, M.B., and Chen, J. (2007). RNF8 transduces the DNA-damage signal via histone ubiquitylation and checkpoint protein assembly. Cell 131, 901-914.

Jackson, D.A., and Pombo, A. (1998). Replicon clusters are stable units of chromosome structure: evidence that nuclear organization contributes to the efficient activation and propagation of S phase in human cells. J Cell Biol 140, 1285-1295.

Jackson, S.P., and Bartek, J. (2009). The DNA-damage response in human biology and disease. Nature 461, 1071-1078.

Kolas, N.K., Chapman, J.R., Nakada, S., Ylanko, J., Chahwan, R., Sweeney, F.D., Panier, S., Mendez, M., Wildenhain, J., Thomson, T.M., et al. (2007). Orchestration of the DNA-damage response by the RNF8 ubiquitin ligase. Science 318, 1637-1640.

Lemacon, D., Jackson, J., Quinet, A., Brickner, J.R., Li, S., Yazinski, S., You, Z., Ira, G., Zou, L., Mosammaparast, N., et al. (2017). MRE11 and EXO1 nucleases degrade reversed forks and elicit MUS81-dependent fork rescue in BRCA2-deficient cells. Nat Commun 8, 860.

Lucchini, R., and Sogo, J.M. (1995). Replication of transcriptionally active chromatin. Nature 374, 276-280.

Lukas, C., Savic, V., Bekker-Jensen, S., Doil, C., Neumann, B., Pedersen, R.S., Grofte, M., Chan, K.L., Hickson, I.D., Bartek, J., et al. (2011). 53BP1 nuclear bodies form around DNA lesions generated by mitotic transmission of chromosomes under replication stress. Nat Cell Biol 13, 243-253.

Maciejowski, J., and de Lange, T. (2017). Telomeres in cancer: tumour suppression and genome instability. Nat Rev Mol Cell Biol 18, 175-186.

Mailand, N., Bekker-Jensen, S., Faustrup, H., Melander, F., Bartek, J., Lukas, C., and Lukas, J. (2007). RNF8 ubiquitylates histones at DNA double-strand breaks and promotes assembly of repair proteins. Cell 131, 887-900.

Mankouri, H.W., Huttner, D., and Hickson, I.D. (2013). How unfinished business from S-phase affects mitosis and beyond. EMBO J 32, 2661-2671.

Mattiroli, F., Vissers, J.H., van Dijk, W.J., Ikpa, P., Citterio, E., Vermeulen, W., Marteijn, J.A., and Sixma, T.K. (2012). RNF168 ubiquitinates K13-15 on H2A/H2AX to drive DNA damage signaling. Cell 150, 1182-1195.

Menin, L., Ursich, S., Trovesi, C., Zellweger, R., Lopes, M., Longhese, M.P., and Clerici, M. (2018). Tel1/ATM prevents degradation of replication forks that reverse after topoisomerase poisoning. EMBO Rep.

Mijic, S., Zellweger, R., Chappidi, N., Berti, M., Jacobs, K., Mutreja, K., Ursich, S., Ray Chaudhuri, A., Nussenzweig, A., Janscak, P., et al. (2017). Replication fork reversal triggers fork degradation in BRCA2-defective cells. Nat Commun 8, 859.

Neelsen, K.J., and Lopes, M. (2015). Replication fork reversal in eukaryotes: from dead end to dynamic response. Nat Rev Mol Cell Biol 16, 207-220.

Neelsen, K.J., Zanini, I.M., Herrador, R., and Lopes, M. (2013). Oncogenes induce genotoxic stress by mitotic processing of unusual replication intermediates. J Cell Biol 200, 699-708.

Neil, A.J., Kim, J.C., and Mirkin, S.M. (2017). Precarious maintenance of simple DNA repeats in eukaryotes. Bioessays 39.

Nowsheen, S., Aziz, K., Aziz, A., Deng, M., Qin, B., Luo, K., Jeganathan, K.B., Zhang, H., Liu, T., Yu, J., et al. (2018). L3MBTL2 orchestrates ubiquitin signalling by dictating the sequential recruitment of RNF8 and RNF168 after DNA damage. Nat Cell Biol 20, 455-464.

Ochs, F., Somyajit, K., Altmeyer, M., Rask, M.B., Lukas, J., and Lukas, C. (2016). 53BP1 fosters fidelity of homology-directed DNA repair. Nat Struct Mol Biol 23, 714-721.

Penengo, L., Mapelli, M., Murachelli, A.G., Confalonieri, S., Magri, L., Musacchio, A., Di Fiore, P.P., Polo, S., and Schneider, T.R. (2006). Crystal structure of the ubiquitin binding domains of rabex-5 reveals two modes of interaction with ubiquitin. Cell 124, 1183-1195.

Petermann, E., and Helleday, T. (2010). Pathways of mammalian replication fork restart. Nat Rev Mol Cell Biol 11, 683-687.

Pietrucha, B., Heropolitanska-Pliszka, E., Geffers, R., Enssen, J., Wieland, B., Bogdanova, N.V., and Dork, T. (2017). Clinical and Biological Manifestation of RNF168 Deficiency in Two Polish Siblings. Front Immunol 8, 1683.

Pinato, S., Gatti, M., Scandiuzzi, C., Confalonieri, S., and Penengo, L. (2011). UMI, a novel RNF168 ubiquitin binding domain involved in the DNA damage signaling pathway. Mol Cell Biol 31, 118-126.

Quinet, A., Lemacon, D., and Vindigni, A. (2017). Replication Fork Reversal: Players and Guardians. Mol Cell 68, 830-833.

Ray Chaudhuri, A., Ahuja, A.K., Herrador, R., and Lopes, M. (2015). Poly(ADP-ribosyl) glycohydrolase prevents the accumulation of unusual replication structures during unperturbed S phase. Mol Cell Biol 35, 856-865.

Ray Chaudhuri, A., Callen, E., Ding, X., Gogola, E., Duarte, A.A., Lee, J.E., Wong, N., Lafarga, V., Calvo, J.A., Panzarino, N.J., et al. (2016). Replication fork stability confers chemoresistance in BRCA- deficient cells. Nature 535, 382-387.

Ray Chaudhuri, A., Hashimoto, Y., Herrador, R., Neelsen, K.J., Fachinetti, D., Bermejo, R., Cocito, A., Costanzo, V., and Lopes, M. (2012). Topoisomerase I poisoning results in PARP-mediated replication fork reversal. Nat Struct Mol Biol 19, 417-423.

Roy, R., Chun, J., and Powell, S.N. (2011). BRCA1 and BRCA2: different roles in a common pathway of genome protection. Nat Rev Cancer 12, 68-78.

Savitsky, K., Bar-Shira, A., Gilad, S., Rotman, G., Ziv, Y., Vanagaite, L., Tagle, D.A., Smith, S., Uziel, T., Sfez, S., et al. (1995). A single ataxia telangiectasia gene with a product similar to PI-3 kinase. Science 268, 1749-1753.

Schlacher, K., Christ, N., Siaud, N., Egashira, A., Wu, H., and Jasin, M. (2011). Double-strand break repair-independent role for BRCA2 in blocking stalled replication fork degradation by MRE11. Cell 145, 529-542.

Schlacher, K., Wu, H., and Jasin, M. (2012). A distinct replication fork protection pathway connects Fanconi anemia tumor suppressors to RAD51-BRCA1/2. Cancer Cell 22, 106-116.

Sirbu, B.M., McDonald, W.H., Dungrawala, H., Badu-Nkansah, A., Kavanaugh, G.M., Chen, Y., Tabb, D.L., and Cortez, D. (2013). Identification of proteins at active, stalled, and collapsed replication forks using isolation of proteins on nascent DNA (iPOND) coupled with mass spectrometry. J Biol Chem 288, 31458-31467.

Smeenk, G., and Mailand, N. (2016). Writers, Readers, and Erasers of Histone Ubiquitylation in DNA Double-Strand Break Repair. Front Genet 7, 122. Specks, J., Nieto-Soler, M., Lopez-Contreras, A.J., and Fernandez-Capetillo, O. (2015). Modeling the study of DNA damage responses in mice. Methods Mol Biol 1267, 413-437.

Stewart, G.S., Panier, S., Townsend, K., Al-Hakim, A.K., Kolas, N.K., Miller, E.S., Nakada, S., Ylanko, J., Olivarius, S., Mendez, M., et al. (2009). The RIDDLE syndrome protein mediates a ubiquitin- dependent signaling cascade at sites of DNA damage. Cell 136, 420-434.

Stewart, G.S., Stankovic, T., Byrd, P.J., Wechsler, T., Miller, E.S., Huissoon, A., Drayson, M.T., West, S.C., Elledge, S.J., and Taylor, A.M. (2007). RIDDLE immunodeficiency syndrome is linked to defects in 53BP1-mediated DNA damage signaling. Proc Natl Acad Sci U S A 104, 16910-16915.

Taglialatela, A., Alvarez, S., Leuzzi, G., Sannino, V., Ranjha, L., Huang, J.W., Madubata, C., Anand, R., Levy, B., Rabadan, R., et al. (2017). Restoration of Replication Fork Stability in BRCA1- and BRCA2-Deficient Cells by Inactivation of SNF2-Family Fork Remodelers. Mol Cell 68, 414-430 e418.

Thangavel, S., Berti, M., Levikova, M., Pinto, C., Gomathinayagam, S., Vujanovic, M., Zellweger, R., Moore, H., Lee, E.H., Hendrickson, E.A., et al. (2015). DNA2 drives processing and restart of reversed replication forks in human cells. J Cell Biol 208, 545-562.

Thorslund, T., Ripplinger, A., Hoffmann, S., Wild, T., Uckelmann, M., Villumsen, B., Narita, T., Sixma, T.K., Choudhary, C., Bekker-Jensen, S., et al. (2015). Histone H1 couples initiation and amplification of ubiquitin signalling after DNA damage. Nature 527, 389-393.

Toledo, L.I., Altmeyer, M., Rask, M.B., Lukas, C., Larsen, D.H., Povlsen, L.K., Bekker-Jensen, S., Mailand, N., Bartek, J., and Lukas, J. (2013). ATR prohibits replication catastrophe by preventing global exhaustion of RPA. Cell 155, 1088-1103.

Villa, M., Bonetti, D., Carraro, M., and Longhese, M.P. (2018). Rad9/53BP1 protects stalled replication forks from degradation in Mec1/ATR-defective cells. EMBO Rep 19, 351-367.

Vindigni, A., and Lopes, M. (2017). Combining electron microscopy with single molecule DNA fiber approaches to study DNA replication dynamics. Biophys Chem 225, 3-9.

Vujanovic, M., Krietsch, J., Raso, M.C., Terraneo, N., Zellweger, R., Schmid, J.A., Taglialatela, A., Huang, J.W., Holland, C.L., Zwicky, K., et al. (2017). Replication Fork Slowing and Reversal upon DNA Damage Require PCNA Polyubiquitination and ZRANB3 DNA Translocase Activity. Mol Cell 67, 882- 890 e885.

Wang, B., and Elledge, S.J. (2007). Ubc13/Rnf8 ubiquitin ligases control foci formation of the Rap80/Abraxas/Brca1/Brcc36 complex in response to DNA damage. Proc Natl Acad Sci U S A 104, 20759-20763.

Xu, Y., Ning, S., Wei, Z., Xu, R., Xu, X., Xing, M., Guo, R., and Xu, D. (2017). 53BP1 and BRCA1 control pathway choice for stalled replication restart. Elife 6.

Zellweger, R., Dalcher, D., Mutreja, K., Berti, M., Schmid, J.A., Herrador, R., Vindigni, A., and Lopes, M. (2015). Rad51-mediated replication fork reversal is a global response to genotoxic treatments in human cells. J Cell Biol 208, 563-579.

Ziv, Y., Bar-Shira, A., Pecker, I., Russell, P., Jorgensen, T.J., Tsarfati, I., and Shiloh, Y. (1997). Recombinant ATM protein complements the cellular A-T phenotype. Oncogene 15, 159-167.

Figure 1

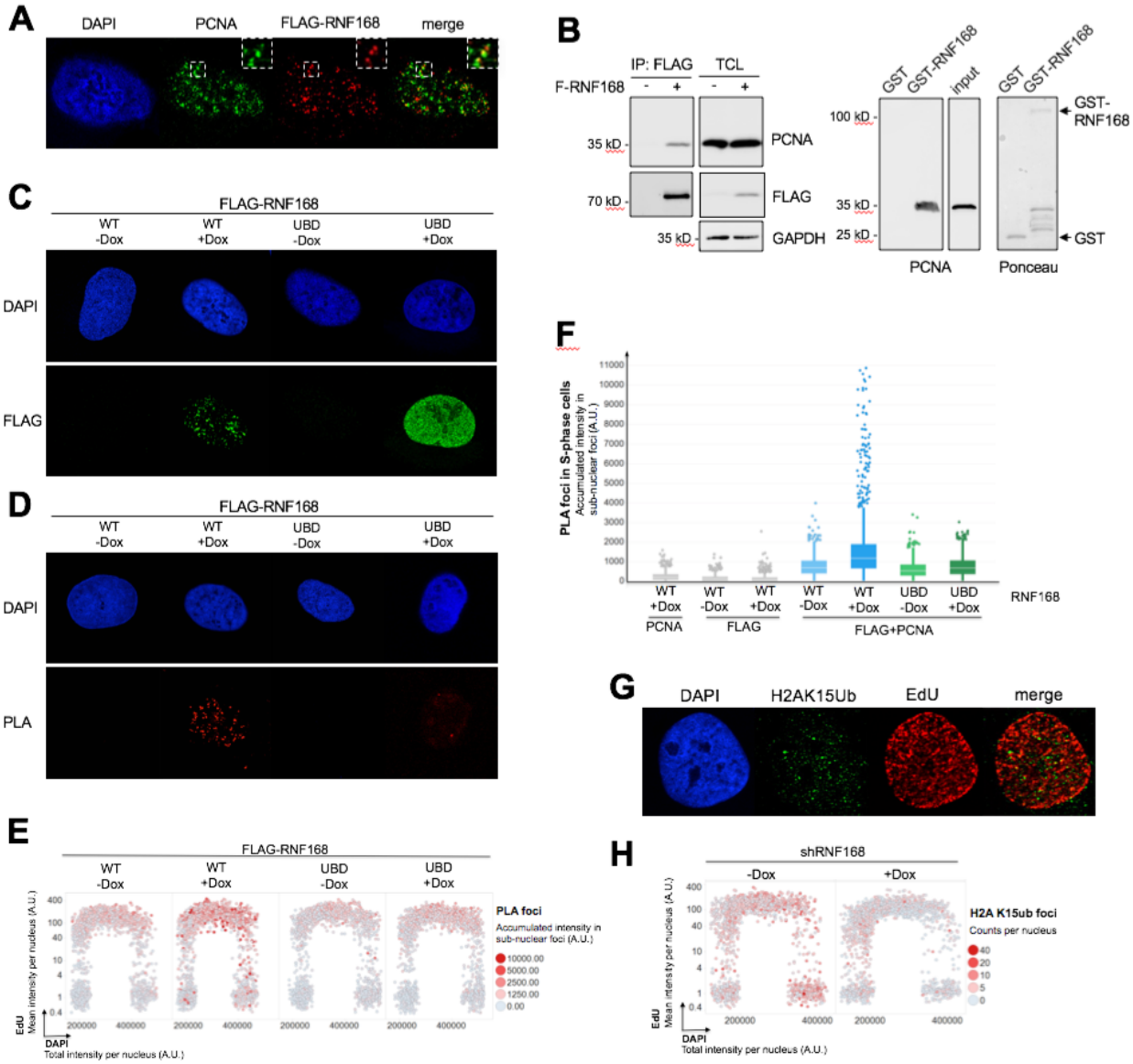

Figure 1. RNF168 localizes at replication forks. (A) Representative micrographs showing the partial colocalization of RNF168 and PCNA in S-Phase U2OS Flp-In T-REx cells expressing doxycycline (Dox) inducible FLAG-RNF168 for 24h. (B) Immunoblots validating the interaction of RNF168 and PCNA by Flag IP and GST pulldown after expression of Flag and GST tagged RNF168 in HeLa cells. (C) Representative micrographs showing the nuclear localization and distribution of FLAG tagged wild type (FLAG-RNF168 WT) and ubiquitin binding deficient RNF168 (UBD) in Dox inducible U2OS Flp-In T-REx cell lines. Both cell lines were either grown in Dox-free growth media (-Dox) or in the presence of Dox (1μg/ml) for 24h (+Dox) before being processed for immunofluorescence. (D) Representative micrographs showing the proximity ligation assay (PLA) signal between wild type RNF168 (FLAG-RNF168 WT) and PCNA as well as between ubiquitin binding deficient RNF168 (UBD) and PCNA, after 24h of induction (+Dox, 1μg/ml). (F) Representative cell cycle distribution of PLA foci between wild type RNF168 (WT) and PCNA as well as between ubiquitin binding deficient RNF168 (UBD) and PCNA in Dox-inducible U2OS Flp-In T-REx expression systems. (E) Quantification of PLA foci intensity in S-phase (EdU positive) cells from the experiment described in Figure 1D. Similar cell numbers were compared for the different conditions. The quantification also depicts controls obtained by incubating the coverslips with single anti-PCNA or anti-FLAG antibody. (G) Representative micrographs showing ubiquitination of histone H2A on K15 (H2AK15Ub) in an EdU positive (S-phase) cell. (H) Cell cycle distribution of RNF168 dependent ubiquitination of histone H2A on K15 (H2AK15Ub) in control (-Dox) and RNF168 depleted cells (+Dox).

Figure 2

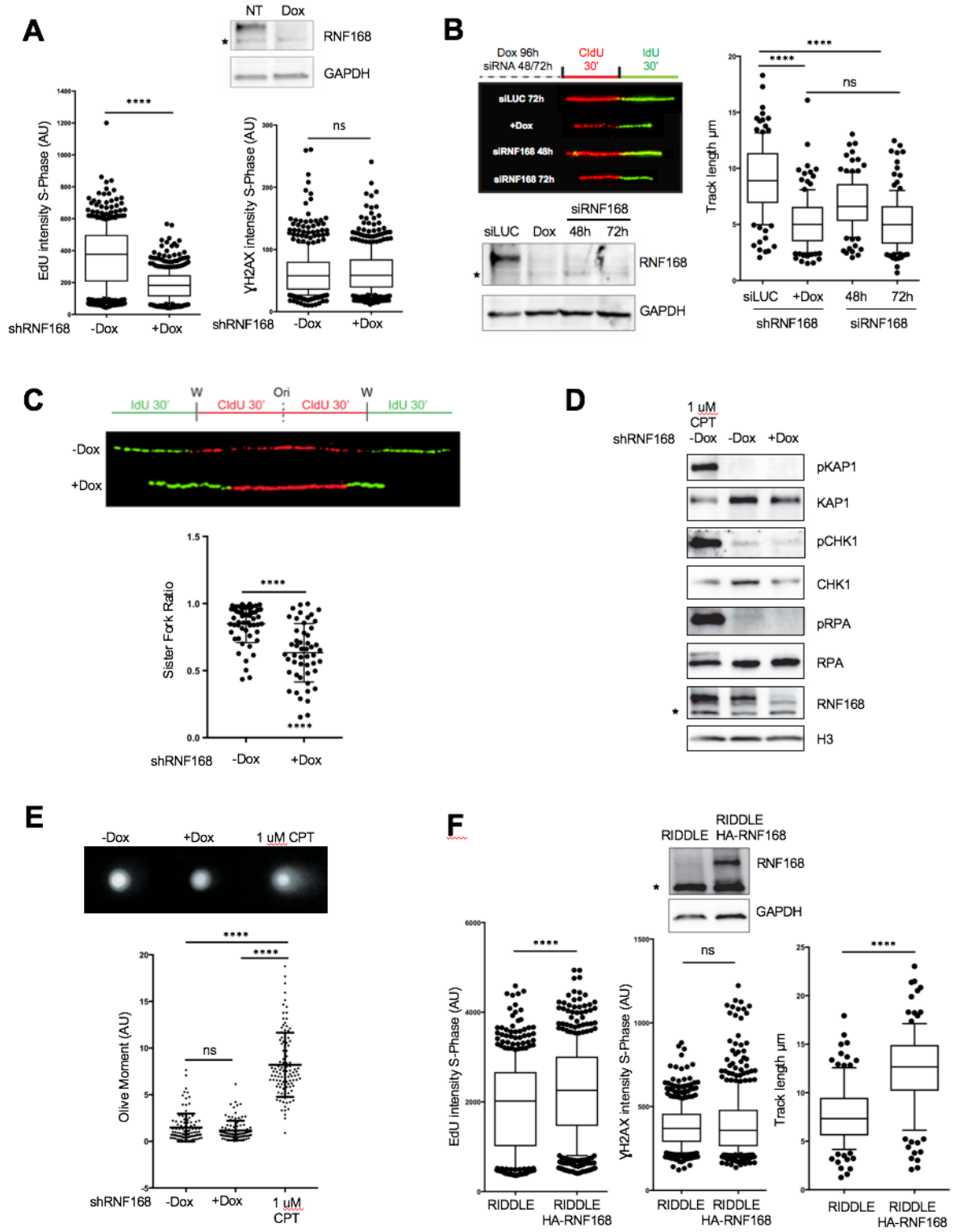
A
NT
Dox
RNF168
GAPDH
EdU intensity S-Phase (AU)
****
shRNF168 -Dox +Dox
γH2AX intensity S-Phase (AU)
ns
shRNF168 -Dox +Dox
B
Dox 96h
siRNA 48/72h
CldU 30'
IdU 30'
siLUC 72h
+Dox
siRNF168 48h
siRNF168 72h
siRNF168
siLUC Dox 48h 72h
RNF168
GAPDH
Track length µm
****
****
ns
siLUC +Dox 48h 72h
shRNF168 siRNF168
C
IdU 30'
W
CldU 30'
Ori
CldU 30'
W
IdU 30'
-Dox
+Dox
Sister Fork Ratio
****
****
shRNF168 -Dox +Dox
D
1 uM CPT
shRNF168 -Dox -Dox +Dox
pKAP1
KAP1
pCHK1
CHK1
pRPA
RPA
RNF168
H3
E
-Dox
+Dox
1 uM CPT
Olive Moment (AU)
****
****
ns
shRNF168 -Dox +Dox 1 uM CPT
F
RIDDLE
RIDDLE HA-RNF168
RNF168
GAPDH
EdU intensity S-Phase (AU)
****
RIDDLE RIDDLE HA-RNF168
γH2AX intensity S-Phase (AU)
ns
RIDDLE RIDDLE HA-RNF168
Track length µm
****
RIDDLE RIDDLE HA-RNF168

Figure 2. RNF168 is required for efficient DNA replication in unperturbed conditions. (A) EdU and γH2AX FACS intensity values from S-phase (EdU positive) control (-Dox) and RNF168 depleted cells (+Dox). The cells were pulse labeled with EdU (10 μM) for 30 min and subsequently stained for EdU and histone H2AX phosphorylation (γH2AX). The intensity values of 500 EdU positive cells per sample were extracted from the raw data and used for statistical analysis. The level of RNF168 depletion was measured by Western blot analysis (top panel) (*unspecific band). (B) DNA fiber spreading analysis of control cells (siLUC, 72h) and cells depleted of RNF168, using either an inducible shRNA (+Dox) or an siRNA of a different sequence (siRNF168, 48h & 72h). A labelling scheme and fibers of representative size are shown for each condition in the top left panel. The cells were pulse labelled with chlorodeoxyuridine (CldU, red) and iododeoxyuridine (IdU, green) for 30 min each. At least 120 IdU tracts were scored per sample and subjected to statistical analysis. The level of RNF168 depletion was measured by Western blot analysis (bottom left panel). (C) Representative images of a symmetric and an asymmetric fork from U2OS shRNF168 cells. Quantification of the sister fork ratio in RNF168 proficient (-Dox) and deficient (+Dox) cells. At least 50 fibers were measured per condition. (D) Immunoblot analysis of ATR (pCHK1) and ATM (pKAP1) activation in control (-Dox) and RNF168 depleted (+Dox) U2OS shRNF168 cells. The blot also displays the expression levels of total DDR proteins (CHK1 and KAP1) and RNF168. RPA32 (RPA) phosphorylation at S4/S8 (pRPA) is used as a marker for the presence of DNA double strand breaks. U2OS shRNF168 cells treated with 1 μM camptothecin (CPT) are used as a positive control for full DDR activation. Histone H3 serves as an internal loading control. (E) Quantification of the olive moment in control (-Dox) and RNF168 depleted (+Dox) U2OS shRNF168 cells from a representative neutral comet assay experiment. 1 μM CPT treatment is used as a positive control for DNA double strand break formation. Mean value and standard deviations are indicated as vertical lines for each sample. A representative cell is shown for each condition in the top panel. (F) The two panels on the left-hand side depict S-Phase EdU and γH2AX intensity values of RIDDLE patient fibroblasts (RIDDLE) and the same cell line reconstituted with HA-RNF168 (RIDDLE HA-RNF168). The values were obtained analogously to figure 2A. Replication fork speed in the same cell lines was assessed using DNA fiber spreading analysis (third panel from the left). RNF168 expression levels were analyzed by immunoblotting (top panel). See also Figure S2.
(**** P Value <0.0001, Whiskers: 10th–90th percentile).

Figure 3

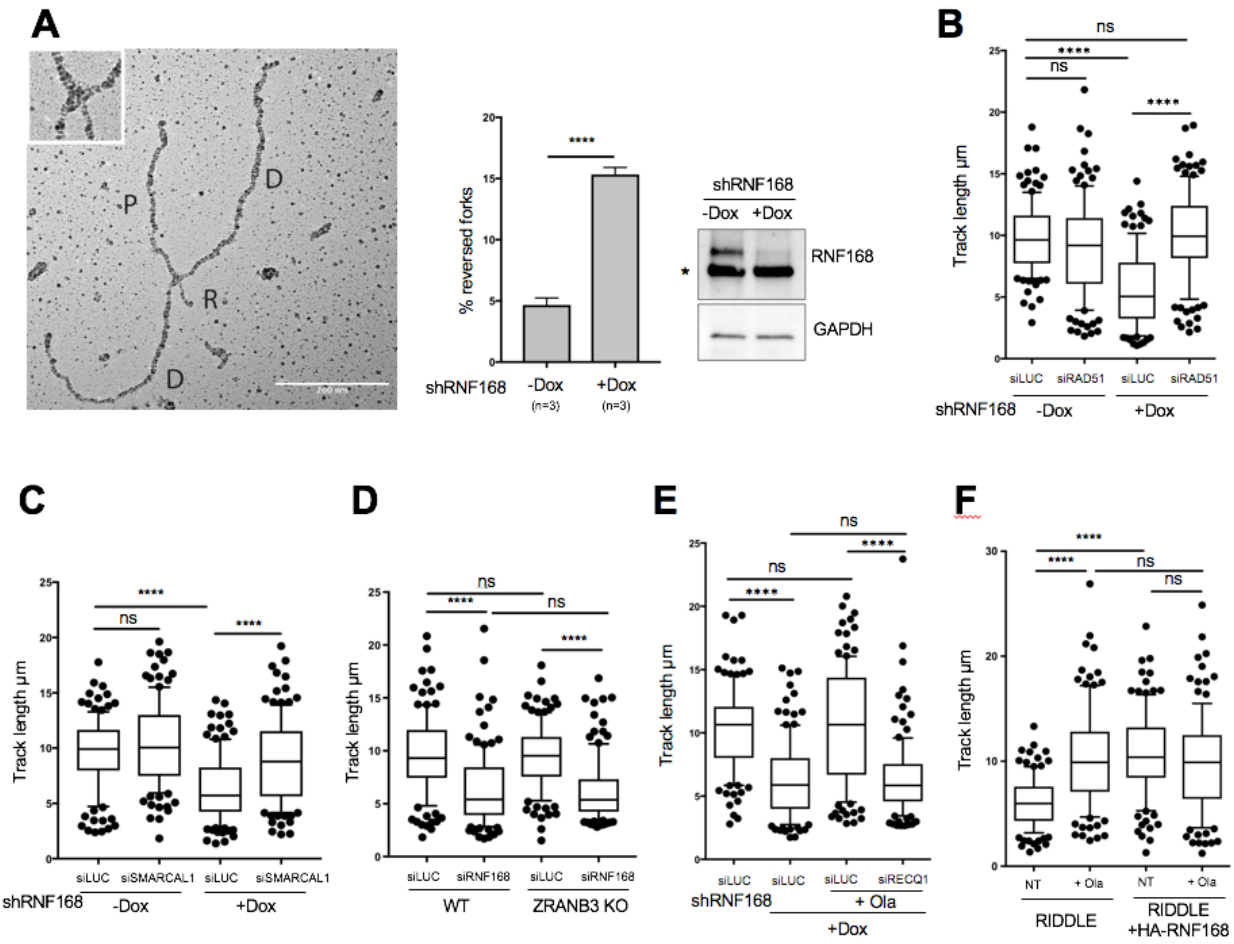

Figure 3. RNF168 depletion leads to accumulation of reversed forks, which is required for fork slowing. (A) Frequency of reversed replication forks in control (-Dox) and RNF168 depleted (+Dox) U2OS shRNF168 cells as found in three separate experiments by transmission electron microscopy. At least 70 molecules were analyzed for each sample (*** P Value =0.001, Paired t test). An electron micrograph of a representative reversed replication fork is presented on the left-hand side (P: Parental duplex, D: Daughter duplexes, R: Regressed arm). The scale bar equals 200 nm. RNF168 expression levels were analyzed by immunoblotting (*unspecific band). (B) DNA fiber spreading analysis in control cells (siLUC, -Dox), or in cells depleted of RAD51 (siRAD51, -Dox), of RNF168 (siLUC, +Dox) or of both proteins (siRAD51, +Dox). (C) Statistical analysis of IdU track length measurements from control (siLUC, -Dox), SMARCAL1 depleted (siSMARCAL1, -Dox), RNF168 depleted (siLUC, +Dox) and Smarcal1/RNF168 co-depleted cells (siSMARCAL1, +Dox). (D) DNA fiber spreading analysis comparing IdU track lengths in control cells (WT, siLUC), RNF168 depleted cells (WT, siRNF168), ZRANB3 KO cells (ZRANB3 KO, siLUC) and ZRANB3 KO cells depleted of RNF168 (ZRANB3 KO, siRNF168). (E) DNA fiber spreading analysis investigating the effect of Olaparib treatment (Ola, 10 µM, 2h) on replication fork speed in RNF168 depleted cells (siLUC, +Ola, +Dox) and cells co-depleted of RNF168 and RECQ1 (siRECQ1, +Ola, +Dox). Replication fork speed in control cells (siLUC) and untreated RNF168 depleted cells (siLUC, +Dox) was included as a reference. (F) Statistical analysis of IdU track length measurements from a representative fiber spreading experiment in RIDDLE patient fibroblasts (RIDDLE) and RIDDLE fibroblasts reconstituted with HA-RNF168 (RIDDLE HA-RNF168). The track length was scored for both cell lines under unperturbed conditions (NT) and upon Olaparib treatment (+Ola, 10 µM, 2h). (**** P Value <0.0001, Whiskers: 10th–90th percentile)

Figure 4

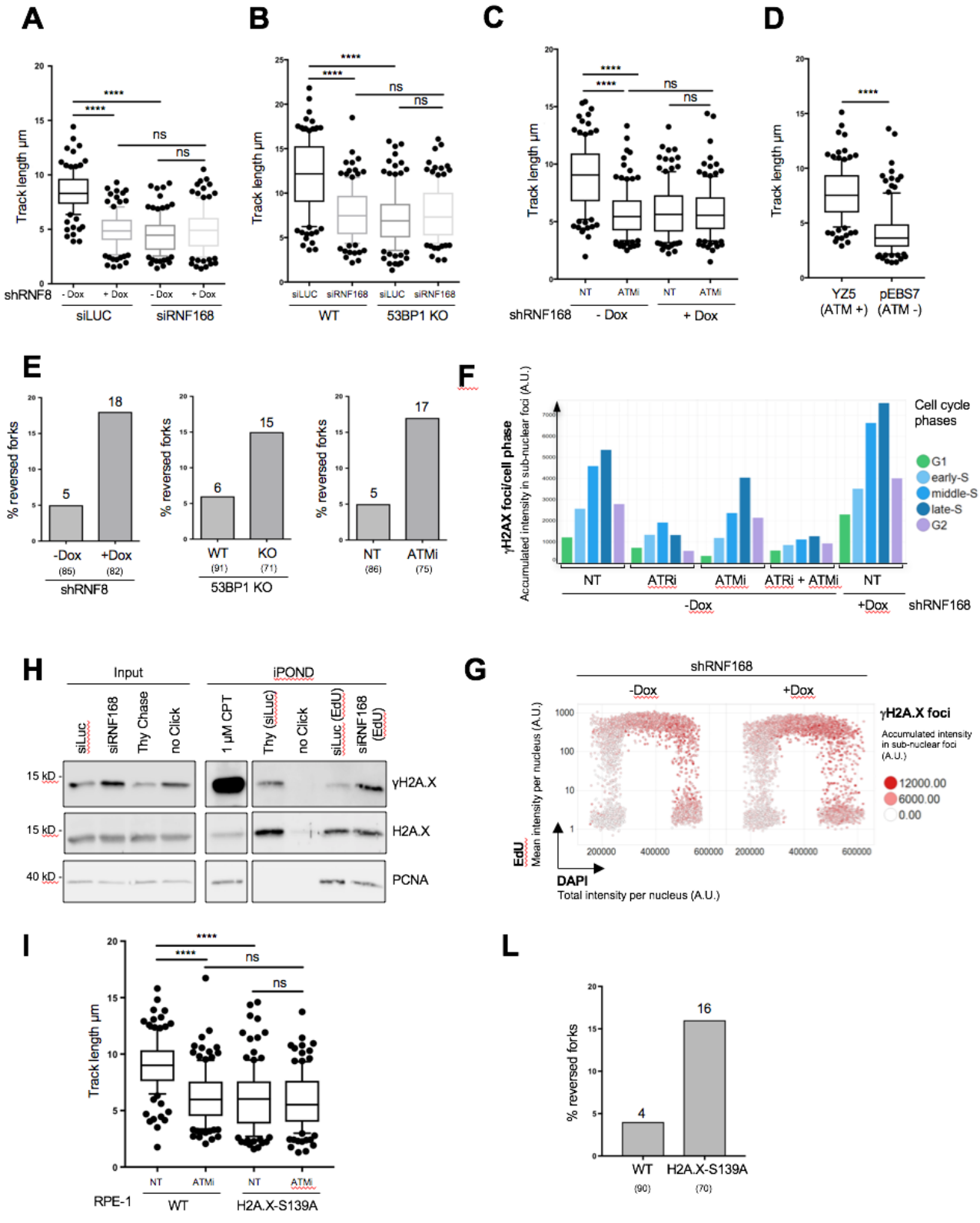
A
B
C
D
Track length µm
shRNF8
- Dox
+ Dox
siLUC
siRNF168
WT
53BP1 KO
shRNF168
NT
ATMi
YZ5 (ATM +)
pEBS7 (ATM -)
E
% reversed forks
-Dox
+Dox
shRNF8
WT
KO
53BP1 KO
NT
ATMi
F
γH2AX foci/cell phase
Accumulated intensity in sub-nuclear foci (A.U.)
Cell cycle phases
G1
early-S
middle-S
late-S
G2
NT
ATRi
ATMi
ATRi + ATMi
H
Input
iPOND
siLuc
siRNF168
Thy Chase
no Click
1 µM CPT
Thy (siLuc)
siLuc (EdU)
siRNF168 (EdU)
15 kD
40 kD
γH2A.X
H2A.X
PCNA
G
shRNF168
-Dox
+Dox
γH2A.X foci
Accumulated intensity in sub-nuclear foci (A.U.)
EdU
Mean intensity per nucleus (A.U.)
DAPI
Total intensity per nucleus (A.U.)
I
RPE-1
H2A.X-S139A
L

Figure 4. Upstream and downstream DDR factors share the replication function of RNF168 and are epistatic to it. (A) Statistical analysis of IdU track length measurements from a DNA fiber spreading experiment performed in control cells (-Dox, siLUC), cells depleted of RNF8 using an inducible shRNA (+Dox, siLUC), cells depleted of RNF168 using an siRNA (-Dox, siRNF168) and cells depleted of both RNF8 and RNF168 (+Dox, siRNF168). (B) CRISPR/Cas generated 53BP1 KO and the WT U2OS cell line from which they originate were subjected to DNA fiber spreading analysis after being transfected either with siLUC or an siRNA for the depletion of RNF168 (siRNF168). (C) DNA fiber spreading analysis of U2OS shRNF168 cells under control conditions (NT, -Dox), after pre-treating with an ATM inhibitor (Ku55933, 10 μM) for 1h before labelling (-Dox, ATMi), upon RNF168 depletion (NT, +Dox) and upon combining ATM inhibition with RNF168 depletion (ATMi, +Dox). (D) DNA fiber spreading analysis comparing replication fork speed of the Ataxia-telangiectasia patient fibroblast cell line AT22IJE-T carrying an empty expression vector (pEBS7) and the same cell line expressing recombinant ATM (YZ5). (E) Frequency of reversed replication forks observed by EM analysis in control cells and cells subjected to the depletion or inhibition of the indicated DDR factors. The numbers in brackets indicate the total of analyzed molecules for each sample. The values written above each column indicate the relative reversal frequencies for the respective sample. Results of additional independent experiments are reported in Table S1B-D. (F) Quantification of γH2AX accumulated intensity in sub-nuclear foci in different cell cycle phases from a QIBC experiment in control (-Dox, NT), ATR inhibited (-Dox, ATRi), ATM inhibited (-Dox, ATMi), ATR/ATM inhibited (-Dox, ATRi+ATMi) and RNF168 depleted cells (+Dox, NT). (G) Representative cell cycle distribution of γH2AX accumulated intensity in sub-nuclear foci of control (- Dox) and RNF168 depleted cells (+ Dox) as measured by QIBC. (H) Immunoblot showing γH2AX protein levels from an IPOND experiment in control (siLUC) and RNF168 depleted (siRNF168) HEK 293T cells. (I) Fiber spreading analysis comparing IdU track lengths in control (WT) and H2AX S139A RPE cells (S139A) under control conditions (NT) and upon ATM inhibition (ATMi). (L) Frequency of reversed replication forks in control (WT) and H2AX S139A RPE cells (S139A) as observed by EM analysis. The numbers in brackets indicate the total of analyzed molecules and the values written above the columns indicate the relative reversal frequencies. Results of an additional independent experiment are reported in Table S1.
(**** P Value <0.0001, Whiskers: 10th–90th percentile). See also Figure S4.

Figure 5

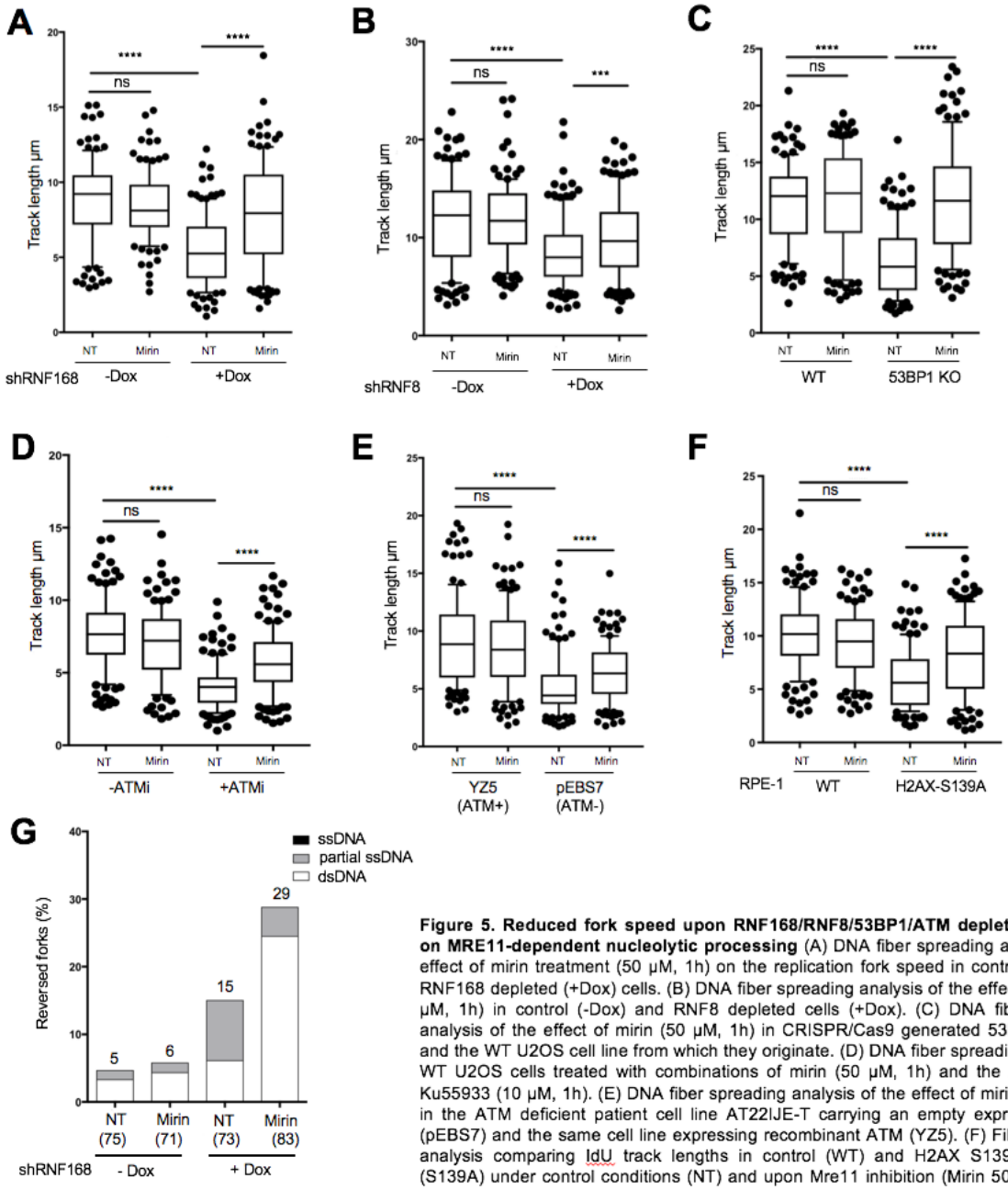

Figure 5. Reduced fork speed upon RNF168/RNF8/53BP1/ATM depletion depends on MRE11-dependent nucleolytic processing (A) DNA fiber spreading analysis of the effect of mirin treatment (50 µM, 1h) on the replication fork speed in control (-Dox) and RNF168 depleted (+Dox) cells. (B) DNA fiber spreading analysis of the effect of mirin (50 µM, 1h) in control (-Dox) and RNF8 depleted cells (+Dox). (C) DNA fiber spreading analysis of the effect of mirin (50 µM, 1h) in CRISPR/Cas9 generated 53BP1 KO cells and the WT U2OS cell line from which they originate. (D) DNA fiber spreading analysis in WT U2OS cells treated with combinations of mirin (50 µM, 1h) and the ATM inhibitor Ku55933 (10 µM, 1h). (E) DNA fiber spreading analysis of the effect of mirin (50 µM, 1h) in the ATM deficient patient cell line AT22IJE-T carrying an empty expression vector (pEBS7) and the same cell line expressing recombinant ATM (YZ5). (F) Fiber spreading analysis comparing IdU track lengths in control (WT) and H2AX S139A RPE cells (S139A) under control conditions (NT) and upon Mre11 inhibition (Mirin 50 µM, 1h). (G) Frequency of reversed replication forks observed by transmission electron microscopy analysis in non-treated control cells (NT, -Dox), mirin (50 µM, 1h) treated control cells (Mirin, -Dox), cells depleted of RNF168 using an inducible shRNA (NT, -Dox) and RNF168 depleted cells treated with mirin (Mirin, +Dox). The numbers in brackets indicate the total number of analyzed molecules for each sample. The respective percentage of reversed forks per sample is indicated above each column. Results of additional independent experiments are reported in Table S1A. The regressed arms of reversed forks were inspected for singe stranded DNA stretches. The percentage of partially single stranded regressed arms is indicated in gray and the percentage of completely single stranded regressed arms in black. (**** P Value <0.0001, *** P Value 0.0002, Whiskers: 10th–90th percentile). See also Figure S5 and Table S1B-C.

Figure 6

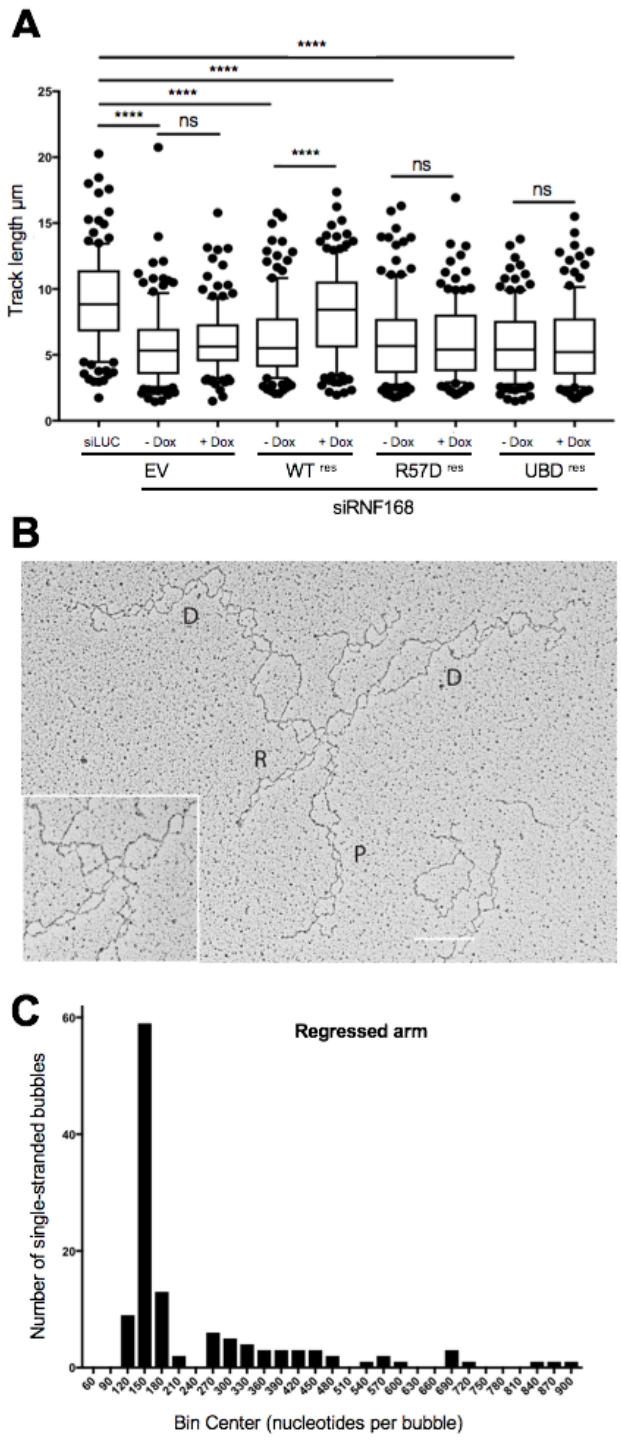

Figure 6. RNF168 ubiquitin ligase activity on histone H2A is required for efficient DNA replication. (A) DNA fiber spreading analysis of replication fork progression rate in four different U2OS Flp-In T-REx cell lines with Dox-inducible expression of siRNA resistant WT or mutant RNF168. The four cell lines employed for this experiment include cell lines carrying an empty vector (EV), an expression vector for WT RNF168 (WT ^{res}), an expression vector for the R57D mutant specifically impaired in the ubiquitination of histone H2A (R57D ^{res}) and a cell line with Dox-inducible expression of a ubiquitin binding deficient mutant of RNF168 (UBD ^{res}). All four cell lines were depleted of endogenous RNF168 by siRNA transfection (siRNF168) for 72h. 12h before the experiment the cells were split and either left un-induced (-Dox) or induced by the addition of Dox (1 µg/ml) to the growth media (+Dox). U2OS Flp-In T-REx cell carrying an empty vector and transfected with control siRNA (siLUC, EV) were included as a reference. See also Figure S4A-C. (B) Representative electron micrograph of a denatured reversed replication fork from U2OS cells depleted of RNF168 using an inducible shRNA (P: Parental duplex, D: Daughter duplexes, R: Regressed arm). The white scale Bar equals 200nm. (C) Frequency distribution of the size of single-stranded bubble size on the regressed arm, as observed by transmission electron microscopic analysis of denatured reversed replication forks from cells treated with 50 nM CPT or from RNF168 depleted cells. Similar distributions were observed on the parental and the two daughter strands of the same molecules and are depicted in Figure S6E-F. (**** P Value <0.0001, Whiskers: 10th–90th percentile).

Figure 7

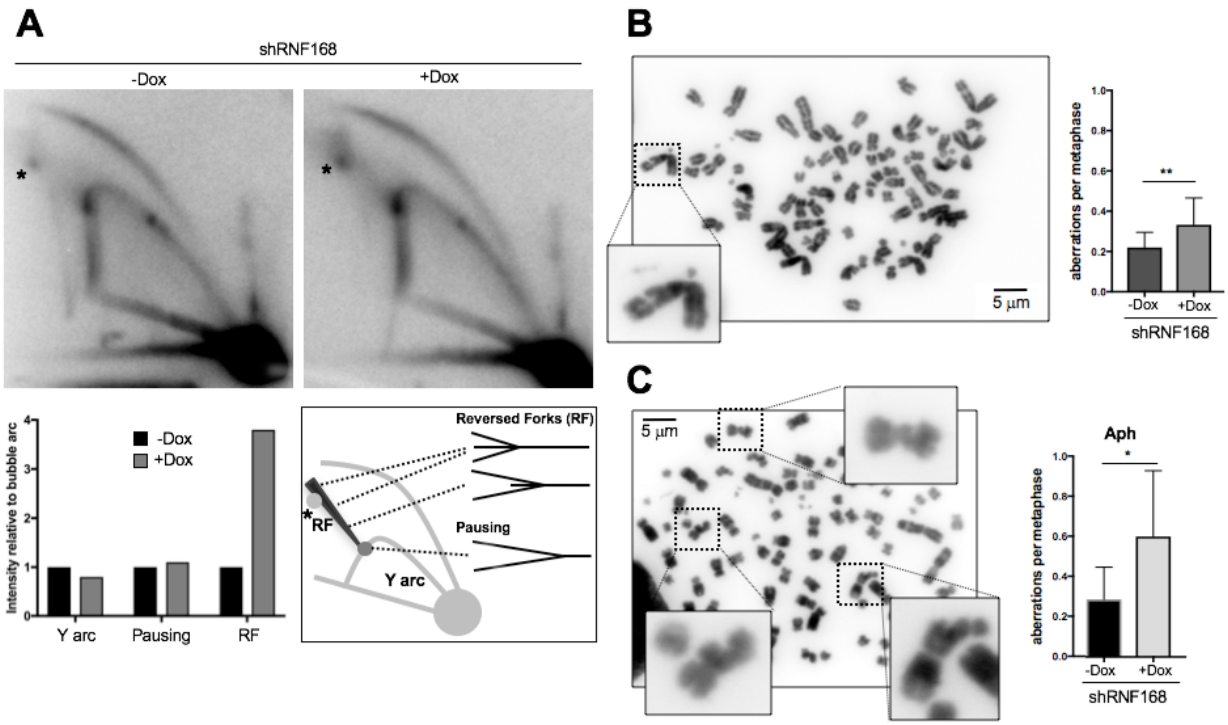

Figure 7. RNF168-deficient cells show defects in replicating repetitive sequences, resulting in chromosomal abnormalities. (A) Representative neutral-neutral 2D gel analysis of an EcoRI digested SV40 based plasmid containing 90 TTC repeats 48h after transfection into control (-Dox) and RNF168 depleted cells (+Dox). Signals corresponding to different categories of replication intermediates were quantified as described in Figure S5A and depicted as bar plots for both samples (black bars correspond to -Dox, grey bars correspond to +Dox). The graph on the right side explains the migration pattern of different replication intermediates of the used plasmid in neutral-neutral 2D gels. The asterisk (*) marks the so-called "X-spot", representing triplex-mediated junctions between replicated duplexes, reported to accumulate after replication of expanded GAA/TTC repeats (Follonier et al., 2013). (B) Metaphase spreads to detect chromosomal aberrations in control (-Dox) and long-term RNF168-depleted U2OS cells (+Dox, 7 days). A representative image is included on the left hand side (scale bar, 5 µm). The graph on the right depicts the number of observed chromosomal abnormalities from three separate experiments. See also Figure S7E and S7F. (C) Number of observed chromosomal abnormalities from three separate metaphase spreading experiments in control (-Dox) and long-term RNF168-depleted U2OS cells (+Dox, 7 days) treated with low dose aphidicolin treatment (Aph, 0.4 µM, 16h). A representative image is included (scale bar, 5 µm). (** P Value <0.005, * P Value <0.05, Paired t test)

Histone ubiquitination by the DNA damage response is required for efficient DNA replication in unperturbed S-phase

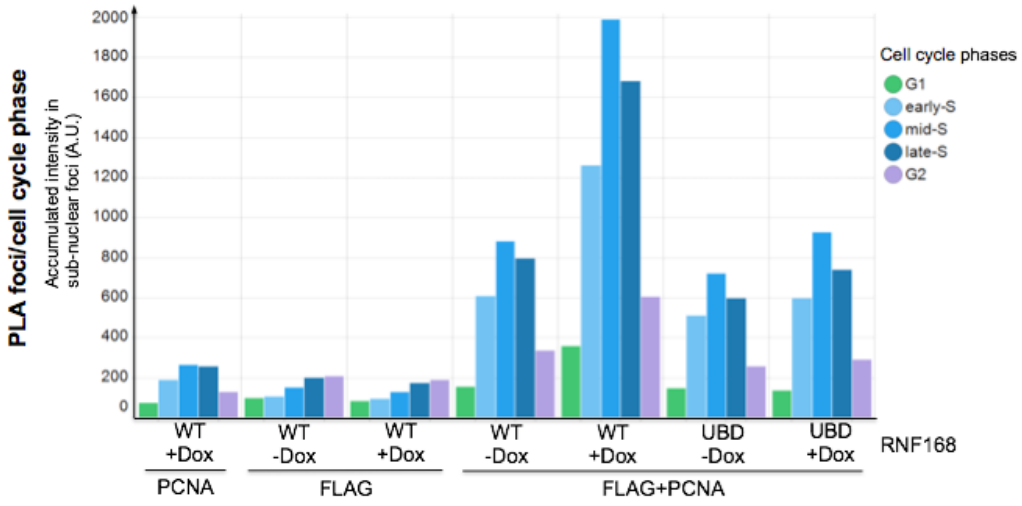

Figure S1. Related to Figure 1
(A) Quantification of PLA *foci* intensity in different cell cycle phases from the experiment described in Figure 1D and 1E.

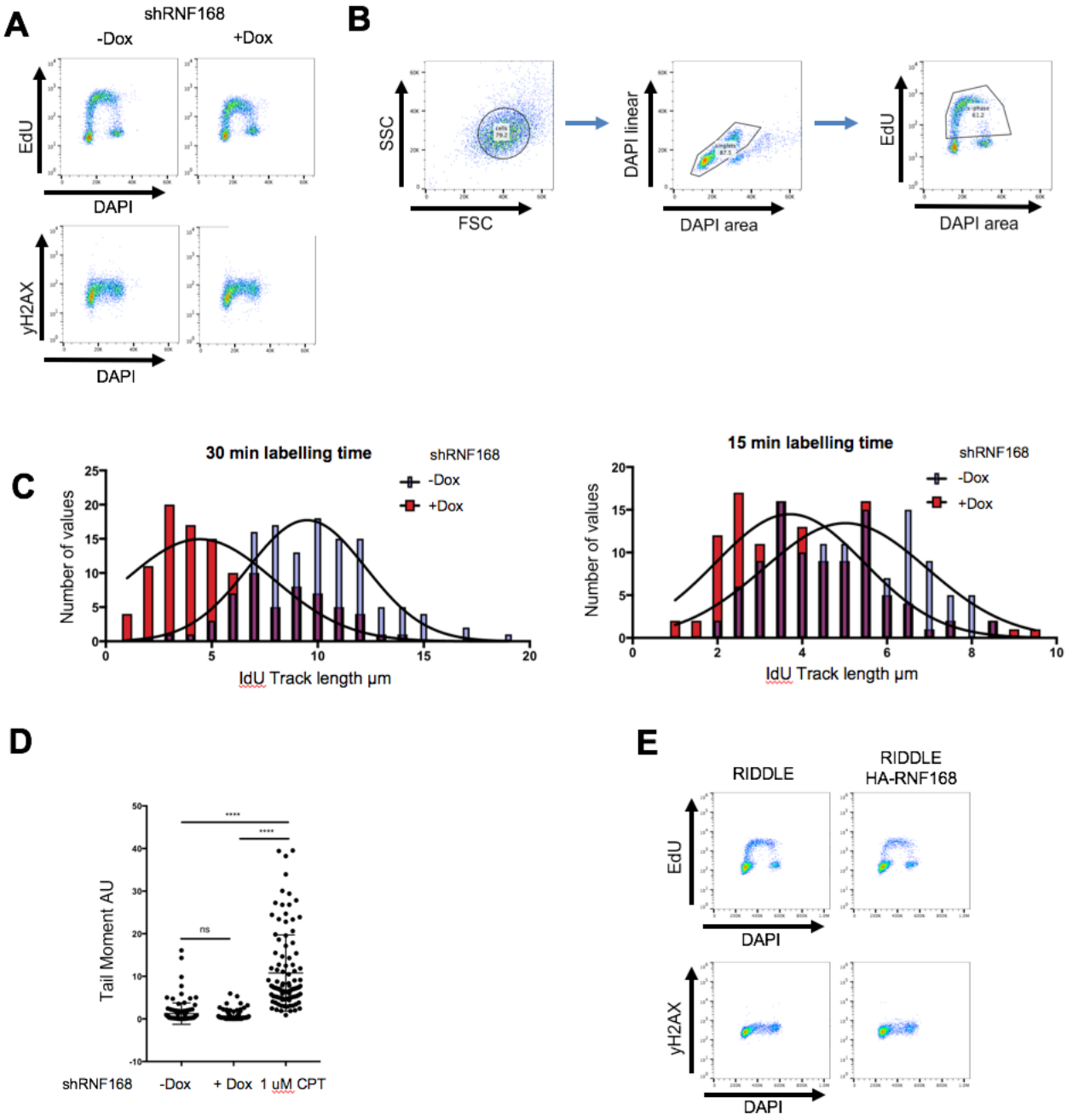

Figure S2. Related to Figure 2

(A) Flow cytometry plots showing the cell cycle distribution and γH2AX intensity profile of control (-Dox) and RNF168 depleted cells (+Dox) from which the intensity values in Figure 2A were extracted. (B) Gating hierarchy used to select S-phase cells from which the EdU and γH2AX intensity values were extracted. The intensity values of 500 S-phase cells per sample were extracted from the raw data and subjected statistical analysis in figure 2A. (C) Frequency distributions of fiber lengths in control (-Dox) and RNF168 depleted cells (+ Dox) with either 30 min (left) or 15 min (right) labelling time. (D) Quantification of the tail moment in control (-Dox) and RNF168 depleted (+Dox) U2OS shRNF168 cells from a representative neutral comet assay experiment. 1μM camptothecin (CPT) treatment is used as a positive control for DNA double-strand break formation. The values for the olive moment from the same experiment are depicted in figure 2D. Mean value and standard deviation are indicated as vertical lines for each sample (**** P Value <0.0001). (E) Flow cytometry plots showing the cell cycle distribution and γH2AX intensity profile of RIDDLE patient fibroblasts (RIDDLE) and the same cell line reconstituted with HA-RNF168 (RIDDLE HA-RNF168). The very same cells were used to extract the S-phase intensity values depicted in Figure 2E.

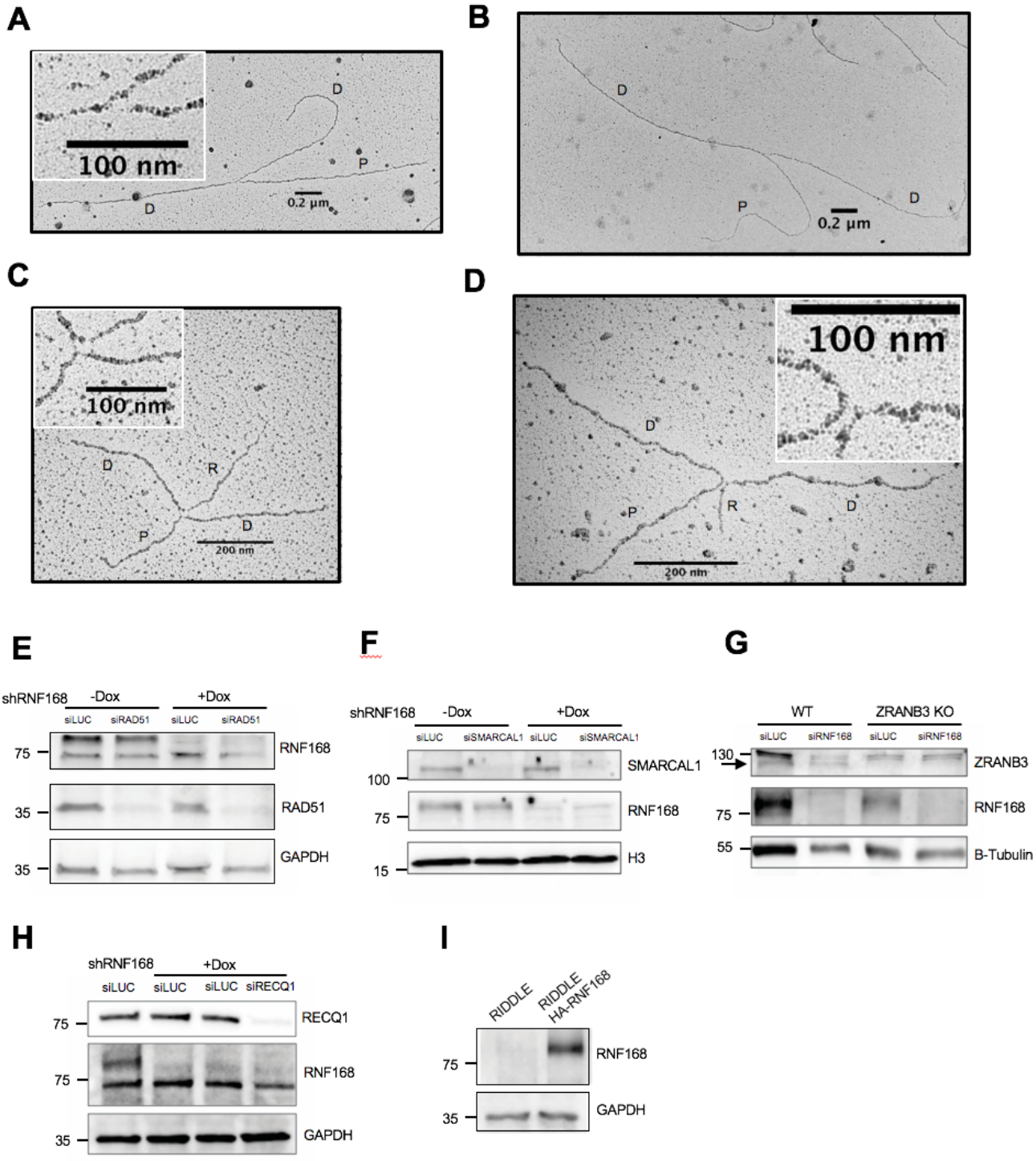

Figure S3. Related to Figure 3
(A) and (B) Electron micrographs of representative normal replication forks (P: Parental duplex, D: Daughter duplexes) (C) and (D) Representative electron micrographs of reversed replication forks (P: Parental duplex, D: Daughter duplexes, R: Regressed arm) (E) Immunoblot showing the expression levels of RNF168 and RAD51 for the experiment depicted in Figure 3B. GAPDH serves as a loading control. (F) Immunoblot showing the expression levels of RNF168 and SMARCAL1 for the experiment depicted in Figure 3C. H3 serves as a loading control. (G) Immunoblot showing the expression levels of RNF168 and ZRANB3 for the experiment depicted in Figure 3D. B-Tubulin serves as a loading control. The arrow head indicates the band corresponding to ZRANB3. (H) Immunoblot showing the expression levels of RNF168 and RECQ1 for the experiment depicted in Figure 3E. (I) Immunoblot showing the expression levels of RNF168 for the experiment depicted in Figure 3F.

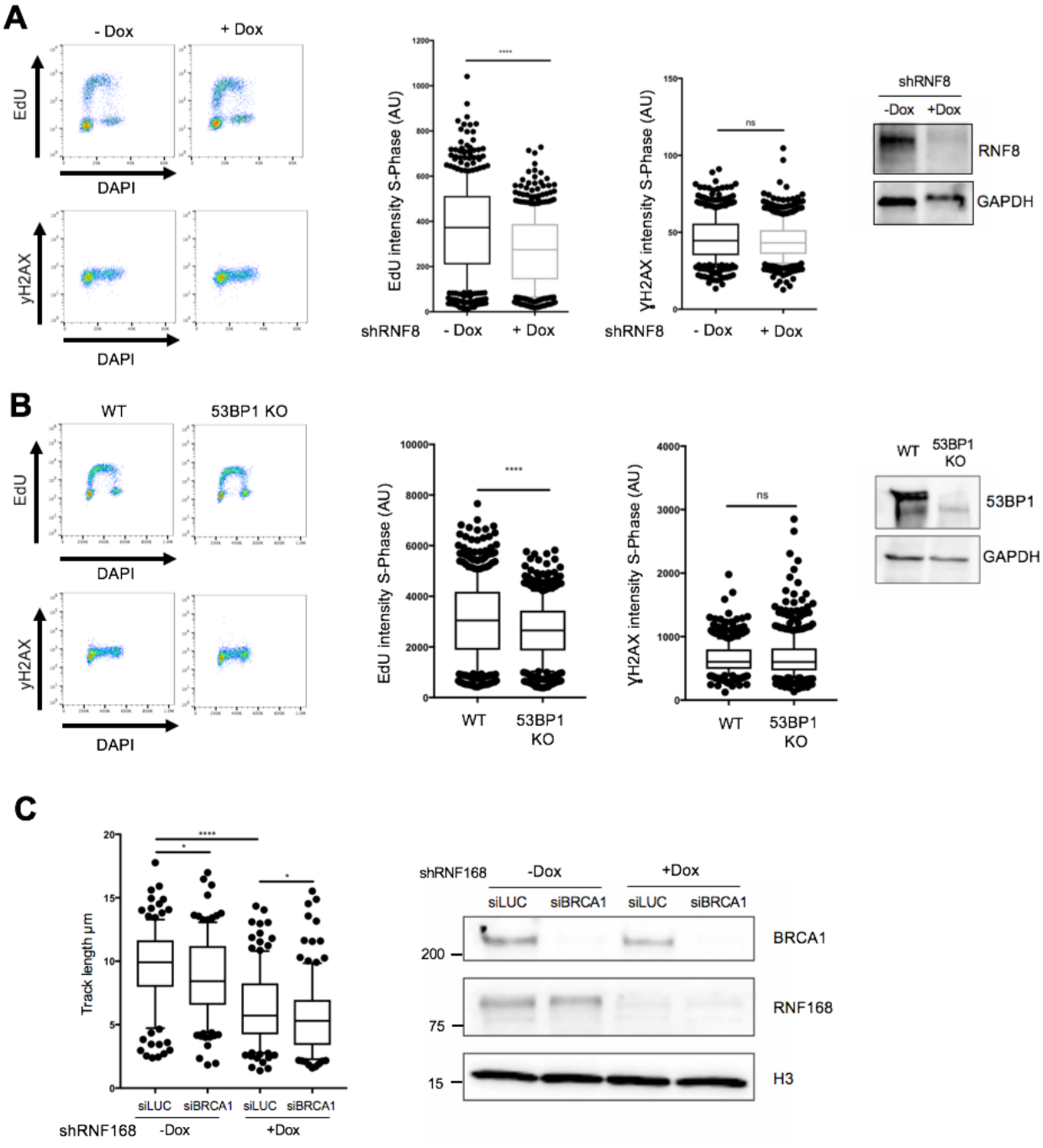

Figure S4. Related to Figure 4

(A) Flow cytometry plots showing the cell cycle distribution and γH2AX intensity profile of control (-Dox) and RNF8 depleted cells (+Dox). The EdU and γH2AX intensity values of 500 S-Phase cells per sample were extracted from the raw data and used for statistical analysis in the two panels in the middle. The immunoblot on the right-hand side shows the expression level of RNF8 in a representative depletion experiment (B) Flow cytometry plots showing the cell cycle distribution and γH2AX intensity profile of CRISPR/Cas9 generated 53BP1 KO cells and the WT U2OS cell line from which they were generated. EdU and γH2AX intensity values of S-phase cells were extracted from the raw data and used for statistical analysis depicted in the two panels in the middle. The immunoblot on the right-hand side shows the expression levels of 53BP1 in WT and 53BP1 KO cells. (C) DNA fiber spreading analysis in control (siLUC, -Dox), BRCA1 depleted (siBRCA1, -Dox), RNF168 depleted (siLUC, +Dox), and BRCA1/RNF168 co-depleted cells. Protein levels for this experiment can be seen on the right hand side immunoblot.
(**** P Value <0.0001, * P Value <0.05, Whiskers: 10th–90th percentile)

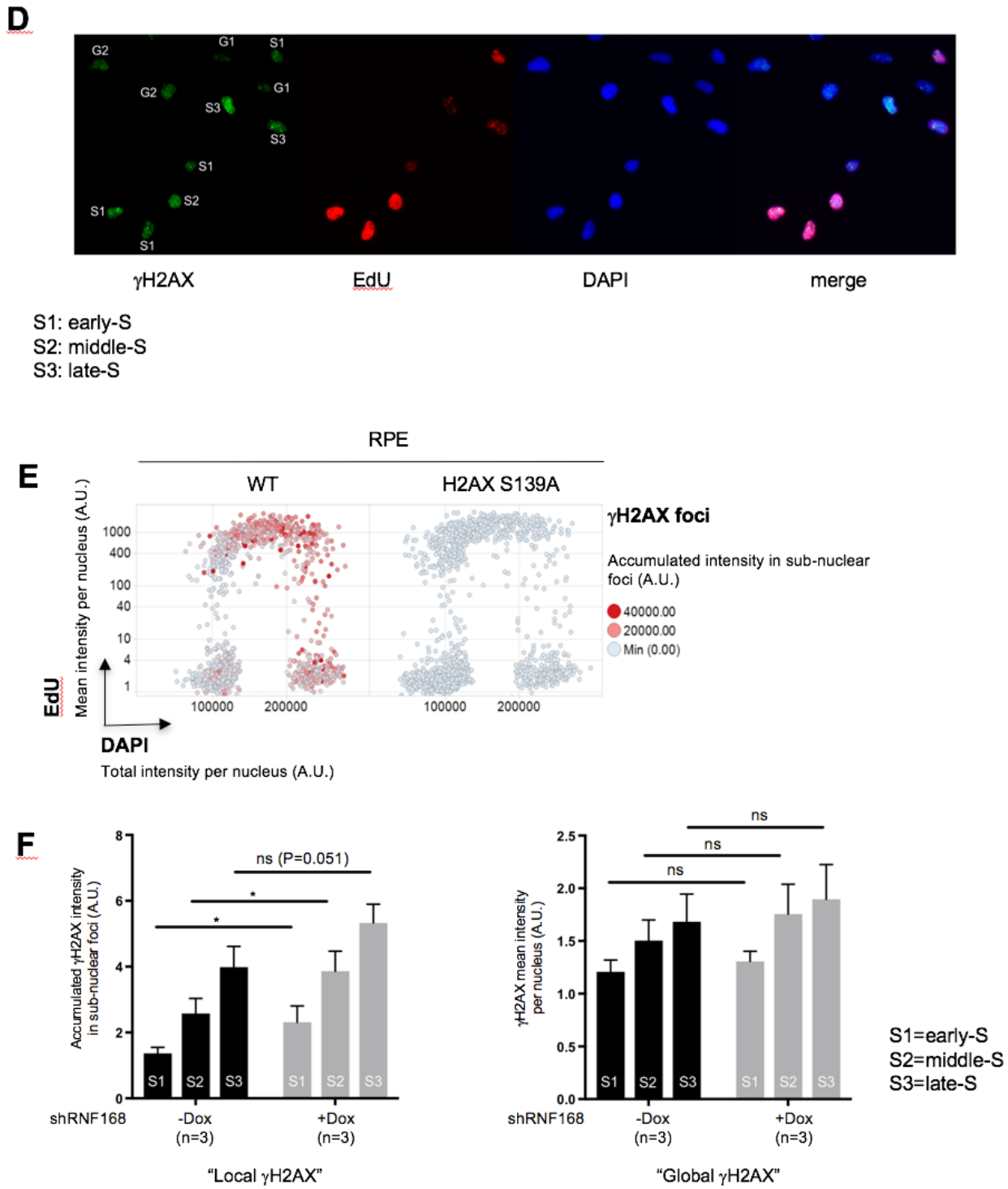

Figure S4. Related to Figure 4 (continued)
(D) Representative micrographs from the experiment depicted in Figure 4G showing γH2AX and EdU levels in different cell cycle phases. (E) Representative cell cycle distribution of γH2AX accumulated intensity in sub-nuclear foci of wildtype (WT) and H2AX S139A RPE cells as measured by QIBC. (F) Median γH2AX accumulated intensity in sub-nuclear foci and γH2AX mean intensity in different sub stages of S-phase from three independent QIBC experiments in control (-Dox, NT) and RNF168 depleted cells (+Dox, NT). P Values (P) were calculated using paired t test (* P Value <0.05).

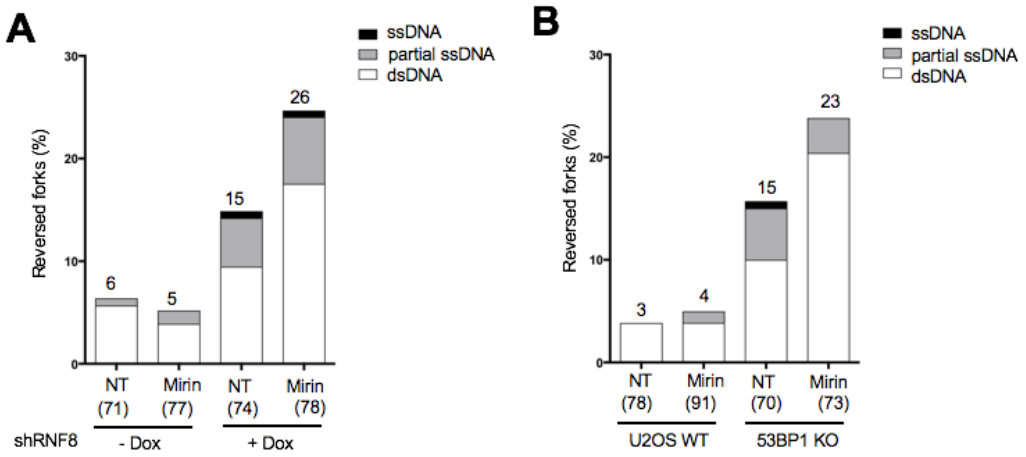

Figure S5. Related to Figure 5
(A) Frequency of reversed replication forks as observed by transmission electron microscopy analysis in untreated control cells (NT, -Dox), mirin (50 μM, 1h) treated control cells (Mirin, -Dox), cells depleted of RNF8 using an inducible shRNA (NT, -Dox) and RNF8 depleted cells treated with mirin (Mirin, +Dox). The numbers in brackets denote the total of analyzed molecules for each sample. The respective percentage of reversed forks per sample is indicated above each column. The regressed arms of reversed forks have been inspected for singe-stranded DNA stretches. The percentage of partially single stranded regressed arms is indicated in gray and the percentage of completely single-stranded regressed arms in black. (B) Replication fork reversal frequencies as observed by transmission electron microscopy analysis in CRISPR/Cas generated 53BP1 KO cells and the WT U2OS cell line from which they were generated. The samples include non-treated WT U2OS cells (NT, U2OS WT), WT cells subjected to mirin treatment (50 μM, 1h) (Mirin, U2OS WT), non-treated 53BP1 KO cells (NT, 53BP1 KO) and Mirin treated 53BP1 KO cells (Mirin, 53BP1 KO). Results of additional independent experiments are reported in Table S1B-C.

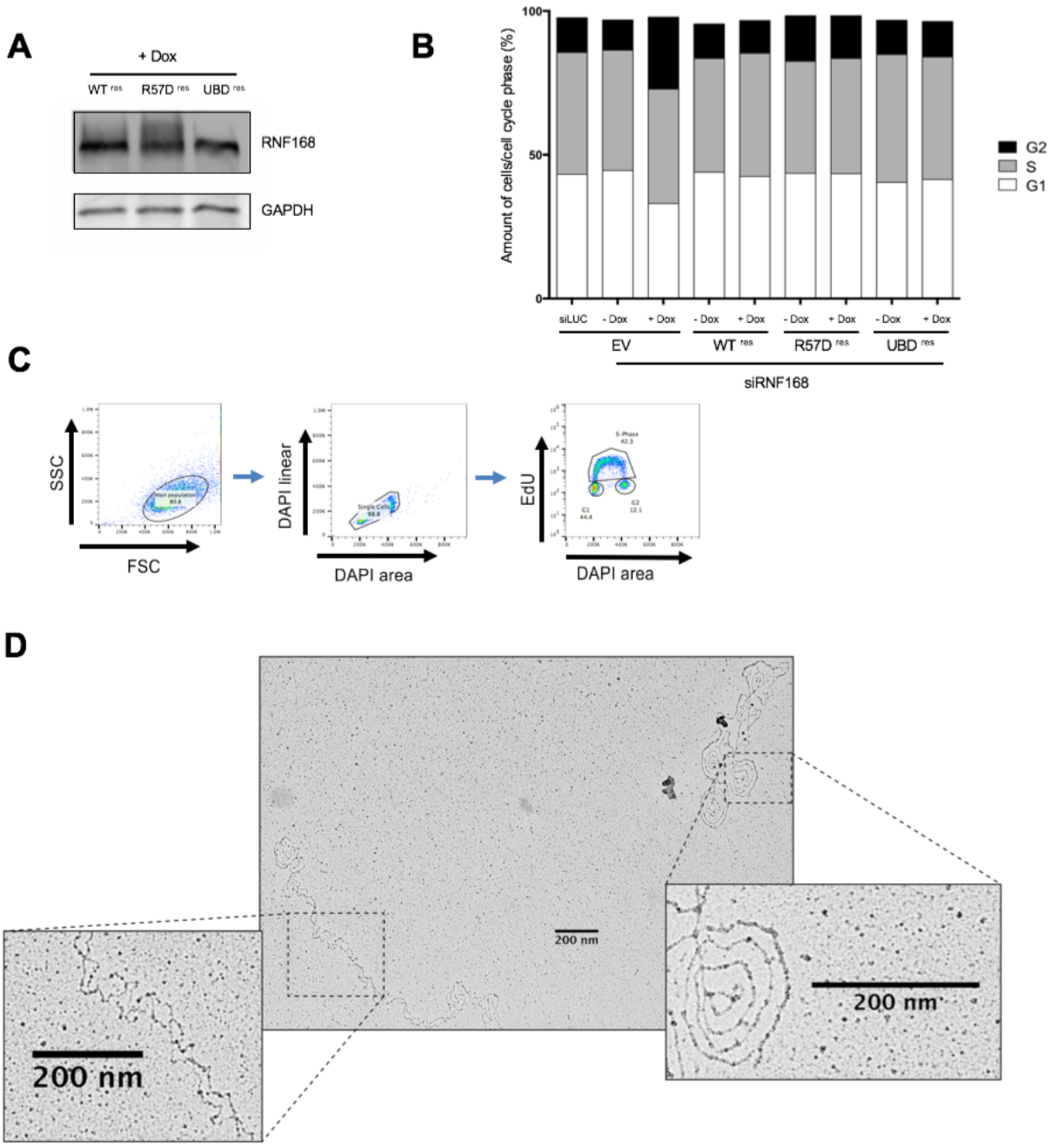

Figure S6. Related to Figure 6.
(A) Immunoblot showing comparable RNF168 expression levels for all three RNF168 expression systems (WT ^{res}, R57D ^{res} and UBD ^{res}) after induction with doxycycline. The protein extracts analyzed here were obtained from the same cells used for the experiment depicted in Figure 6A. (B) Relative cell cycle distribution of the four doxycycline inducible U2OS Flp-In T-REx cell lines used in Figure 6A (EV, WT ^{res}, R57D ^{res} and UBD ^{res}). All four cell lines were depleted of endogenous RNF168 by siRNA transfection (siRNF168) for 72h. 12h before the experiment the cells were split and either left either uninduced (-Dox) or induced by the addition of doxycycline (1 μg/ml) to the growth media (+Dox). U2OS Flp-In T-REx cells carrying an empty vector and transfected with control siRNA (siLUC, EV) were included as a reference. (C) Gating hierarchy used to compute the relative cell cycle distributions depicted in figure S4B. (D) Representative electron micrograph from a denatured DNA sample enriched for mitochondrial DNA from U2OS cells. The magnified area on the lower left hand side shows the typical bubble structure of genomic DNA, while the double stranded molecule on the top right hand side is of mitochondrial origin. The scale bars equal 200nm

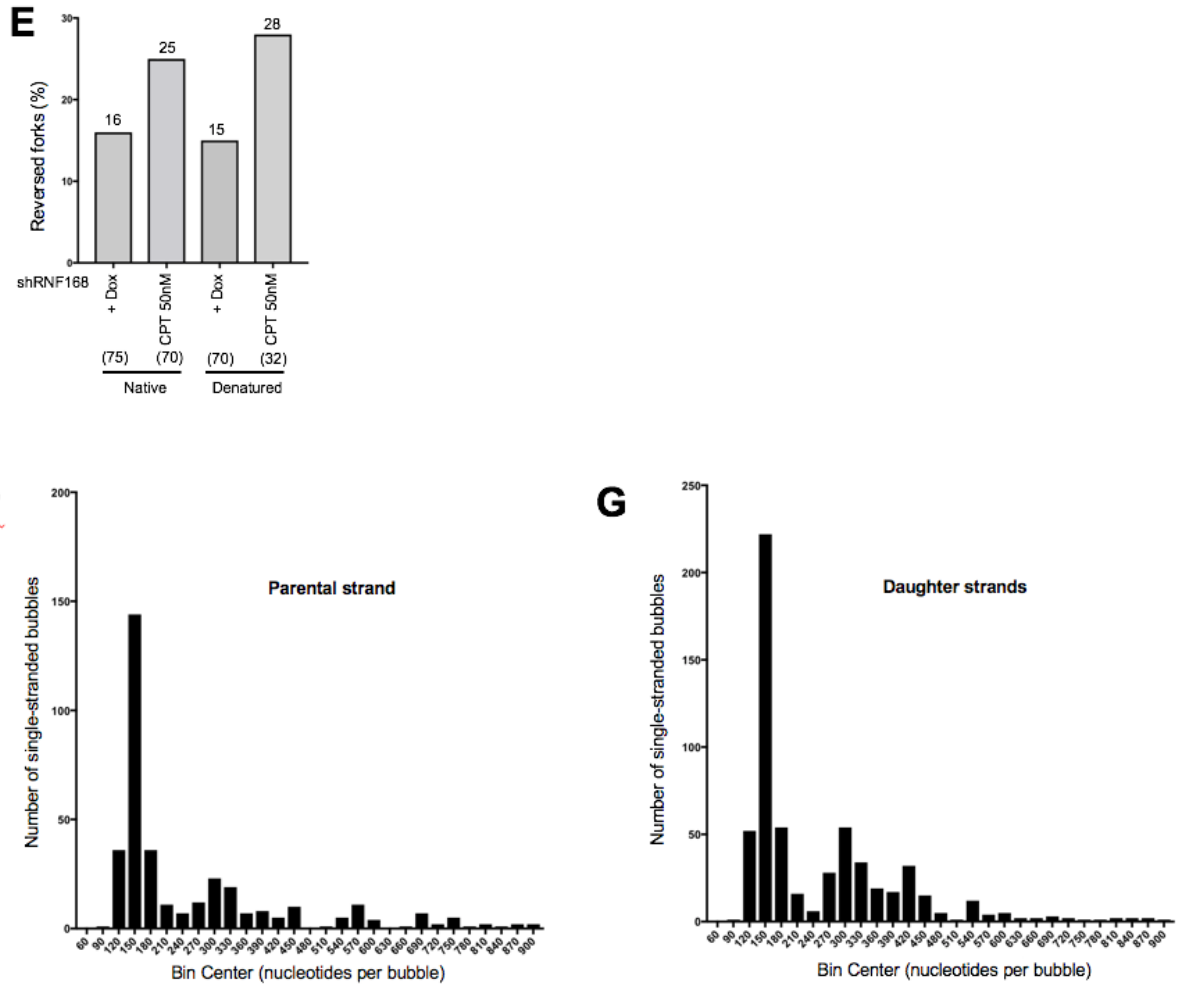

Figure S6. Related to Figure 6 (continued)
(E) Relative frequency of reversed forks found by native and denaturing transmission electron microscopy in the two samples used to compute the values presented in figure 6C and figure S4E and S4F. The respective percentage of reversed forks per sample is indicated above each column. The numbers in brackets denote the total a of analyzed molecules for each sample. (F) Frequency distribution of the bubble size on the parental strand of denatured reversed replication forks found in transmission electron microscopy. The same molecules as in figure 6C were analyzed and plotted as histograms with a bin width of 30 nucleotides. (G) Frequency distribution of the bubble size on the daughter strands of denatured reversed replication forks found in transmission electron microscopy.

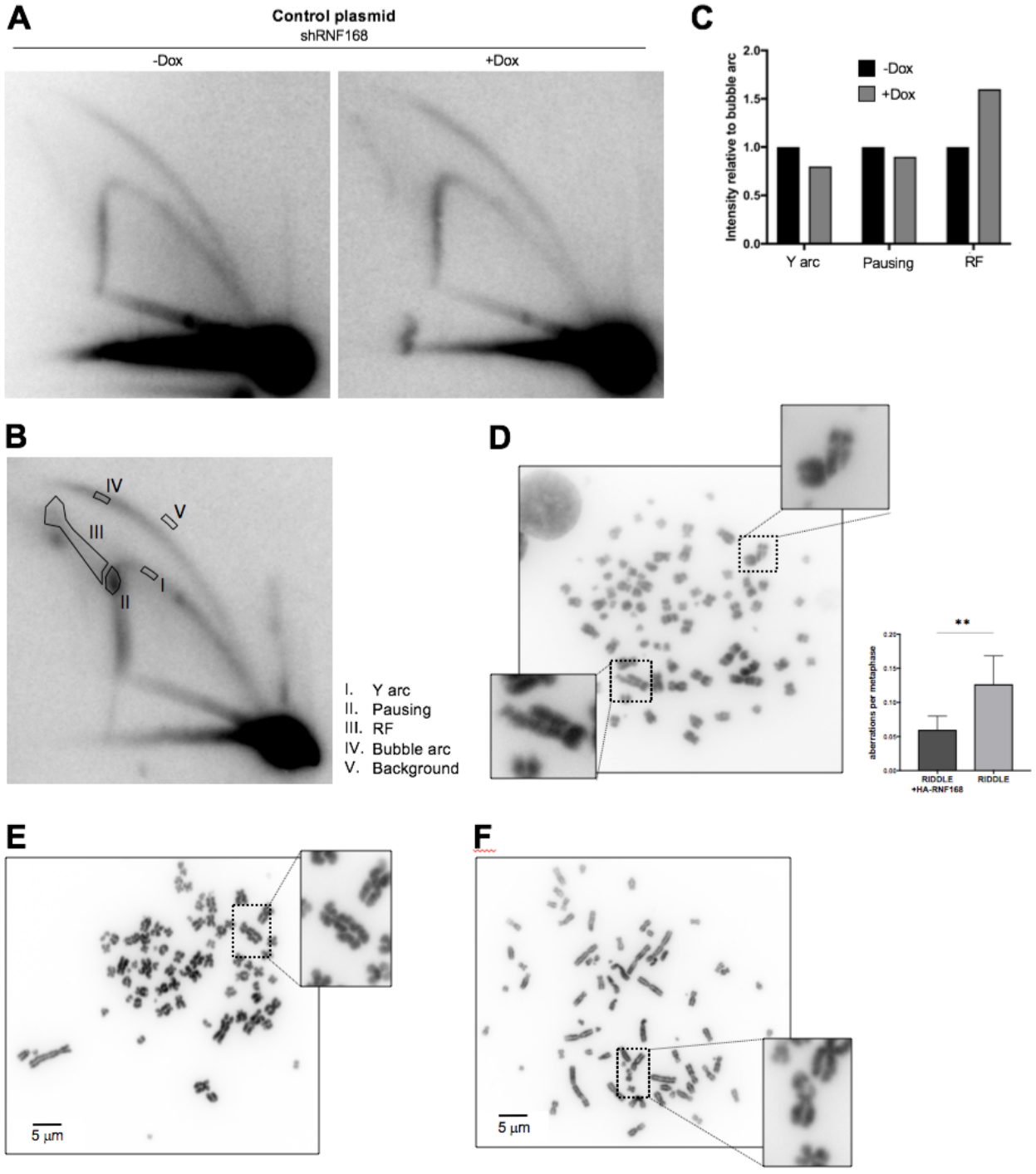

Figure S7. Related to Figure 7.
(A) Typical 2D gel pattern of control plasmid 48h after transfection into control (-Dox) and RNF168 depleted cells (+Dox) (B) 2D gel pattern with highlighted areas indicating the different regions of the gel that are used for accurate signal quantification. (C) Repetition of the experiment presented in Figure 7A showing comparable results. (D) Number of chromosomal abnormalities observed in RIDDLE patient fibroblasts (RIDDLE) and RIDDLE fibroblasts reconstituted with HA-RNF168 (** P Value <0.01, Paired t test). A representative image is included. (E) and (F) Additional representative images for the metaphase spreads (Figure 7B) to detect chromosomal aberrations in RNF168-depleted U2OS cells.

A

U2OS shRNF168	NT	Mirin	Dox	Dox + Mirin
%RF Exp #1	5 (66)	-	16 (75)	-
%RF Exp #2	4 (73)	5 (72)	15 (73)	32 (74)
%RF Exp #3	5 (75)	6 (70)	15 (73)	29 (82)

B

U2OS shRNF8	NT	Mirin	Dox	Dox + Mirin
%RF Exp #1	5 (85)	-	18 (82)	-
%RF Exp #2	6 (71)	5 (77)	15 (74)	25 (77)
%RF Exp #3	7 (74)	7 (81)	18 (74)	22 (72)

C

U2OS	WT NT	WT Mirin	53BP1Δ NT	53BP1Δ Mirin
%RF Exp #1	4 (78)	5 (91)	16 (70)	24 (74)
%RF Exp #2	6 (92)	5 (80)	15 (71)	22 (74)

D

U2OS	NT	ATMi
%RF Exp #1	5 (86)	17 (75)
%RF Exp #2		21 (82)

E

RPE	WT	H2AX S139A
%RF Exp #1	4 (90)	16 (70)
%RF Exp #2	6 (77)	15 (70)

Table S1. Electron microscopy data for Figures 3-5 and Figure S3 (A-D). **(A)** Percentage of observed reversed forks (% RF) in three independent EM experiments for samples in Figure 3A and Figure 5G. **(B)** Percentage of observed reversed forks (% RF) in three independent EM experiments for samples in Figure 4E (first panel) and Figure S5A. **(C)** Percentage of observed reversed forks (% RF) in two independent EM experiments for samples in Figure 4E (second panel) and Figure S5B. **(D)** Percentage of observed reversed forks (% RF) in two independent EM experiments for samples in Figure 4E (third panel). **(E)** Percentage of observed reversed forks (% RF) in two independent EM experiments for samples in Figure 4L.
Number of analyzed molecules per sample is indicated in brackets.

5. Preliminary results

This chapter presents preliminary results that were not discussed in Schmid et. al. Part of this data was also included in my master thesis but will be discussed again to give a complete account of the results obtained during my project.

5.1. The role of Ub chains in unperturbed DNA replication

Ubiquitin signalling has in recent years emerged as a key regulator of the replication process and of the cellular responses to DNA lesions (Smeenk & Mailand 2016). However, the mechanistic function of individual ubiquitin linkage types in replication has not yet been studied in a systematic way. In this part of my project I have investigated the role of ubiquitin signalling and especially K63-linked Ub chains in unperturbed DNA replication. Although intriguing results were obtained, this sub-project was not brought to completion since I focused my efforts on the data presented in Schmid et. al 2018.

5.1.1. Proteasome inhibition

One of the most emblematic functions of the Ub signalling system is to target proteins for degradation by the 26S proteasome, a process that is mediated primarily via K48-linked chains. Upon treating cells with proteasome inhibitors, K48 chains rapidly accumulate, thereby depleting the cellular pool of free ubiquitin (Yau & Rape 2016). Thus, proteasome inhibitors can be used to interfere with normal Ub signalling in the cell. To get an impression whether ubiquitin signalling plays a role during unperturbed DNA replication HEK 293T cells were treated with increasing concentrations of the proteasome inhibitor MG-132 and subjected to EdU/γH2AX/DAPI flow cytometry (FACS) analysis (Figure P1).

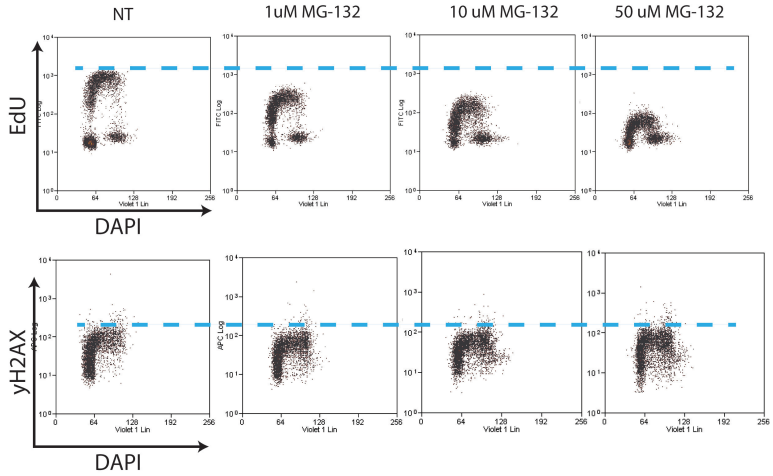

Figure P1: MG-132 treatment leads to a slowdown of DNA replication
EdU/γH2AX/DAPI flow cytometry analysis of HEK 293T cells treated with increasing concentrations of MG-132 for 4h. The dashed lines indicate normal levels of EdU incorporation and H2AX phosphorylation in S-phase.

MG-132 treatment led to a marked decrease in EdU incorporation rates in a concentration dependent manner without causing a detectable increase in H2AX phosphorylation levels. This indicates that efficient DNA synthesis under unperturbed conditions requires functional Ub signalling.

5.1.2. Ubiquitin depletion

Proteasome inhibition is a very indirect way to study the function of Ub signalling in replication. Furthermore, proteasome inhibitors are toxic agents that may cause unanticipated problems in cells subjected to such treatments. To get a more direct assessment of the role of ubiquitination in unperturbed S-phase, I investigated the effect of Ub depletion on cell cycle progression and replication. To this end, I transiently reduced Ub expression levels in HEK 293T cells using a combination of two different siRNAs that specifically target the ubiquitin precursors UBA52 and RPS27A (Adam et al. 2013) while monitoring effects on cell cycle progression and replication by EDU/DAPI/γH2AX flow cytometry (FACS) analysis (Figure P2).

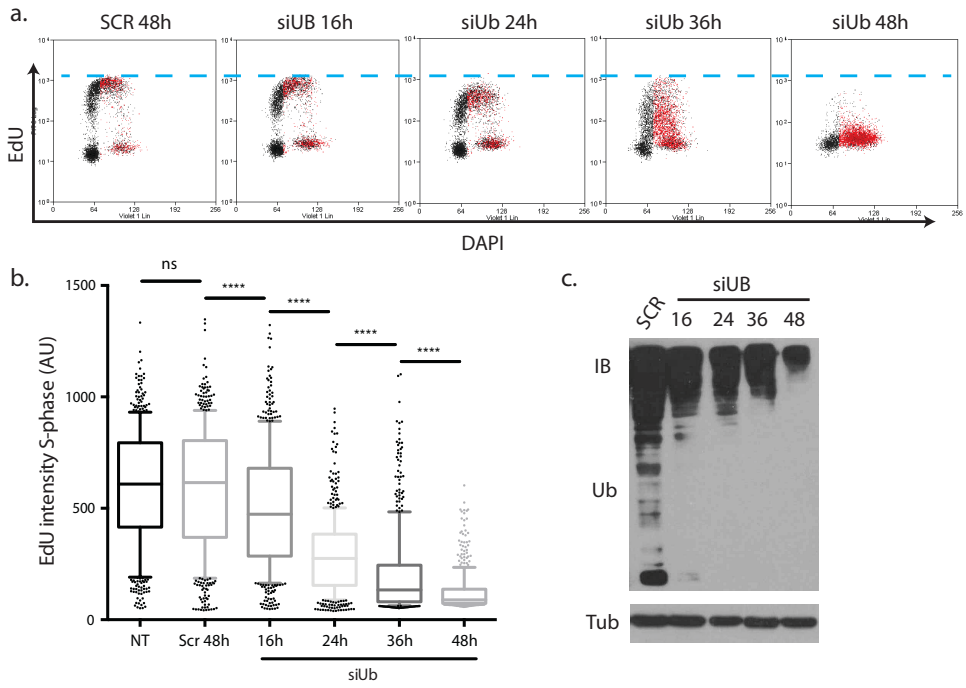

Figure P2: Ub depletion affects DNA synthesis, causes H2AX phosphorylation and ultimately blocks replication.
a. EdU/γH2AX/DAPI FACS analysis of HEK 293T cells transiently depleted of Ub for increasing time spans (16, 24, 36 and 48h). Red dots represent γH2AX positive cells. Transfection of a scrambled oligo (SCR) was used as a control. The dashed blue line indicates normal levels of EdU incorporation. **b.** Statistical analysis of EdU intensity values from 500 randomly selected S-phase cells extracted from the FACS data depicted in panel a. Intensities are indicated as arbitrary units (AU) and analyzed using Mann-Whitney-U test (**** p-value< 0.0001, Whiskers: 10^{th}-90^{th} percentile). **c.** Western blot analysis showing the level of Ub depletion in whole cell extracts from HEK 293T cells at different time-points of Ub knockdown (siUB). A scrambled oligo (SCR) was used as a control. Tubulin (Tub) serves as a loading control.

FACS analysis at different time-points after transfection (16h, 24h, 36h and 48h) (Figure P2) revealed that lowering ubiquitin Ub availability markedly affects the rate of DNA synthesis, as assessed by EdU incorporation rates, and leads to high levels of H2AX phosphorylation. Both effects are detectable well

before cells undergo replication block, a cell cycle arrest in S-phase with partially replicated DNA, after prolonged Ub depletion.

The decrease in DNA synthesis rates observed upon Ub knockdown in HEK 293T cells could be caused by a reduction of origin firing, a slowdown of replication fork progression or a combination of both. Next, I performed DNA fiber spreading experiments to assess at single molecule level the potential effect of Ub depletion on fork progression (Figure P3). These two conditions were chosen because they showed a clear effect on EdU intensity but no apparent replicative arrest in the previous FACS experiments (see Figure P2). A statically significant reduction in fork speed was observed at both time-points. After 24h of Ub depletion the median speed of individual replication forks was decreased by 21% while after 36h this reduction amounted to 52% as compared to control cells. Hence, depleting the cellular pool of free Ub clearly affects the speed of individual replication forks. However, this does not exclude that replication origin firing is impaired as well. These results indicate that ubiquitination events are essential to the replication process under unperturbed conditions.

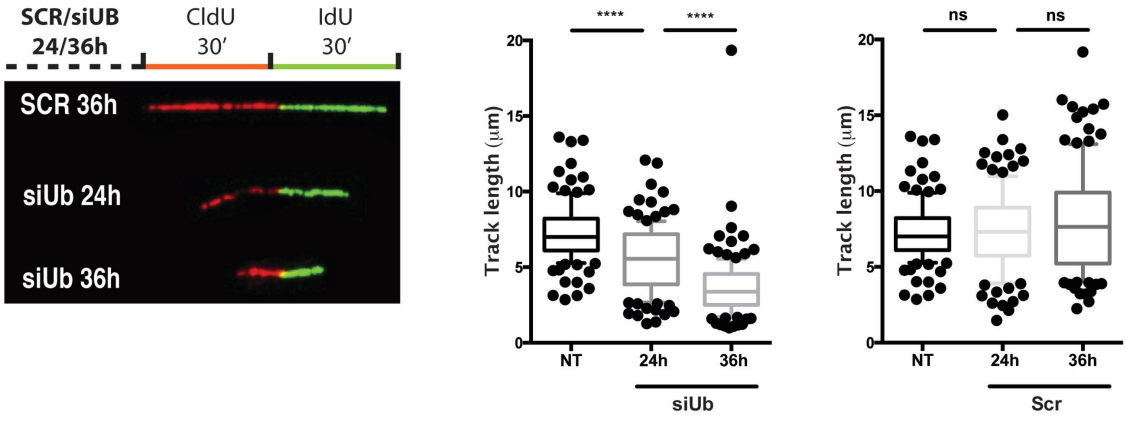

Figure P3. Effect of Ub depletion on individual replication forks.
Statistical analysis of IdU track lengths from DNA fiber spreading assays at 24h and 36h of Ub depletion in HEK 293T cells. Transfection of a scrambled oligo (SCR) was used as a control. The left most panel shows the transfection and labeling scheme including a representative fiber for each time-point of Ub depletion. Statistical analysis was done by Mann-Whitney-U test (**** p-value< 0.0001, Whiskers: 10^{th}-90^{th} percentile).

Even though HEK 293T cells have several advantages as an experimental system, they are not an optimal model to study DNA replication. HEK 293Ts express SV40 large T antigen and contain portions of various human adenoviruses (zur Hausen 1967; McDougall 1971; Fu & Manley 1987). This is likely to modify the replicative process in this cell line, making it difficult to compare to untransformed human cells. Therefore, the previously presented results were reproduced in U2OS cells, which are a standard model in the field of DNA replication research. The same set of siRNAs was used for Ub knockdown but shorter transfection periods were chosen, as U2OS cells show lower protein production than HEK 293Ts and Ub depletion was thus expected to occur faster. Cell cycle progression and DNA synthesis rates were again monitored by flow cytometry analysis of EdU incorporation and DAPI intensity. Ub expression levels were assessed simultaneously by FK2 staining, an antibody that specifically recognizes Ub conjugates but not free Ub (Figure P4).

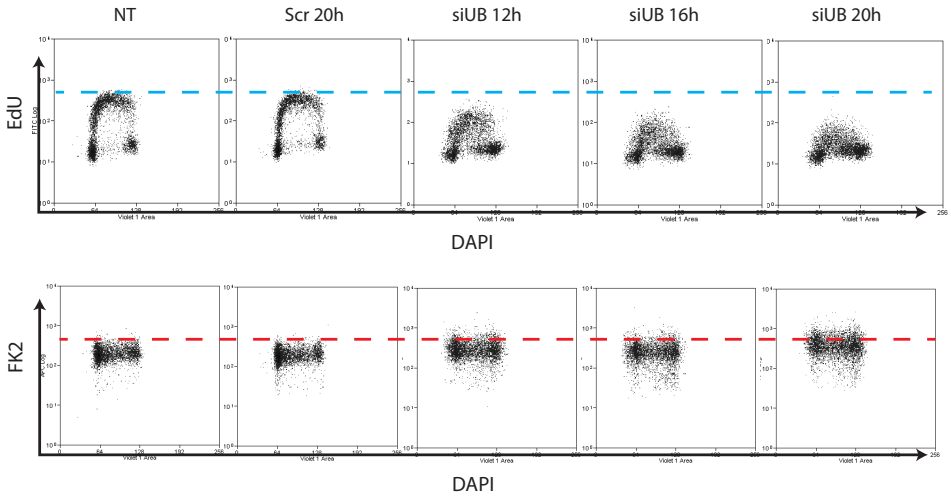

Figure P4: Ub depletion also affects the rate of DNA synthesis in U2OS cells
EdU/FK2/DAPI flow cytometry analysis of U2OS cells depleted of Ub for different amounts of time. The dashed lines depict normal Edu incorporation rates in S phase and normal Ub conjugate levels respectively.

The experiment showed that Ub depletion also clearly affects DNA synthesis under unperturbed conditions in U2OS cells. In U2OS, the effect on EdU incorporation occurs faster than in HEK 293Ts, possibly reflecting lower baseline levels of Ub. But, the general trend of impaired DNA synthesis rates at early time-points (12h and 16h) followed by a partial replication block (20h) is overall comparable between the two cell lines.

Transfecting cells with siRNAs can induce various forms of cellular stress (Andrews et al. 1997). It is thus difficult to separate the consequences of transfection stress from the effects of protein depletion, which is an inherent problem with transient knockdown systems. To overcome this shortcoming, I employed a previously established U2OS based RNAi system for the tetracycline-inducible knock down of ubiquitin (M. Xu et al. 2009). This cell line (*U2OS shUb*), stably expresses multiple copies of two tetracycline-inducible shRNAs that target all four Ub precursors in the human genome (UBC, UBA52, UBB and RPS27A). I performed a time-course experiment to assess the effects of Ub depletion on unperturbed DNA replication in this system, treating the cells with 1 µg/ml of tetracycline (Tet) for 16, 24 and 36 hours and subjecting them to EDU/DAPI/FK2 FACS analysis (Figure P5).

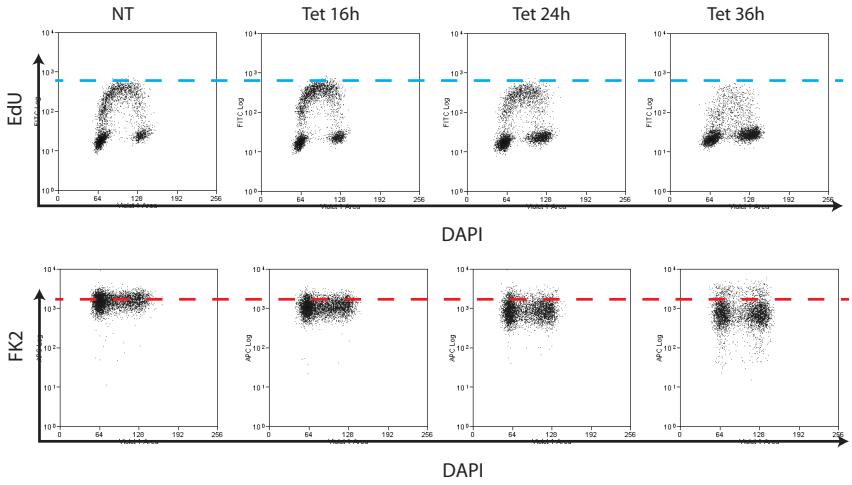

Figure P5: Ub knockdown in U2OS shUb impairs replication and cell cycle progression
Flow cytometry analysis of U2OS shUb cells at different time-points of tetracycline treatment (Tet, 1µg/ml) staining for EdU, DAPI and FK2. The dashed blue and red lines depict normal Edu incorporation rates in S phase and normal levels of Ub conjugates (FK2) respectively.

This experiment yielded two main observations. First, the induction of Ub knockdown is highly effective in this cellular system and can already be observed by a marked drop in FK2 intensity after 16h of Tet treatment. Second, just as in the transient knockdown system, Ub depletion clearly impairs DNA replication. Replication problems are already apparent after 24h of tetracycline treatment. At this point the EdU intensity of the mid S-phase population is shifted downwards and cells start to accumulate in G2. After 36h of Tet exposure, most S-phase cells show severely reduced EdU incorporation rates combined with an intermediate DNA content, indicating that they have undergone replicative arrest. This acute impairment of DNA synthesis is accompanied by a marked accumulation of cells in the G1- and G2-phase of the cell cycle. The replication defects upon Ub depletion by Tet-inducible shRNA expression thus resemble the observations made by siRNA-mediated Ub knockdown in HEK 293Ts and wildtype U2OS cells. This shows that absence of effective Ub signalling substantially interferes with DNA replication independent of the cell line and the system of Ub depletion.

5.1.3. Ubiquitin replacement and the role of K63-linked chains in DNA replication

To investigate the role of specific Ub linkages I took advantage of a panel of Ub mutants impaired in the formation of individual chain types, so called K/R mutants. In these mutants, a single lysine residue of Ub (K6, K11, K27, K29, K33, K48 or K63) is replaced by the structurally related amino acid arginine (R). Since Ub cannot be conjugated onto an arginine residue, the formation of one specific type of Ub chain is not possible with these mutant polypeptides. This allows to evaluate if the presence of an individual Ub linkage type is necessary for a distinct cellular process such as DNA replication. However, the functional consequences of expressing K/R mutants in human cells can only be appreciated if the endogenous Ub is depleted at the same time, which constitutes a replacement experiment. To determine if specific Ub chains are required for efficient replication, I aimed to perform replacement studies in U2OS shUb cells, depleting endogenous Ub by Tet treatment and transiently expressing shRNA resistant Ub mutants. To evaluate the practicality of this experimental strategy, I first tried to

rescue replication speed in Ub depleted cells by ectopically expressing wildtype (WT) Ub. Based on the experiment shown in Figure P5, a Tet treatment of 36 hours was chosen to deplete endogenous Ub. The rescue constructs for the expression of FLAG-tagged WT Ub were transfected 12 hours prior to Tet addition. This was expected to give the cells time to express the construct and deal with the stress of transfection before the actual Ub depletion is initiated. Cell cycle progression, replication speed and expression levels of FLAG-tagged WT Ub were monitored by EDU/DAPI/Flag FACS (Figure P6). Monitoring FLAG levels by FACS has two advantages. First, it allows to determine the expression efficiency of the rescue construct, which was approximately 35% in this experiment. Second, it enables the creation of gates to specifically compare the EdU intensity pattern of FLAG positive and negative cells. These gates helped to reveal that a partial rescue of EdU incorporation rates is achieved in cells positive for the FLAG-tagged construct. Looking at the EdU intensity levels reveals that even the transfection of an empty vector (EV) significantly aggravates the replication defects observed upon Ub depletion.

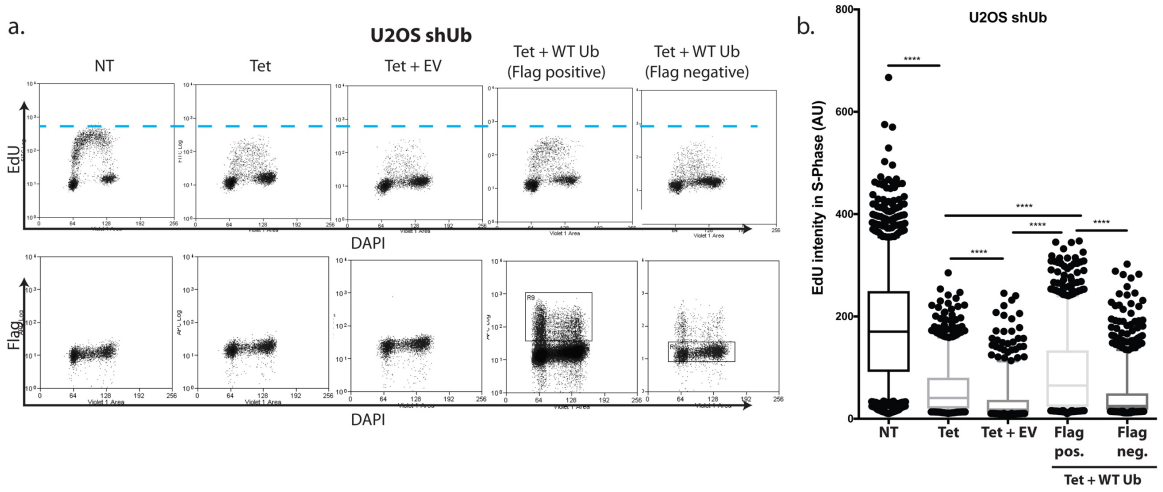

Figure P6: Transient Ub replacement in U2OS shUb cells leads to a partial rescue of EdU incorporation rates
a. U2OS shUb cells were subjected to Tet for 36h to deplete endogenous Ub. To rescue Ub expression, one set of cells was transfected with a shRNA resistant rescue constructs for the expression of FLAG-tagged WT Ub, 12h prior to the Tet treatment. Transfection of an empty vector (EV) was used as a control. The cells were monitored by EDU/DAPI/Flag FACS. Gating allows to specifically observe the EdU pattern of FLAG positive and negative cells. **b.** Extracted S-Phase EdU intensity values from the experiment depicted in panel a. Statistical analysis was done by Mann-Whitney-U test (**** p-value< 0.0001, Whiskers: 10^{th}-90^{th} percentile).

Since plasmid transfection alone exerts such a high level of stress in Ub depleted cells, it would be difficult to clearly assess the effect of K/R mutants using the current protocol. Furthermore, transient replacement systems are prone to considerable experimental variation and transfection efficiencies will never reach 100 percent, making this approach suboptimal for population studies, including DNA fiber spreading and electron microscopy analysis.

To overcome these limitations, I employed previously established Ub replacement cell lines for WT Ub (*U2OS Ub WT*) and K63R mutant Ub (*U2OS K63R*) that are based on the *U2OS shUb* system (M. Xu et al. 2009). These cell lines carry the same set of Tet-inducible shRNAs to knock down the expression of

endogenous Ub, but additionally express RNAi-resistant Ub constructs, also induced by Tet. To uncover possible replication effects occurring upon Ub replacement in these cellular systems, another FACS based time-course experiment was performed. DAPI content, EdU incorporation and the levels of Ub conjugates (FK2) were monitored after subjecting both cell lines to Tet treatment (1 µg/ml) of increasing duration (24, 48, 72 and 96h) (Figure P7). The 96h end point was chosen because the original publication describing these cell lines indicated that the maximum Ub replacement efficiency occurs at 4 days of exposure to Tet (M. Xu et al. 2009).

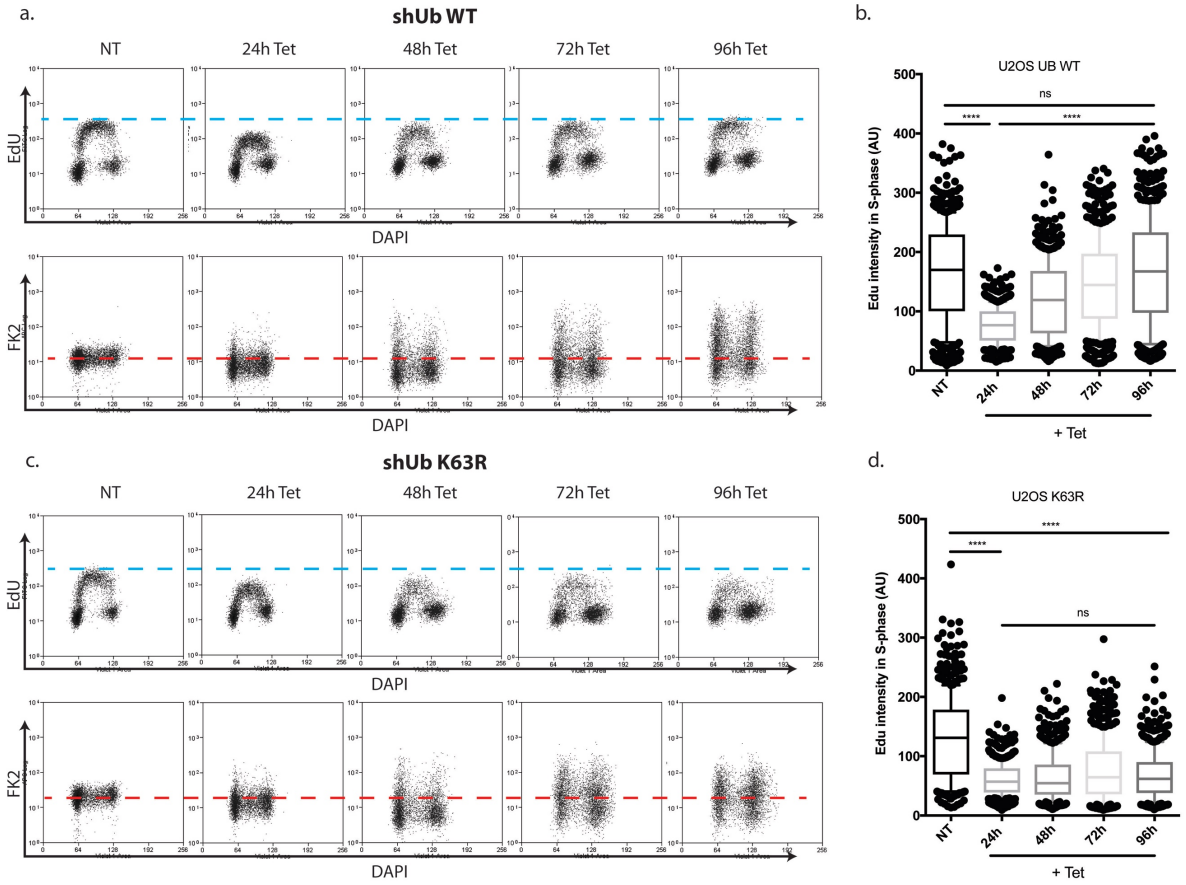

Figure P7: Ub K63 is required to ensure normal rates of DNA synthesis
a. FACS analysis of *U2OS Ub WT* cells stained for EdU, DAPI and Ub conjugates (FK2) at different time-points of tetracycline treatment (Tet, 1µg/ml). The dashed lines indicate normal Edu incorporation rates in S phase and normal Ub levels respectively. **b.** Extracted S-phase EdU intensity values from the experiment shown in panel a. **c.** FACS analysis of *U2OS Ub K63R* cells treated and stained as in panel a. **d.** Extracted EdU intensity values from the FACS experiment depicted in panel c (**** p-value< 0.0001, Whiskers: 10^{th}-90^{th} percentile).

Both cell lines experience significantly reduced EdU incorporation rates after 24 hours of Tet treatment. At the same time, a sharp drop of Ub conjugate levels can be observed in most cells. This suggests that the Ub knockdown initially proceeds faster than the expression of shRNA resistant WT and K63R Ub respectively. After 96 hours, approximately half of the cells from both cell lines show higher levels of Ub conjugates than the non-treated control (NT). DNA synthesis rates in U2OS WT Ub cells are fully rescued under these conditions, whereas replication is still severely impaired in *U2OS K63R* cells.

Similar discrepancies between the two cell lines are already observed after 72 hours of Tet treatment, albeit the rescue in U2OS Ub WT cells is less pronounced. This experiment demonstrates that the presence of Ub K63 is required to ensure efficient rates of DNA synthesis in unperturbed S-phase. Monitoring EdU incorporation rates by FACS can however not reveal whether this impairment of replication is brought about by reduced origin firing, impaired replication fork progression or a combination of both.

To find out if the absence of Ub K63 has a direct effect on the speed of individual replication forks, a DNA fiber spreading experiment was performed in both cell lines (Figure P8). Based on the FACS analysis presented in Figure P7, a Tet exposure of 72 hours was considered optimal for this experiment. Under these treatment conditions, there is a clear rescue of EdU incorporation rates in U2OS Ub WT while DNA synthesis is still strongly impaired in U2OS K63R. Furthermore, hardly any dead cells were observed upon 72h of Tet treatment. In contrast, exposing the cells to Tet for 96 hours caused extensive cell death in the U2OS K63R cells (data not shown), which made this treatment duration impractical for fiber analysis. Since both shRNA resistant Ub replacement constructs carry an HA tag, their expression could be followed by Western blot (Figure P8c). Exposure to Tet for 72h did not affect the length of DNA fibers in U2OS Ub WT cells. In contrast, the same treatment in U2OS K63R cells led to an approximately 30% reduction in median fiber length (Figure P8b). This shows that the progression of individual replication forks in unperturbed S-phase is significantly impaired in the absence of K63-linked Ub chains.

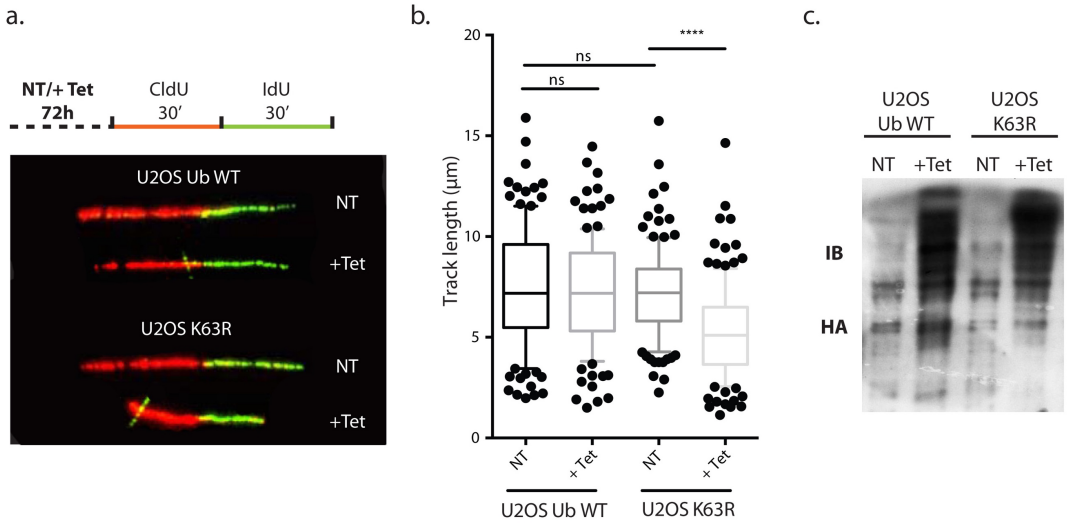

Figure P8: Absence of K63-linked Ub chains impairs replication fork speed
a. Treatment and labeling protocol for the DNA fiber spreading experiment presented in panel b. A representative fiber is shown for each treatment. **b.** Statistical analysis of IdU track lengths from a DNA fiber spreading experiment in *U2OS Ub WT* and *U2OS K63R* under non-treated (NT) conditions and upon 72h of exposure to tetracycline (1µg/ml) (+ Tet) (**** p-value< 0.0001, Whiskers: 10^{th}-90^{th} percentile). **c.** Immunoblot showing the expression of HA-tagged WT Ub and K63R mutant Ub under non-treated conditions (NT) and after 72h of Tet treatment (1µg/ml).

Overall the data presented in this subchapter indicates that Ub signalling is essential for efficient DNA replication under unperturbed conditions and that K63-linked chains play a central role in this process.

5.2. Additional data on the role of RNF168 in DNA replication

Several experiments investigating the role of RNF168 in DNA replication, cell growth and replication fork protection were not discussed in Schmid et. al, because they went beyond the well-defined scope of the manuscript. The data obtained from these experiments will be presented in the following sub-chapters.

5.2.1. Effects of RNF168 depletion on cell survival and proliferation

The marked replication defects in RNF168 depleted cells discussed in previous chapters raised the question if cell survival or proliferation may also be affected in the absence of this E3 ligase. To investigate this, I performed a clonogenic assay and a growth curve experiment (Figure P9). While the former assay measures cell survival, the latter reflects a combination of cell survival and proliferation rates. These experiments showed that cell survival is not significantly impaired upon RNF168 knockdown, as the number of colony forming cells in the clonogenic assay was unchanged. In contrast, proliferation is mildly but significantly affected in RNF168 depleted cells, as can be seen in the growth curve depicted in Figure P9b. Thus, RNF168 depletion results in cell cycle delays, which affect the rate of cell proliferation.

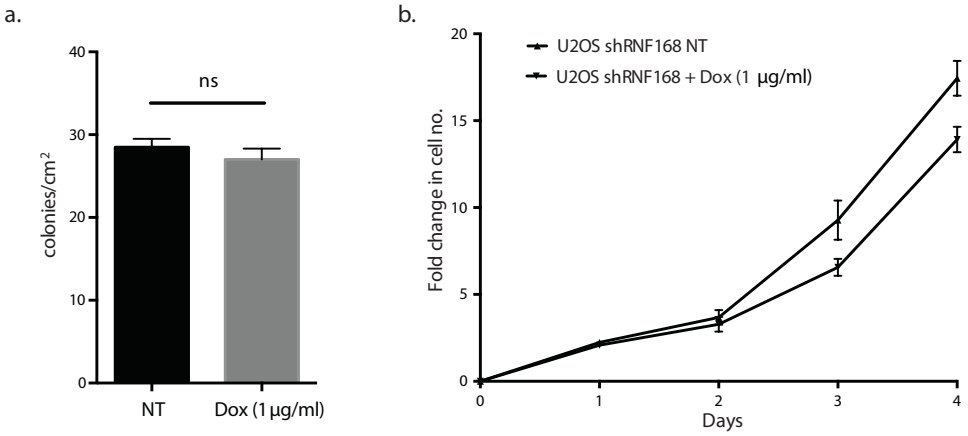

Figure P9: Clonogenic assay and growth curve
a. Clonogenic assay showing the number of colony forming cells in presence (NT) and absence of RNF168 expression (Dox).
b. Growth curve comparing cell proliferation rates of RNF168 depleted cells (Dox) to control cells (NT)

5.2.2. Consequences of RNF168 depletion under replication stress

In Schmid et al. 2018 it has been shown that RNF168 is necessary to ensure efficient DNA replication under unperturbed conditions. During my project, I also investigated whether this factor plays a role in the cellular response to exogenous replication stress induced by genotoxic agents.

First, I aimed to detect general sensitivities of RNF168 depleted cells to a diverse set of DNA damaging agents (CPT, ETP, MMC, APH and UV) at different doses. This was done by Cell Titer blue assay (CTB), which yields information on cell survival and proliferation upon different treatment conditions. A low and a high dose was chosen for each genotoxic agent. The lower doses were previously shown to only marginally affect survival and proliferation but still induce replication stress in U2OS cells, while the higher doses were found to have a clear impact on cell survival (Zellweger et al. 2015). The fluorescence

signals recorded for all different treatments in the CTB assay were normalized to the signal from an unperturbed control sample and then depicted as bar plots (Figure P10). RNF168 depleted cells showed no specific sensitivity to any of these genotoxic treatments and reacted comparable to control cells. This experiment was repeated four times, consistently yielding similar results. However, a suboptimal response to replication stress does not necessarily translate into impaired survival and proliferation. Thus, the CTB assay is not fully informative on the possible role of RNF168 in this cellular process.

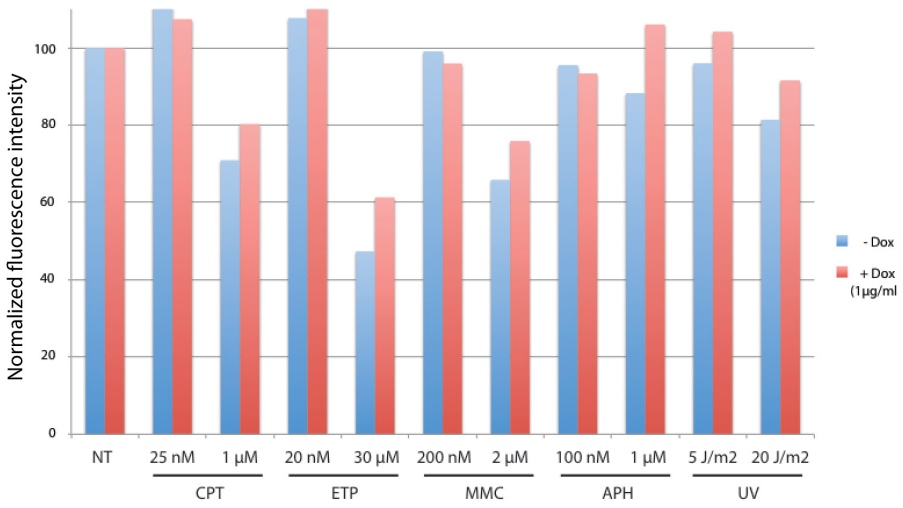

Figure P10: CTB assay does not reveal sensitivities of RNF168 depleted cells to genotoxic treatments
Control (- Dox) and RNF168 depleted cells (+ Dox 1 µg/ml) were exposed to a diverse set of genotoxic agents and subsequently analyzed by CellTiter blue assay. The depicted intensity values have been normalized to the non-treated (NT) condition for both control and RNF168 deficient cells.

To get a more detailed view of possible defects in replication stress response caused by the absence of RNF168, I performed multiple EdU/DAPI FACS experiments. A similar set of genotoxic agents as in the previous CTB experiment was employed, checking for their effect on EdU incorporation rates in presence and absence of RNF168 (Figure P11). In addition to the agents tested in the CTB experiment, the effects of hydroxyurea (HU) and trimethylpsoralen (TMP) were assessed as well. TMP induces interstrand crosslinks upon photo activation by UV-A (Cech & Pardue 1977) and a paper in 2015 suggested that lesions induced through this compound may be repaired by a mechanism involving RNF168 (Raschle et al. 2015). All genotoxic agents tested in these FACS experiments had a clear impact on DNA synthesis rates in control cells, but the impact of RNF168 depletion markedly varied between different treatments. In most analysed cases, the combination of genotoxic treatments and knockdown of RNF168 had a significant additive impact on the rate of DNA synthesis.

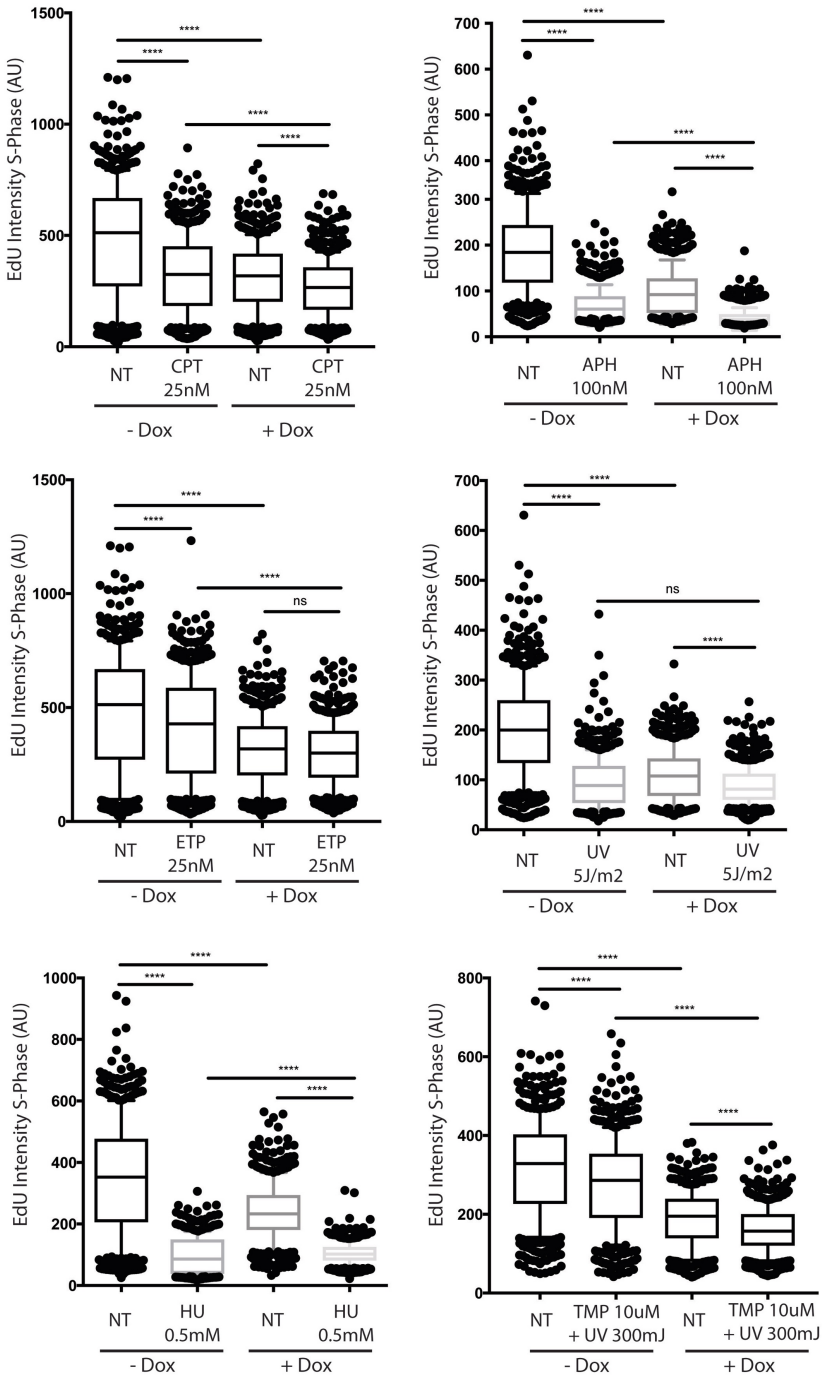

Figure P11: FACS experiments checking for sensitivities of RNF168 depleted cells to genotoxic agents
Extracted S-phase EdU intensity values from Edu/DAPI flow cytometry experiments in U2OS shRNF168 cells. All indicated genotoxic treatments were assessed in control (- Dox) and RNF168 depleted cells (+ Dox)
(**** p-value< 0.0001, Whiskers: 10^{th}-90^{th} percentile).

There are two notable exceptions to this. Etoposide (ETP) did not exacerbate the effect of RNF168 depletion on EdU incorporation. Moreover, upon HU treatment, the absence of RNF168 even led to a slight but significant increase in median EdU intensity. These results are difficult to interpret. RNF168 depletion as such significantly impairs replication. However, whether the loss of RNF168 has more than just an additive effect on DNA synthesis in response to genotoxic treatments cannot be concluded from these experiments.

To find out if similar effects are present at the level of replication fork progression, I performed several DNA fiber spreading experiments in U2OS shRNF168 cells (Figure P12). APH (100nM) and CPT (25nM) were selected as two treatments that showed clear additive effects in the FACS experiments presented in Figure P11. In addition, they represent two mechanistically distinct classes of genotoxic agents, i.e. an inhibitor of DNA synthesis and a topoisomerase inhibitor respectively.

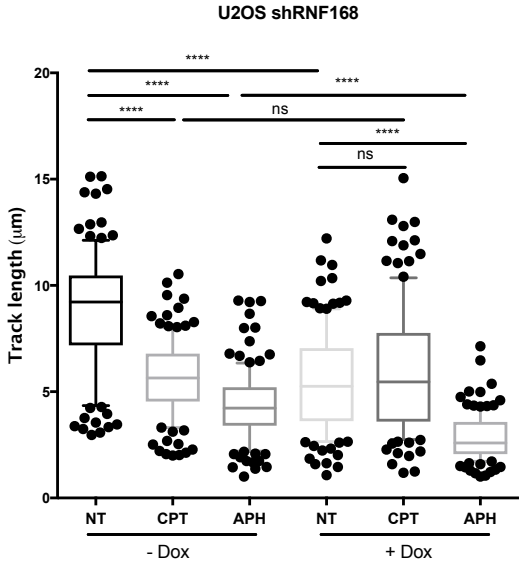

Figure P12: Distinct effects of genotoxic agents on fork speed in RNF168 depleted cells.
Statistical analysis of IdU track lengths from a DNA fiber experiment investigating the effect of CPT (25nM) and APH (200nM) on fork progression in control (- Dox) and RNF168 depleted cells (+ Dox) (**** p-value< 0.0001, Whiskers: 10^{th}-90^{th} percentile).

Interestingly, treatment with these two genotoxic agents led to very distinct outcomes in RNF168 depleted cells. APH had a clear additive effect, further slowing the already impaired fork progression rates observed upon RNF168 knockdown. In contrast, the combination of CPT treatment and knockdown of RNF168 did not significantly diminish replication fork speed compared to CPT treatment or RNF168 depletion alone.

The divergent effects of APH and CPT on fork progression in RNF168 deficient cells were surprising and prompted the question if similar discrepancies could be observed in terms of replication fork architecture. To investigate the effect of these genotoxic treatments on the frequency of reversed forks upon RNF168 depletion, I performed an electron microscopy (EM) experiment under the same treatment conditions used in the fiber experiment (Figure P13).

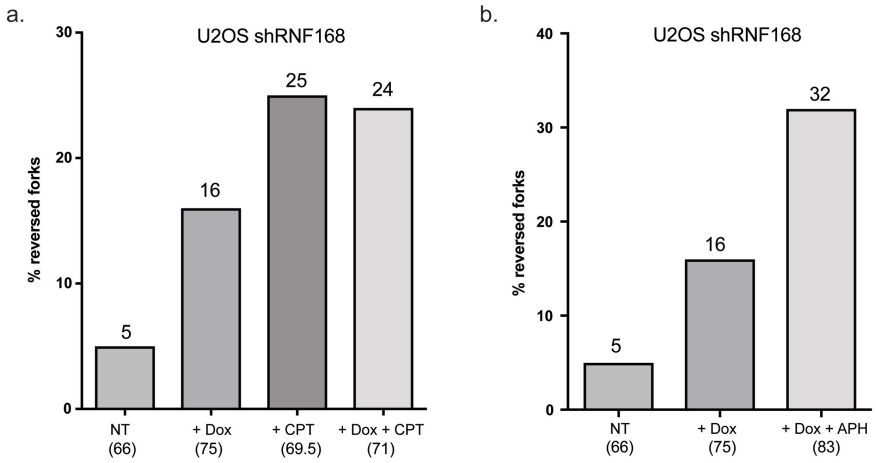

Figure P13: CPT and APH exert different effects on the frequency of reversed forks upon RNF168 depletion
a. EM experiment investigating the effect of CPT treatment (25nM) on the frequency of reversed forks in control and RNF168 depleted cells (+ Dox). The numbers in brackets indicate the total of analyzed molecules for each sample. The values written above each column indicate the relative reversal frequencies for the respective sample. **b.** EM experiment investigating the effect of APH treatment (200nM) on the frequency of reversed forks in RNF168 depleted cells (+ Dox).

Like in the previous fiber experiment, the combination of RNF168 knockdown and CPT treatment did not have an additive effect but led to the same frequency of reversed forks as observed upon CPT treatment alone. APH treatment led to a 32% frequency of reversed forks in RNF168 depleted cells. The previously reported fork reversal frequency upon APH treatment in U2OS cells is only 23% (Zellweger et al. 2015), suggesting that APH could have an additive effect on fork reversal in cells lacking RNF168. It is possible that APH and CPT treatment cause distinct architectural features of reversed forks and/or the recruitment of separate sets of signalling and processing factors, which may underlie the different requirement of RNF168 for their restart or turn-over. Further experiments would be needed to evaluate these possibilities.

5.3. Effects of MDC1 loss on unperturbed DNA replication

The scaffold protein MDC1 serves as a platform for the ATM dependent recruitment of RNF8 to sites of DNA double strand breaks and thus lies upstream of RNF168 in the Ub-dependent DDR pathway (Stewart et al. 2003; Goldberg et al. 2003; Mailand et al. 2007; Huen et al. 2007). In Schmid et al. 2018 we showed that both ATM and RNF8 are epistatic to RNF168 in protecting stalled replication forks during unperturbed S-phase. We therefore expected that MDC1 could also be epistatic to RNF168 in this context. To test if the loss of MDC1 has an impact on DNA replication and whether it is epistatic to RNF168, we performed several fiber spreading experiments using a CRISPR/Cas generated MDC1 knockout cell line (Figure P14)

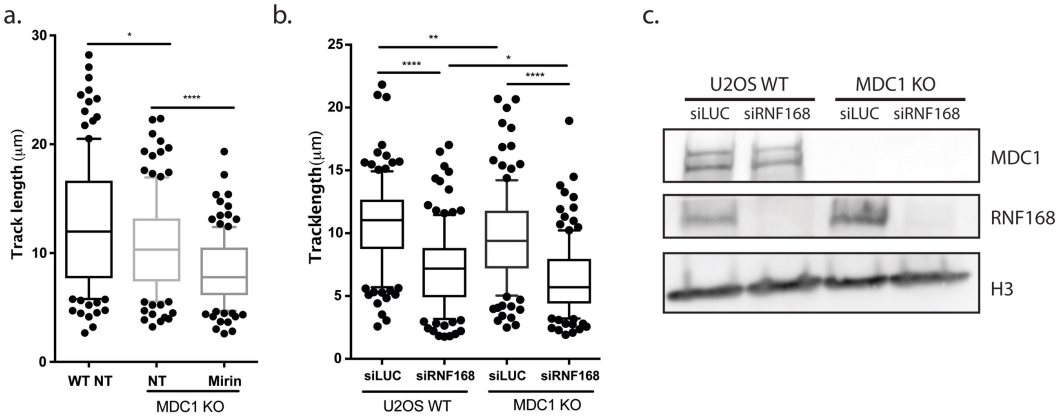

Figure P14: MDC1 knockout impairs fork progression in presence and absence of RNF168
a. Statistical analysis of IdU track lengths from a DNA fiber spreading experiment performed in U20S wild type (WT) and MDC1 KO cells under non-treated conditions (NT) and upon 1h treatment with 50μM mirin (Mirin) (**** p-value< 0.0001, * p-value< 0.05, Whiskers: 10^{th}-90^{th} percentile). **b.** Statistical analysis of IdU track lengths in control (siLUC, U2OS WT), RNF168 depleted (siRNF168, U2OS WT), MDC1 KO (siLUC, MDC1 KO) and RNF168/MDC1 co-depleted cells (siRNF168, MDC1 KO). (**** p-value< 0.0001, ** p-value< 0.01, * p-value< 0.05, Whiskers: 10^{th}-90^{th} percentile). **c.** Immunoblot showing the expression levels of MDC1 and RNF168 for the samples used in panel b. H3 is used as a loading control.

MDC1 KO cells show a mild but nonetheless significant reduction in replication fork speed. In contrast to its rescuing effect upon depletion of other DDR factors, mirin treatment exacerbated slow fork progression in MDC1 deficient cells. Furthermore, co-depletion of MDC1 and RNF168 had an additive impact on replication fork speed, suggesting that the two factors are not fully epistatic in the context of DNA replication. It is therefore likely that recruitment and activation of the DDR cascade is differently regulated in the context of unperturbed replication, in respect to the classical DDR pathway characterized in response to DSBs.

5.4. The role of NHEJ factors in replication and fork reversal

Besides HR, non-homologous end joining (NHEJ) is an alternative mechanism downstream of the Ub-dependent DDR pathway, through which the repair of DNA double strand breaks can be channelled (Schwertman et al. 2016). Due to the close functional relationship between DDR signalling and NHEJ in DSB repair, we were interested to investigate if a similar interplay exists during unperturbed DNA replication.

5.4.1. The Ku70/80 complex is a DNA replication factor

The central NHEJ factor Ku70/80 is a known ubiquitination target of RNF8 (Feng & Chen 2012) and has recently been suggested to regulate the resection of reversed replication forks in *Schizosaccharomyces pombe* (Teixeira-Silva et al. 2017). This raised the potential that the Ku complex could be involved in the DDR mediated fork protection pathway we investigated in Schmid et al. 2018. To test this possibility, I conducted DNA fiber spreading experiments while depleting the Ku complex with two siRNAs targeting the Ku70 and Ku80 subunit respectively. These experiments were performed both in the presence and absence of RNF168 to check if the two factors are epistatic in this context (Figure P15).

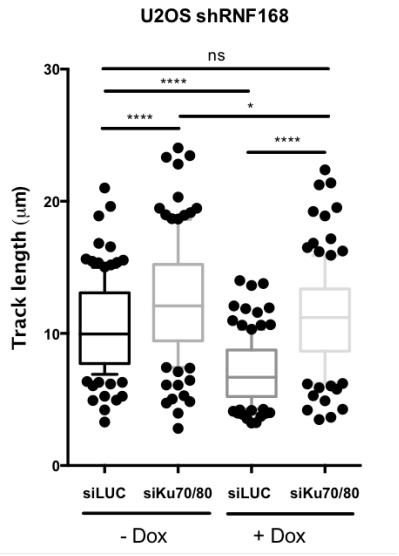

Figure P15: Knock down of Ku70/80 leads to an increase in replication fork speed in control and RNF168 depleted cells.
Statistical analysis of IdU track lengths from a DNA fiber spreading analysis in control (siLUC, - Dox), Ku70/80 depleted (siKu70/80, - Dox), RNF168 depleted (siLuc, + Dox) and in Ku70/80 and RNF168 co-depleted cells (siKu70/80, + Dox) (**** p-value< 0.0001, *** p-value< 0.001, * p-value< 0.05, Whiskers: 10^{th}-90^{th} percentile).

Knockdown of Ku70/80 led to a significant increase in replication fork speed both in presence and absence of RNF168. Clearly the Ku complex restrains replication fork progression in both genetic backgrounds.

Since Ku70/80 is known for its high binding affinity to double stranded DNA ends (Grundy et al. 2014), we hypothesised that the complex could also bind the regressed arm of reversed replication forks and thereby temporarily stabilize these structures. In the absence of the Ku complex cells might therefore not be able to effectively keep forks in a reversed state, which could explain the unrestrained fork progression observed in the previously shown fiber experiment. To investigate this hypothesis, I compared the frequency of reversed replication forks in control and Ku70/80 depleted cells upon CPT treatment, a condition that induces high levels of fork reversal in U2OS (Ray Chaudhuri et al. 2012) (Figure P16).

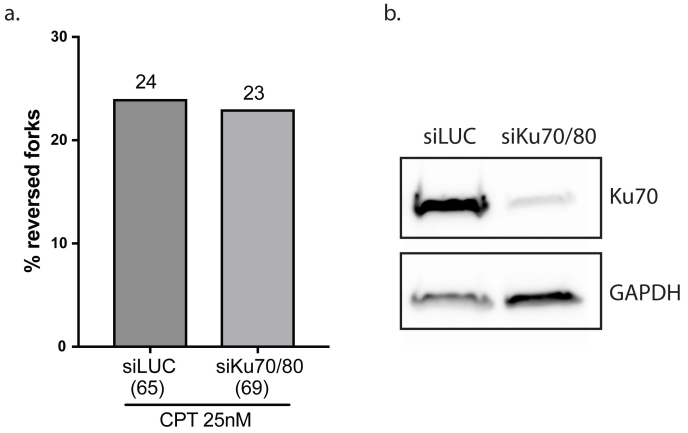

Figure P16: Knock down of Ku70/80 has no detectable effect on fork reversal frequency
a. EM experiment investigating the effect of CPT treatment (25nM) on the frequency of reversed forks in control (siLUC) and Ku70/80 depleted cells (siKu70/80). The numbers in brackets indicate the total of analyzed molecules for each sample. The frequency of reversed forks is shown above each column. **b.** Immunoblot showing Ku70 expression levels.

Unexpectedly, the knock down of Ku70/80 had no detectable effect on the frequency of reversed forks upon CPT treatment. Hence, it seems unlikely that the Ku complex is necessary to stabilize reversed forks under conditions of genotoxic stress.

5.4.2. Effects of DNA-PK inhibition on replication fork progression

After observing intriguing effects of Ku70/80 depletion on replication fork progression, we were interested to see if the loss of other NHEJ factors would invoke similar consequences. The PI3K-related kinase DNA-PKc is a major interactor of the Ku complex and the apical kinase of the NHEJ pathway (Blackford & Jackson 2017), thus presenting an interesting entry point for further investigations into the role of this pathway in DNA replication. To explore the potential function of this kinase, I treated control and RNF168-depleted cells with a DNA-PKc inhibitor (DNA-Pki, Nu7441) and then subjected them to DNA fiber spreading analysis (Figure P17).

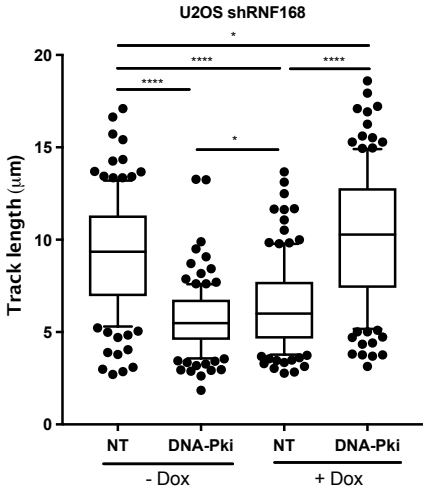

Figure P17: DNA-PKc inhibition has opposite effects on replication fork progression in presence and absence of RNF168
a. Statistical analysis of IdU track lengths from a DNA fiber spreading experiment in U2OS shRNF168 cells. The presented samples include control cells (NT, - Dox), cells treated with 1μM of the DNA-PKc inhibitor Nu7441 for 1h (DNA-Pki, -Dox), cells depleted of RNF168 (NT, + Dox) as wells cells depleted of RNF168 and treated with Nu7441 (DNA-Pki, + Dox) (**** p-value< 0.0001, * p-value< 0.05, Whiskers: 10^{th}-90^{th} percentile).

Surprisingly, DNA-PKc inhibition had opposite effects on fork progression in presence and absence of RNF168. In control cells, DNA-Pki treatment led to a marked decrease in the rate of replication fork progression strongly contrasting with the results obtained upon Ku70/80 knockdown (see Figure P15). Interestingly, inhibiting DNA-PKc has a significantly stronger effect on fork speed than RNF168 depletion. However, upon knockdown of RNF168, DNA-PKc inhibition caused a dramatic increase in replication fork speed, significantly exceeding the rates observed in control cells. These results underline that many double strand repair proteins play a hitherto unappreciated role in unperturbed DNA replication. The functional outcome of inhibiting one or more of these factors is difficult to predict, suggesting that they may be part of an intricate signalling network regulating replication fork speed, restart and protection in numerous – and yet elusive - ways.

6. Discussion and outlook

The role of ubiquitin chains in unperturbed DNA replication:

The finding that depletion of the free ubiquitin pool has a severe impact on DNA replication in unperturbed S-phase (see Figures P1-P5) is not entirely unexpected. Ub signaling has previously been implicated in promoting cell cycle progression through S-phase (Nakayama & Nakayama 2006), and in regulating origin licensing (Havens & Walter 2011) and replication termination (Maric et al. 2014; Moreno et al. 2014). Moreover, impairing ubiquitination is known to abolish the turnover of short-lived proteins in the cell and leads to an accumulation of misfolded proteins within the lumen and membrane of the endoplasmatic reticulum (Hyer et al. 2018). Such proteotoxic stress triggers a downstream signaling cascade called the unfolded protein response (UPR) which can promote cell cycle arrest and apoptosis (Hetz et al. 2015). Hence, ubiquitin depletion *per se* is inevitably going to elicit highly pleiotropic effects on DNA replication, cell cycle progression, and almost every other cellular process. This multifaceted impact on proliferating cells is also elected as the reason for the effectiveness of anti-cancer drugs that interfere with normal Ub signaling (Singhal et al. 2003; Hyer et al. 2018).

In contrast, ubiquitin replacement experiments using K/R mutants can be more informative, since only a limited number of signaling processes will be perturbed by the absence of a specific Ub linkage type. Due to my commitment to other research lines, I was only able to investigate the impact on replication of preventing the formation of K63 linked Ub chains in human cells (see Figures P7 and P8). The absence of K63-linked chains led to slower overall DNA synthesis and to a decrease of replication fork speed in the absence of genotoxic treatments. This appears in line with my finding that RNF8 depletion impairs fork progression in unperturbed S-phase (see Schmid et al. Figure 4), since RNF8 has been shown to assemble K63 chains on chromatin (Thorslund et al. 2015). However, K63 linked poly-ubiquitin constitutes the second most abundant chain type in human cells, regulating a plethora of different cellular mechanisms ranging from DNA repair to cytokine signaling (Chen & Sun 2009). It therefore seems unlikely that the observed replication problems in U2OS K63R cells are solely the result of impaired RNF8 dependent fork protection. A more plausible explanation is that they reflect the deregulation of several K63-dependent signaling pathways. To address this question one could deplete RNF8 and/or RNF168 in cells lacking K63 chains and check for epistatic effects on fork progression by DNA fiber analysis. Another interesting experiment would be to test whether mirin treatment can partially rescue replication fork speed in U2OS K63R, analogous to the situation in RNF8-depleted cells.

One key technical problem with the Ub replacement cell lines we used is that – before the replacement is complete - they undergo a phase of low ubiquitin expression and severe replication stress at early time points of tetracycline-induced Ub replacement (see Figure P7). Hence, the cells might have accumulated considerable DNA damage before their endogenous ubiquitin is fully replaced by the K63R mutant. I would expect that they are subsequently unable to properly repair these lesions since K63 chains are vital for an efficient DNA damage response. Thus, the replication problems we observe under such conditions may simply be caused by unrepaired DNA lesions resulting from the ubiquitin replacement process. This idea is supported by the observation that U2OS K63R cells start to die in large numbers after 96h of tetracycline treatment (data not shown). It would be advisable to check for DNA damage markers by FACS and immunoblot as well as for the presence of DSBs by comet assay,

thereby evaluating the severity of DNA lesions after full ubiquitin replacement. This would allow drawing solid conclusions about the role of K63 chains in unperturbed replication.

Overall the data on the function of Ub chains in DNA replication presented in this manuscript is not yet conclusive. The cellular Ub replacement systems used in my experiments have considerable shortcomings and the ubiquitin chain project was abandoned at an early stage to focus on the role of the Ub dependent DNA damage response in unperturbed replication.

Histone ubiquitination by the DNA damage response is required for efficient DNA replication in unperturbed S-phase (Schmid et al.)

In Schmid et al. we demonstrate that multiple players of the ubiquitin-dependent DNA damage response (DDR), well-characterized upon DSB induction (Schwertman et al. 2016), are necessary for efficient DNA replication under unperturbed conditions. A central factor of this pathway is the ubiquitin E3 ligase RNF168, which poly-ubiquitinates K13/15 on histones H2A and appears to play a crucial role for the protection of replication forks that reverse at difficult to replicate sequences.

In Figure 1 of Schmid et al., we show by immune fluorescence microscopy and proximity ligation assay that RNF168 partially co-localizes with PCNA, a marker of active replication factories, in unstressed U2OS cells. In addition, we demonstrate that this association with replication factories depends on RNF168s ubiquitin-binding domains, also necessary for its recruitment to DSBs (Doil et al. 2009). The PLA signal appears most pronounced in mid to late S-phase, which coincides with the duplication of difficult to replicate DNA sequences in human cells (Glover et al. 2017). Interestingly, using quantitative immune fluorescence analysis we observed that the abundance of H2A K13/15 ubiquitination, the Ub mark generated by RNF168, also peaks in late S-phase, in keeping with a previous report (Pellegrino et al. 2017). The association between RNF168 and PCNA was also confirmed by biochemical interaction studies (Co-immunoprecipitation and GST pull down). Taken together these observations indicate that RNF168 localizes to active replication factories during unperturbed replication in a Ub-dependent manner, which is in line with published proteomics results (Alabert et al. 2014). However, it remains unclear whether the association between RNF168 and PCNA in cells is direct and how exactly it is regulated during unperturbed replication.

We further found that RNF168 depletion leads to significantly reduced DNA synthesis rates and slower replication fork progression, in the absence of genotoxic stress and detectable DSBs (see Figure 2 in Schmid et al.). Analysis of sister fork symmetry showed that this slowdown is at least partially attributable to an increased frequency of replication fork stalling. Median fork speed upon RNF168 depletion is reduced by more than 30%, which is comparable to the effect of low dose genotoxic treatments (Zellweger et al. 2015). Surprisingly, this drastic effect on replication speed is not accompanied by detectable global checkpoint activation, as measured by FACS analysis of γH2AX levels and Western blot analysis of ATR and ATM activation. However, using quantitative IF we could detect a mild but significant increase in the number and intensity of γH2AX foci in S-phase cells upon RNF168 depletion. Combined with the negative data described above, these results imply that H2AX phosphorylation in RNF168 deficient cells is a highly local event happening at distinct and spatially restricted sites in the nucleus. Performing iPOND in cells depleted of RNF168, we found that at least some of these local phosphorylation events occur at active replication forks. Furthermore, we observe slower fork progression in RIDDLE syndrome patient cells, which raises the intriguing possibility that

several of the clinical symptoms observed in RIDDLE patients (Stewart, Stankovic, Byrd, Wechsler, Miller, Huissoon, Drayson, West, Elledge & a M. R. Taylor 2007; Pietrucha et al. 2017) may be related to replication defects caused by RNF168 deficiency.

Interestingly, we found that besides a slowdown in fork progression, RNF168 depletion also reproducibly leads to a threefold increase (from approximately 5% to 15%) in the abundance of reversed replication forks (see Figure 3 in Schmid et al.). When assessing replication fork speed upon co-depletion of known fork-remodelling factors and RNF168, we found that knockdown of the RAD51 recombinase (Zellweger et al. 2015) and of SMARCAL1 annealing helicase (Bétous et al. 2012) both rescue replication fork speed in RNF168 deficient cells. In addition, treating RNF168 depleted cells with the PARP inhibitor olaparib – previously reported to impair reversed fork accumulation (Berti et al. 2013) - rescued fork speed in a RECQ1 dependent manner. These results suggest that slow fork progression in RNF168 depleted cells depends on active fork reversal. However, depletion of the ZRANB3 translocase – also implicated in damage-induced fork reversal (Ciccia et al. 2012; Vujanovic et al. 2017) - did not have any effect on replication fork progression in unperturbed conditions, whether in presence or absence of RNF168. The discrepancies between the effect of depleting SMARCAL1 and ZRANB3 in RNF168 deficient cells may potentially reflect distinct functions of these two annealing helicases in reversing replication forks during unperturbed S-phase. Indeed, while SMARCAL1 has previously been suggested to play an important role for fork reversal in unperturbed replication (Poole & Cortez 2017), ZRANB3 deficient cells were found to have moderately elevated levels of reversed forks in the absence of genotoxic stress.

Just as in the case of RNF168, depletion/inhibition of other DDR proteins, including RNF8, 53BP1 and ATM in U2OS cells causes a significant decrease in replication fork speed and an approximately threefold increase in the frequency of reversed replication forks (see Figure 4 in Schmid et al.). This slowdown in fork progression was not exacerbated when co-depleting RNF168 in the same cells, suggesting that these DDR factors are epistatic in the context of DNA replication. Interestingly, AT patient cells also show reduced replication fork speed, opening the possibility that some of the symptoms observed in ataxia telangiectasia patients may be a consequence of impaired DNA replication. Furthermore, we found that cells carrying a point mutation in the H2AX gene, converting serine 139 to arginine (S139A), show significantly slower replication fork progression and an increase in the level of reversed forks compared to control cells. Inhibiting ATM in S139A cells does not lead to a further reduction of fork speed implying that ATM-dependent H2AX phosphorylation is necessary to ensure efficient DNA replication during unperturbed S-phase. This result is nicely consistent with our observation that H2AX phosphorylation is locally increased at replication forks upon RNF168 depletion, suggesting that ATM signaling at forks may increase to compensate downstream defects in the DDR pathway.

53BP1 and BRCA1 are both downstream of RNF168 in the classical DDR pathway and have recently been implicated in the protection of stalled replication forks from nucleases (Schlacher et al. 2012; Xu et al. 2017). In contrast to what we observe for 53BP1, knocking down BRCA1 in U2OS cells only leads to a very mild slowdown of fork progression and the co-depletion of BRCA1 and RNF168 shows a clear additive effect on replication fork speed. This could indicate that while the signaling cascade of the DDRs NHEJ branch is preserved in the context of unperturbed DNA replication, the HR branch acts independently of RNF168 under these conditions.

The surprising finding, that Mre11 inhibition partially rescues fork speed while at the same time exacerbating the accumulation of reversed forks in DDR deficient cells (see Figure 5 in Schmid et al.) is not trivial to interpret. While reversed replication forks are relatively rare at any given time during unperturbed S-Phase, they have previously been shown to accumulate to 20-25% of total forks when different mechanisms involved in their restart are impaired (Berti et al. 2013; Thangavel et al. 2015). As discussed above, we observe 15-18% reversed forks in DDR deficient cells and this level increases to approximately 25% upon Mre11 inhibition. This suggests that defects in DDR signaling lead to impaired restart of replication forks reversing under unperturbed conditions and that these persistently reversed forks become entry points for Mre11 dependent degradation. Based on the available data we cannot deduce how exactly Mre11 activity leads to slow fork progression in DDR defective cells, but two possible mechanisms come to mind. The first possibility is that Mre11 initiates mid to long range resection of newly synthesized DNA resulting in extensive backtracking of replication forks. Such a process can be observed in BRCA2 depleted cells upon prolonged fork stalling by HU, where the resection depends on the joint activity of Mre11 and EXO1 (Schlacher et al. 2011; Ray Chaudhuri et al. 2016; Mijic et al. 2017; Lemaçon et al. 2017). The second possible mechanism is that Mre11 dependent degradation of reversed forks may produce a DNA intermediate that would require extensive processing before replication can be resumed efficiently at the same fork. Such a mechanism can be expected to cause widespread replication fork stalling, which we indeed observe upon RNF168 depletion. Using currently available methods it would be difficult to distinguish between these two mechanisms and they are in fact not mutually exclusive. One could, for example, imagine a situation where Mre11 initiates limited backtracking, followed by slow replication restart due to lengthy fork processing.

As mentioned in previous chapters, the canonical activity of RNF168 known from its role in DNA double-strand break repair is to ubiquitinate histone variants H2A and H2AX on K13/15, which constitutes a recruitment signal for repair factors including 53BP1 (Schwertman et al. 2016). Measuring replication fork speed in cells expressing the R57D mutant of RNF168 specifically impaired in the ubiquitination of H2A and H2AX (Mattiroli et al. 2012), we found that the same activity is also required during unperturbed DNA replication (see Figure 6 in Schmid et al.). This could imply that – reminiscent of the classical DDR pathway- RNF168 ubiquitinates histone variants H2A on reversed replication forks and thereby recruits downstream protection and restart factors. A prime target for such ubiquitination events is the fourth regressed arm of reversed forks, which presents a double stranded DNA end and is – as we show in Figure 6 of Schmid et al. – fully chromatinised. It must however be stressed, that our current data does not prove that RN168 ubiquitinates histones on regressed arms. I am not aware of experimental methods to study post-translational modifications on specific arms of reversed forks and thus it must for the moment remain unclear where exactly the ubiquitination targets of RNF168 are located within the context of these intermediates.

Nonetheless, the finding that regressed arms of reversed forks are chromatinized reveals an additional structural similarity between such intermediates and DNA double-strand breaks. Both structure present unshielded DNA ends, contain nucleosomes and are protected and processed by an overlapping set of proteins. One may even assume that it would be difficult for the cell to clearly distinguish between these two highly similar DNA configurations and it is thus not completely surprising that related pathways are involved in the resolution of both structures.

The findings described so far suggest that multiple factors of the DDR pathway promote the protection and restart of replication forks that reverse at difficult to replicate regions in unperturbed S-phase. An archetype of such difficult to replicate regions are repetitive DNA sequences, which are a prominent source of endogenous replication stress (Neil et al. 2017; Padeken et al. 2015). Interestingly, 2D gel analysis of repeat containing plasmids extracted from RNF168 deficient cells revealed elevated levels of reversed forks compared to the same plasmids extracted from control cells (see Figure 7 in Schmid et al.). This indicates that inefficient restart and protection of replication forks reversing at repetitive DNA sequences are one source of the replication defects observed in RNF168 depleted cells. Repetitive sequences make up an estimated 50-70% of the human genome (Padeken et al. 2015), which may at least partially explain the global replication fork slow down observed in DDR deficient cells as a majority of replication forks can be expected to encounter such regions within the labelling time of a standard DNA fiber experiment. Interestingly, diseases associated with changes in repetitive DNA sequences and especially in repeat number, commonly lead to neurological and developmental deficiencies (Neil et al. 2017). This opens the possibility that the neurological abnormalities observed in AT and RIDDLE patients may at least partially be fostered by inadequate replication of repetitive DNA regions. Such a mechanism is of course highly speculative and would have to be substantiated by checking for changed repeat frequencies in AT and RIDDLE patient cells.

Performing metaphase spread analysis, we found that RNF168 deficient cells show significantly higher levels of chromosomal abnormalities than control cells, even in absence of exogenous genotoxic stress (see Figure 7 in Schmid et al.). These findings indicate that the replication problems observed in the absence of RNF168 result in frequent insults to the genome, whose subsequent repair is impaired due to the absence of a functional DNA damage response. The expected high degree of genomic instability in such cells is a likely cause of the increased cancer prevalence in people carrying bi- or mono-allelic mutations in certain DDR genes (Swift et al. 1987; Rothblum-Oviatt et al. 2016; Pietrucha et al. 2017; Mantere et al. 2017).

In summary, we have shown that multiple prominent players of the DDR pathway play a crucial role in the protection and restart of replication forks that reverse at difficult to replicate DNA sequence in unperturbed S-phase. In addition, we have demonstrated for the first time that the regressed arm of reversed replication forks contains nucleosomes and can thus serve as a potential target for chromatin modifications. These findings highlight the striking parallels between the repair of DNA double-strand breaks and the resolution of reversed replication forks. Furthermore, they deepen our understanding of the underlying causes behind the two human DNA damage response deficiency disorders RIDDLE syndrome and ataxia telangiectasia as well as the increased cancer prevalence in people with mono-allelic mutations in the RNF168 and ATM gene.

Consequences of RNF168 depletion under replication stress

The FACS screen depicted in Figure P11 of the preliminary results chapter suggests that RNF168 is also required for efficient DNA replication under conditions of genotoxic stress. The DNA synthesis defects resulting from various genotoxic agents were in most cases exacerbated by RNF168 depletion. The only treatments upon which RNF168 did not have a significant additive impact on EdU incorporation rates were low dose ETP and HU. Measuring EdU intensities in S-phase cells represents a rather crude assessment of replication speed, since it cannot distinguish between effects on replication fork

progression and changes in origin firing. It is thus difficult to judge from this data alone why some drugs do not seem to have an additive impact on DNA synthesis in the absence of RNF168.

I also assessed the effect of low dose CPT and APH treatment on fork progression in presence and absence of RNF168 by DNA fiber spreading analysis (Figure P12) and was surprised to find, that while APH has a clear additive impact on replication fork speed in RNF168 depleted cells, no such additive effect could be found upon treating the cells with CPT. Similarly, the two genotoxic agents have distinct effects on the frequency of reversed replication forks in cells lacking RNF168 (Figure P13). Based on the presented data one can only speculate why the two drugs lead to such different outcomes in RNF168 deficient cells. CPT and APH have highly dissimilar mechanisms of action and cause different types of DNA lesions in the cell (Pommier 2013; Michaelis et al. 2001). We know from previous studies that the two genotoxic agents also elicit distinct patterns of DNA damage response signaling. Low dose CPT treatment induces robust ATR dependent H2AX phosphorylation, while APH does not induce any detectable global ATR or ATM signaling above background levels (Zellweger et al. 2015). It is conceivable that these differences in checkpoint signaling could cause the two drugs to have distinct effects on fork progression in RNF168 deficient cells. For instance, the strong ATR activation upon CPT treatment may promote fork protection and restart via alternative factors that act independently of RNF168. A prime candidate for such a redundant protection factor is BRCA2, which has already been shown to mediate fork protection when cells are subjected to low doses of CPT (Mijic et al. 2017). Another potential reason for the different requirement of RNF168 in the restart and turn-over of reversed forks upon APH and CPT treatment could be that the two drug treatments may cause distinct architectural features of reversed forks necessitating different processing steps for their restart.

Effects of MDC1 loss on unperturbed DNA replication

The scaffold protein MDC1 has long been established as an essential recruitment factor for RNF8 and consequently also plays a central role for the downstream RNF168 activity in the classical DDR pathway (Mailand et al. 2007; Huen et al. 2007). We were thus very surprised to find that MDC1 knockout cells showed a much milder reduction in replication fork speed than RNF168 depleted cells and that the knockdown of RNF168 exacerbated slow fork progression in MDC1 null cells (Figure P14b), suggesting that the two factors are not fully epistatic in the context of unperturbed DNA replication. Furthermore, mirin treatment appeared to aggravate rather than alleviate the replication defects in MDC1 knockout cells (Figure P14a). These observations open the possibility that MDC1 is not required for the recruitment of RNF168 to reversed replication forks but is instead involved in an alternative pathway ensuring efficient replication under unperturbed conditions. To test this hypothesis one should perform a proximity ligation assay between RNF168 and PCNA in control and MDC1 null cells. Unfortunately, time restrictions did not allow me to perform such an experiment. Interestingly, the mild replication defects in MDC1 KO cells that are exacerbated by co-depletion of RNF168, are reminiscent of the data obtained for BRCA1 depletion (see Schmid et al.). This may hint towards a requirement of MDC1 for BRCA1 recruitment to replication forks, which is of course purely speculative at this state.

The role of NHEJ factors in replication and fork reversal

The NHEJ regulator complex Ku70/80 is a known ubiquitination target of RNF8 and has recently been proposed to regulate the processing of reversed replication forks in *Schizosaccharomyces pombe*

(Teixeira-Silva et al. 2017; Feng & Chen 2012). We were thus interested to explore whether the Ku complex may also be involved in the DDR dependent fork protection pathway presented in previous chapters. Surprisingly, we found that knockdown of the Ku-complex led to a significant increase of replication fork speed in control cells and rescued fork speed when co-depleted with RNF168 (Figure P15). This indicates that the Ku complex restrains fork progression both in presence and absence of RNF168, but whether there is a functional connection to RNF168-mediated fork protection in unperturbed S-phase is difficult to conclude from this data. The Ku-complex is known to have a very high binding affinity to double-stranded DNA ends (Grundy et al. 2014) and we therefore hypothesized that it might play a role in the stabilization of reversed replication forks. If the loss of Ku70/80 would render replication forks unable to assume a sufficiently stable reversed conformation, one could indeed expect faster fork progression under control conditions as well as strongly reduced fork degradation in DDR deficient cells. We found however that the frequency of reversed forks was comparable in control and Ku70/80 deficient cells upon low dose CPT treatment, a condition known to induce high levels of fork reversal (Ray Chaudhuri et al. 2012) (Figure P16). This suggests that Ku70/80 is not required to stabilize replication forks reversing upon CPT treatment. It may however be advisable to monitor the levels of reversed forks in Ku70/80 deficient cells upon different genotoxic treatments and when co-depleting the Ku complex together with RNF168 before fully rejecting a role of Ku70/80 in the stabilization of reversed forks. We also investigated whether inhibition of DNA-PKc - the apical kinase of the NHEJ pathway (Blackford & Jackson 2017) - would have similar effects on replication fork progression as the knockdown of Ku70/80 (Figure P17). Perplexingly, inhibiting DNA-PKc led to a significant reduction in the rate of fork progression in control cells while dramatically increasing replication fork speed in an RNF168 deficient background. Based on currently available results it is difficult to suggest a straightforward mechanistic explanation for these paradoxical findings and further experiments would be needed before any conclusions can be drawn.

Altogether, the various observations made during this project highlight the possibility that many, if not all, double-strand break repair factors have additional and thus far unappreciated functions during unperturbed DNA replication and/or in the response to replication stress. The inhibition or depletion of one or multiple DSB repair factors has been found to cause unpredictable effects on DNA replication, which strongly suggests that these proteins are involved in a complex network regulating replication fork progression, remodelling and restart both in presence and absence of replication stress. To some extent, it may not be completely surprising that evolution would foster the repurposing of similar tools to process almost identical structures in the nucleus, rather than reinventing separate pathways. We may thus look forward to the impending discovery of hitherto unrecognized functions of many more DSB repair proteins in DNA replication and stand in awe at natures infinite inventiveness.

7. Materials and Methods

Cell lines

U2OS shRNF168: Human osteosarcoma U2OS cell line expressing a doxicycline inducible shRNA against RNF168 (kindly provided by J. Lukas) was cultured in DMEM supplemented with 10% FBS, 100 U/ml penicillin, 100 μg/ml streptomycin 1 μg/ml puromycin and 5 μg/ml blasticidin in an atmosphere containing 6% CO2 at 37°C. shRNA expression was induced by adding doxicycline to the growth media at a final concentration of 1 μg/ml for 96h.

U2OS shRNF8: Human osteosarcoma U2OS cell line expressing a doxicycline inducible shRNA against RNF8 (kindly provided by N. Mailand) was cultured in DMEM supplemented with 10% FBS, 100 U/ml penicillin, 100 μg/ml streptomycin 1 μg/ml puromycin and 5 μg/ml blasticidin in an atmosphere containing 6% CO2 at 37°C. shRNA expression was induced by adding doxicycline to the growth media at a final concentration of 1 μg/ml for 96h.

U2OS 53BP1 KO and matching WT U2OS: CRISPR/Cas generated 53BP1 KO and the WT U2OS cell line from which they originate (both kindly provided by S. Jackson) were cultured in DMEM supplemented with 10% FBS, 100 U/ml penicillin, and 100 μg/ml streptomycin in an atmosphere containing 6% CO2 at 37°C.

RIDDLE and RIDDLE HA-RNF168: RIDDLE patient fibroblasts and the same cell line reconstituted with HA-RNF168 (both kindly provided by G. Stewart) were cultured in DMEM supplemented with 10% FBS, 100 U/ml penicillin, and 100 μg/ml streptomycin in an atmosphere containing 6% CO2 at 37°C.

U2OS: Human osteosarcoma U2OS cells were cultured in DMEM supplemented with 10% FBS, 100 U/ml penicillin, and 100 μg/ml streptomycin in an atmosphere containing 6% CO2 at 37°C.

AT22IJE-T cell lines: Ataxia-telangiectasia fibroblast cell line AT22IJE-T carrying an empty expression vector (pEBS7) and the same cell line expressing recombinant ATM (YZ5) (kindly provided by Y Shiloh) were cultured in DMEM supplemented with 20% FBS, 100 U/ml penicillin, and 100 μg/ml streptomycin in an atmosphere containing 6% CO2 at 37°C.

U2OS Flp-In T-REx cell lines: The four cell lines for the doxicycline inducible expression of wildtype or mutant RNF168 presented in this manuscript (EV, WT res, R57D res and UBD res) were generated by transfecting 160.000 U2OS Flp-In T-REx cells (kindly provided by D. Durocher) with 2μg of a 9:1 mixture of pOG44 Flp-Recombinase Expression Vector (Thermo Fisher) and the respective expression plasmid. The transfected cells were then cultured in DMEM supplemented with 10% FBS, 100 U/ml penicillin, 100 μg/ml streptomycin, 10 μg/ml hygromycin B and 5 μg/ml blasticidin in an atmosphere containing 6% CO2 at 37°C for 2 weeks to select for positive transformants. After the selection phase the cell lines were grown in DMEM supplemented with 10% FBS, 100 U/ml penicillin, 100 μg/ml streptomycin, 5 μg/ml hygromycin B and 5 μg/ml blasticidin in an atmosphere containing 6% CO2 at 37°C. Expression of the respective constructs was induced by adding doxicycline to the growth media at a final concentration of 1 μg/ml for 12h.

HEK 293T: Human embryonic kidney cells were cultured in DMEM supplemented with 10% FBS, 100 U/ml penicillin, and 100 μg/ml streptomycin in an atmosphere containing 6% CO2 at 37°C.

U2OS shUb: U2OS shUB (kindly provided by Z. Chen) were cultured in DMEM supplemented with 10% tetracycline-free FBS (Biowest S181T) as well as 100 U/ml penicillin, 100 µg/ml streptomycin and puromycin (1 µg/ml). Induction of the shRNAs against ubiquitin was performed by addition of tetracycline (1 µg/ml) to the culture medium.

U2OS Ub WT and U2OS K63R: The ubiquitin replacement systems (kindly provided by Z. Chen) were cultured in media of the same composition as for U2OS shUb but supplemented with G418 (400 µg/ml). Ub replacement was induced by adding tetracycline (1 µg/ml) to the media.

RPE S139A and FRT: RPE cells with a S139A point mutation in H2AX and the matched wildtype cells (FRT) (both kindly provided by S. Jackson) were cultured in DMEM supplemented with 10% FBS, 100 U/ml penicillin, and 100 µg/ml streptomycin in an atmosphere containing 6% CO2 at 37°C.

U2OS ZRANB3 KO: Human osteosarcoma U2OS ZRANB3 KO cells (kindly provided by D. Cortez) were cultured in DMEM supplemented with 10% FBS, 100 U/ml penicillin, and 100 µg/ml streptomycin in an atmosphere containing 6% CO2 at 37°C.

Immunofluorescence

U2OS cells were grown on sterile 12-mm diameter glass coverslip, incubated for 30 min with 10uM EdU, washed with PBS, fixed in 4% buffered paraformaldehyde, washed three time with PBS, permeabilized for 10 min at room temperature in 0.3% Triton X-100 (Sigma-Aldrich) in PBS and washed twice in PBS. EdU detection was performed with a Click-iT Plus EdU Alexa Fluor 647 Imaging Kit according to the manufacturer's recommendations (Thermo Fisher Scientific) before incubation with primary antibodies. All primary and secondary antibodies were diluted in PBS supplemented with 3% BSA. Incubation with primary antibodies was performed at room temperature for 2 hours. Coverslips were washed three times with PBS containing 0.1% Tween-20 (Sigma-Aldrich). Secondary-antibody incubations were performed at room temperature for 1 hour. After one wash with PBS containing 0.1% Tween-20 and one with PBS, coverslips were incubated for 10 min with PBS containing DAPI (0.5 mg/mL) at room temperature to stain DNA. Following three washing steps in PBS, coverslips were briefly washed with distilled water, dried on 3mm paper and mounted in 5µL Prolong Gold antifade reagent (Invitrogen).

Confocal microscopy

Imaging was performed with support of the Centre for Microscopy and Image Analysis, University of Zurich. Representative IF images were acquired on a Leica SP8 automated upright confocal laser scanning microscope using an HCX PL APO CS2 63x immersion oil objective (NA 1.4). Z-series were de-convolved using Huygens Deconvolution software and a representative single Z slice is shown.

Proximity Ligation Assay (PLA)

U2OS cells were grown on sterile 12-mm diameter glass coverslip, incubated for 30 min with 10 µM EdU, washed with cold PBS and pre-extracted in CSK buffer (HEPES-KOH 20mM pH 7.4, 100mM NaCl, 3mM MgCl2, 1mM EGTA and 0.5% Triton X-100) for 5 min on ice. After one washed with cold PBS, cells were fixed in 4% buffered paraformaldehyde, washed three time with PBS, permeabilized for 10 min at room temperature in 0.3% Triton X-100 (Sigma-Aldrich) in PBS and washed twice in PBS. EdU detection was performed according to the manufacturer's recommendations (Thermo Fisher Scientific)

before incubation with primary antibodies. Coverslip were then incubated with anti-FLAG and anti-PCNA antibody and in situ proximity ligation was performed using a Duolink Detection Kit (Sigma-Aldrich).

Quantitative image-based microscopy (QIBC)

Automated multichannel wide-field microscopy for QIBC was performed as described previously (Altmeyer et al., 2013; Toledo et al., 2013) on an Olympus ScanR Screening System equipped with wide-field optics, a 20x, 0.75-NA (UPLSAPO 20x), an inverted motorized Olympus IX83 microscope, a motorized stage, IR-laser hardware autofocus, a fast emission filter wheel with single-band emission filters, and a 12-bit digital monochrome Hamamatsu ORCA-FLASH 4.0 V2 sCMOS camera (dynamic range 4,000:1, 2,048 3 2,948 pixel of size 6.5 3 6.5 mm, 12-bit dynamics). Images were acquired in an automated fashion with the ScanR acquisition software (Olympus 2.6.1). Images containing at least 2,000 cells per condition were acquired under non-saturating conditions and identical settings were applied to all samples within one experiment. Images were processed and analysed with the inbuilt Olympus ScanR Image Analysis Software Version 2.5.1, a dynamic background correction was applied, nuclei segmentation was performed using an integrated intensity-based object detection module using the DAPI signal, and foci segmentation was performed using an integrated spot-detection module. Fluorescence intensities were quantified and are depicted as arbitrary units. These values were then exported and analysed with Spotfire data visualization software (TIBCO, version 5.0.0). Within one experiment, similar cell numbers were compared for the different conditions. To visualize discrete data in scatterplots (e.g., foci numbers), mild jittering (random displacement of data points along the discrete data axes) was applied to demerge overlapping data points. Representative scatterplots and quantifications of independent experiments, typically containing several thousand cells each, are shown.

Transfections

For siRNA experiments, cells were transfected with the indicated siRNAs for an indicated amount of time using jetPRIME® (Polyplus transfection) according to manufacturer's instruction. siLuc (72h 40 nM; 5'-CGUACGCGGAAUACUUCGAUUdTdT-3'); siRNF168 (72h 40 nM: 5'-CGUGGAACUGUGGACGAUAAUUCAAdTdT-3'); siRAD51 (24h 40 nM: 5'-GACUGCCAGGAUAAAGCUUdTdT-3'); siRECQ1 (72h 40 nM: SMART pool against human RECQ1, NM_032941, Dharmacon); siUb (12/16/20/24/36/48h 40 nM: 5'-ACACCAUUGAGAAUGUCdTdT-3' and 5'-AGGCCAAGAUCCAGGAUdTdT-3'); SCR (20/24/36h 40 nM: 5'-CCGGAACUAGACAGUAUdTdT-3'); siBRCA2 (48h 40 nM: 5'-UUGACUGAGGCUUGCUCAGUUdTdT-3'); siKu70 (72h 10 nM: XRCC6 silencer select Cat# 439249); siKu80 (72h 10 nM: XRCC5 silencer select Cat# 439240); siBRCA1(72h 40 nM: 5'-GGAACCUGUCUCCACAAAGdTdT-3') siSmarcal1 (48h 40 nM:5'-AAGCAAGGCCCAUCCCAAAdTdT-3').

Flow cytometric analysis

All cell lines subjected to this analysis were labelled with 10 µM EdU for 30 min, harvested by standard trypsinization and subsequently fixed for 10 min in 4% formaldehyde/PBS. Cells were then washed twice and blocked over night at 4°C with 1% BSA/PBS, pH 7.4. They were permeabilized the next day with 0.5% saponin/1% BSA/PBS, and stained with the respective primary antibody diluted in 0.5% saponin/1% BSA/PBS for 2 h. This was followed by incubation with a suitable secondary antibody

diluted at 1:125 in 0.5% saponin/1% BSA/PBS for 30 min. The incorporated EdU was labelled according to the manufacturer's instructions (Thermo Fisher). Total DNA was stained with 1 µg/ml DAPI dissolved in 1% BSA/PBS, pH 7.4. Samples were measured on an Attune NxT Flow Cytometer (Thermo Fisher) and analysed using FlOWJO software V.10.0.8 (FlowJo, LLC). Statistical analysis was carried out using GraphPad Prism 7.

Replication fork progression by DNA fiber analysis

This protocol is based on Jackson and Pombo 1998. All cell lines subjected to this analysis were grown asynchronously and labelled with 30 µM of the thymidine analogue chlorodeoxyuridine (CldU; Sigma-Aldrich) for 30 min, they were then washed three times with warm PBS and subsequently exposed to 250 µM of 5- iodo-2'-deoxyuridine (IdU) for 30 min. All cells were collected by standard trypsinization and resuspended in cold PBS at 3.5 × 105 cells/ml. The labelled cells were mixed 1:8 with unlabeled cells. 2.5 µl of this cell suspension were then mixed with 7.5 µl of lysis buffer (200 mM Tris-HCl, pH 7.5, 50 mM EDTA, and 0.5% [w/vol] SDS) on a glass slide. After an incubation of 9 min at RT, the slides were tilted at a 45° angle to stretch the DNA fibers onto the slide. The resulting DNA spreads were air dried, fixed in 3:1 methanol/acetic acid, and stored at 4°C overnight The DNA fibers were denatured by incubating them in 2.5 M HCl for 1h at RT, washed five times with PBS and blocked with 2% BSA in PBST (PBS and Tween 20) for 40 min at RT. The newly replicated CldU and IdU tracks were stained for 2.5h at RT using two different anti-BrdU antibodies recognizing CldU (Abcam, ab6326) and IdU (Becton Dickinson, 347580) respectively. After washing five times with PBST (PBS and Tween 20) the slides were stained with Anti-mouse Alexa 488 (Invitrogen, A-11001) and anti-rat Cy3 (Immuno Research, 712-166-1530) secondary antibodies for 1h at RT in the dark. The slides were mounted in 30uL Prolong Gold antifade reagent (Invitrogen). Microscopy was done using an Olympus IX81 microscope with a CCD camera (Hamamatsu). IdU rack lengths of at least 120 fibers per sample were measured using the line tool in ImageJ64 software. Statistical analysis was carried out using GraphPad Prism 7.

Neutral comet assay

Asynchronously growing U2OS shRNF168 cells were either left uninduced or depleted of RNF168 by adding doxycycline to the growth media at a final concentration of 1 µg/ml for 96h. One uninduced sample was treated with 1 µM camptothecin (CPT) for 1h and used as a positive control for DNA double-stranded break formation. Cells were collected by standard trypsinization and resuspended in cold PBS at a concentration of 106 cells/ml. 20 ul of cell suspension was then mixed with 600 ul of 0.8% w/v Low Melting Point (LMP) agarose (Lonza) in PBS, previously equilibrated to 37°C. 60 ul of the cell-LMP mixture was then spread onto a comet slide (CometAssay® Kit, Trevigen). Slides were incubated at 4°C for 20 min to allow solidification of the LMP. They were subsequently put in lysis buffer (CometAssay® Lysis Solution, Trevigen) pre-equilibrated to 4°C and refrigerated overnight. The following day, slides were incubated in cold electrophoresis buffer (300 mM sodium acetate, 100 mM Tris, pH 8.3) for 1 hour at 4°C and then subjected to electrophoresis in a comet chamber for 30min at 21Volt/300mA. After electrophoresis, the slides were rinsed twice in water, fixed in 70% ethanol at 4°C for 20 min and then dried at37°C. The comets were than stained using SYBR® Gold (Thermo Fisher Scientific) diluted at 1:30'000 in Tris-EDTA (10 mM Tris-HCl pH 7.5, 1 mM EDTA) for 30 min in dark. Microscopy was performed on a Leica DM6 B upright digital research microscope equipped with a DFC360 FX Leica camera at 10x magnification. The images were analysed using the Open Comet plugin

(http://www.cometbio.org/) for Fiji. At least 105 cells were analysed per sample. Statistical analysis was carried out using GraphPad Prism 7.

Protein extraction and Western blotting:

Extracts for ubiquitin detection were prepared using RIPA buffer (150 mM NaCL, 1% Triton X-100, 1% deoxycholic acid, 0.1% SDS and 50 mM Tris-HCl, pH 7.4) supplemented with a diverse set of inhibitors (50 mM NaF, 20 mM NaPyrophosphate, 1 µM Na3VO4, 1x proteases inhibitor cocktail (Roche) and 20 µM N-Ethylmaleimide [NEM]). Extracts for all other immunoblot experiments were prepared in Laemmli sample buffer (4% SDS, 20% glycerol, and 120 mM Tris-HCl, pH 6.8). 40 µg total protein from cell isolates were loaded onto 4-20% Mini-PROTEAN® TGXTM Precast Protein Gels (BIO RAD). Proteins were separated by electrophoresis at 16 mA followed by transferring the proteins to Immobilon-P membranes (Thermo Fisher Scientific) for 1h at 350mA (4°C) in transfer buffer (25 mM Tris and 192 mM glycine) containing 10% methanol. Before addition of primary antibodies, membranes were blocked for 1h in TBS containing 0.1% Tween 20 and 5% milk.

Enrichment for mitochondrial DNA

Mitochondrial DNA was enriched using a mitochondrial DNA Isolation Kit (Abnova Cat# KA0895) according to the manufacturers instructions. Subsequently the DNA was purified and concentrated, using Amicon size-exclusion columns (Amicon ultra 100K membrane, Millipore) and finally resuspended in TE (Tris-EDTA) buffer.

Neutral and denaturing EM analysis of DNA RIs in human cells

The procedure was performed as recently described (Zellweger & Lopes 2018) and in the same manner for all cellular systems presented in this manuscript. A total of 2.5 – 5.0 x106 asynchronously growing subconfluent cells were harvested by standard trypsinization and resuspended in 10ml cold PBS. In vivo psoralen cross- linking of the DNA was performed by exposing twice the living cells to 4,5',8-trimethylpsoralen at a final concentration of 10 µg/ml followed by short (3 min) irradiation pulses with UV 365-nm monochromatic light (UV Stratalinker 1800; Agilent Technologies). The cells were then washed repeatedly with cold PBS and lysed using a cell lysis buffer (1.28 M sucrose, 40 mM Tris-Cl, pH 7.5, 20 mM MgCl2, and 4% Triton X-100). The thus obtained nuclei were then digested using a digestion buffer (800 mM guanidine–HCl, 30 mM Tris–HCl, pH 8.0, 30 mM EDTA, pH 8.0, 5% Tween 20, and 0.5% Triton X-100) supplemented with 1 mg/ml proteinase K at 50°C for 2 h. A 24:1 Chloroform:Isoamyl alcohol mixture was used to extract genomic DNA by phase separation (centrifugation at 8.000 rpm for 20 min at 4°C). The DNA was then precipitated by addition of equal amount of isopropanol to the aqueous phase, followed by another centrifugation step (8.000 rpm for 10 min at 4°C). The resulting DNA pellet was washed once with 1 ml of 70% ethanol, air dried at RT, and finally resuspended by incubating it overnight in 200 µl TE (Tris-EDTA) buffer at RT. 12 µg of the extracted genomic DNA was digested for 5h at 37°C with 100 U restriction enzyme PvuII high-fidelity. QIAGEN-tip 20 Plasmid Mini Kit columns were used for RI enrichment. The surface tension of the columns was reduced by incubation with QBT buffer (750 mM NaCl, 50 mM MOPS, pH 7.0, 15% isopropanol [v/v], 0.15% Triton X-100 [v/v]), they were then washed three times with washing buffer 1 (1M NaCl, 10mM Tris-HCl, pH 8.0) and finally equilibrated using equilibration buffer (300mM NaCl, 10mM Tris-HCl, pH 8.0). Next, the digested genomic DNA was applied to the columns followed by washing twice with washing buffer 2

(900mM NaCl, 10mM Tris-HCl, pH7.0). The DNA was then eluted with 0.6 ml elution buffer (1M NaCl 10mM Tris-HCl 1.8% caffeine). Subsequently the DNA was purified and concentrated, using Amicon size-exclusion columns (Amicon ultra 100K membrane, Millipore) and finally resuspended in TE (Tris-EDTA) buffer. For native DNA spreading the benzyldimethylalkylammonium chloride (BAC) method was used to spread the DNA on a water surface and then load it on carbon-coated 400-mesh magnetic nickel grids. For denaturing spreading the spreading mix consisted of 1.0µl formamide, 0.2µl glyoxal and 1µl DNA sample (10-50ng). This mixture was incubated for 10 min at 42°C in a water bath and chilled immediately after on ice. After this denaturation step the mixture was spread by the BAC method onto carbon- coated 400-mesh magnetic nickel grids. After the spreading procedure, the DNA was platinum coated by platinum-carbon rotary shadowing (High Vacuum Evaporator MED 020; Bal-Tec) to make it electron dense. The grids were scanned using a transmission electron microscope (Tecnai G2 Spirit; FEI; LaB6 filament; high tension ≤120 kV) and pictures were acquired with a side mount charge-coupled device camera (2,600 × 4,000 pixels; Orius 1000; Gatan, Inc.). The images were processed with DigitalMicrograph Version 1.83.842 (Gatan, Inc.) and analysed using ImageJ64. Graphs were prepared using GraphPad Prism 7.

Chromosomal breakage and abnormalities by metaphase spreading

Asynchronously and sub-confluent cells were incubated in fresh medium containing 200 ng/ml nocodazole for 16h. They were then harvested by standard trypsinization and swollen with 75mM KCl for 20 min at 37°C. The swollen mitotic cells were fixed using a fixing solution (3:1 methanol:acetic acid). The fixing step was repeated twice and the cells subsequently resuspend in 200 - 400 µL of fixing solution. The cells were then dropped onto pre-hydrated glass microscopy slides and air-dried overnight. The slides were mounted the following day using VECTASHIELD Antifade Mounting Medium with DAPI (VECTOR Laboratories). For the experiments with aphidicolin asynchronously growing cells were synchronized in late G2 phase of cell cycle by incubation with 9 µM RO-3306 for 16h along with 0.4 µM Aphidicolin. Cells were subsequently washed in PBS and released into fresh media (pre-warmed to 37◦C) containing 0.1µg/ml Colcemid for up to 60min. Cells were then harvested and treated using the same protocol as for Nocodazole treatment. Microscopy was performed on a Leica DM6 B upright digital research microscope equipped with a DFC360 FX Leica camera. Images were analyzed using ImageJ64 and visible chromatid breaks/ gaps were counted. Statistical analysis was performed in GraphPad Prism7 forMacOSX using paired T test.

Neutral-neutral 2D-gel analysis

Asynchronously growing U2OS shRNF168 cells either left untreated or depleted of RNF168 by adding doxycycline to the growth media (1 µg/ml final concentration, 96h) were transfected with an SV40 based plasmid containing 90 TTC repeats using jetPRIME® (Polyplus transfection). The cells were harvested 48h after transfection and plasmid DNA was extracted using a modified QIAprep Spin Miniprep protocol. The cells were first resuspended in buffer P1 (QIAprep Spin Miniprep kit), lysed with 0.66% SDS and finally incubated with 0.5 mg/ml proteinase K for 1.5 h at 37°C. The DNA was denatured by 25mM NaOH for 1 min followed by neutralization with buffer P3 (QIAprep Spin Miniprep kit), and spun for 15 min in a benchtop centrifuge at 18.200 rpm. The resulting supernatant was processed on miniprep columns (QIAprep Spin Miniprep kit) according to manufacturer's instructions. The thus extracted plasmid intermediates were digested by EcoRI- DpnI-XmnI followed by EtOH precipitation

and resuspension in TE buffer. The intermediates were then loaded onto 2D gels. The first dimension was run on a 0.4% agarose gel (50V, 14.5h) and the second dimension was run on a 1% agarose gel with EtBr (140V, 9h). All gels were blotted onto Bio-Rad Zeta-probe membranes and probed with radioactively labelled SV40 DNA.

Drugs and reagents

Camptothecin was made fresh for every experiment by dissolving in dimethyl sulfoxide (DMSO) to yield a 20mM stock (7mg/ml). Olaparib (AZD2281, Ku-0059436; S1060, Selleckchem) was prepared in DMSO to yield a concentration of 20 mM, aliquoted, and stored at −20 °C. Mirin (M9948, Sigma-Aldrich) was dissolved in DMSO to produce a 50mM stock, aliquoted and stored at −80 °C. The ATM inhibitor KU-55933 (Sigma-Aldrich) was dissolved in DMSO to yield a stock concentration of 10 mM, aliquoted and stored at −20 °C. A 10 mM stock solution of ETP (Sigma-Aldrich) was prepared in DMSO and aliquots were stored at -20°C. A stock for APH (Sigma-Aldrich) was prepared in DMSO a concentration of 3mM and aliquots were also stored at -20°C. HU (Sigma-Aldrich) and MMC (Sigma-Aldrich) solutions were dissolved in double-distilled H2O (ddH2O). The stock concentration of HU was 500 mM and that of MMC 3 mM. HU stock was freshly made for each experiment, while MMC aliquots were frozen away at -20°C. TMP (4,5′,8-trimethylpsoralen) powder (Sigma-Aldrich) was dissolved in ethanol to yield a stock concentration of 200 μg/ml. This stock was stored protected from light at 4°C. In the case of TMP treatments, irradiation was administered by a UV Stratalinker 1800 (Agilent Technologies) generating UV 365-nm monochromatic light. All other UV pulse treatments were delivered with the help of a UV 254-nm lamp. MG-132 (Sigma-Aldrich) was dissolved in DMSO at a stock concentration of 20 mM and stored at -20°C. The DNA-PKc inhibitor Nu7441 (KU-57788, Selleckchem) was dissolved in DMSO at a stock concentration of 5 mM, aliquoted and stored at -20°C.

Antibodies

The following primary antibodies were used for western blotting: GAPDH (MAB374, Millipore, kindly provided by A. Sartori), B tubulin (sc-9104; Santa Cruz Biotechnology) CHK1 pS345 rabbit (2348; Cell Signaling Technology), CHK1 mouse (sc-8408; Santa Cruz Biotechnology), KAP1 pS824 rabbit (A300-767A; Bethyl Laboratories), KAP1 rabbit (A300-274A; Bethyl Laboratories), phospho-RPA32 (S4/S8) rabbit (A300-245A; Bethyl Laboratories), RPA32 rabbit (A300-244A; Bethyl Laboratories), RAD51 (H-92) rabbit (sc-8349; Santa Cruz Biotechnology), 53BP1 rabbit (ab36823 Abcam) RNF168 rabbit (generated by R. Freire), RNF8 rabbit (generated by R. Freire). RECQ1 rabbit (ABC1428, Sigma-Aldrich, kindly provided by A. Vindigni), total ubiquitin mouse (P4D1, sc-8017; Santa Cruz Biotechnology). Secondary antibodies used for western blotting were anti-rabbit and anti-mouse ECL (GE Healthcare). The following primary and secondary antibodies were used for FACS stainings: mouse anti–γH2AX (05-636; EMD Millipore), rabbit polyclonal anti-FLAG (F7425, Sigma-Aldrich), FK2 mouse monoclonal antibody (BML-PW8810, Enzo life sciences), goat anti-mouse Alexa 647 antibody (A-21235, Thermo Fisher), donkey anti-rabbit Alexa 647 (A-31573, Thermo Fisher)The following primary antibodies were used for IF and PLA: FLAG rabbit (F7425, Sigma-Aldrich), FLAG mouse (M2 clone, F1804, Sigma-Aldrich), PCNA mouse (P10, sc-56, Santa Cruz Biotechnology), H2AK15Uub mouse (generated and kindly provided by the lab of Z. Zhang Mayo Clinic College of Medicine, Rochester, Minnesota, USA). Antibodies recognizing human RNF8 and RNF168 were raised in rabbits. To obtain the purified immunogens, the cDNA corresponding to full length human RNF8 and to the C-terminal part of human RNF168 (amino

acids 300-571) were cloned into pET28a (Novagen) vector for expression in Escherichia coli. Subsequently, the recombinant immunogens were purified using Ni-NTA (Qiagen) following the manufacturer's instructions and then used to immunize rabbits. After eight immunizations, serum was obtained and used for western blots.

Clonogenic assay:

A total of 4'000 cells were seeded in triplicates on cell culture dishes of 10 cm diameter. The dishes were left to grow for 9 days at 37°C and 6% CO2. The respective cell culture medium was replaced every 3 days. After this 9 day incubation, the medium was removed, cells were washed once with PBS and finally fixed/stained with 0.5% Cristal violet in 20% ethanol for 30 min at RT. The colonies that got visualized this way were counted under a binocular and the number of colonies per cm2 was calculated for each dish. The data was plotted and statistically analyzed in Prism 6 (GraphPad) using the Mann-Whitney-U-test.

Growth Curve:

Twelve 10 cm dishes were seeded with 3 x 10^5 cells each. The number of cells per dish was then measured in triplicates every 24 hours using an automated cell counter. The total of 12 dishes allowed for measurements on 4 consecutive days (Three dishes a day). The fold change in cell number was calculated and the data was plotted using Prism 6 (GraphPad).

Celltiter blue (CTB) viability and proliferation assay:

1'000 cells were seeded into the wells of a 96 well plate. The outer most wells on each side of the plate were filled with PBS instead of the cell suspension, as they are prone to evaporation and thus not suitable for CTB measurements. The plate was then incubated at 37°C and 6% CO_2 over night to give the cells time to attach. Cells were then subjected to drug treatments for 1 hour. 8 wells each were treated with the same dosage of a drug, 8 wells were left as an unperturbed control and another 8 were needed to set the blank in the following fluorescence measurement. This allowed to assesse the effect of 4 different drug treatments on one 96 well plate. After the 1 hour of treatment the cells were washed with warm PBS and incubated with fresh cell culture medium for 72 hours at 37°C and 6% CO_2. Following this incubation time 20 µl of the celltiter blue reagent resazurin (Promega) were added to each well, except the ones destined for the blank measurement. The plates were then Incubate for 3 hours at 37°C to give the cells time to metabolize the resazurin. After that the fluorescence was measured at $560_{Ex}/590_{EM}$ using a Fluoroskan Ascent plate reader (Labsystems). The blank measurement was subtracted from all other measurements and the data was plotted using Microsoft excel.

Quantification and statistical analysis

For DNA fiber experiments at least 120 IdU tracts were scored per sample for fork progression analysis and at least 50 sister forks for sister fork symmetry analysis. Every experiment was repeated at least twice. The results were analysed using GraphPad Prism7 for MacOSX, using Mann – Whitney test. Whiskers: 10-90th percentile (**** $p < 0.0001$; *** $p < 0.001$; ns, non-significant). Flow cytometry data was analysed using FlOWJO software V.10.0.8 (FlowJo, LLC). The intensity values of 500 EdU positive cells per sample were extracted from the raw data and subjected to statistical analysis using GraphPad Prism 7 (**** P Value <0.0001, Whiskers: 10th–90th percentile) For the neutral comet assay, at least

105 cells were analysed per sample for Olive- and Tail-moment using the Open Comet plugin (http://www.cometbio.org/) for Fiji. The experiment was repeated 3 times with comparable results. The results were analysed using GraphPad Prism7 for MacOSX, using Mann – Whitney test. Displayed as scatter plots with mean and SD (**** $p < 0.0001$; ns, non-significant). For quantitative image-based microscopy images were processed and analysed with the inbuilt Olympus ScanR Image Analysis Software Version 2.5.1. Fluorescence intensities were quantified and depicted as arbitrary units. These values were then exported and analyse with Spotfire data visualization software (TIBCO, version 5.0.0). Within one experiment, similar cell numbers were compared for all different conditions. To visualize discrete data in scatterplots (e.g., foci numbers), mild jittering (random displacement of data points along the discrete data axes) was applied to demerge overlapping data points. Representative scatterplots and quantifications of independent experiments, typically containing several thousand cells each, are shown. Every neutral electron microscopy experiment was repeated twice the number of molecules per sample is indicated in the respective figures and the accompanying EM table. The data was depicted as bar plots with GraphPad Prism7 for MacOSX. For denaturing EM analysis, the bubble size from 20 reversed forks was measured using ImageJ64 resulting in a total of 123 bubbles for the regressed arm, 372 for the parental strand and 600 for the two daughter strands. Frequency distributions for all strand types were computed using GraphPad Prism7 for MacOSX and plotted as histograms with a bin width of 30 nucleotides.

8. References

Adam, S., Polo, S.E. & Almouzni, G., 2013. Transcription Recovery after DNA Damage Requires Chromatin Priming by the H3 . 3 Histone Chaperone HIRA. *Cell*, 155, pp.94–106.

Al-Hakim, A. et al., 2010. The ubiquitous role of ubiquitin in the DNA damage response. *DNA repair*, 9(12), pp.1229–40.

Alabert, C. et al., 2014. Nascent chromatin capture proteomics determines chromatin dynamics during DNA replication and identifies unknown fork components. *Nature cell biology*, 16(3), pp.281–93.

Alexandrov, L.B. et al., 2013. Signatures of mutational processes in human cancer. *Nature*, 500(7463), pp.415–421.

Andrews, J.M., Newbound, G.C. & Lairmore, M.D., 1997. Transcriptional modulation of viral reporter gene constructs following induction of the cellular stress response. *Nucleic Acids Research*, 25(5), pp.1082–1084.

Arias, E.E. & Walter, J.C., 2007. Strength in numbers: preventing rereplication via multiple mechanisms in eukaryotic cells. *Genes & Development*, 21, pp.497–518.

Aunan, J.R. et al., 2017. The Biology of Aging and Cancer: A Brief Overview of Shared and Divergent Molecular Hallmarks. *Aging and Disease*, 8(5), pp.1–15.

Balakrishnan, L. & Bambara, R.A., 2013. Okazaki Fragment Metabolism. *Cold Spring Harbor Perspect Biol*, 5.

Barlow, J.H. et al., 2013. Identification of early replicating fragile sites that contribute to genome instability. *Cell*, 152(3), pp.620–632.

Bass, T.E. et al., 2016. ETAA1 acts at stalled replication forks to maintain genome integrity. *Nature Cell Biology*, 18(11), pp.1185–1195.

Berti, M. et al., 2013. Human RECQ1 promotes restart of replication forks reversed by DNA topoisomerase I inhibition. *Nature structural & molecular biology*, 20(3), pp.347–54.

Berti, M. & Vindigni, A., 2016. Replication stress: getting back on track. *Nature Structural & Molecular Biology*, 23(2), pp.103–109.

Bester, A.C. et al., 2011. Nucleotide Deficiency Promotes Genomic Instability in Early Stages of Cancer Development. *Cell*, 145(3), pp.435–446.

Bétous, R. et al., 2012. SMARCAL1 catalyzes fork regression and holliday junction migration to maintain genome stability during DNA replication. *Genes and Development*, 26(2), pp.151–162.

Blackford, A.N. & Jackson, S.P., 2017. ATM, ATR, and DNA-PK: The Trinity at the Heart of the DNA Damage Response. *Molecular Cell*, 66(6), pp.801–817.

Boulos, R.E. et al., 2015. Structural organization of human replication timing domains. *FEBS Letters*, 589(20), pp.2944–2957.

Branzei, D. & Foiani, M., 2010. Maintaining genome stability at the replication fork. *Nature reviews. Molecular cell biology*, 11(3), pp.208–219.

Bucknall, R.A. et al., 1973. Antiviral Effects of Aphidicolin , a New Antibiotic Produced by Cephalosporium aphidicola. *ANTIMICROBAL AGENTS AND CHEMOTHERAPY*, 4(3), pp.294–298.

Burgers, P.M. & Kunkel, T.A., 2017. Eukaryotic DNA Replication Fork. *Annual review of biochemistry*, (41), pp.3–6.

Burtner, C.R. & Kennedy, B.K., 2010. Progeria syndromes and ageing: What is the connection? *Nature Reviews Molecular Cell Biology*, 11(8), pp.567–578.

Byun, T.S. et al., 2005. Functional uncoupling of MCM helicase and DNA polymerase activities activates the ATR-dependent checkpoint. *Genes and Development*, 19(9), pp.1040–1052.

Ceccaldi, R., Rondinelli, B. & D'Andrea, A.D., 2016. Repair Pathway Choices and Consequences at the Double-Strand Break. *Trends in Cell Biology*, 26(1), pp.52–64.

Cech, T. & Pardue, M.L., 1977. Cross-linking of DNA with trimethylpsoralen is a probe for chromatin structure. *Cell*, 11(3), pp.631–40.

Chang, H.H.Y. et al., 2017. Non-homologous DNA end joining and alternative pathways to double-strand break repair. *Nature Reviews Molecular Cell Biology*, 18(8), pp.495–506..

Chen, Z.J. & Sun, L.J., 2009. Nonproteolytic Functions of Ubiquitin in Cell Signaling. *Molecular Cell*, 33(3), pp.275–286.

Christiano, C., Chini, S. & Chen, J., 2003. Human Claspin Is Required for Replication Checkpoint Control. *The Journal of biological chemistry*, 278(32), pp.30057–30062.

Ciccia, A. et al., 2012. Polyubiquitinated PCNA recruits the ZRANB3 translocase to maintain genomic integrity after replication stress. *Molecular cell*, 47(3), pp.396–409.

Dalgaard, J.Z., 2012. Causes and consequences of ribonucleotide incorporation into nuclear DNA. *Trends in Genetics*, 28(12), pp.592–597.

Deans, A.J. & West, S.C., 2011. DNA interstrand crosslink repair and cancer. *Nature Reviews Cancer*, 11(7), pp.467–480.

Deshaies, R.J. & Joazeiro, C. a P., 2009. RING domain E3 ubiquitin ligases. *Annual review of biochemistry*, 78, pp.399–434.

Devgan, S.S. et al., 2011. Homozygous deficiency of ubiquitin-ligase ring-finger protein RNF168 mimics the radiosensitivity syndrome of ataxia-telangiectasia. *Cell Death and Differentiation*, 18(9), pp.1500–1506.

Dewar, J.M., Budzowska, M. & Walter, J.C., 2015. The mechanism of DNA replication termination in vertebrates. *Nature*, 525(7569), pp.345–350.

Doil, C. et al., 2009. RNF168 binds and amplifies ubiquitin conjugates on damaged chromosomes to allow accumulation of repair proteins. *Cell*, 136(3), pp.435–46.

Dungrawala, H. et al., 2015. The Replication Checkpoint Prevents Two Types of Fork Collapse without Regulating Replisome Stability. *Molecular Cell*, 59(6), pp.998–1010.

Errico, A. & Costanzo, V., 2012. Mechanisms of replication fork protection: A safeguard for genome stability. *Critical Reviews in Biochemistry and Molecular Biology*, 47(3), pp.222–235.

Fachinetti, D. et al., 2010. Replication termination at eukaryotic chromosomes is mediated by Top2 and occurs at genomic loci containing pausing elements . *Molecular cell*, 39(4), pp.595–605.

Feng, L. & Chen, J., 2012. The E3 ligase RNF8 regulates KU80 removal and NHEJ repair. *Nature Structural & Molecular Biology*, 19(2), pp.201–206.

Follonier, C. et al., 2013. Friedreich's ataxia-associated GAA repeats induce replication-fork reversal and unusual molecular junctions. *Nature structural & molecular biology*, 20(4), pp.486–94.

Fragkos, M. et al., 2015. DNA replication origin activation in space and time. *Nature Reviews Molecular Cell Biology*, 16(6), pp.360–374..

Friedberg, E.C., 2008. A brief history of the DNA repair field. *Cell Research*, 18(1), pp.3–7.

Fu, X.Y. & Manley, J.L., 1987. Factors influencing alternative splice site utilization in vivo. *Molecular and cellular biology*, 7(2), pp.738–748.

Fugger, K. et al., 2015. FBH1 catalyzes regression of stalled replication forks. *Cell Reports*, 10(10), pp.1749–1757.

García-Muse, T. & Aguilera, A., 2016. Transcription-replication conflicts: How they occur and how they are resolved. *Nature Reviews Molecular Cell Biology*, 17(9), pp.553–563.

Gatti, M. et al., 2015. RNF168 Promotes Noncanonical K27 Ubiquitination to Signal DNA Damage. *Cell Reports*, 10(2), pp.226–238.

Gatti, R.A. et al., 1988. Localization of an ataxia-telangiectasia gene to chromosome 11q22-23. *Nature*, 336.

Glover, T.W., Wilson, T.E. & Arlt, M.F., 2017. Fragile sites in cancer: More than meets the eye. *Nature Reviews Cancer*, 17(8), pp.489–501.

Goldberg, M. et al., 2003. MDC1 is required for the intra-S-phase DNA damage checkpoint. *Nature*, 421(6926), pp.952–956.

Gotter, A.L., Suppa, C. & Emanuel, B.S., 2007. Mammalian TIMELESS and Tipin are Evolutionarily Conserved Replication Fork-associated Factors. *Journal of Molecular Biology*, 366(1), pp.36–52.

Graham, J.E., Marians, K.J. & Kowalczykowski, S.C., 2017. Independent and Stochastic Action of DNA Polymerases in the Replisome. *Cell*, 169(7), p.1201–1213.e17.

Grundy, G.J. et al., 2014. One ring to bring them all — The role of Ku in mammalian non-homologous end joining. *DNA Repair*, 17, pp.30–38.

Gudjonsson, T. et al., 2012. TRIP12 and UBR5 suppress spreading of chromatin ubiquitylation at damaged chromosomes. *Cell*, 150(4), pp.697–709.

Guillén-Mancina, E., Calderón-Montaño, J.M. & López-Lázaro, M., 2018. Avoiding the ingestion of cytotoxic concentrations of ethanol may reduce the risk of cancer associated with alcohol consumption. *Drug and Alcohol Dependence*, 183(October 2017), pp.201–204.

Haahr, P. et al., 2016. Activation of the ATR kinase by the RPA-binding protein ETAA1. *Nature Cell Biology*, 18(11), pp.1196–1207.

Hamperl, S. & Cimprich, K.A., 2016. Conflict Resolution in the Genome: How Transcription and Replication Make It Work. *Cell*, 167(6), pp.1455–1467.

Hanahan, D. & Weinberg, R. a, 2011. Hallmarks of cancer: the next generation. *Cell*, 144(5), pp.646–74.

zur Hausen, H., 1967. Induction of Specific Chromosomal Aberrations Induction of Specific Chromosomal Aberrations by Adenovirus Type 12 in Human Embryonic Kidney Cells. *Journal of Virology*, 1(6), pp.1174–1185.

Havens, C.G. & Walter, J.C., 2011. Mechanism of CRL4 Cdt2 , a PCNA-dependent E3 ubiquitin ligase. *Genes & Development*, 25, pp.1568–1582.

Helleday, T. et al., 2008. DNA repair pathways as targets for cancer therapy. *Nature reviews. Cancer*, 8(march), pp.193–204.

Helmrich, A., Ballarino, M. & Tora, L., 2011. Collisions between Replication and Transcription Complexes Cause Common Fragile Site Instability at the Longest Human Genes. *Molecular Cell*, 44(6), pp.966–977.

Hetz, C., Chevet, E. & Oakes, S.A., 2015. Proteostasis control by the unfolded protein response. *Nature Cell Biology*, 17(7).

Hoeijmakers, J.H.J., 2009. DNA Damage, Aging, and Cancer. *New England Journal of Medicine*, 361, pp.1475–1485.

Hoeijmakers, J.H.J., 2001. Genome maintenance mechanisms for preventing cancer. *Nature*, 411(6835), pp.366–374.

Huen, M.S.Y. et al., 2007. RNF8 Transduces the DNA-Damage Signal via Histone Ubiquitylation and Checkpoint Protein Assembly. *Cell*, 131(5), pp.901–914.

Husnjak, K. & Dikic, I., 2012. Ubiquitin-Binding Proteins : Decoders of Ubiquitin- Mediated Cellular Functions. *Annual review of biochemistry*, 81, pp.291–322.

Hustedt, N. & Durocher, D., 2017. The control of DNA repair by the cell cycle. *Nat Cell Biol*, 19(1), pp.1–9.

Hyer, M.L. et al., 2018. A small-molecule inhibitor of the ubiquitin activating enzyme for cancer treatment. *Nature medicine*, 24(2), pp.186–193.

IARC, 2012. Agents Classified by the IARC Monographs , Volumes 1 – 120. *IARC Monographs*, 7(000050), pp.1–25.

IARC Working Group on the Evaluation of Carcinogenic Risks to Humans, 2010. Chemical agents and related occupations. *IARC Monographs*, 100 F, pp.111–133.

Jeggo, P.A., Pearl, L.H. & Carr, A.M., 2015. DNA repair, genome stability and cancer: a historical perspective. *Nature Reviews Cancer*, 16(1), pp.35–42.

Jiricny, J., 2013. Postreplicative mismatch repair. *Cold Spring Harbor perspectives in biology*, 5(4), p.a012633. Available at: http://www.ncbi.nlm.nih.gov/pubmed/23545421

Jones, D.L. & Rando, T.A., 2011. Emerging models and paradigms for stem cell ageing. *Nature Cell Biology*, 13(5), pp.506–512.

Kalb, R. et al., 2014. BRCA1 Is a Histone-H2A-Specific Ubiquitin Ligase. *Cell Reports*, 8(4), pp.999–1005.

Kelly, T.J. & Brown, G.W., 2000. Regulation of chromosome replication. *Annual review of biochemistry*, 69, pp.829–80.

Kerzendorfer, C. & Driscoll, M.O., 2009. Human DNA damage response and repair deficiency syndromes : Linking genomic instability and cell cycle checkpoint proficiency. *DNA Repair*, 8, pp.1139–1152.

Kile, A.C. et al., 2015. HLTF's Ancient HIRAN Domain Binds 3' DNA Ends to Drive Replication Fork Reversal. *Molecular Cell*, 58(6), pp.1090–1100.

Kolinjivadi, A.M. et al., 2017. Smarcal1-Mediated Fork Reversal Triggers Mre11-Dependent Degradation of Nascent DNA in the Absence of Brca2 and Stable Rad51 Nucleofilaments. *Molecular Cell*, pp.1–15.

Komander, D. & Rape, M., 2012. The ubiquitin code. *Annual review of biochemistry*, 81, pp.203–29.

Kowalczykowski, S.C., 2015. An Overview of the Molecular Mechanisms of Recombinational DNA Repair. *Cold Spring Harbor Perspectives in Biology*, 7(11), p.a016410.

Kulathu, Y. & Komander, D., 2012. Atypical ubiquitylation - the unexplored world of polyubiquitin beyond Lys48 and Lys63 linkages. *Nature reviews. Molecular cell biology*, 13(8), pp.508–23.

Labib, K., Tercero, A. & Diffley, J.F.X., 2000. Uninterrupted MCM2-7 Function Required for DNA Replication Fork Progression. , 1643(2000), pp.1643–1648.

Lemaçon, D. et al., 2017. MRE11 and EXO1 nucleases degrade reversed forks and elicit MUS81-dependent fork rescue in BRCA2-deficient cells . *Nature Communications*.

López-Otín, C. et al., 2013. The hallmarks of aging. *Cell*, 153(6), pp.1194–217.

Lord, C.J. & Ashworth, A., 2012. The DNA damage response and cancer therapy. *Nature*, 481, pp.287–294.

Lukas, J., Lukas, C. & Bartek, J., 2011. More than just a focus: The chromatin response to DNA damage and its role in genome integrity maintenance. *Nature Cell Biology*, 13(10), pp.1161–1169.

Macheret, M. & Halazonetis, T.D., 2015. DNA Replication Stress as a Hallmark of Cancer. *Annual Review of Pathology: Mechanisms of Disease*, 10(1), pp.425–448.

Madaan, K., Kaushik, D. & Verma, T., 2012. Hydroxyurea: a key player in cancer chemotherapy. *Expert review of anticancer therapy*, 12(1), pp.19–29.

Maga, G. & Hübscher, U., 2003. Proliferating cell nuclear antigen (PCNA): a dancer with many partners. *Journal of Cell Science*, 116(15), pp.3051–3060.

Mailand, N. et al., 2007. RNF8 ubiquitylates histones at DNA double-strand breaks and promotes assembly of repair proteins. *Cell*, 131(5), pp.887–900.

Mantere, T. et al., 2017. Case-control analysis of truncating mutations in DNA damage response genes connects TEX15 and FANCD2 with hereditary breast cancer susceptibility. *Scientific Reports*, 7(1), p.681.

Maric, M. et al., 2014. Cdc48 and a ubiquitin ligase drive disassembly of the CMG helicase at the end of DNA replication. *Science*, 346(6208).

Masuda-Ozawa, T. et al., 2013. Single-molecule sorting reveals how ubiquitylation affects substrate recognition and activities of FBH1 helicase. *Nucleic Acids Research*, 41(6), pp.3576–3587.

Mattiroli, F. et al., 2012. RNF168 ubiquitinates K13-15 on H2A/H2AX to drive DNA damage signaling. *Cell*, 150(6), pp.1182–95.

McDougall, J.K., 1971. Adenovirus-induced Chromosome Aberrations in Human Cells. *Journal of general Virology*, 12, pp.43–51.

McGarry, T.J. & Kirschner, M.W., 1998. Geminin, an inhibitor of DNA replication, is degraded during mitosis. *Cell*, 93(6), pp.1043–1053.

Merrikh, H., 2017. Spatial and Temporal Control of Evolution through Replication–Transcription Conflicts. *Trends in Microbiology*, 25(7), pp.515–521.

Michaelis, M. et al., 2001. Treatment of drug-resistant human neuroblastoma cells with cyclodextrin inclusion complexes of aphidicolin. *Anti-Cancer Drugs*, 12(5), pp.467–473.

Mijic, S. et al., 2017. Replication fork reversal triggers fork degradation in BRCA2-defective cells. *Nature Communications*, 8(856), pp.1–24.

Moreno, S.P. et al., 2014. Polyubiquitylation drives replisome disassembly at the termination of DNA replication. , 346(6208), pp.477–482.

Morris, J.R. & Solomon, E., 2004. BRCA1: BARD1 induces the formation of conjugated ubiquitin structures, dependent on K6 of ubiquitin, in cells during DNA replication and repair. *Human Molecular Genetics*, 13(8), pp.807–817.

Moskalev, A.A. et al., 2013. The role of DNA damage and repair in aging through the prism of Koch-like criteria. *Ageing Research Reviews*, 12(2), pp.661–684.

Nahas, S.A. & Gatti, R.A., 2009. DNA double strand break repair defects , primary immunodeficiency disorders , and ‘ radiosensitivity .’ *Current Opinion in Allergy and Clinical Immunology*, 9, pp.510–516.

Nakada, S. et al., 2010. Non-canonical inhibition of DNA damage-dependent ubiquitination by OTUB1. *Nature*, 466(7309), pp.941–946.

Nakayama, K.I. & Nakayama, K., 2006. Ubiquitin ligases: cell-cycle control and cancer. *Nature reviews. Cancer*, 6(5), pp.369–381.

Neelsen, K.J. et al., 2013. Oncogenes induce genotoxic stress by mitotic processing of unusual replication intermediates. *Journal of Cell Biology*, 200(6), pp.699–708.

Neelsen, K.J. & Lopes, M., 2015. Replication fork reversal in eukaryotes: from dead end to dynamic response. *Nature Reviews Molecular Cell Biology*, 9(February).

Neil, A.J., Kim, J.C. & Mirkin, S.M., 2017. Precarious maintenance of simple DNA repeats in eukaryotes. *BioEssays*, 39(9), pp.1–10.

Nicassio, F. et al., 2007. Human USP3 Is a Chromatin Modifier Required for S Phase Progression and Genome Stability. *Current Biology*, 17(22), pp.1972–1977.

Nishitani, H. et al., 2006. Two E3 ubiquitin ligases, SCF-Skp2 and DDB1-Cul4, target human Cdt1 for proteolysis. *The EMBO journal*, 25(5), pp.1126–1136.

Nowsheen, S. et al., 2018. L3MBTL2 orchestrates ubiquitin signalling by dictating the sequential recruitment of RNF8 and RNF168 after DNA damage. *Nature Cell Biology*, 20(4), p.455.

O’Connor, M.J., 2015. Targeting the DNA Damage Response in Cancer. *Molecular Cell*, 60(4), pp.547–560.

Olivier, M., Hollstein, M. & Hainaut, P., 2010. TP53 Mutations in Human Cancers: Origins,

Consequences, and Clinical Use. *Cold Spring Harbor Perspect Biol*, pp.1–17.

Padeken, J., Zeller, P. & Gasser, S.M., 2015. Repeat DNA in genome organization and stability. *Current Opinion in Genetics & Development*, 31, pp.12–19.

Pellegrino, S. et al., 2017. Replication-Coupled Dilution of H4K20me2 Guides 53BP1 to Pre-replicative Chromatin. *Cell Reports*, 19(9), pp.1819–1831.

Peña-Diaz, J. & Rasmussen, L.J., 2016. Approaches to diagnose DNA mismatch repair gene defects in cancer. *DNA Repair*, 38, pp.147–154.

Perera, F. et al., 2005. DNA Damage from Polycyclic Aromatic Hydrocarbons Measured by Benzo [a] pyrene-DNA Adducts in Mothers and Newborns from Northern Manhattan , The World Trade Center Area , Poland , and China. *Cancer Epidemiology, Biomarkers & Prevention*, 14(March).

Pfeifer, G.P. et al., 2002. Tobacco smoke carcinogens, DNA damage and p53 mutations in smoking-associated cancers. *Oncogene*, 21(48), pp.7435–7451.

Pietrucha, B. et al., 2017. Clinical and Biological Manifestation of RNF168 Deficiency in Two Polish Siblings. *Frontiers in Immunology*, 8(December), pp.4–11.

Pommier, Y., 2013. Drugging topoisomerases: Lessons and Challenges. *ACS Chemical Biology*, 8, pp.82–95.

Pommier, Y. et al., 2016. Roles of eukaryotic topoisomerases in transcription, replication and genomic stability. *Nature Reviews Molecular Cell Biology*, 17(11), pp.703–721.

Poole, L.A. & Cortez, D., 2017. Functions of SMARCAL1, ZRANB3, and HLTF in maintaining genome stability. *Critical Reviews in Biochemistry and Molecular Biology*, 52(6), pp.696–714..

Quinet, A., Lemaçon, D. & Vindigni, A., 2017. Replication Fork Reversal: Players and Guardians. *Molecular Cell*, 68(5), pp.830–833.

Ranjha, L., Howard, S.M. & Cejka, P., 2018. Main steps in DNA double-strand break repair : an introduction to homologous recombination and related processes. *Chromosoma*.

Raschle, M. et al., 2015. Proteomics reveals dynamic assembly of repair complexes during bypass of DNA cross-links. *Science*, 348(6234), p.539-.

Ray Chaudhuri, A. et al., 2016. Replication fork stability confers chemoresistance in BRCA-deficient cells. *Nature*, 535(7612), pp.382–387.

Ray Chaudhuri, A. et al., 2012. Topoisomerase I poisoning results in PARP-mediated replication fork reversal. *Nature Structural & Molecular Biology*, 19(4), pp.417–423.

Rivera-Mulia, J.C. & Gilbert, D.M., 2016. Replicating Large Genomes: Divide and Conquer. *Molecular Cell*, 62(5), pp.756–765.

Rothblum-Oviatt, C. et al., 2016. Ataxia telangiectasia: A review. *Orphanet Journal of Rare Diseases*, 11(1), pp.1–21.

Roy, R., Chun, J. & Powell, S.N., 2012. BRCA1 and BRCA2 : different roles in a common pathway of genome protection. *Nat Rev Cancer*, 12(1), pp.68–78.

Savitsky, K. et al., 1995. A Single Ataxia Telangiectasia Gene with a Product Similar to P1-3 Kinase. , 268(June), pp.1749–1754.

Schlacher, K. et al., 2011. Double-strand break repair-independent role for BRCA2 in blocking stalled replication fork degradation by MRE11. *Cell*, 145(4), pp.529–542.

Schlacher, K., Wu, H. & Jasin, M., 2012. A Distinct Replication Fork Protection Pathway Connects Fanconi Anemia Tumor Suppressors to RAD51-BRCA1/2. *Cancer Cell*, 22(1), pp.106–116.

Schvartzman, J.B. & Stasiak, A., 2004. A topological view of the replicon. *EMBO reports*, 5(3), pp.256–261.

Schwertman, P., Bekker-Jensen, S. & Mailand, N., 2016. Regulation of DNA double-strand break repair by ubiquitin and ubiquitin-like modifiers. *Nat Rev Mol Cell Biol*, 17(6), pp.379–394.

Shao, G. et al., 2009. The Rap80-BRCC36 de-ubiquitinating enzyme complex antagonizes RNF8-Ubc13-dependent ubiquitination events at DNA double strand breaks. *Proceedings of the National Academy of Sciences of the United States of America*, 106(9), pp.3166–3171.

Singh, A. & Xu, Y., 2016. The Cell Killing Mechanisms of Hydroxyurea. *Genes*, 7(99).

Singhal, S. et al., 2003. A Phase 2 Study of Bortezomib in Relapsed, Refractory Myeloma. *New England Journal of Medicine*, pp.2609–2617.

Smeenk, G. & Mailand, N., 2016. Writers, Readers, and Erasers of Histone Ubiquitylation in DNA Double-Strand Break Repair. *Frontiers in Genetics*, 7(June), pp.1–14.

Snedeker, J., Wooten, M. & Chen, X., 2017. The Inherent Asymmetry of DNA Replication. *Annual Review of Cell and Developmental Biology*, (August), pp.1–28.

Somyajit, K. et al., 2017. Redox-sensitive alteration of replisome architecture safeguards genome integrity. *Science*, 802(November), pp.797–802.

Stewart, G.S. et al., 2003. MDC1 is a mediator of the mammalian DNA damage checkpoint. *Nature*, 421(2000), pp.961–966.

Stewart, G.S., Stankovic, T., Byrd, P.J., Wechsler, T., Miller, E.S., Huissoon, A., Drayson, M.T., West, S.C., Elledge, S.J. & Taylor, A.M.R., 2007. RIDDLE immunodeficiency syndrome is linked to defects in 53BP1-mediated DNA damage signaling. *Proceedings of the National Academy of Sciences of the United States of America*, 104(43), pp.16910–5.

Stewart, G.S., Stankovic, T., Byrd, P.J., Wechsler, T., Miller, E.S., Huissoon, A., Drayson, M.T., West, S.C., Elledge, S.J. & Taylor, a M.R., 2007. RIDDLE immunodeficiency syndrome is linked to defects in 53BP1-mediated DNA damage signaling. *Proceedings of the National Academy of Sciences of the United States of America*, 104(43), pp.16910–5.

Swift, M. et al., 1987. Breast and other cancers in families with ataxia-telangiectasia. *New England Journal of Medicine*, 316(21), pp.1289–1294.

Taglialatela, A. et al., 2017. Restoration of Replication Fork Stability in BRCA1- and BRCA2-Deficient Cells by Inactivation of SNF2-Family Fork Remodelers. *Molecular Cell*, 68(2), p.414–430.e8..

Técher, H. et al., 2017. The impact of replication stress on replication dynamics and DNA damage in vertebrate cells. *Nature Reviews Genetics*, 18(9), pp.535–550.

Teive, H.A.G. et al., 2015. Ataxia-telangiectasia - A historical review and a proposal for a new designation: ATM syndrome. *Journal of the Neurological Sciences*, 355(1–2), pp.3–6.

Teixeira-Silva, A. et al., 2017. The end-joining factor Ku acts in the end-resection of double strand break-free arrested replication forks. *Nature Communications*, 8(1), p.1982.

Thangavel, S. et al., 2015. DNA2 drives processing and restart of reversed replication forks in human cells. *JCB*, 208(5), pp.545–562.

Thorslund, T. et al., 2015. Histone H1 couples initiation and amplification of ubiquitin signalling after DNA damage. *Nature*, advance on.

Toledo, L., Neelsen, K.J. & Lukas, J., 2017. Perspective Replication Catastrophe : When a Checkpoint Fails because of Exhaustion. *Molecular Cell*, 66(6), pp.735–749.

Tomasetti, C. & Vogelstein, B., 2015. Variation in cancer risk among tissues can be explained by the number of stem cell divisions. *Science*, 347(78).

Tubbs, A. & Nussenzweig, A., 2017. Endogenous DNA Damage as a Source of Genomic Instability in Cancer: Cell. *Cell*, 168, pp.644–656.

Villa, M. et al., 2018. Rad9/53BP1 protects stalled replication forks from degradation in Mec1/ATR-defective cells. *EMBO reports*, p.e44910.

Vujanovic, M. et al., 2017. Replication Fork Slowing and Reversal upon DNA Damage Require PCNA Polyubiquitination and ZRANB3 DNA Translocase Activity. *Molecular Cell*, 67(5), p.882–889.e6.

Wohlschlegel, J.A. et al., 2000. Inhibition of eukaryotic DNA replication by geminin binding to Cdt1. *Science*, 290, pp.2309–2312.

Wu, S. et al., 2016. Substantial contribution of extrinsic risk factors to cancer development. *Nature*, 529(7584), pp.43–47.

Xu, M. et al., 2009. A ubiquitin replacement strategy in human cells reveals distinct mechanisms of IKK activation by TNFalpha and IL-1beta. *Molecular cell*, 36(2), pp.302–14.

Xu, P. et al., 2009. Quantitative proteomics reveals the function of unconventional ubiquitin chains in proteasomal degradation. *Cell*, 137(1), pp.133–45.

Xu, Y. et al., 2017. 53BP1 and BRCA1 control pathway choice for stalled replication restart. *eLife*, 6, p.e30523.

Yau, R. & Rape, M., 2016. The increasing complexity of the ubiquitin code. *Nature cell biology*, 18(6), pp.579–586.

Yazinski, S.A. & Zou, L., 2016. Functions, Regulation, and Therapeutic Implications of the ATR Checkpoint Pathway. *Annual Review of Genetics*, 50(1), pp.155–173.

Ye, Y. & Rape, M., 2009. Building ubiquitin chains: E2 enzymes at work. *Nature Reviews Molecular Cell Biology*, 10(11), pp.755–764.

Zellweger, R. et al., 2015. Rad51-mediated replication fork reversal is a global response to genotoxic treatments in human cells. *JCB*, 208(5), pp.563–579.

Zeman, M.K. & Cimprich, K.A., 2014. Causes and consequences of replication stress. *Nature Cell Biology*, 16(1), pp.2–9.

9. Personal contribution in other projects

This chapter discusses contributions I have made to other projects published during my PhD.

Rad51 -mediated replication fork reversal is a global response to genotoxic treatments in human cells

This publication investigates the effect of a large set of DNA-damaging agents on replication fork progression and remodeling. It demonstrates that replication fork uncoupling and reversal are a general response to replication stress in human cells and that the Rad51 recombinase is a necessary factor to mediate the reversal of uncoupled replication forks. Furthermore, it suggests that fork slowing, ssDNA accumulation and fork reversal upon genotoxic treatments is not necessarily coupled to detectable ATR or ATM activation.

My personal contribution to this manuscript consist of the FACS analysis presented in figure 4D demonstrating no correlation between slowing of DNA synthesis and H2AX phosphorylation. In addition, I performed not shown pre-experiments to optimize conditions for the iPOND experiment in figure 6B that show Rad51 at active replication forks.

Published March 2, 2015

Rad51-mediated replication fork reversal is a global response to genotoxic treatments in human cells

Ralph Zellweger,[1]* Damian Dalcher,[1]* Karun Mutreja,[1] Matteo Berti,[2] Jonas A. Schmid,[1] Raquel Herrador,[1] Alessandro Vindigni,[2] and Massimo Lopes[1]

[1]Institute of Molecular Cancer Research, University of Zurich, 8057 Zurich, Switzerland
[2]Department of Biochemistry and Molecular Biology, Saint Louis University School of Medicine, St. Louis, MO 63104

Replication fork reversal protects forks from breakage after poisoning of Topoisomerase 1. We here investigated fork progression and chromosomal breakage in human cells in response to a panel of sublethal genotoxic treatments, using other topoisomerase poisons, DNA synthesis inhibitors, interstrand cross-linking inducers, and base-damaging agents. We used electron microscopy to visualize fork architecture under these conditions and analyzed the association of specific molecular features with checkpoint activation. Our data identify replication fork uncoupling and reversal as global responses to genotoxic treatments. Both events are frequent even after mild treatments that do not affect fork integrity, nor activate checkpoints. Fork reversal was found to be dependent on the central homologous recombination factor RAD51, which is consistently present at replication forks independently of their breakage, and to be antagonized by poly (ADP-ribose) polymerase/RECQ1-regulated restart. Our work establishes remodeling of uncoupled forks as a pivotal RAD51-regulated response to genotoxic stress in human cells and as a promising target to potentiate cancer chemotherapy.

Introduction

One of the most widely used approaches in cancer chemotherapy is to kill cancer cells or arrest their rapid proliferation by targeting DNA replication. As genome duplication is essential for every cell division, replication interference is inherently more toxic to rapidly proliferating cancer cells than to untransformed, mostly quiescent somatic cells. Different strategies for replication interference have been explored and are often combined in chemotherapeutic regimens. A first class of drugs target DNA topoisomerases, essential factors to release torsional stress accumulating during replication (Pommier, 2013 and references therein). Topoisomerase I (Top1) inhibitors of the class of camptothecin (CPT) are commonly used to treat ovarian, lung, and colorectal cancer and act by trapping the enzyme on the DNA after strand cleavage. The same principle of "interfacial inhibition" applies to Topoisomerase II (Top2) inhibitors, such as etoposide (ETP) and doxorubicin (DOX), both potent chemotherapeutic drugs commonly used to treat various cancers (Pommier, 2013 and references therein). ETP is the most selective Top2 inhibitor available in the clinics and, at clinically relevant doses, mostly induces single-strand breaks, by asymmetrical trapping of Top2 homodimers (Kerrigan et al., 1987). Conversely, DOX intercalates in the DNA molecule and induces "concerted" trapping of Top2 complexes, mostly leading to double-strand breaks (DSBs; Zwelling et al., 1981). A second frequent strategy for replication interference in cancer chemotherapy makes use of antimetabolites to block nucleotide biosynthesis or DNA polymerization, as for the ribonucleotide reductase inhibitor hydroxyurea (HU) or the DNA polymerase inhibitor aphidicolin (APH). HU is commonly used to treat hematological malignancies and has been extensively used in basic research to investigate the consequences of replication fork stalling (Madaan et al., 2012). Similarly, APH has been used to study chromosome fragility during replication (Arlt et al., 2012) but has also been considered to potentiate specific

*R. Zellweger and D. Dalcher contributed equally to this paper.

Correspondence to Massimo Lopes: Massimo Lopes lopes@imcr.uzh.ch

Abbreviation used in this paper: ANOVA, analysis of variance; APH, aphidicolin; CDDP, cis-diamminedichloroplatinum; CldU, chlorodeoxyuridine; CPT, camptothecin; DDR, DNA damage response; DNA-PK, DNA-dependent protein kinase; DOX, doxorubicin; DSB, double-strand break; EdU, 5′-ethynyl-2′-deoxyuridine; ETP, etoposide; FA, Fanconi anemia; HR, homologous recombination; HU, hydroxyurea; ICL, interstrand cross-link; IdU, 5-iodo-2′-deoxyuridine; MMC, mitomycin C; MMS, methyl methanesulfonate; PARP, poly (ADP-ribose) polymerase; PFGE, pulsed field gel electrophoresis; RI, replication intermediate; ssDNA, single-stranded DNA; Top1, Topoisomerase I; Top2, Topoisomerase II.

Supplemental Material can be found at:
http://jcb.rupress.org/content/suppl/2015/02/26/jcb.201406099.DC1.html

The Rockefeller University Press $30.00
J. Cell Biol. Vol. 208 No. 5 563–579
www.jcb.org/cgi/doi/10.1083/jcb.201406099

Published March 2, 2015

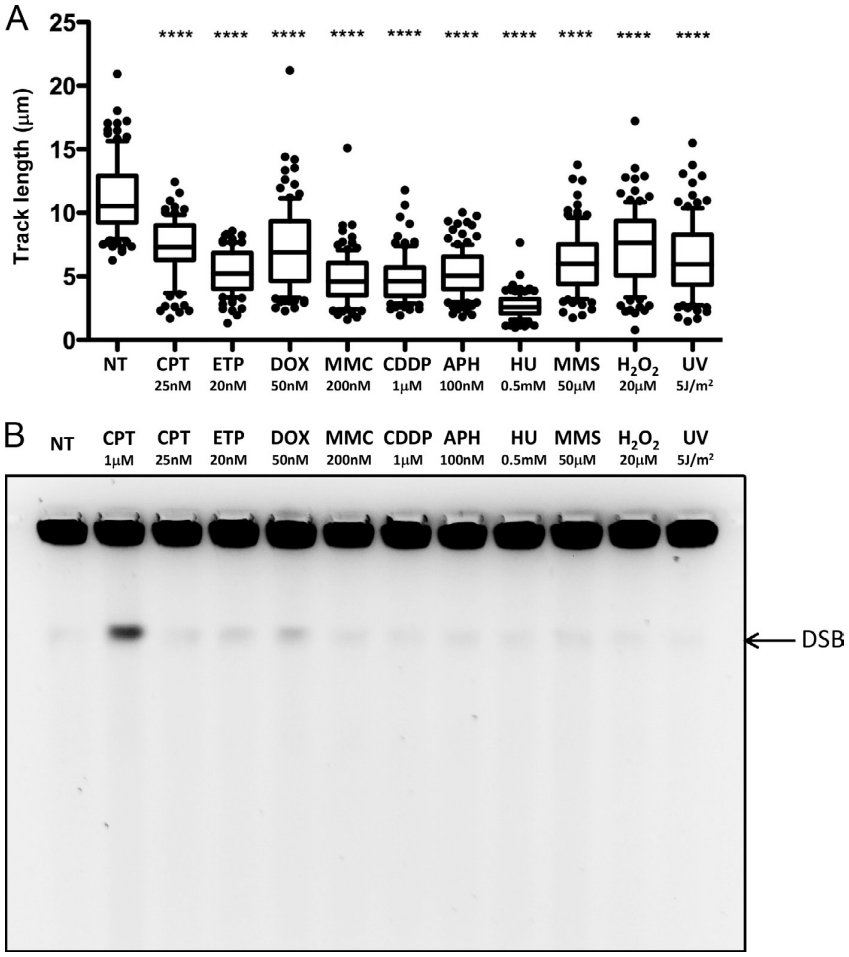

Figure 1. **Mild genotoxic stress induces marked fork slowing in the absence of chromosomal breakage.** (A) DNA fiber spreading. Statistical analysis of IdU replicated track length in U2OS cells, comparing not treated (NT) conditions with the indicated treatments. The labeling protocol and representative fibers are included in Fig. S1. At least 100 tracks were scored per sample. Horizontal lines represent the median value, and boxes and whiskers show 10–90th percentiles. Statistical analysis *t* test according to Mann–Whitney, results are ns, not significant; ****, $P \leq 0.0001$. All experiments have been repeated at least twice, with very similar results. (B) PFGE analysis for DNA breakage detection in untreated U2OS cells and upon 1-h treatment of the indicated doses of genotoxic treatments. 1 μM camptothecin (CPT) treatment is used as a positive control for DSB formation. See also Fig. S1 for the selection of appropriate doses for each treatment. Fig. 4 and Fig. S4 include data on DDR activation possibly associated with minor levels of DSB detected in B.

anticancer therapies (Michaelis et al., 2001). DNA cross-linking agents, such as mitomycin C (MMC) and cisplatin (or cis-diamminedichloroplatinum [CDDP]), are also extensively used to treat many different cancers (Deans and West, 2011). Although their cytotoxicity is commonly related to the induction of inter-strand cross-links (ICL), these drugs induce a complex combination of different adducts. ICL-inducing agents have become increasingly popular in basic research because of the isolation of numerous defects in genome stability genes sensitizing cells specifically to these agents and resulting in the cancer-prone human syndrome Fanconi anemia (FA; Deans and West, 2011). Finally, several additional treatments are known to damage the DNA bases, interfering with replication fidelity and progression (Hoeijmakers, 2009). Among the most investigated sources of base damage are UV-C irradiation, the methlyating agent methyl methanesulfonate (MMS), and oxidative DNA damage, which can be easily induced by short treatments with hydrogen peroxide (H_2O_2). Although this plethora of genotoxic agents share the observable ability to challenge the replication process, the mechanistic details of replication interference have been mostly studied in vitro or in model systems, and the detailed cellular responses have remained largely elusive in higher eukaryotic cells. However, mechanistic insight is required to inform the choice of specific chemotherapeutic regimens, to improve the anticancer response, and to avoid resistance or relapse of specific cancer types.

Replication fork reversal—i.e., the conversion of a replication fork into a four-way junction by reannealing of parental strands and coordinated annealing of nascent strands—was initially proposed by (Higgins et al., 1976), as a model for damage bypass during replication in human cells. Albeit conceptually attractive, the model has long remained unsubstantiated, and fork reversal has been rather associated with unscheduled transactions at unprotected replication forks in specific yeast mutants (Lopes et al., 2001, 2006; Sogo et al., 2002; Bermejo et al., 2011). More recently, however, fork reversal was reported as a strikingly frequent event upon mild Top1 poisoning in wild-type yeast cells, as well as mouse and human cells, and *Xenopus laevis* egg extracts (Ray Chaudhuri et al., 2012). Genetic interference with this process leads to a drastic increase in fragility of replicating chromosomes, suggesting fork reversal as a protective, evolutionarily conserved response to topological constraints in replication (Ray Chaudhuri et al., 2012). The identification of poly (ADP-ribose) polymerase (PARP) and RECQ1 as central modulators of reversed fork restart upon Top1 poisoning further implicated fork remodeling as a genetically controlled, physiological response in higher eukaryotes (Berti et al., 2013) and revived significant interest for fork reversal

Published March 2, 2015

in genome stability and cancer (León-Ortiz et al., 2014; Zeman and Cimprich, 2014; Neelsen and Lopes, 2015). However, key biological questions remain open, such as whether reversed forks are detected upon other types of replication stress and, in that case, whether their stability and restart are controlled by a common set of cellular factors. Furthermore, although several factors were shown to induce replication fork reversal in biochemical reconstitution—including RECQ helicases, SWI/SNF (Switch/Sucrose Nonfermentable) proteins, and FANCM (Kanagaraj et al., 2006; Machwe et al., 2006; Ralf et al., 2006; Gari et al., 2008; Blastyák et al., 2010; Bugreev et al., 2011; Bétous et al., 2012, 2013; Ciccia et al., 2012; Burkovics et al., 2014)—the lack of a reliable readout for fork reversal in vivo has so far hampered the identification of fork reversing activities in the living cell.

Several homologous recombination (HR) mechanisms have been proposed to assist replication restart upon fork stalling or collapse (Petermann and Helleday, 2010). The function of HR factors in replication has been consistently related to DSB formation at stalled forks, in light of the known involvement of HR in DSB repair. However, growing evidence suggests a DSB repair-independent role for HR factors in replication stress. The central vertebrate recombinase RAD51 is detected on chromatin during unperturbed replication and is recruited to stalled forks upstream of DSB formation (Hashimoto et al., 2010; Petermann et al., 2010). Upon prolonged fork stalling, HR factors—as well as numerous FA factors—are required to prevent excessive nucleolytic degradation of nascent strands and this function can be genetically uncoupled from DSB repair (Hashimoto et al., 2010; Schlacher et al., 2011, 2012). Furthermore, HR factors reportedly involved in DSB resection (i.e., MRE11, NBS1, and CtIP) were recently involved in fork processing and ATR signaling (Shiotani et al., 2013; Murina et al., 2014; Yeo et al., 2014). Most recently, the HR cancer susceptibility gene *BRCA1* was shown to promote specific recombination events at Tus/Ter-stalled mammalian forks, which can be distinguished from canonical DSB repair (Willis et al., 2014). Altogether, these recent observations suggest the mechanistic involvement of HR and possibly other FA factors in replication fork metabolism, independently from repair of chromosomal breakage.

In this work, we show that replication fork reversal is a global response to several different sources of replication stress. We suggest single-stranded DNA (ssDNA) accumulation as common precursor of fork reversal upon different types of genotoxic stress. We identify the central recombinase RAD51 as stable replisome component, independent of fork breakage, and as first cellular factor assisting in vivo the reversal process. Furthermore, we extend the role of PARP and RECQ1 to the controlled restart of reversed forks induced by different treatments.

Results

Sublethal doses of genotoxic treatments in human cells consistently induce replication fork slowing, without detectable chromosomal breakage

To investigate at the molecular level replication interference induced by different cancer chemotherapeutic drugs and other genotoxic treatments, we exposed the Rb/p53-proficient osteosarcoma cell line U-2 OS (U2OS) to a panel of clinically relevant genotoxic treatments (see Introduction), including topoisomerase inhibitors (CPT, ETP, and DOX), ICL-inducing agents (MMC and CDDP), DNA synthesis inhibitors (APH and HU), and base-damaging agents (MMS, H_2O_2, and UV-C irradiation, shortly UV). To allow the effective comparison of the cellular responses to these treatments, we selected for each of these genotoxic agents an appropriate dose that would induce marginal effects on cell survival and proliferation (Fig. S1 A). We next confirmed, by prolonged treatments and flow cytometric analysis, that the selected dose would permit completion of bulk genome duplication but delay transition through S phase (Fig. S1 B), indicating mild interference of these treatments with the replication process. We next used an established protocol for DNA fiber spreading analysis, after incorporation of halogenated nucleotides (Jackson and Pombo, 1998), to investigate at single molecule level the effect of these genotoxic treatments on replication fork progression (Fig. S1 C). Remarkably, despite the moderate effects on cell survival and cell cycle progression, all selected treatments quickly and markedly affected replication fork progression, spanning from 25% (H_2O_2) to 80% (HU) reduction in fork speed (Fig. 1 A). 1-h treatment with the selected dose of each genotoxic agent did not reveal any significant increase in the level of chromosomal breakage above background levels, as assessed by pulsed field gel electrophoresis (PFGE; Fig. 1 B). Minor DSB levels, close to the detection level of this approach (100 DSB/cell; Ray Chaudhuri et al., 2012), possibly induced by a subset of drugs are addressed by further experiments described below (see Structural determinants of ATR and ATM activation upon genotoxic treatments in human cells). Collectively, these data suggest that mild treatments with cancer chemotherapeutics and other genotoxic agents induce a marked slowdown of replication fork progression, largely uncoupled from fork breakage.

Fork slowing by all genotoxic treatments is associated with fork uncoupling and accumulation of postreplicative ssDNA gaps

We next used psoralen cross-linking coupled to EM (Neelsen et al., 2014) to investigate in vivo possible alterations of replication fork architecture associated with the observed fork slowing. This technique allows reliable identification of ssDNA regions on DNA molecules, based on local reduction of filament thickness (Neelsen et al., 2014 and references therein). Short (~40 nt) ssDNA regions are expected to arise during lagging strand synthesis in eukaryotes and are promptly detected at a subset of unperturbed replication forks (untreated). However, all genotoxic treatments induced a significant accumulation of larger ssDNA stretches at replication forks, increasing their median length by 1.5–2-fold and leading to occasional ssDNA stretches up to 500-nt long (Fig. 2, A and B). Thus, whether replication stress is induced by DNA damage, topological stress, or enzymatic inhibition of DNA synthesis, replication fork uncoupling is a common structural feature associated with genotoxic treatments in human cells. It is likely that the length of these ssDNA regions reflects how strongly each treatment interferes with

Published March 2, 2015

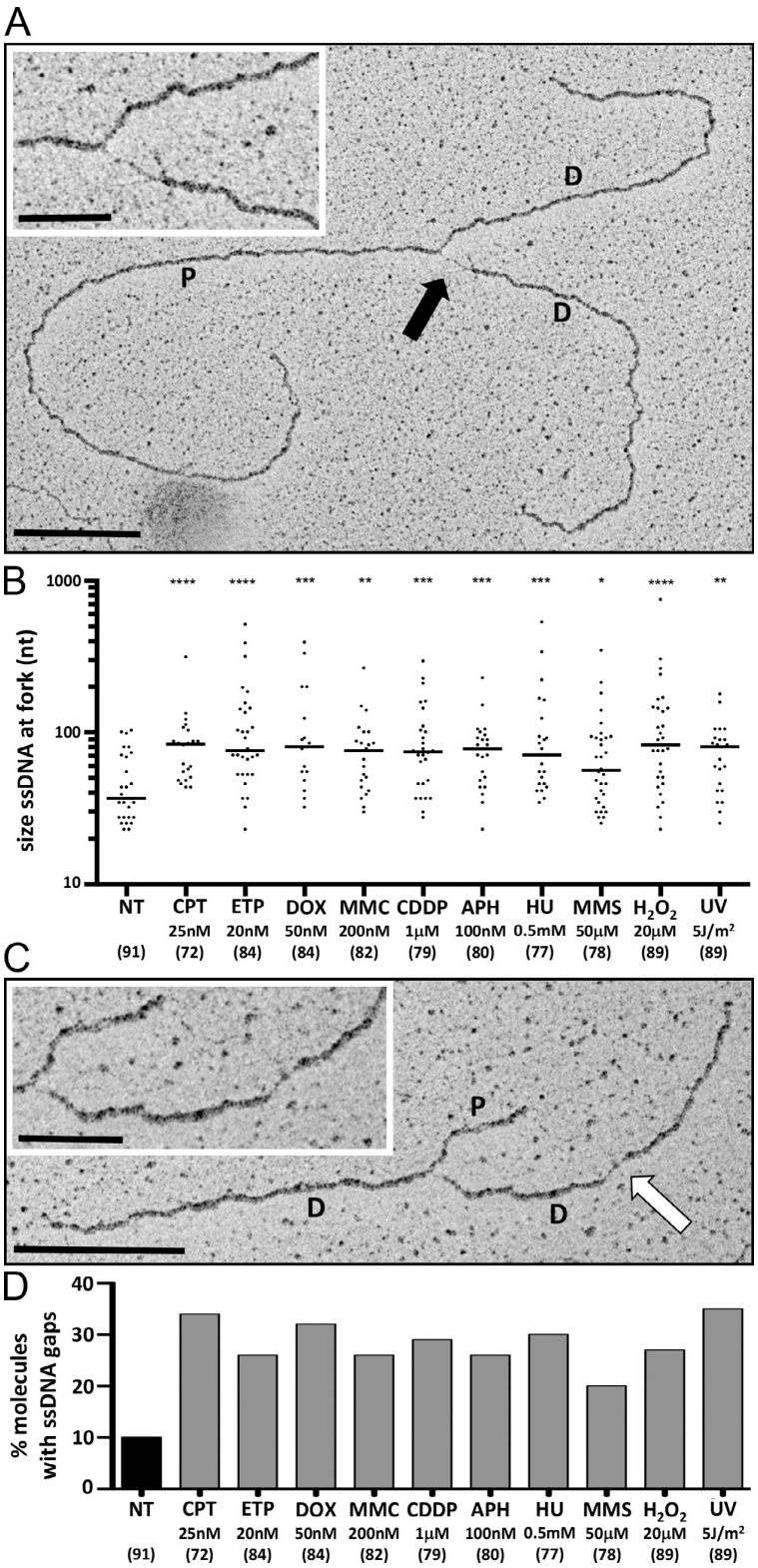

Figure 2. **Genotoxic treatments lead to extended ssDNA regions at replication forks and ssDNA gaps on replicated duplexes.** (A and C) Electron micrographs of representative replication fork from U2OS cells, after 1-h treatment with 100 nM APH (A) and 50 µM MMS (C), respectively. P indicates the parental duplex, whereas D indicates daughter duplexes. The black arrow points to an ssDNA region at the fork, whereas the white arrow indicates an ssDNA gap on a replicated duplex. The relevant portions of the molecules are magnified in the insets. Bars: (main images) 0.5 kb; (insets) 0.2 kb. (B) Graphical distribution of ssDNA length at the junction (black arrow in A) in not treated (NT) U2OS cells and upon the indicated treatments (UV pulse or 1-h treatment). Only molecules with detectable ssDNA stretches are included in the analysis. The lines show the median lengths of the ssDNA regions at the fork in the specific set of analyzed molecules. Statistical analysis *t* test according to Mann–Whitney results are *, $P \leq 0.1$; **, $P \leq 0.01$; ***, $P \leq 0.001$; ****, $P \leq 0.0001$. In brackets, the total number of analyzed molecules is given. (D) Frequency of replication forks with at least one ssDNA gap (white arrow in C) in untreated U2OS cells and upon the indicated treatments. In brackets, the total number of analyzed molecules is given. Similar results to those displayed in B and D were obtained in at least one independent experiment (see also Fig. S2 and Fig. 6 A).

continuous DNA synthesis on the leading strand (Lopes et al., 2006), via modulating template availability, polymerase processivity, nucleotide abundance, and/or torsional constraints. Furthermore, careful observation of the replicated duplexes in the analyzed population of intermediates revealed that 20–30% of the replication forks exposed at least one postreplicative

Published March 2, 2015

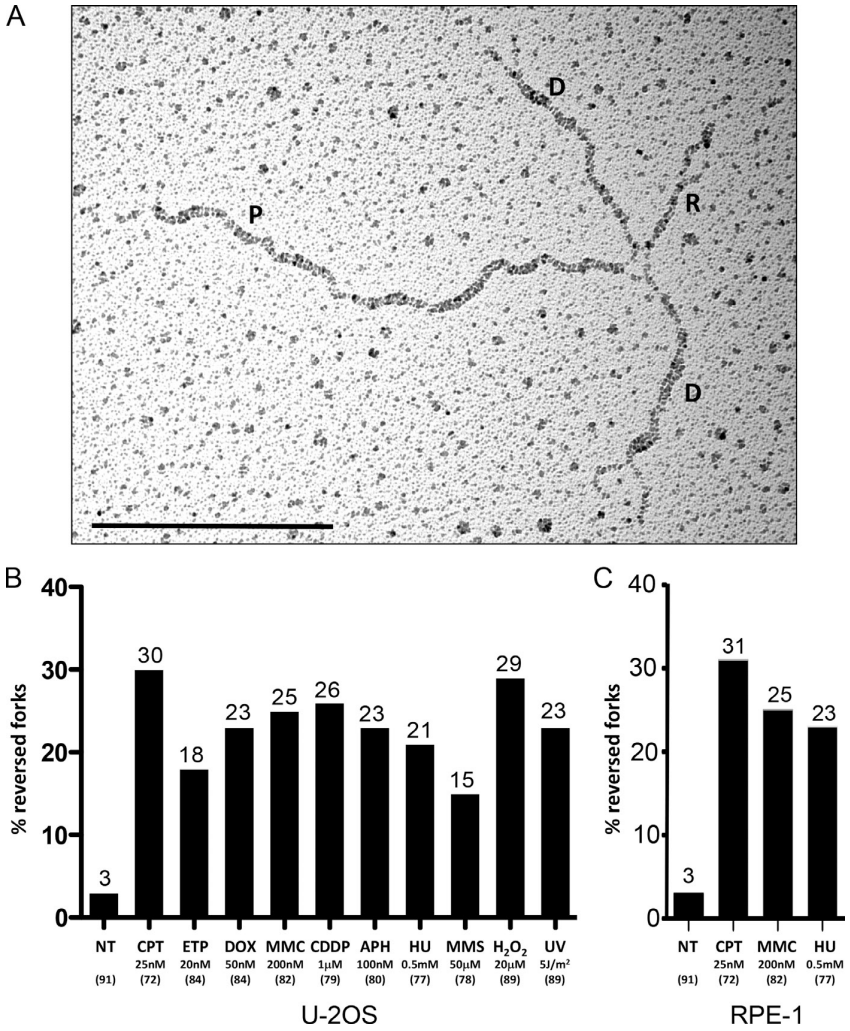

Figure 3. **All tested sources of genotoxic stress lead to frequent replication fork reversal.** (A) Electron micrograph of a representative reversed replication fork from U2OS cells treated for 1 h with 20 nM ETP. P indicates the parental duplex, D indicates daughter duplexes, and R indicates the regressed arm. Bar, 0.5 kb. (B and C) Frequency of reversed replication forks in U2OS (B) or RPE-1 cells (C) either not treated (NT) or upon the indicated treatments (UV pulse or 1-h treatment). In brackets, the total number of analyzed molecules is given. Above each column, the percentage of reversed forks is indicated. Similar results were obtained in at least one independent experiment (see also Fig. S3 and Fig. 6 A).

ssDNA gap, corresponding to a two- to threefold increase over the level observed in untreated cells (Fig. 2, C and D; and Fig. S2 A). Interestingly, the frequency of postreplicative ssDNA gaps upon different treatments generally correlated with the length of the ssDNA regions observed at the fork (Fig. 2, B and D), suggesting DNA synthesis repriming events at uncoupled replication forks, in line with previous observations in yeast (Lopes et al., 2006). However, the size of these ssDNA gaps varied significantly between different drugs (Fig. S2 B), possibly reflecting DNA synthesis restart at a different distance from the original block and/or damage-specific repair and processing events. Very similar observations on ssDNA accumulation at replication intermediates (RIs) were made on the untransformed human epithelial cell line RPE-1 treated with a subset of the genotoxic agents (Fig. S2, C and D).

Replication fork reversal is a widespread global response to replication stress in human cells

We recently reported that—upon mild, clinically relevant doses of Top1 poisons—a large fraction of forks undergo reversal (Fig. 3 A), i.e., they form a fourth regressed arm, by local reannealing of parental strands and simultaneous annealing of the newly synthesized strands (Ray Chaudhuri et al., 2012; Neelsen and Lopes, 2015). Although reversed forks were also reported upon genetic perturbations associated with early tumorigenesis (Neelsen et al., 2013a,b), a key open question was whether this DNA transaction was induced by any treatment interfering with the replication process (León-Ortiz et al., 2014). We now report high frequency of replication fork reversal (15–30%) upon all tested genotoxic treatments (Fig. 3 B). Considering the calculated number of active replication forks in a typical S phase (3,000–12,000; Ge and Blow, 2010), this corresponds to ∼500–4,000 reversed forks per cell, under different types of mild genotoxic stress compatible with cell proliferation and survival (Fig. S1 A). As previously reported for Top1 poisoning (Ray Chaudhuri et al., 2012), the observed frequency of fork reversal is already high at sublethal doses of genotoxic agents and does not significantly increase with a 10-fold higher dose (Fig. S3 A). In vivo cross-linking of RI before extraction excludes that these structures form in vitro during sample preparation (Neelsen et al., 2014). Furthermore, the relative abundance of reversed forks is not changed by omitting from the EM procedure the RI-enrichment step (Fig. S3 B; Neelsen et al., 2014).

Published March 2, 2015

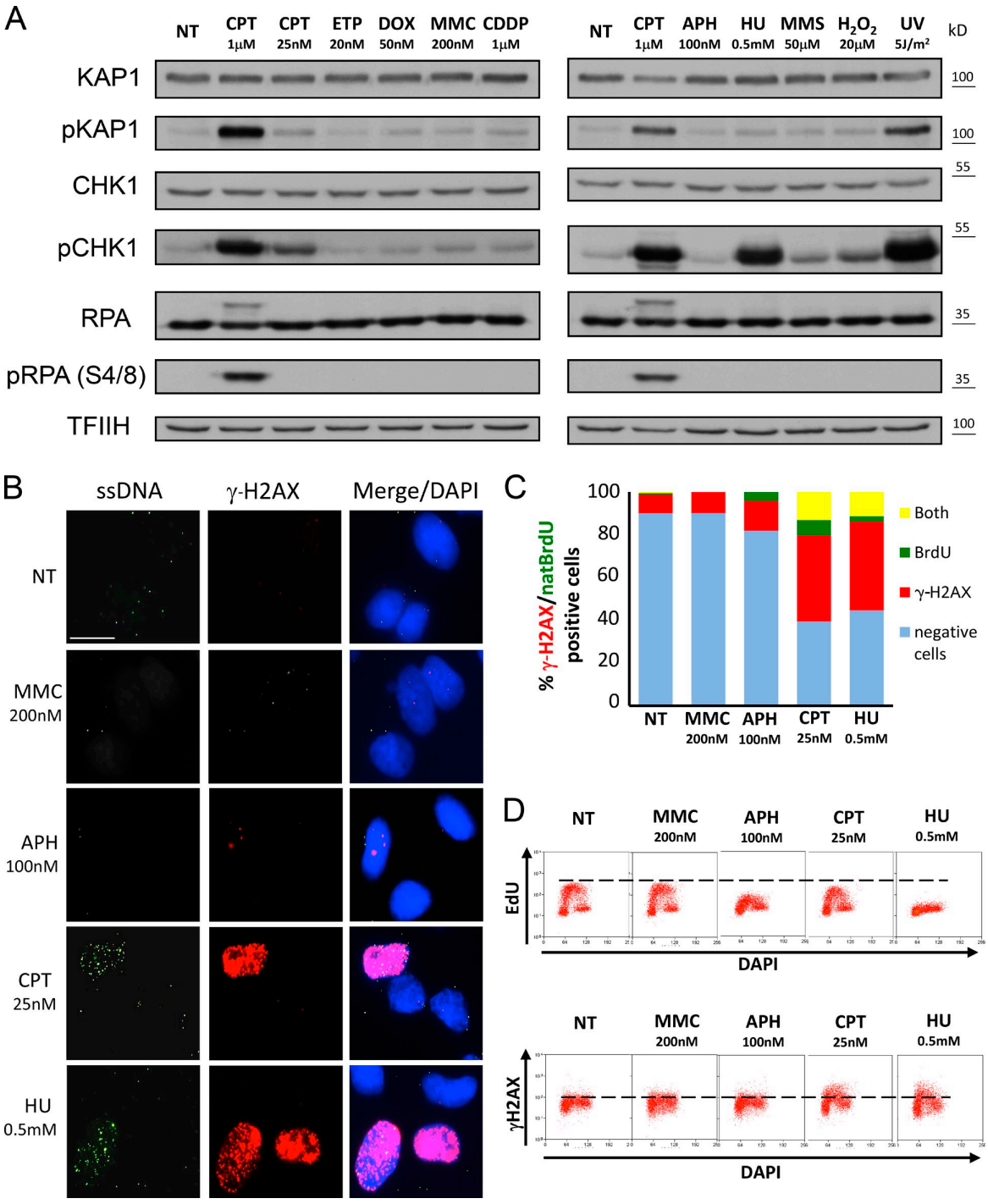

Figure 4. **Differential ATR and ATM activation upon different genotoxic treatments, despite similar structural features of RIs.** (A) Immunoblot for ATR (pCHK1) and ATM (pKAP1) activation and total DDR proteins (CHK1 and KAP1) in not treated (NT) U2OS cells and upon the indicated treatments (UV pulse or 1-h treatment). RPA32 (RPA) phosphorylation at S4/S8 indicates ATM/DNA-dependent protein kinase (DNA-PK) activation and is typically used as a DSB marker. Total RPA32 levels (and phosphorylation-associated mobility shift) are also displayed. 1 μM CPT treatment is used as positive control for full DDR activation. TFIIH is used as a loading control. (B) Native immunofluorescence staining for cells grown with 10 μM BrdU for 48 h and treated with the indicated drugs for 1 h. Red staining, γ-H2AX; green staining, BrdU (ssDNA); blue, DAPI. Bar, 15 μM. (C) Relative quantification of double-negative cells and cells positive for γ-H2AX, native BrdU staining (natBrdU), or both for the experiment in B. The data shown are from a single representative experiment out of three repeats, with $n > 100$. (D) Flow cytometry analysis of DNA synthesis (EdU), DNA content (DAPI), and DDR activation (γ-H2AX) in untreated U2OS cells and upon the indicated treatments. Dashed line indicates threshold for EdU incorporation and γ-H2AX positivity, respectively. See also Fig. S4 and Tables 1 and 2.

Published March 2, 2015

Table 1. **Relevant parameters for ATR activation upon a subset of genotoxic treatments**

Parameter	Approach	Figure	NT	MMC (200 nM)	APH (100 nM)	CPT (25 nM)	HU (0.5 mM)
Fork reversal	EM analysis	3, B and C	−/+	++	++	++	++
Fork slowing	DNA fiber spreading	1 A	−	++	++	+	+++
Impaired DNA synthesis	EdU incorporation (FACS)	4 D	−	−/+	++	+	+++
ssDNA at forks	EM analysis	2, A and B; S2; and S3	−	+	+	+	+
Total exposed ssDNA	Native BrdU staining	4 B	−	−	−	++	++
ATR signaling at forks	iPOND γ-H2AX	6 B	−	−/+	ND	++	+++
ATR signaling total	WB pCHK1	4 A	−	−	−	+	+++
ATR signaling total	IF/FACS γ-H2AX	4, B–D	−	−	−	++	++

Parameters were assessed by different investigation methods, as displayed in the indicated figures. −/+, +, ++, and +++ indicate increasingly clear phenotypes. IF, immunofluorescence; NT, not treated; WB, Western blot.

Importantly, very similar frequencies of reversed forks were induced by genotoxic treatments in RPE-1 cells (Fig. 3 C), extending our observations to noncancerous cells. Thus, replication fork reversal genuinely represents a general, widespread, physiological response to replication interference in human cells. With the exception of CPT and H_2O_2, which induced significantly longer regressed arms, the length of the fourth arm at reversed forks averaged around 300 bp in all conditions and only rarely exceeded 1 kb (Fig. S3 C). We also investigated the possible presence of ssDNA on the regressed arm, which may result from reversal of uncoupled forks and/or nucleolytic processing of the regressed arm. We observed that 20–50% of the regressed arms exposed ssDNA ends or gaps, whereas <15% were entirely single stranded (Fig. S3, D and E). The relative proportion of these categories shows subtle variations, but no strong bias, among the different treatments.

Structural determinants of ATR and ATM activation upon genotoxic treatments in human cells

Activation of the ATR-mediated replication checkpoint has been linked to excess ssDNA at RIs (Zou and Elledge, 2003). However, ATR activation requires multiple protein–protein interactions and recently revealed unexpected complexity (Nam and Cortez, 2011; Shiotani et al., 2013; Kumar et al., 2014). Furthermore, ATR activation can also be a secondary consequence of nucleolytic processing of DSB, frequently associated with prolonged replication stress, limiting our mechanistic understanding of ATR activation upon replication interference. We thus reckoned that our extensive in vivo RI visualization under mild genotoxic treatments, i.e., not associated with detectable chromosomal breakage, could provide valuable information on the structural determinants of ATR activation. We noted that, despite consistent fork slowing, frequent fork reversal, and accumulation of ssDNA upon all genotoxic treatments, several treatments (ETP, DOX, MMC, CDDP, and APH) induced no—or marginal—ATR activation, as detected by phosphorylation of its direct target CHK1 (Fig. 4 and Table 1). Furthermore, the marked CHK1 phosphorylation detected upon HU and UV treatment was not specifically associated with excessive accumulation of ssDNA regions at uncoupled forks, at postreplicative gaps, or at regressed arms (Fig. 4 A; Fig. 2, B and D; Fig. S2, A and B; Fig. S3 E; and Table 1). Differently from ssDNA visualization by EM (Figs. 2 and S2), detection of total exposed ssDNA by native BrdU staining revealed marked differences among the treatments. Although BrdU staining and γ-H2AX staining correlated at the population level, they colocalized only in a minority of the cells (Fig. 4, B and C), further uncoupling ssDNA accumulation from ATR signaling. Surprisingly, we also found no strict correlation across treatments between impairment of DNA synthesis (5′-ethynyl-2′-deoxyuridine [EdU] incorporation) and ATR activation (γ-H2AX), as APH treatment severely impairs DNA synthesis in the absence of detectable ATR activation (Fig. 4, B–D). Marked ATR activation upon HU and UV treatments is also not an indirect consequence of chromosomal breakage, as it was associated with no detectable accumulation of DSB by PFGE (Fig. 1 B) or phosphorylation of RPA32 on S4/S8 (Fig. 4; see also Fig. 6 B), a recognized DSB marker (Oakley and Patrick, 2010). Overall, ATR activation in our experimental conditions does not directly mirror the extent of replication interference, nor the amount of ssDNA detected at RIs (Table 1), and likely reflects yet-undefined signaling determinants that escape systematic cell-based and single-molecule analyses.

We also detected phosphorylation of ATM and its target KAP1 upon mild treatments with CPT and UV, albeit not accompanied by RPA S4/S8 phosphorylation or detectable DSBs (Figs. 1 B and 4). To assess the possibility that both approaches may not be sensitive enough to reveal minor DSB levels, we increased 10-fold the dose of each genotoxic treatments and reassessed physical chromosomal breakage and cellular responses. In the case of CPT, DOX, H_2O_2, and UV, the higher doses did lead to detectable DSBs, expectedly associated with ATM, KAP1, and RPA32-S4/S8 phosphorylation (Fig. S4). Lack of S4/S8 phosphorylation upon DOX treatments may reflect specific effects of this drug in DSB signaling. Interestingly, at higher doses, MMS also induced ATM/KAP1 phosphorylation without detectable DSB and RPA32 S4/S8 phosphorylation (Fig. S4), as already seen for mild CPT and UV treatments (Figs. 4 A and S4), supporting the notion that under certain conditions, replication stress can activate ATM in the absence of DSB (Table 2; Ray Chaudhuri et al., 2012). However—as for the strong ATR activation upon UV and HU treatments—we could not unambiguously associate this DSB-independent ATM

Published March 2, 2015

Table 2. **Relevant parameters for ATM activation upon a subset of genotoxic treatments**

Parameter	Approach	Figure	NT	MMC (200 nM)	DOX (50 nM)	UV (5 J/m^2)	CPT (25 nM)	CPT (1 µM)
Fork reversal	EM analysis	3, B and C	−/+	++	++	++	++	++
DSBs	PFGE	1 B and S4	−	−	−/+	−	−	++
ATM signaling at forks	iPOND pRPA32	6 B	−	−	−	−	−	++
ATM signaling total	WB pRPA32	4 and S4	−	−	−	−	−	++
ATM signaling total	WB pKAP1	4 and S4	−	−	+/−	+	+/−	++
ATM signaling total	WB pATM	S4	−	−	+/−	+	+	++

Parameters were assessed by different investigation methods, as displayed in the indicated figures. −/+, +, ++, and +++ indicate increasingly clear phenotypes. NT, not treated; WB, Western blot.

signaling to any specific structural feature detectable by EM analysis (Table 2). Finally, APH and ETP, despite their marked effect on DNA synthesis, fork uncoupling, and reversal already at low doses (Figs. 1 A, 2 B, 3 B, and 4 C), did not induce detectable ATR or ATM activation even at 10-fold higher doses. Altogether, these data suggest that fork slowing, fork reversal, and ssDNA accumulation are by themselves nonpredictive parameters for ATR or ATM activation upon replication stress.

RECQ1 and PARP activities regulate the restart of reversed forks induced by different types of replication stress

After identification of replication fork reversal as a frequent DNA transaction upon Top1 poisoning in human cells (Ray Chaudhuri et al., 2012), we reported reversed fork accumulation in these conditions to depend on transient PARP-mediated inhibition of the specific restart activity of the RECQ1 helicase, thus linking fork restart to DNA repair and PARP inactivation (Berti et al., 2013). We therefore decided to investigate by DNA fiber and EM analysis whether similar mechanisms would control the restart of reversed forks observed upon other genotoxic treatments. We focused this analysis on MMC and HU, as prototypes of replication stress induced by template cross-linking and DNA synthesis inhibition, respectively, thus mechanistically distinct from the replication stress induced by Top1 poisons. As previously reported for CPT (Sugimura et al., 2008; Ray Chaudhuri et al., 2012), PARP inactivation by olaparib largely abolished MMC-induced fork slowing and only partially restored replication fork progression in HU, in which nucleotide shortage cannot be overcome (HU; Fig. 5 A). Importantly, the effect of olaparib upon both treatments was dependent on the RECQ1 helicase, showing that fork slowing upon different sources of replication stress is an active process mediated by transient PARP-mediated inhibition of RECQ1 activity (Fig. 5 A). Furthermore, PARP inactivation markedly reduced reversed fork accumulation upon MMC and HU treatments. RECQ1 depletion induced by itself a threefold accumulation of reversed forks under unperturbed conditions (Fig. 5 B), associated with mild ATM/KAP1 phosphorylation and no accumulation of ssDNA gaps (Fig. S5, A and B). Importantly, RECQ1 depletion largely abolished PARP requirement for reversed fork accumulation upon both treatments and prevented the rapid decline in reversed fork frequency observed upon drug removal (Fig. 5 B). Altogether, these data strongly suggest that PARP-controlled RECQ1 activity is largely responsible to promote fork restart and progression, irrespective of whether fork reversal is induced by topological stress (CPT; Berti et al., 2013), DNA cross-linking (MMC), or DNA synthesis inhibition (HU).

The human recombinase RAD51 is recruited to replication forks in the absence of DSBs and modulates fork progression and integrity

The extensive EM analysis described in this work identifies fork uncoupling and reversal as common parallel transactions upon replication interference by various genotoxic treatments. We tested the functional correlation of these events by plotting the frequency of reversed forks versus the median size of ssDNA stretches at the forks for all EM samples analyzed (Fig. 6 A). This analysis shows that our EM measurements of fork reversal and ssDNA accumulation were highly reproducible in independent experiments for each drug. Although a general association of the two events is not unexpected, the striking correlation that we found between the two parameters (Fig. 6 A) prompted us to investigate whether they were not only correlatively associated, but rather mechanistically linked. Accumulation of ssDNA is a crucial structural feature of upstream intermediates in DSB repair by HR and is actively induced by DNA end resection for the controlled loading of the central recombinase factor RAD51, which then drives homology-directed strand invasion (Symington and Gautier, 2011). We thus tested whether, in our experimental conditions, RAD51 could be detected at replication forks, as suggested by a recent screening (Alabert et al., 2014). Using an iPOND approach with different labeling protocols (Sirbu et al., 2011; Fig. S5 C), we detected mild, but reproducible, RAD51 association with replication forks even in unperturbed conditions, which was lost—as for other replisome components, e.g., proliferating cell nuclear antigen—upon thymidine chase, and enriched by mild treatments with HU, MMC, and CPT (Fig. 6 B). Upon mild HU and CPT treatments, γ-H2AX is clearly detected at forks, confirming our results on ATR activation (Fig. 4). However, differently from acute treatments affecting fork integrity (1 µM CPT), no RPA32-S4/8 phosphorylation is present on EdU-labeled DNA upon any of the mild genotoxic treatments, confirming that the enrichment of RAD51 at forks facing replication stress is uncoupled from fork breakage (Fig. 6 B). Similarly, we observed by single-cell labeling that RAD51 is chromatin loaded in unperturbed S phase cells (EdU$^+$) and is enriched in numerous foci upon

Published March 2, 2015

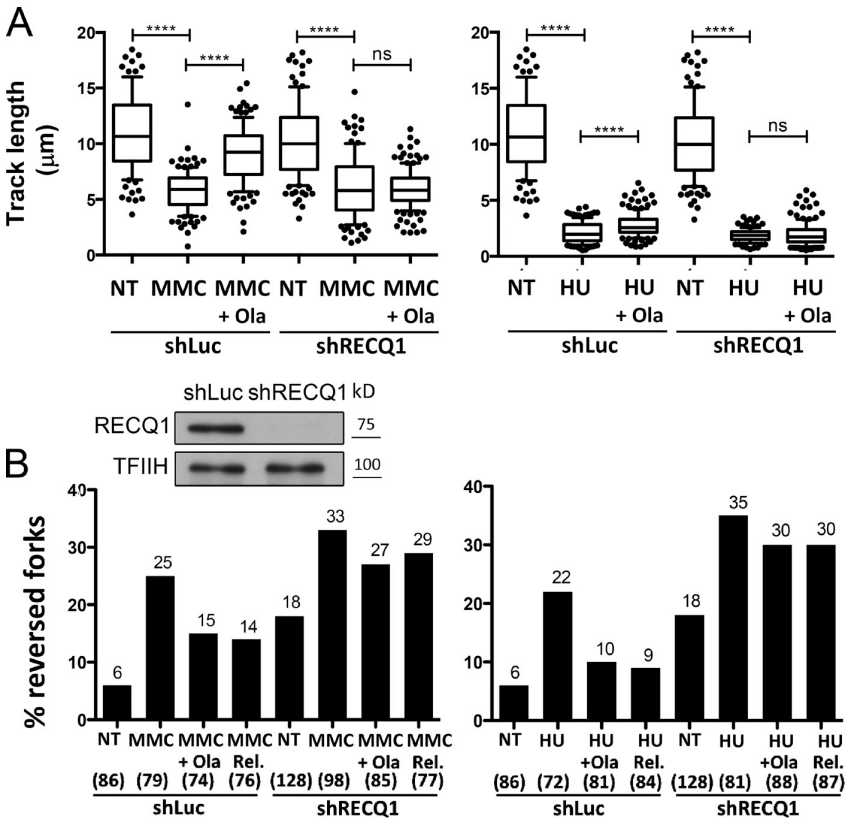

Figure 5. **RECQ1 and PARP activity control replication fork progression and accumulation/restart of reversed forks upon different types of genotoxic stress.** (A) Statistical analysis of IdU track length measurements, according to the labeling protocol in Fig. S1, in U2OS cells stably transduced (shRNA) for Luciferase (shLuc) or RECQ1 (shRECQ1) depletion. 200 nM MMC and 500 µM HU were optionally added concomitantly with the second label (IdU). The PARP inhibitor olaparib (Ola; 10 µM) was optionally added 2 h before CldU labeling and maintained during labeling. At least 100 tracks were scored for each dataset. Horizontal lines represent the median value, and boxes and whiskers indicate the 10–90th percentiles. *t* test according to Mann–Whitney; ns, not significant; ****, $P < 0.0001$. Similar results were obtained in at least one independent experiment. (B) Frequency of reversed forks detected by EM in U2OS cells stably transfected (shRNA) for Luciferase or RECQ1 depletion. The cells were optionally treated for 1 h with 200 nM MMC or 500 µM HU, after an optional 2-h pretreatment with olaparib. Reversed fork restart was assessed by measuring the frequency of reversed forks 3 h after drug removal (release [Rel.]). In brackets, the total number of analyzed molecules is given. Above each column, the percentage of reversed forks is indicated. Similar results were obtained in at least one independent experiment. RECQ1 levels after shRNA-mediated depletion were detected by immunoblotting. TFIIH was used as a loading control. NT, not treated.

both mild and acute genotoxic treatments (Fig. 6 C). siRNA-mediated down-regulation of RAD51 largely abolished active replication fork slowing observed upon MMC and CPT treatments, whereas had no significant effect when fork progression was physically impaired by nucleotide shortage (HU), suggesting RAD51 loading as a crucial modulator of fork progression upon genotoxic stress (Fig. 6 D). Furthermore, RAD51 depletion also impacted on replication fork integrity, leading to a significant induction of DSBs already in unperturbed conditions, with marginal further increase observable upon exogenous genotoxic stress (Fig. 6 E).

RAD51 is required to limit replication fork uncoupling and drive fork reversal upon different genotoxic treatments

In light of our previously reported data upon Top1 poisoning (Ray Chaudhuri et al., 2012), the observations reported here were highly suggestive of a role for RAD51 in replication fork reversal. We thus tested the hypothesis that, by analogy to HR mechanisms at DSBs, RAD51 could be loaded on extended ssDNA regions at uncoupled forks and drive fork reversal by template reannealing. EM analysis of U2OS cells treated with CPT, MMC, or HU upon siRNA-mediated RAD51 depletion revealed that effective fork reversal upon all treatments strictly requires RAD51 (Fig. 7 A). This held true using different siRAD51 oligonucleotides and extracting RI 24 h after siRNA transfection (Fig. 7 B), when protein depletion was yet incomplete and cells showed no alteration in their cell cycle and replication potential (Fig. S5, D and E). Furthermore, stable expression of exogenous, siRNA-resistant RAD51 completely restored the frequency of CPT-induced fork reversal observed in control cells (Fig. 7 C). RAD51 depletion also abolished the increased level of reversed forks observed in unperturbed RECQ1-depleted cells (Fig. S5 F), proving that RAD51 is required for replication fork reversal upon both endogenous and exogenous genotoxic stress. Importantly, upon all tested treatments, defective fork reversal was accompanied by a significant increase in RIs displaying long ssDNA regions at the fork (Fig. 7, D and E), strongly suggesting that uncoupled forks are precursors of RAD51-mediated fork reversal. Despite the effects on replication fork remodeling, RAD51 depletion had no noticeable impact on the abundance of the postreplicative ssDNA gaps induced by the genotoxic drugs (Fig. 7 F), differently from what previously shown in yeast and *Xenopus* egg extracts (Hashimoto et al., 2010). Altogether, these data imply RAD51-mediated recombinational mechanisms in the remodeling of uncoupled replication forks upon different types of replication stress.

Discussion

In this study, we have performed an unprecedented structural survey on the impact of genotoxic treatments on the replication process in human cells. The differential sensitivity of cancer and normal cells, often related to cancer-specific defects in the DNA damage response (DDR), is uncovered at relatively mild

Published March 2, 2015

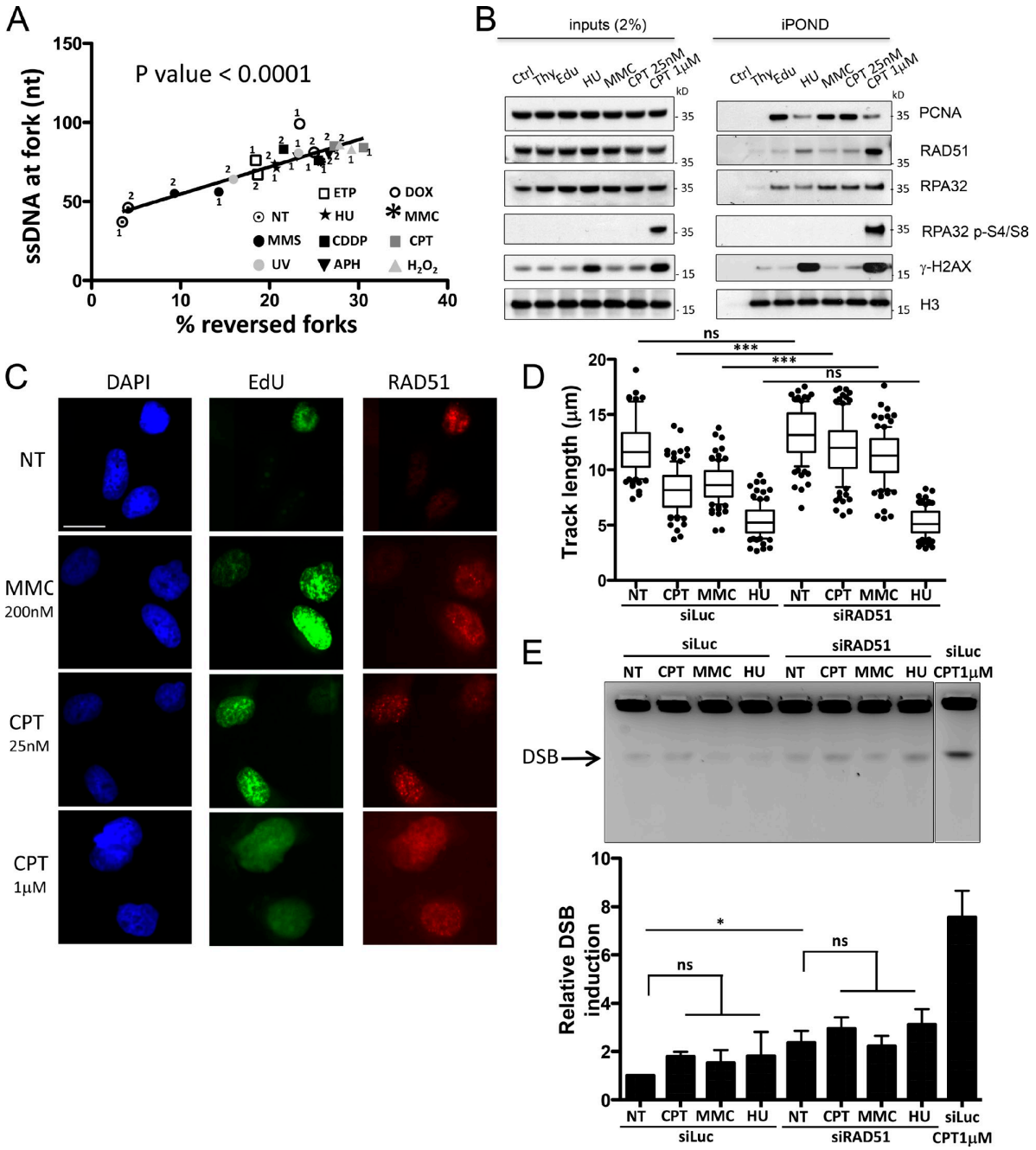

Figure 6. **RAD51 is present at forks upon mild genotoxic stress and modulates fork progression and integrity.** (A) Linear regression analysis shows strict direct correlation ($P < 0.0001$) between accumulation of ssDNA at the fork (median values of ssDNA regions at the junction) and frequency of fork reversal. Results from two independent experiments are displayed for untreated U2OS cells and for each genotoxic treatment. (B) HEK293T cells were EdU-labeled as indicated in Fig. S5 C and treated with sublethal doses of genotoxic drugs (0.5 mM HU, 200 nM MMC, or 25 nM CPT). Proteins and relative post-translational modifications associated with replication forks were isolated by iPOND procedure and detected with the indicated antibodies. The thymidine (Thy; 10 µM) chase experiment is used to discriminate proteins associated with chromatin behind replicating forks. In the control (Ctrl) experiment, the click reaction is performed using DMSO instead of biotin azide. 1 µM CPT treatment is used as positive control to induce high replication stress and DSBs. (C) Immunofluorescence staining for U2OS cells grown on coverslips and treated with the indicated drugs for 1 h. Red staining, RAD51; green staining, EdU; blue, DAPI. Bar, 15 µM. (D) DNA fiber spreading. Statistical analysis of IdU replicated track length in U2OS cells, comparing not treated (NT) conditions with the indicated treatments. U2OS cells were transfected with siRNA against luciferase (siLuc) or RAD51 (siRAD51) 24 h before CldU or IdU labeling. At least 100 tracks were scored per sample. Horizontal lines represent the median value, and boxes and whiskers indicate 10–90th percentiles. Statistical analysis: one-way ANOVA; ns, not significant; ***, $P \leq 0.001$. (E) PFGE analysis for DNA breakage detection in untreated U2OS cells and upon 1-h treatment with indicated doses of genotoxic treatments. U2OS cells were transfected with siRNA against luciferase or RAD51 24 h before treatments. 1 µM camptothecin (CPT) treatment is used as a positive control for DSB formation. The graph shows quantitative DSB induction from three independent experiments and includes average value and standard deviations (error bars). Statistical analysis: two-way ANOVA; ns, not significant; *, $P \leq 0.05$.

Published March 2, 2015

doses of the genotoxic agents used in cancer therapy (Bouwman and Jonkers, 2012 and references therein). We thus decided to investigate the effects of different genotoxic agents at doses that caused minimal lethality to the Rb/p53-proficient osteosarcoma human cell line, mostly used in this study (U2OS). These conditions enabled us to dissect the consequences of replication interference in the absence of detectably compromised chromosome integrity.

Despite diverse modes of interference with DNA synthesis (base damage, DNA intercalation and cross-linking, nucleotide depletion, polymerase inhibition, and torsional constraints), all tested genotoxic agents lead to strikingly similar mechanistic consequences on the replication process, i.e., marked fork slowing, ssDNA accumulation, and fork reversal. Importantly, these conclusions hold true in a nontransformed human cell line (RPE-1). The rapid accumulation of replication forks with extended ssDNA at the junction may represent the indirect consequence of continued helicase activity ahead of the fork, whereas DNA synthesis is asymmetrically delayed by the genotoxic treatment (Fig. 8), as reported in UV-irradiated yeast cells (Lopes et al., 2006). However, the extent of fork uncoupling may also be regulated by replisome-associated factors, specifically engaged in the replication process upon genotoxic stress, as recently suggested for the minichromosome maintenance–associated FA factor FANCD2 (Lossaint et al., 2013). Furthermore, the extent of ssDNA at replication forks challenged by genotoxic stress could be controlled by regulated nucleolytic processing of newly synthesized DNA, which becomes particularly evident after prolonged stress and pathological conditions (Schlacher et al., 2011, 2012). Interestingly, several factors previously involved in DSB resection—e.g., MRE11, NBS1, and CtIP—have been recently involved in fork metabolism and ATR activation upon genotoxic stress (Schlacher et al., 2011; Shiotani et al., 2013; Murina et al., 2014; Yeo et al., 2014), suggesting that ssDNA regions at damaged replication forks may be subjected to similar processing as DSB.

Indeed, one important implication of our data is that replication fork remodeling upon genotoxic stress shares an important mechanistic step with DSB repair, i.e., RAD51-mediated strand invasion, rapidly and effectively leading to replication fork reversal (Fig. 8; Neelsen and Lopes, 2015). As originally suggested by (Higgins et al., 1976), remodeling of uncoupled replication forks in human cells, besides limiting excessive ssDNA accumulation, would also allow more time for template repair and promote efficient DNA damage bypass directly at the fork, thus limiting reliance on postreplicative repair. Intriguingly, replication forks in wild-type yeast cells—which are devoid of PARPs—do not detectably undergo reversal upon most genotoxic treatments. In keeping with our model, yeast cells accumulate much longer ssDNA stretches at the junction and postreplicative ssDNA gaps, favoring fork restart by repriming (Sogo et al., 2002; Lopes et al., 2006). In line with this notion, genetic inactivation of HR-mediated repair (RAD51) upon genotoxic stress results in marked accumulation of postreplicative gaps in *Saccharomyces cerevisiae* (Lopes et al., 2006; Hashimoto et al., 2010) but not in human cells (Fig. 7 F).

Both aberrant RIs consistently and abundantly detected upon all tested genotoxic treatments—i.e., forks with extended ssDNA regions and reversed forks—carry intrinsic signaling potential. Excess ssDNA at replication forks has been linked to ATR activation (Zou and Elledge, 2003), whereas the formation of a new DNA end at regressed arms may potentially activate ATM in the absence of DSBs. Albeit conceptually attractive, our structural data argue against both of these models. Although ssDNA accumulation—at forks, gaps, or regressed arms—was observed at similar extents with several genotoxic treatments, some of them induced strong ATR activation (UV and HU), whereas others (APH and ETP) failed to detectably activate ATR, even at doses 10-fold higher than those required to drastically impair fork progression. Compared with EM analysis of ssDNA at RI, total ssDNA detection by native BrdU staining shows more pronounced differences among treatments and a stronger correlation with ATR activation, suggesting that ssDNA accumulation uncoupled from RI may be more relevant for ATR signaling. However, cells scoring positive in this assay still represent a minority of those showing γ-H2AX. Thus, ATR signaling in these conditions seems largely uncoupled from ssDNA/RPA accumulation, in keeping with other studies challenging this dogma (Ball et al., 2005; Recolin et al., 2012), and may reflect alternative yet-undefined mechanisms (Kumar et al., 2014). Similarly, high frequencies of reversed forks are observed with all treatments but are associated with detectable ATM activation only upon exposure to CPT and UV. Thus, besides these basic structural determinants (ssDNA and DNA ends, respectively), ATR and ATM activation at replication forks may require additional molecular features, which may be difficult to identify by EM analysis. Alternatively, checkpoint activation may entail a specific chromatin or topological context, or recruitment/removal of cellular factors at/from replication forks, which may only occur under specific conditions.

We show that the same molecular mechanism—i.e., PARP-regulated RECQ1 helicase activity—is largely responsible for the accumulation of reversed forks upon different types of genotoxic stress and to restart these forks once the stress is relieved (Figs. 5 and 8; Berti et al., 2013). An important mechanistic implication of these findings is that local PARP activation must result from a common structural determinant induced by all treatments, including genotoxic agents that do not directly cause DNA damage or breakage (e.g., HU). The unambiguous identification of this structural determinant will require further investigation. It should be noted, however, that the discontinuities present on nascent strands—as well as the DNA end at the regressed arm upon reversal—may be structurally identical to the strand breaks that are reportedly responsible for PARP activation in DNA repair (Pines et al., 2013) and that four-way junctions carry by themselves the potential to activate PARP (Lonskaya et al., 2005).

Our data clearly consolidate previous evidence that RAD51 is a stable component of replicating chromatin in metazoan, independently of fork breakage (Hashimoto et al., 2010; Petermann et al., 2010; Alabert et al., 2014). How is RAD51 recruited to uncoupled forks to promote template reannealing and thereby fork reversal (Fig. 8)? The presence of extended ssDNA

Published March 2, 2015

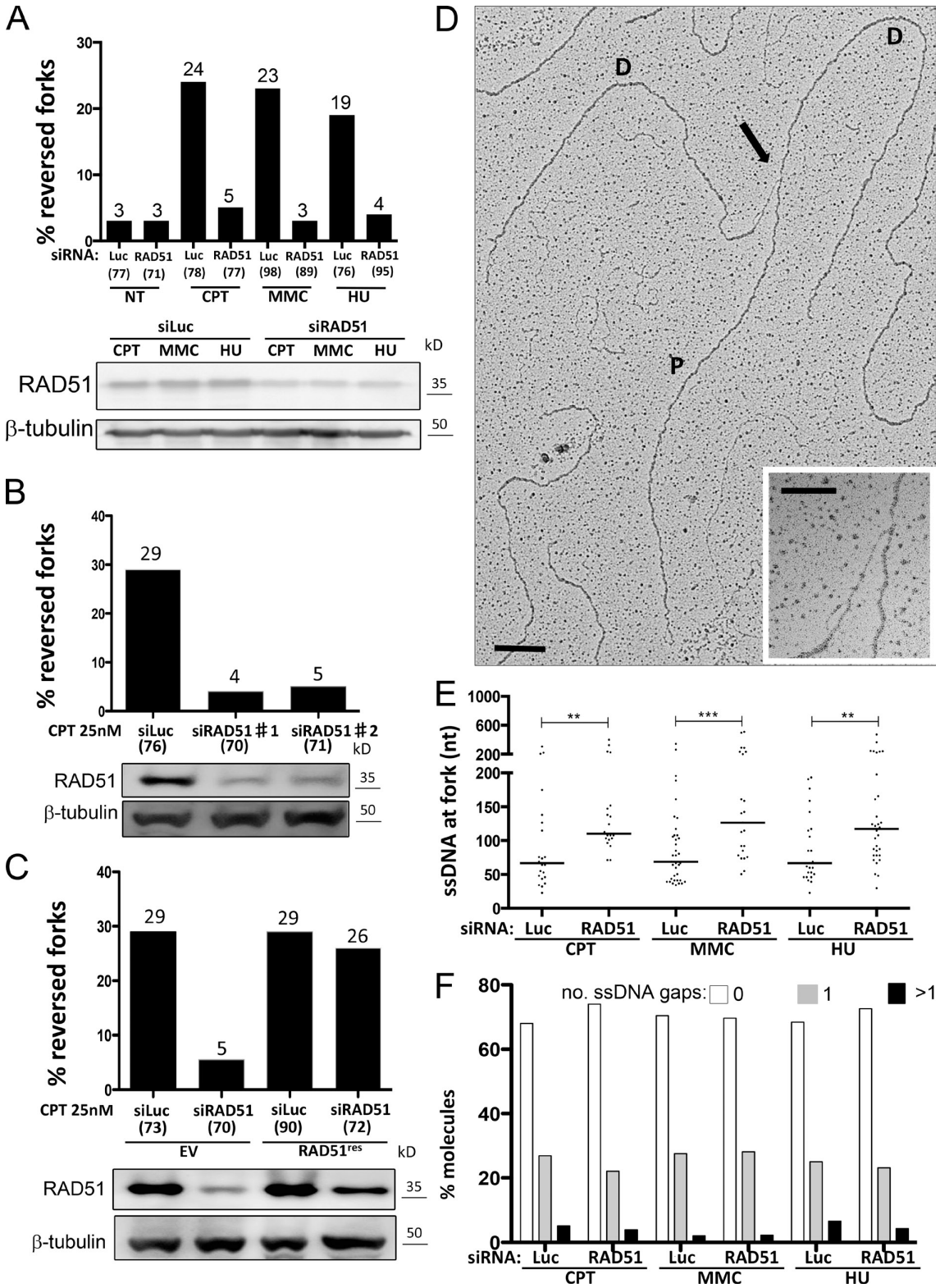

Figure 7. **RAD51 is required to convert uncoupled forks into reversed forks in response to different genotoxic treatments.** (A–C) Frequency of reversed replication forks detected by EM in U2OS cells. In A, U2OS cells were transfected with Luciferase siRNA (siLuc) or RAD51siRNA (siRAD51) 72 h before DNA extraction from untreated cells or cells treated with 25 nM CPT, 200 nM MMC, or 500 nM HU for 1 h. In B, U2OS cells were transfected with Luciferase or RAD51 siRNA 24 h before treatment with 25 nM CPT for 1 h. In C, U2OS cells containing an empty vector, and U2OS cells expressing exogenous RAD51 were transfected with Luciferase or RAD51 siRNA (against 3′ UTR region of RAD51) 24 h before treatment with 25 nM CPT for 1 h. In brackets,

Published March 2, 2015

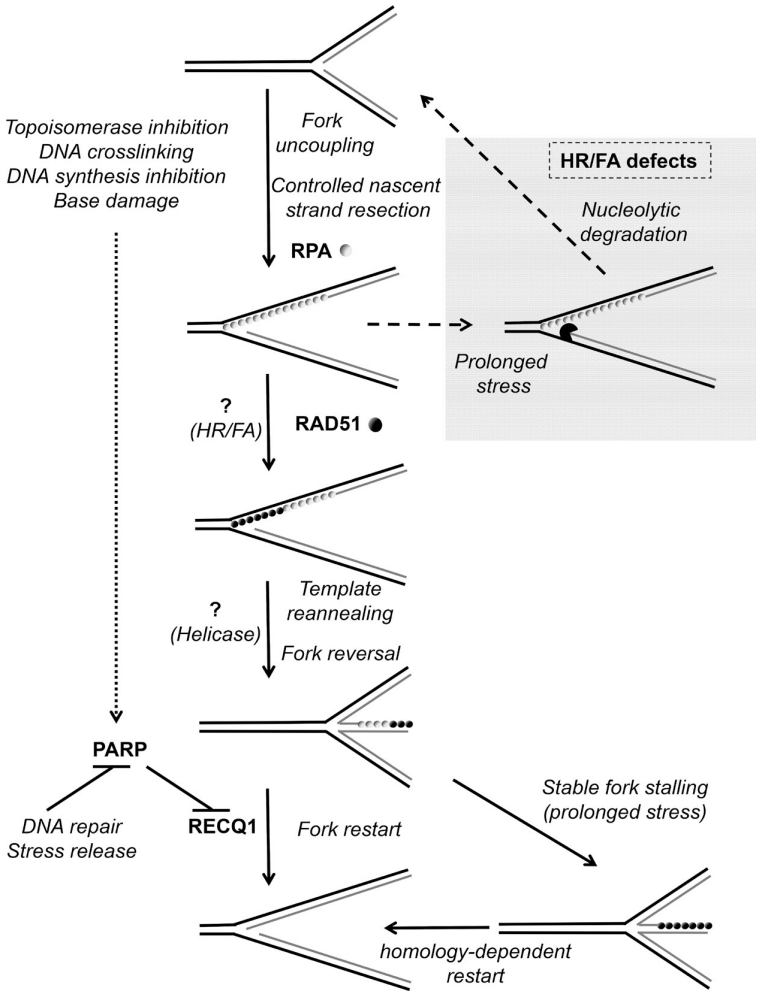

Figure 8. **Schematic model for replication fork reversal and restart upon different types of replication stress.** Template damage, DNA synthesis inhibition, or torsional stress rapidly impair symmetric elongation of nascent strands and induce replication fork uncoupling, leading to extended ssDNA regions at the fork. Controlled nascent strand resection may participate in ssDNA exposure. As characterized during DSB processing and repair, when ssDNA regions reach a critical size, the recombinase RAD51 partially replaces RPA at uncoupled forks, possibly assisted by cofactors belonging to the homologous recombination (HR) and Fanconi anemia (FA) pathways. RAD51-mediated template reannealing primes replication fork reversal, probably in concert with yet-unidentified specialized enzymatic activities, assisting template repair and limiting nucleolytic degradation of nascent strands upon prolonged stalling. PARP activation at discontinuous nascent strands and/or regressed arms stabilizes the forks in the reversed state, by transiently inhibiting the specific restart activity of RECQ1 helicase until the damage is repaired or the stress is released. RAD51 loading on regressed arms may further protect forks after reversal and promote alternative homology-mediated pathways of fork restart upon prolonged stalling.

regions—an ideal target for RAD51 binding—may by itself explain RAD51 loading to forks upon various genotoxic treatments. However, the competition with RPA for ssDNA binding in classical HR-dependent DSB repair implies that RAD51 loading is assisted by accessory proteins, such as the RAD51 paralogues and/or the cancer susceptibility genes *BRCA1* and *BRCA2* (Suwaki et al., 2011). Importantly, many of these factors have been recently reported to play a pivotal role also at stalled replication forks, promoting recombinational mechanisms that are structurally and/or genetically distinct from canonical DSB repair (Schlacher et al., 2011; Adelman et al., 2013; Willis et al., 2014). Furthermore, several additional FA factors are required for the same DSB repair-independent fork protection mechanism (Schlacher et al., 2012). Intriguingly, inactivation of the RAD51 paralogue XRCC3 in DT40 cells phenocopies PARP inactivation in suppressing fork slowing by Top1 poisons (Sugimura et al., 2008). Based on all this evidence, it will be a crucial challenge for future studies to assess in vivo the contribution of individual HR/FA factors in replication fork remodeling upon different types of genotoxic stress, by possibly mediating RAD51 loading or stabilization at fork-associated ssDNA regions (Fig. 8). In this view, these factors could contribute to genome stability by supporting DNA damage tolerance and preventing DSB formation, besides their reported role in repairing chromosomal breaks.

the total number of analyzed molecules is given. Above each column, the percentage of reversed forks is indicated. Similar results were obtained in at least one independent experiment. RAD51 levels after siRNA-mediated depletion were detected by immunoblotting. β-Tubulin is used as a loading control. EV, empty vector. (D) Electron micrograph of a representative replication fork with an extended ssDNA region at the junction (black arrow, magnified in the inset) upon RAD51 depletion and treatment with 25 nM CPT for 1 h. Bars: (main image) 0.5 kb; (inset) 0.2 kb. P indicates the parental duplex, and D indicates daughter duplexes. (E) Graphical distribution of ssDNA length at the junction (black arrow in C) in U2OS cells transfected with Luciferase siRNA and RAD51 siRNA and treated with 25 nM CPT, 200 nM MMC, and 500 nM HU for 1 h. The lines show the median length of the ssDNA region at the fork in the specific set of analyzed molecules. Statistical analysis *t* test according to Mann–Whitney, results are **, $P \leq 0.01$; ***, $P \leq 0.001$. Similar results were obtained in at least one independent experiment. (F) Frequency of replication forks with ssDNA gaps (Fig. 2 C and Fig. S2) in U2OS cells transfected with Luciferase or RAD51 siRNA 48 h before treatment with 25 nM CPT, 200 nM MMC, or 500 nM HU for 1 h. Similar results were obtained in at least one independent experiment. NT, not treated.

Published March 2, 2015

It will also be important to identify specific enzymatic activities required to assist RAD51 in driving replication fork reversal in vivo (Fig. 8; Neelsen and Lopes, 2015), presumably included in the list of factors showing fork remodeling activity in vitro (Kanagaraj et al., 2006; Machwe et al., 2006; Ralf et al., 2006; Gari et al., 2008; Blastyák et al., 2010; Bugreev et al., 2011; Bétous et al., 2012, 2013; Ciccia et al., 2012; Burkovics et al., 2014). Conversely, in light of our data, it will be important to extend the limited information on how the addition of RAD51 and RPA in the reactions may impact the biochemical properties of these fork remodeling proteins (Kanagaraj et al., 2006; Bugreev et al., 2011; Bétous et al., 2013; Burkovics et al., 2014).

Although we propose that the observed nascent strand degradation upon HR defects (Schlacher et al., 2011) is primarily a consequence of defective fork reversal upon prolonged fork stalling, our data do not exclude an additional role of RAD51 in stabilizing reversed forks during prolonged replication stress—as originally proposed (Schlacher et al., 2011)—by protecting the regressed arms from unscheduled nucleolytic attacks and assisting homology-directed fork restart (Fig. 8). It should be noted, however, that controlled regressed arm resection, which contributes to fork restart upon prolonged fork stalling, is genetically distinct from the extensive nascent strand degradation observed upon HR/FA defects (Schlacher et al., 2011; see Thangavel et al., in this issue).

Impairment of replication fork reversal may contribute to explain the potentiating effects of PARP inhibitors on several chemotherapeutic treatments (Rouleau et al., 2010; Ray Chaudhuri et al., 2012) and may also provide alternative mechanistic explanations for the observed synthetic lethality of PARP inhibition and HR defects (Farmer et al., 2005; Neelsen and Lopes, 2015). By analogy, the search for biochemical activities specifically required for fork reversal in vivo holds great potential to identify novel targets to potentiate cancer chemotherapy based on replication interference.

Materials and methods

Cells and cell culture

Human osteosarcoma U2OS cells, RPE-1 cells, or HEK293T cells were cultured in DMEM supplemented with 10% FBS, 100 U/ml penicillin, and 100 µg/ml streptomycin in an atmosphere containing 6% CO_2 at 37°C. Cells were treated with different cancer chemotherapeutics and DNA-damaging agents as indicated, trypsinized, and processed for cell cycle analysis, Western blots, PFGE, and EM DNA extraction.

Genetic inactivation by sh/siRNA

shRNA-mediated down-regulation was achieved by cloning the sequence targeting RECQ1 (5′-GAGCTTATGTTACCAGTTA-3′) into the pLKO.1 (plasmid #10878; Addgene) lentiviral shRNA expression vector. Lentiviral particles were generated by transient cotransfection of pLKO.1 and the packaging plasmids psPAX2 (plasmid #12260; Addgene) and pM2D.G (plasmid #12259; Addgene) into HEK293T cells. Viral supernatants were filtered through a 0.45-µM filter and transduced on U2OS cells for 24 h followed by selection with 8 µg/ml puromycin for 3 d. Control transductions were performed using the pLKO.1 vector expressing a shRNA targeting Luciferase (5′-ACGCTGAGTACTTCGAAATGT-3′). For siRNA experiments, cells were transfected with the indicated siRNA using RNAiMAX (Invitrogen) according to manufacturer's instruction. The experiments were performed 24 or 72 h after transfection. Purchased sequences were as follows: *Luc* siRNA (40 nM; 5′-CGUACGCGGAAUACUUCGA-3′), *RAD51 #1* siRNA (40 nM; 5′-GAGCUUGACAAACUACUUC-3′), and *RAD51 #2* siRNA (40 nM: 5′-GACUGCCAGGAUAAAGCUU-3′).

Drugs and reagents

CPT (Sigma-Aldrich) and cis-diammineplatinum(II)dichloride (Sigma-Aldrich) were dissolved in DMSO to yield a 20-mM (7 mg/ml) and a 15-mM (4.5 mg/ml) stock, respectively (freshly made). ETP (Sigma-Aldrich) and DOX (Sigma-Aldrich) were dissolved in DMSO to a stock concentration of 10 mM (6 mg/ml) and 5 mM, respectively, with aliquots stored at 4°C, protected from light. APH (Sigma-Aldrich) was dissolved in DMSO to yield a 3-mM stock, and aliquots were stored at −20°C. HU (Sigma-Aldrich) and MMC (Sigma-Aldrich) were prepared in double-distilled H_2O to obtain a 100-mM (7.6 mg/ml) and a 3-mM (1 mg/ml) stock (freshly made), respectively. MMS purchased as a 10-M solution was stored at 4°C. Hydrogen peroxide solution (H_2O_2) 35% by weight in H_2O (Sigma-Aldrich) was dissolved in double-distilled H_2O. UV irradiation was administered using a UV 254-nm lamp.

Cell cycle analysis

Asynchronous subconfluent cultures of U2OS cells were treated with the indicated dose of the genotoxic agents for 8, 24, and 48 h. Time point 0 h represents cell cycle distribution of nontreated cells. The cells were then trypsinized, collected, and spun down at 400 *g* for 5 min (using 12 × 75–mm falcon tubes). The cells were washed with 1–2 ml PBS and spun down at 400 *g* for 5 min. After discarding PBS, control and treated cells were fixed with 70% ethanol at 4°C (for ≥30 min), washed, digested with 100 µg/ml RNase A, stained with 25 µg/ml propidium iodide, subjected to flow microfluorimetry on a flow cytometer (FACScan; BD), and analyzed by the FlowJo software (Tree Star). Flow cytometric analysis for γ-H2AX/EdU/DAPI, cells were labeled for 30 min with 10 µM EdU, harvested, and fixed for 10 min with 4% formaldehyde/PBS. Cells were washed with 1% BSA/PBS, pH 7.4, permeabilized with 0.5% saponin/1% BSA/PBS, and stained with mouse anti–γ-H2AX antibody (05-636; EMD Millipore) for 2 h followed by incubation with a suitable secondary antibody for 30 min. Incorporated EdU was labeled according to the manufacturer's instructions (Invitrogen). DNA was stained with 1 µg/ml DAPI. Samples were measured on a flow cytometer (CyAn ADP; Beckman Coulter) and analyzed with Summit software v4.3 (Beckman Coulter).

Immunofluorescence microscopy

Cells were grown on coverslips in 10 µM BrdU for 48 h before the treatment with drugs. Cells were then treated with the aforementioned drugs for 1 h. After treatment, cells were washed with PBS and preextracted (25 mM Hepes, pH 7.4, 50 mM NaCl, 1 mM EDTA, 3 mM $MgCl_2$, 300 mM sucrose, and 0.5% Triton X-100) on ice. Cells were then fixed using 4% formaldehyde for 15 min at RT. Fixed cells were then incubated with primary antibodies against BrdU mouse (347580; BD) and γ-H2AX rabbit (9718; Cell Signaling Technology) in a moist chamber for 1 h. Cells were incubated with secondary antibodies (anti–mouse 488 [A11029; Invitrogen] and anti–rabbit 594 [A11037; Invitrogen]) in a moist chamber for 1 h. For RAD51 and EdU, coverslips were preextracted in preextraction buffer (80 mM NaCl and 3 mM $MgCl_2$) and fixed with 4% paraformaldehyde in PBS followed by permeabilization with 0.5% Triton X-100 in PBS. Subsequently, Click-iT reaction was performed using the manufacturer's protocol (Invitrogen). Next, cells were blocked in 1% BSA and incubated with primary antibody against RAD51 rabbit (gift from F. Esashi, Sir William Dunn School of Pathology, University of Oxford, Oxford, England, UK) in a moist chamber. Coverslips were then incubated with secondary antibody (anti–rabbit 594; A11037). Coverslips were then washed with PBS, mounted with 4 µl Vectashield/DAPI, and sealed with nail polish. Cells were washed between all steps.

Microscopy was performed with a fluorescence microscope (DMRB; Leica; objective lenses: HCX Plan Apochromat 63×/1.40-0.60 NA oil) and acquired with a camera (DFC 360FX; Leica). The images were processed with Leica Application Suite Version 3.3.0.

Cell proliferation and viability

CellTiter blue reagent was used to estimate the number of viable cells present in multiwell plates after treating 2,000 cells/well with the doses of the genotoxic agents indicated in Fig. S1. 20 µl of CellTiter blue reagent was added to 100 µl of medium in the 96-well plate followed by incubation for 3 h at 37°C. The fluorescent signal was measured by recording fluorescence (560 nm$(20)_{Ex}$/590 nm$(10)_{Em}$) using a plate reader (Fluoroskan Ascent; Labsystems).

Human fork progression by DNA fiber analysis

The procedure was essentially performed according to Jackson and Pombo (1998), with previously described modifications (Ray Chaudhuri et al., 2012). In brief, asynchronously growing U2OS cells were labeled with

Published March 2, 2015

30 µM chlorodeoxyuridine (CldU; Sigma-Aldrich), a thymidine analogue, for 30 min, washed twice with PBS, treated with appropriate dosage with any of the genotoxic agents (or nontreated as control), and exposed to 250 µM 5-iodo-2′-deoxyuridine (IdU). The cells were quickly trypsinized and resuspended in PBS at 2.5 × 10^5 cells/ml. The labeled cells were diluted 1:8 with unlabeled cells, and 2.5 µl of cells were mixed with 7.5 µl of lysis buffer (200 mM Tris-HCl, pH 7.5, 50 mM EDTA, and 0.5% [wt/vol] SDS) on a glass slide. After 9 min, the slides were tilted at 15–45°, and the resulting DNA spreads were air dried, fixed in 3:1 methanol/acetic acid, and refrigerated overnight. The DNA fibers were denatured with 2.5 M HCl for 1 h, washed with PBS, and blocked with 2% BSA in PBST (PBS and Tween 20) for 40 min. The newly replicated CldU and IdU tracks were labeled (for 2.5 h in the dark, at RT) with anti-BrdU antibodies recognizing CldU (rat; Abcam) and IdU mouse (BD), respectively. After washing for 5 × 3 min in PBST (0.2%), the following secondary antibodies were used (incubated for 1 h in the dark, at RT): anti–mouse Alexa Fluor 488 (Molecular Probes) and anti–rat Cy3 (Jackson ImmunoResearch Laboratories, Inc.). After washing for 5 × 3 min in PBST (0.2%), the slides were air dried completely, mounted with 20 µl/slide Antifade gold (Invitrogen), and sealed to a coverslip by transparent nail polish. Microscopy was performed with a fluorescence microscope (IX81; Olympus; objective lenses: LC Plan Fluor 60×, 1.42 NA oil) and acquired with a charge-coupled device camera (Orca AG; Hamamatsu Photonics). The images were processed with CellR software (version2.6; Olympus). Statistical analysis of track length was performed using Prism (GraphPad Software). The significance of the difference between the means was determined by *t* test or by one-way analysis of variance (ANOVA).

DSB detection by PFGE

The procedure was essentially performed as previously described (Ray Chaudhuri et al., 2012). Asynchronous subconfluent cultures of U2OS cells were treated with defined doses of the genotoxic agents for 1 h. Cells were harvested by trypsinization, and agarose plugs of 2.5 × 10^5 cells were prepared in a disposable plug mold (Bio-Rad Laboratories). Plugs were then incubated in lysis buffer (100 mM EDTA, 1% [wt/vol] sodium lauroyl sarcosinate, 0.2% [wt/vol] sodium deoxycholate, and 1 mg/ml proteinase K) at 37°C for 72 h. Plugs were then washed four times in 20 mM Tris-HCl, pH 8.0, and 50 mM EDTA before loading onto an agarose gel. Electrophoresis was performed for 21 h at 14°C in 0.9% (wt/vol) Pulse Field Certified Agarose (Bio-Rad Laboratories) containing Tris-borate/EDTA buffer in a PFGE apparatus (CHEF DR III; Bio-Rad Laboratories), according to the following protocol (block I: 9 h, 120° included angle, 5.5 V/cm, 30 to 18-s switch; block II: 6 h, 117° included angle, 4.5 V/cm, 18 to 9-s switch; block III: 6 h, 112° included angle, 4.0 V/cm, 9 to 5-s switch). The gel was then stained with ethidium bromide and analyzed by the AlphaImager system (ProteinSimple). Relative DSB levels were assessed by comparing DSB signals for each treatment to the background levels observed in untreated conditions. Statistical analysis was performed using Prism. The significance was determined by using two-way ANOVA.

Protein extraction and Western blotting

Levels of intracellular pATM, pCHK1, pKAP1, and pRPA proteins were determined by Western blot analysis of cell extracts. Mammalian cell extracts were prepared in Laemmli sample buffer (4% SDS, 20% glycerol, and 120 mM Tris-HCl, pH 6.8). 50 µg total protein from cell isolates was loaded onto 9% polyacrylamide gel. Proteins were separated electrophoretically at 12 mA (for one gel; two gels at 24 mA) for 15–30 min and then at 18 mA until the end (for one gel; two gels at 36 mA) followed by transferring the proteins to Immobilon-P membrane (Thermo Fisher Scientific) for 2 h at 100 V (4°C) in a transfer buffer (25 mM Tris and 192 mM glycine) containing 15% methanol. Before addition of primary antibodies, membranes were blocked for 1 h in TBS containing 0.1% Tween 20 and 2% ECL blocking solution (GE Healthcare). Membranes were probed for pATM, total ATM, pChk1, total Chk1, pKAP1, total KAP1, RPA32 (S4/S8), total RPA, Rad51, RecQ1, β-Tubulin (loading control), and TFIIH (loading control). ATM p1981 rabbit (2152-1; Epitomics), ATM (2C1) mouse (GTX70103; GeneTex), CHK1 pS345 rabbit (2348; Cell Signaling Technology), CHK1 mouse (sc-8408; Santa Cruz Biotechnology, Inc.), KAP1 pS824 rabbit (A300-767A; Bethyl Laboratories, Inc.), KAP1 rabbit (A300-274A; Bethyl Laboratories, Inc.), phospho-RPA32 (S4/S8) rabbit (A300-245A; Bethyl Laboratories, Inc.), RPA32 rabbit (A300-244A; Bethyl Laboratories, Inc.), RAD51 (H-92) rabbit (sc-8349; Santa Cruz Biotechnology, Inc.), RECQ1 rabbit (NB100-618; Novus Biologicals), β-Tubulin (H-235) rabbit (sc-9104; Santa Cruz Biotechnology, Inc.), and TFIIH p89 rabbit (S-19; sc-293; Santa Cruz Biotechnology, Inc.). Secondary antibodies were ECL anti–mouse/rabbit IgG and horseradish peroxidase–linked whole antibody from sheep (GE Healthcare). The membrane was then exposed to an ECL system (detection reagent final volume equivalent to 0.125-ml/cm^2 membrane; GE Healthcare), and a charge-coupled device image analyzer was used to visualize immunoreactive bands.

EM analysis of DNA RIs in human cells

The procedure was essentially performed as previously described (Neelsen et al., 2014). Asynchronous subconfluent cultures of U2OS cells were treated with defined doses of the genotoxic agents for 1 h. In vivo psoralen cross-linking of the DNA was achieved by a repetitive exposure of living cells to 4,5′,8-trimethylpsoralen (10 µg/ml final concentration) followed by irradiation pulses with UV 365-nm monochromatic light (UV Stratalinker 1800; Agilent Technologies). The cells were then lysed with cell lysis buffer (buffer C1: 1.28 M sucrose, 40 mM Tris-Cl, pH 7.5, 20 mM $MgCl_2$, and 4% Triton X-100; QIAGEN) and then digested by digestion buffer (QIAGEN buffer G2: 800 mM guanidine–HCl, 30 mM Tris–HCl, pH 8.0, 30 mM EDTA, pH 8.0, 5% Tween 20, and 0.5% Triton X-100) and 1 mg/ml proteinase K at 50°C for 2 h. Chloroform/Isoamyl alcohol (24:1) was used to collect DNA via phase separation (centrifugation at 8,000 rpm for 20 min) followed by DNA precipitation by adding 0.7× volume of isopropanol. The DNA was then washed with 70% ethanol, air dried, and resuspended in 200 µl TE (Tris-EDTA) buffer. 100 U restriction enzyme PvuII high-fidelity was used for 12 µg mammalian genomic DNA digestion (4–5-h incubation). Poly-Prep chromatography columns were used for RI enrichment. Benzoylated naphthoylated DEAE–cellulose granules were resuspended in 10 mM Tris-HCl, pH 8.0, and 300 mM NaCl to a final concentration of 0.1 g/ml. The columns were washed and equilibrated with 10 mM Tris-HCl, pH 8.0, and 1 M NaCl and 10 mM Tris-HCl, pH 8.0, and 300 mM NaCl, respectively. The sample DNA was then loaded and incubated for 0.5 h. After washing the columns (10 mM Tris-HCl, pH 8.0, and 1 M NaCl), the DNA was eluted in caffeine solution (10 mM Tris-HCl, pH 8.0, 1 M NaCl, and 1.8% [wt/vol] caffeine) for 10 min followed by sample collection. DNA is then purified and concentrated, using an Amicon size-exclusion column and resuspended in TE. With DNA spreading by the "BAC method," the DNA was loaded on carbon-coated 400-mesh copper grids. The DNA was then coated with platinum by platinum-carbon rotary shadowing (High Vacuum Evaporator MED 020; Bal-Tec). Microscopy was performed with a transmission electron microscope (Tecnai G2 Spirit; FEI; LaB6 filament; high tension ≤120 kV) and acquired with a side mount charge-coupled device camera (2,600 × 4,000 pixels; Orius 1000; Gatan, Inc.). The images were processed with DigitalMicrograph Version 1.83.842 (Gatan, Inc.) and analyzed with ImageJ (National Institutes of Health).

iPOND

iPOND was essentially performed as originally described (Sirbu et al., 2011, 2012) with minor modifications. HEK293T cells were labeled with 10 µM EdU (Life Technologies) and treated with the different drugs as indicated. For the pulse-chase experiments with thymidine, cells were washed with cell culture medium and incubated for 45 min in medium supplemented with 10 µM thymidine (Sigma-Aldrich). Then, the cells were cross-linked with 1% formaldehyde for 15 min at RT, quenched with 0.125 M glycine for 5 min, and washed three times with PBS. For the conjugation of EdU with biotin azide, cells were permeabilized with 0.25% Triton X-100/PBS, washed twice with PBS, and incubated in click reaction buffer (10 mM sodium-L-ascorbate, 20 µM biotin azide [Life Technologies], and 2 mM $CuSO_4$) for 1 h at RT. DMSO was used instead of biotin azide for the "no click" control. Cells were washed twice with PBS, resuspended in lysis buffer (50 mM Tris-HCl, pH 8.0, and 1% SDS) supplemented with protease inhibitors (Sigma-Aldrich), and chromatin was solubilized by sonication in a Bioruptor (Diagenode) at 4°C at the highest setting for 10 min (30 s on and 45 s off cycles). After centrifugation for 30 min at 14,000 rpm, supernatants were diluted with 1:1 PBS (vol/vol) containing protease inhibitors and incubated overnight with streptavidin-agarose beads (EMD Millipore). Beads were washed once with lysis buffer, once with 1 M NaCl, twice with lysis buffer, and once with PBS, and captured proteins were eluted by boiling beads in 2× NuPAGE LDS Sample Buffer (Life Technologies) containing 100 mM DTT for 30 min at 95°C. Proteins were resolved by electrophoresis using NuPAGE Novex 4–12% Bis-Tris gels and detected by Western blotting with the indicated antibodies: RAD51 rabbit polyclonal (1:1,000; H92; Sigma-Aldrich), proliferating cell nuclear antigen mouse monoclonal (F2; 1:2,000; Sigma-Aldrich), RPA32 mouse monoclonal (NA19L; 1:1,000; EMD Millipore), RPA32-S4/S8 rabbit polyclonal (A300-245A; 1:1,000; Bethyl Laboratories), γ-H2AX–S139 rabbit

Published March 2, 2015

monoclonal (1:1,000; 20E3; Cell Signaling Technology), and H3 rabbit polyclonal (1:1,000; ab1791; Abcam).

Online supplemental material

Fig. S1 shows cell proliferation (CellTiter blue) and cell cycle analyses (FACS) performed to identify mild doses of different genotoxic treatments interfering with DNA replication but not significantly affecting cell survival. Fig. S2 shows frequency and size of ssDNA gaps arising on replicated duplexes of U2OS or RPE-1 cells upon different genotoxic treatments. Fig. S3 shows control experiments for the frequency of reversed forks, the size of the regressed arms, and their possible exposure of ssDNA at forks reversed by different genotoxic stresses, providing examples of different categories of reversed forks. Fig. S4 shows Western blot and PFGE analyses upon genotoxic treatments at different doses and complement similar observations published in Figs. 1 and 5. Fig. S5 includes checkpoint activation and ssDNA gap accumulation in RECQ1-depleted cells, the labeling scheme for the iPOND experiments, cell cycle profiles upon progressive RAD51 depletion, and the dependency on RAD51 of reversed forks accumulating in RECQ1-depleted cells. Online supplemental material is available at http://www.jcb.org/cgi/content/full/jcb.201406099/DC1.

We thank the Center for Microscopy and Image Analysis of the University of Zurich for technical assistance with EM. We are grateful to F. Esashi for sharing multiple reagents, to R. Santoro for indirect support, to K. Neelsen for critical reading of the manuscript, and to all current and past members of the Lopes group for useful discussions.

This work was supported by the Swiss National Science Foundation grant 31003A_146924 to M. Lopes and by the National Institutes of Health grant R01GM108648 to A. Vindigni.

The authors declare no competing financial interests.

Submitted: 24 June 2014
Accepted: 26 January 2015

References

Adelman, C.A., R.L. Lolo, N.J. Birkbak, O. Murina, K. Matsuzaki, Z. Horejsi, K. Parmar, V. Borel, J.M. Skehel, G. Stamp, et al. 2013. HELQ promotes RAD51 paralogue-dependent repair to avert germ cell loss and tumorigenesis. *Nature*. 502:381–384. http://dx.doi.org/10.1038/nature12565

Alabert, C., J.C. Bukowski-Wills, S.B. Lee, G. Kustatscher, K. Nakamura, F. de Lima Alves, P. Menard, J. Mejlvang, J. Rappsilber, and A. Groth. 2014. Nascent chromatin capture proteomics determines chromatin dynamics during DNA replication and identifies unknown fork components. *Nat. Cell Biol.* 16:281–293. http://dx.doi.org/10.1038/ncb2918

Arlt, M.F., T.E. Wilson, and T.W. Glover. 2012. Replication stress and mechanisms of CNV formation. *Curr. Opin. Genet. Dev.* 22:204–210. http://dx.doi.org/10.1016/j.gde.2012.01.009

Ball, H.L., J.S. Myers, and D. Cortez. 2005. ATRIP binding to replication protein A-single-stranded DNA promotes ATR-ATRIP localization but is dispensable for Chk1 phosphorylation. *Mol. Biol. Cell*. 16:2372–2381. http://dx.doi.org/10.1091/mbc.E04-11-1006

Bermejo, R., T. Capra, R. Jossen, A. Colosio, C. Frattini, W. Carotenuto, A. Cocito, Y. Doksani, H. Klein, B. Gómez-González, et al. 2011. The replication checkpoint protects fork stability by releasing transcribed genes from nuclear pores. *Cell*. 146:233–246. http://dx.doi.org/10.1016/j.cell.2011.06.033

Berti, M., A. Ray Chaudhuri, S. Thangavel, S. Gomathinayagam, S. Kenig, M. Vujanovic, F. Odreman, T. Glatter, S. Graziano, R. Mendoza-Maldonado, et al. 2013. Human RECQ1 promotes restart of replication forks reversed by DNA topoisomerase I inhibition. *Nat. Struct. Mol. Biol.* 20:347–354. http://dx.doi.org/10.1038/nsmb.2501

Bétous, R., A.C. Mason, R.P. Rambo, C.E. Bansbach, A. Badu-Nkansah, B.M. Sirbu, B.F. Eichman, and D. Cortez. 2012. SMARCAL1 catalyzes fork regression and Holliday junction migration to maintain genome stability during DNA replication. *Genes Dev.* 26:151–162. http://dx.doi.org/10.1101/gad.178459.111

Bétous, R., F.B. Couch, A.C. Mason, B.F. Eichman, M. Manosas, and D. Cortez. 2013. Substrate-selective repair and restart of replication forks by DNA translocases. *Cell Reports*. 3:1958–1969. http://dx.doi.org/10.1016/j.celrep.2013.05.002

Blastyák, A., I. Hajdú, I. Unk, and L. Haracska. 2010. Role of double-stranded DNA translocase activity of human HLTF in replication of damaged DNA. *Mol. Cell. Biol.* 30:684–693. http://dx.doi.org/10.1128/MCB.00863-09

Bouwman, P., and J. Jonkers. 2012. The effects of deregulated DNA damage signalling on cancer chemotherapy response and resistance. *Nat. Rev. Cancer*. 12:587–598. http://dx.doi.org/10.1038/nrc3342

Bugreev, D.V., M.J. Rossi, and A.V. Mazin. 2011. Cooperation of RAD51 and RAD54 in regression of a model replication fork. *Nucleic Acids Res.* 39:2153–2164. http://dx.doi.org/10.1093/nar/gkq1139

Burkovics, P., M. Sebesta, D. Balogh, L. Haracska, and L. Krejci. 2014. Strand invasion by HLTF as a mechanism for template switch in fork rescue. *Nucleic Acids Res.* 42:1711–1720. http://dx.doi.org/10.1093/nar/gkt1040

Ciccia, A., A.V. Nimonkar, Y. Hu, I. Hajdu, Y.J. Achar, L. Izhar, S.A. Petit, B. Adamson, J.C. Yoon, S.C. Kowalczykowski, et al. 2012. Polyubiquitinated PCNA recruits the ZRANB3 translocase to maintain genomic integrity after replication stress. *Mol. Cell*. 47:396–409. http://dx.doi.org/10.1016/j.molcel.2012.05.024

Deans, A.J., and S.C. West. 2011. DNA interstrand crosslink repair and cancer. *Nat. Rev. Cancer*. 11:467–480. http://dx.doi.org/10.1038/nrc3088

Farmer, H., N. McCabe, C.J. Lord, A.N. Tutt, D.A. Johnson, T.B. Richardson, M. Santarosa, K.J. Dillon, I. Hickson, C. Knights, et al. 2005. Targeting the DNA repair defect in BRCA mutant cells as a therapeutic strategy. *Nature*. 434:917–921. http://dx.doi.org/10.1038/nature03445

Gari, K., C. Décaillet, A.Z. Stasiak, A. Stasiak, and A. Constantinou. 2008. The Fanconi anemia protein FANCM can promote branch migration of Holliday junctions and replication forks. *Mol. Cell*. 29:141–148. http://dx.doi.org/10.1016/j.molcel.2007.11.032

Ge, X.Q., and J.J. Blow. 2010. Chk1 inhibits replication factory activation but allows dormant origin firing in existing factories. *J. Cell Biol.* 191:1285–1297. http://dx.doi.org/10.1083/jcb.201007074

Hashimoto, Y., A. Ray Chaudhuri, M. Lopes, and V. Costanzo. 2010. Rad51 protects nascent DNA from Mre11-dependent degradation and promotes continuous DNA synthesis. *Nat. Struct. Mol. Biol.* 17:1305–1311. http://dx.doi.org/10.1038/nsmb.1927

Higgins, N.P., K. Kato, and B. Strauss. 1976. A model for replication repair in mammalian cells. *J. Mol. Biol.* 101:417–425. http://dx.doi.org/10.1016/0022-2836(76)90156-X

Hoeijmakers, J.H. 2009. DNA damage, aging, and cancer. *N. Engl. J. Med.* 361:1475–1485. http://dx.doi.org/10.1056/NEJMra0804615

Jackson, D.A., and A. Pombo. 1998. Replicon clusters are stable units of chromosome structure: evidence that nuclear organization contributes to the efficient activation and propagation of S phase in human cells. *J. Cell Biol.* 140:1285–1295. http://dx.doi.org/10.1083/jcb.140.6.1285

Kanagaraj, R., N. Saydam, P.L. Garcia, L. Zheng, and P. Janscak. 2006. Human RECQ5β helicase promotes strand exchange on synthetic DNA structures resembling a stalled replication fork. *Nucleic Acids Res.* 34:5217–5231. http://dx.doi.org/10.1093/nar/gkl677

Kerrigan, D., Y. Pommier, and K.W. Kohn. 1987. Protein-linked DNA strand breaks produced by etoposide and teniposide in mouse L1210 and human VA-13 and HT-29 cell lines: relationship to cytotoxicity. *NCI Monogr.* 4:117–121.

Kumar, A., M. Mazzanti, M. Mistrik, M. Kosar, G.V. Beznoussenko, A.A. Mironov, M. Garrè, D. Parazzoli, G.V. Shivashankar, G. Scita, et al. 2014. ATR mediates a checkpoint at the nuclear envelope in response to mechanical stress. *Cell*. 158:633–646. http://dx.doi.org/10.1016/j.cell.2014.05.046

León-Ortiz, A.M., J. Svendsen, and S.J. Boulton. 2014. Metabolism of DNA secondary structures at the eukaryotic replication fork. *DNA Repair (Amst.)*. 19:152–162. http://dx.doi.org/10.1016/j.dnarep.2014.03.016

Lonskaya, I., V.N. Potaman, L.S. Shlyakhtenko, E.A. Oussatcheva, Y.L. Lyubchenko, and V.A. Soldatenkov. 2005. Regulation of poly(ADP-ribose) polymerase-1 by DNA structure-specific binding. *J. Biol. Chem.* 280:17076–17083. http://dx.doi.org/10.1074/jbc.M413483200

Lopes, M., C. Cotta-Ramusino, A. Pellicioli, G. Liberi, P. Plevani, M. Muzi-Falconi, C.S. Newlon, and M. Foiani. 2001. The DNA replication checkpoint response stabilizes stalled replication forks. *Nature*. 412:557–561. http://dx.doi.org/10.1038/35087613

Lopes, M., M. Foiani, and J.M. Sogo. 2006. Multiple mechanisms control chromosome integrity after replication fork uncoupling and restart at irreparable UV lesions. *Mol. Cell*. 21:15–27. http://dx.doi.org/10.1016/j.molcel.2005.11.015

Lossaint, G., M. Larroque, C. Ribeyre, N. Bec, C. Larroque, C. Décaillet, K. Gari, and A. Constantinou. 2013. FANCD2 binds MCM proteins and controls replisome function upon activation of s phase checkpoint signaling. *Mol. Cell*. 51:678–690. http://dx.doi.org/10.1016/j.molcel.2013.07.023

Machwe, A., L. Xiao, J. Groden, and D.K. Orren. 2006. The Werner and Bloom syndrome proteins catalyze regression of a model replication fork. *Biochemistry*. 45:13939–13946. http://dx.doi.org/10.1021/bi0615487

Madaan, K., D. Kaushik, and T. Verma. 2012. Hydroxyurea: a key player in cancer chemotherapy. *Expert Rev. Anticancer Ther.* 12:19–29. http://dx.doi.org/10.1586/era.11.175

Michaelis, M., J. Cinatl, J.U. Vogel, P. Pouckova, P.H. Driever, and J. Cinatl. 2001. Treatment of drug-resistant human neuroblastoma cells with cyclodextrin inclusion complexes of aphidicolin. *Anticancer Drugs*. 12:467–473. http://dx.doi.org/10.1097/00001813-200106000-00008

Published March 2, 2015

Murina, O., C. von Aesch, U. Karakus, L.P. Ferretti, H.A. Bolck, K. Hänggi, and A.A. Sartori. 2014. FANCD2 and CtIP cooperate to repair DNA interstrand crosslinks. *Cell Reports*. 7:1030–1038. http://dx.doi.org/10.1016/j.celrep.2014.03.069

Nam, E.A., and D. Cortez. 2011. ATR signalling: more than meeting at the fork. *Biochem. J.* 436:527–536. http://dx.doi.org/10.1042/BJ20102162

Neelsen, K.J., and M. Lopes. 2015. Replication fork reversal in eukaryotes: from dead end to dynamic response. *Nat. Rev. Mol. Cell Biol.* In press.

Neelsen, K.J., I.M. Zanini, R. Herrador, and M. Lopes. 2013a. Oncogenes induce genotoxic stress by mitotic processing of unusual replication intermediates. *J. Cell Biol.* 200:699–708. http://dx.doi.org/10.1083/jcb.201212058

Neelsen, K.J., I.M. Zanini, S. Mijic, R. Herrador, R. Zellweger, A. Ray Chaudhuri, K.D. Creavin, J.J. Blow, and M. Lopes. 2013b. Deregulated origin licensing leads to chromosomal breaks by rereplication of a gapped DNA template. *Genes Dev.* 27:2537–2542. http://dx.doi.org/10.1101/gad.226373.113

Neelsen, K.J., A.R. Chaudhuri, C. Follonier, R. Herrador, and M. Lopes. 2014. Visualization and interpretation of eukaryotic DNA replication intermediates in vivo by electron microscopy. *Methods Mol. Biol.* 1094:177–208. http://dx.doi.org/10.1007/978-1-62703-706-8_15

Oakley, G.G., and S.M. Patrick. 2010. Replication protein A: directing traffic at the intersection of replication and repair. *Front Biosci (Landmark Ed)*. 15:883–900. http://dx.doi.org/10.2741/3652

Petermann, E., and T. Helleday. 2010. Pathways of mammalian replication fork restart. *Nat. Rev. Mol. Cell Biol.* 11:683–687. http://dx.doi.org/10.1038/nrm2974

Petermann, E., M.L. Orta, N. Issaeva, N. Schultz, and T. Helleday. 2010. Hydroxyurea-stalled replication forks become progressively inactivated and require two different RAD51-mediated pathways for restart and repair. *Mol. Cell*. 37:492–502. http://dx.doi.org/10.1016/j.molcel.2010.01.021

Pines, A., L.H. Mullenders, H. van Attikum, and M.S. Luijsterburg. 2013. Touching base with PARPs: moonlighting in the repair of UV lesions and double-strand breaks. *Trends Biochem. Sci.* 38:321–330. http://dx.doi.org/10.1016/j.tibs.2013.03.002

Pommier, Y. 2013. Drugging topoisomerases: lessons and challenges. *ACS Chem. Biol.* 8:82–95. http://dx.doi.org/10.1021/cb300648v

Ralf, C., I.D. Hickson, and L. Wu. 2006. The Bloom's syndrome helicase can promote the regression of a model replication fork. *J. Biol. Chem.* 281:22839–22846. http://dx.doi.org/10.1074/jbc.M604268200

Ray Chaudhuri, A., Y. Hashimoto, R. Herrador, K.J. Neelsen, D. Fachinetti, R. Bermejo, A. Cocito, V. Costanzo, and M. Lopes. 2012. Topoisomerase I poisoning results in PARP-mediated replication fork reversal. *Nat. Struct. Mol. Biol.* 19:417–423. http://dx.doi.org/10.1038/nsmb.2258

Recolin, B., S. Van der Laan, and D. Maiorano. 2012. Role of replication protein A as sensor in activation of the S-phase checkpoint in *Xenopus* egg extracts. *Nucleic Acids Res.* 40:3431–3442. http://dx.doi.org/10.1093/nar/gkr1241

Rouleau, M., A. Patel, M.J. Hendzel, S.H. Kaufmann, and G.G. Poirier. 2010. PARP inhibition: PARP1 and beyond. *Nat. Rev. Cancer*. 10:293–301. http://dx.doi.org/10.1038/nrc2812

Schlacher, K., N. Christ, N. Siaud, A. Egashira, H. Wu, and M. Jasin. 2011. Double-strand break repair-independent role for BRCA2 in blocking stalled replication fork degradation by MRE11. *Cell*. 145:529–542. http://dx.doi.org/10.1016/j.cell.2011.03.041

Schlacher, K., H. Wu, and M. Jasin. 2012. A distinct replication fork protection pathway connects Fanconi anemia tumor suppressors to RAD51-BRCA1/2. *Cancer Cell*. 22:106–116. http://dx.doi.org/10.1016/j.ccr.2012.05.015

Shiotani, B., H.D. Nguyen, P. Håkansson, A. Maréchal, A. Tse, H. Tahara, and L. Zou. 2013. Two distinct modes of ATR activation orchestrated by Rad17 and Nbs1. *Cell Reports*. 3:1651–1662. http://dx.doi.org/10.1016/j.celrep.2013.04.018

Sirbu, B.M., F.B. Couch, J.T. Feigerle, S. Bhaskara, S.W. Hiebert, and D. Cortez. 2011. Analysis of protein dynamics at active, stalled, and collapsed replication forks. *Genes Dev.* 25:1320–1327. http://dx.doi.org/10.1101/gad.2053211

Sirbu, B.M., F.B. Couch, and D. Cortez. 2012. Monitoring the spatiotemporal dynamics of proteins at replication forks and in assembled chromatin using isolation of proteins on nascent DNA. *Nat. Protoc.* 7:594–605. http://dx.doi.org/10.1038/nprot.2012.010

Sogo, J.M., M. Lopes, and M. Foiani. 2002. Fork reversal and ssDNA accumulation at stalled replication forks owing to checkpoint defects. *Science*. 297:599–602. http://dx.doi.org/10.1126/science.1074023

Sugimura, K., S. Takebayashi, H. Taguchi, S. Takeda, and K. Okumura. 2008. PARP-1 ensures regulation of replication fork progression by homologous recombination on damaged DNA. *J. Cell Biol.* 183:1203–1212. http://dx.doi.org/10.1083/jcb.200806068

Suwaki, N., K. Klare, and M. Tarsounas. 2011. RAD51 paralogs: roles in DNA damage signalling, recombinational repair and tumorigenesis. *Semin. Cell Dev. Biol.* 22:898–905. http://dx.doi.org/10.1016/j.semcdb.2011.07.019

Symington, L.S., and J. Gautier. 2011. Double-strand break end resection and repair pathway choice. *Annu. Rev. Genet.* 45:247–271. http://dx.doi.org/10.1146/annurev-genet-110410-132435

Thangavel, S., M. Berti, M. Levikova, C. Pinto, S. Gomathinayagam, M. Vujanovic, R. Zellweger, H. Moore, E.H. Lee, E.A. Hendrickson, P. Cejka, S. Stewart, M. Lopes, and A. Vindigni. 2015. DNA2 drives processing and restart of reversed replication forks in human cells. *J. Cell Biol.* 208:545–562.

Willis, N.A., G. Chandramouly, B. Huang, A. Kwok, C. Follonier, C. Deng, and R. Scully. 2014. BRCA1 controls homologous recombination at Tus/Ter-stalled mammalian replication forks. *Nature*. 510:556–559. http://dx.doi.org/10.1038/nature13295

Yeo, J.E., E.H. Lee, E.A. Hendrickson, and A. Sobeck. 2014. CtIP mediates replication fork recovery in a FANCD2-regulated manner. *Hum. Mol. Genet.* 23:3695–3705. http://dx.doi.org/10.1093/hmg/ddu078

Zeman, M.K., and K.A. Cimprich. 2014. Causes and consequences of replication stress. *Nat. Cell Biol.* 16:2–9. http://dx.doi.org/10.1038/ncb2897

Zou, L., and S.J. Elledge. 2003. Sensing DNA damage through ATRIP recognition of RPA-ssDNA complexes. *Science*. 300:1542–1548. http://dx.doi.org/10.1126/science.1083430

Zwelling, L.A., S. Michaels, L.C. Erickson, R.S. Ungerleider, M. Nichols, and K.W. Kohn. 1981. Protein-associated deoxyribonucleic acid strand breaks in L1210 cells treated with the deoxyribonucleic acid intercalating agents 4′-(9-acridinylamino) methanesulfon-m-anisidide and adriamycin. *Biochemistry*. 20:6553–6563. http://dx.doi.org/10.1021/bi00526a006

Zellweger et al., http://www.jcb.org/cgi/content/full/jcb.201406099/DC1

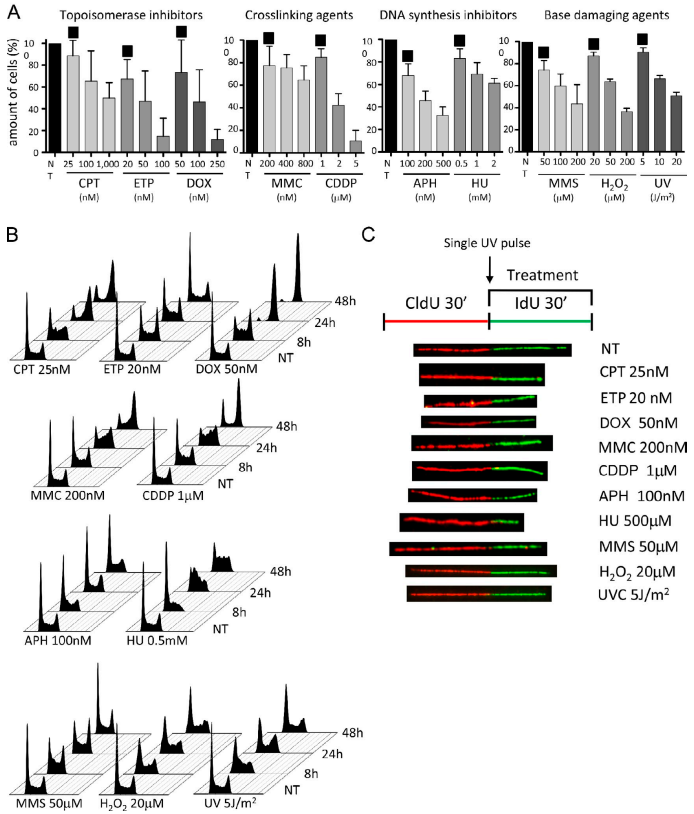

Figure S1. **Selection of sublethal doses of genotoxic treatments that interfere with DNA replication in human cells.** (A) Cell survival and proliferation was assessed by CellTiter blue assay (see Materials and methods). The number of living U2OS cells was measured 72 h after treatment with different doses of the indicated genotoxic treatments. Drugs were maintained for 1 h followed by washing with PBS and addition of fresh media to the cells. Error bars indicate standard deviations from three independent experiments. The black square indicates the sublethal dose of each treatment selected for further studies. (B) FACS analysis of cell cycle progression (DNA content, detected by propidium iodide staining) in U2OS cell treated with the selected dose (see A) of different genotoxic agents for the indicated time. For UV, cells were given a single pulse of 5 J/m^2 and then assessed at the indicated time points. (C) DNA fiber spreading labeling protocol of mock- or genotoxin-treated U2OS cells (see Materials and methods). CldU/IdU-containing tracks were immunostained in red and green, respectively. One representative fiber per experiment is shown. NT, not treated.

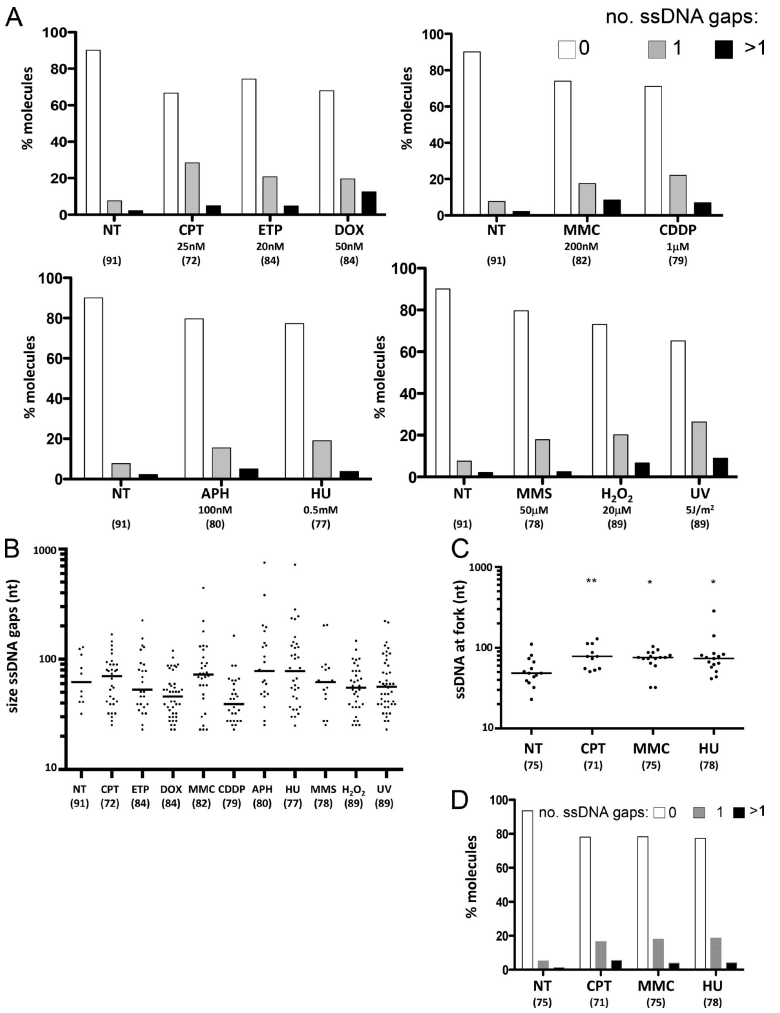

Figure S2. **Accumulation of ssDNA gaps on replicated duplexes upon different genotoxic treatments in human cells.** (A) Frequency of molecules containing no ssDNA gaps, one ssDNA gap, or more than one ssDNA gap along replicated duplexes (Fig. 2 C, white arrow) in not treated (NT) U2OS cells and upon the indicated treatments (UV pulse or 1-h treatment). Similar results were obtained in one independent experiment. (B) Graphical distribution of the size of ssDNA gaps along replicated duplexes for the same sets of molecules analyzed in A. The lines show the median of the ssDNA gap size in the specific set of analyzed molecules. Similar results were obtained in one independent experiment. In brackets, the total number of analyzed molecules is given. (C) Graphical distribution of ssDNA length at the junction in untreated RPE-1 cells and upon 25 nM CPT, 200 nM MMC, and 0.5 mM HU treatments. Only molecules with detectable ssDNA stretches are included in the analysis. The lines show the median length of the ssDNA region at the fork in the specific set of analyzed molecules. In brackets, the total number of analyzed molecules is given. (D) Frequency of molecules containing no ssDNA gaps, one ssDNA gap, or more than one ssDNA gap along replicated duplexes (Fig. 2 C, white arrow) in untreated RPE-1 cells and upon the indicated 25 nM CPT, 200 nM MMC, and 0.5 mM HU treatments. In brackets, the total number of analyzed molecules is given.

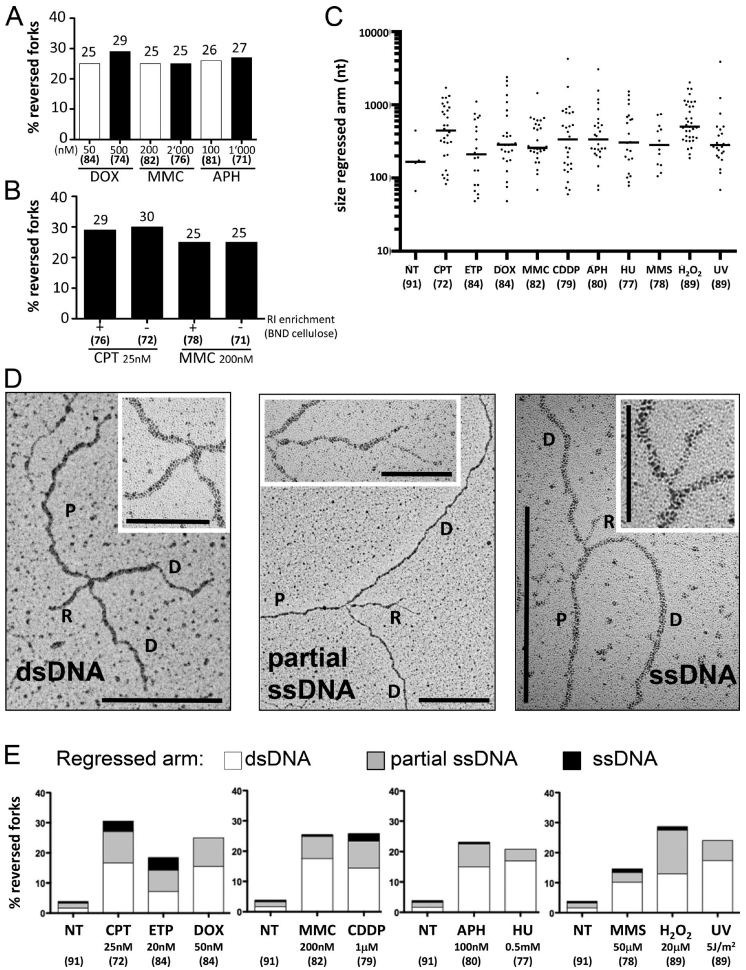

Figure S3. **Dose–response, enrichment independency, and molecular architecture of reversed forks induced by different genotoxic treatments.** (A) Frequency of reversed replication forks in U2OS cells treated with 50 nM or 500 nM DOX, 200 nM or 2 µM MMC, and 100 nM or 1 µM APH. (B) Frequency of reversed forks in U2OS cells with/without RI enrichment procedure (benzoylated naphthoylated DEAE–cellulose; Neelsen et al., 2014) treated upon 25 nM CPT and 200 nM MMC. In A and B, the total number of analyzed molecules is in brackets. Above each column, the percentage of reversed forks is indicated. (C) Graphical distribution of regressed arm length (in nucleotides) for the same sets of molecules analyzed in Fig. 3 B. The line shows the median length of the regressed arms in the specific set of analyzed molecules. Similar results were obtained in at least one independent experiment. In brackets, the total number of analyzed molecules is given. (D) Electron micrographs of representative reversed replication forks on genomic DNA from U2OS cells, after 1-h treatment with 50 µM MMS, 100 nM APH, and 500 µM HU (left to right). The left micrograph represents a fork with a fully double-stranded regressed arm (dsDNA); in the middle a reversed fork with a partially single-stranded regressed arm (partial ssDNA); the right micrograph shows a fork with a fully single-stranded regressed arm (ssDNA). Insets show the magnified four-way junctions and regressed arms. P indicates the parental duplex, D indicates daughter duplexes, and R indicates the regressed arm. Bars: (main images) 0.5 kb; (insets) 0.2 kb. (E) Frequency of reversed replication forks with fully double-stranded, partially single-stranded, and fully single-stranded regressed arms in not treated (NT) U2OS cells and upon the indicated treatments (UV pulse or 1-h treatment). In brackets, the total number of analyzed molecules is given. Similar results were obtained in at least one independent experiment.

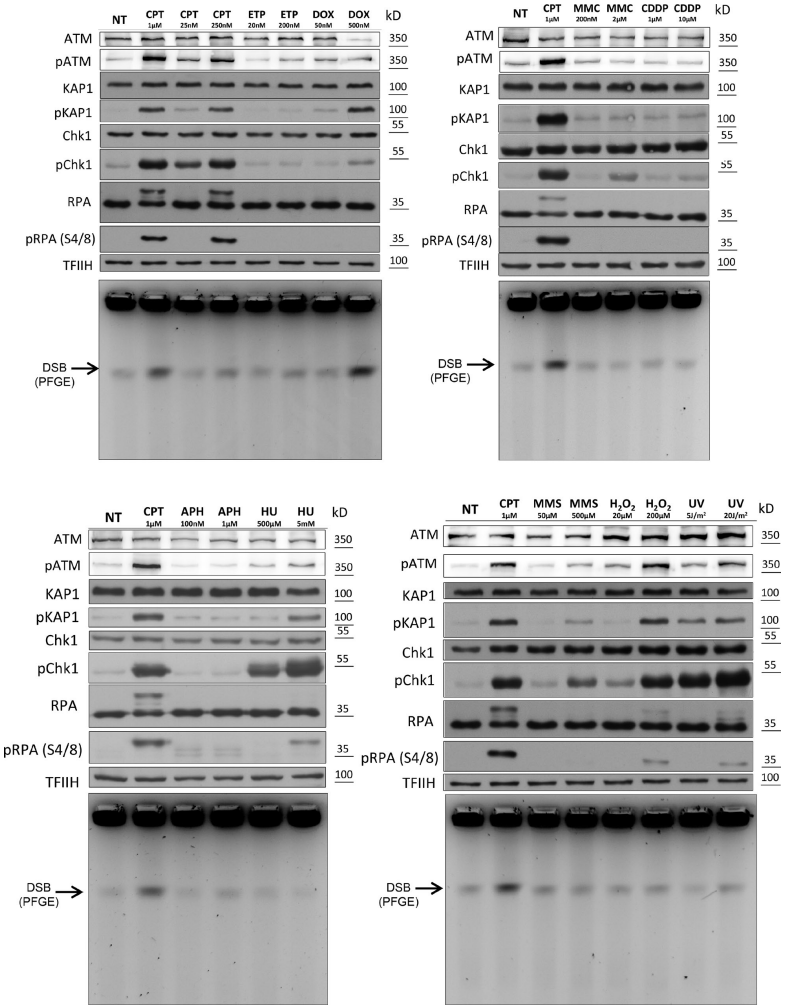

Figure S4. **Dose-dependent DSB induction and differential activation of the DDR upon different genotoxic treatments in human cells.** Immunoblot for ATR (pCHK1) and ATM (pATM and pKAP1) activation and total DDR proteins (ATM, CHK1, and KAP1) in not treated (NT) U2OS cells and upon the indicated treatments (UV pulse or 1-h treatment). RPA32 (RPA) phosphorylation at S4/S8 indicates ATM/DNA-PK activation and is typically used as DSB marker. Total RPA32 levels (and phosphorylation-associated mobility shift) are also displayed. DSB formation is also physically assessed by PFGE. 1 µM CPT treatment is used as positive control for DSB induction and full DDR activation. TFIIH is used as a loading control. Similar results were obtained in at least one independent experiment.

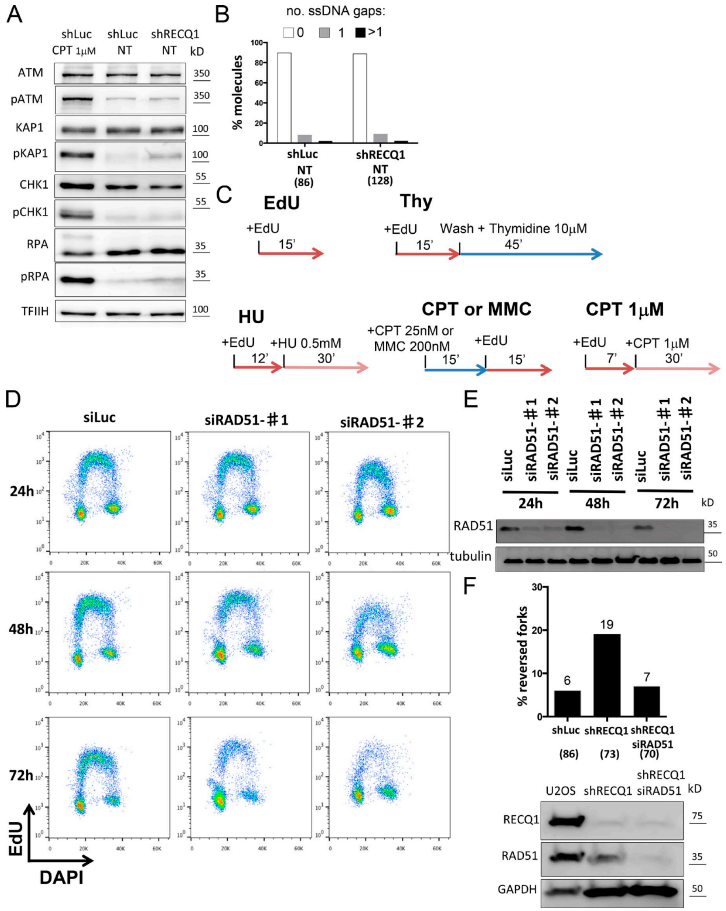

Figure S5. **ssDNA accumulation and checkpoint activation in unperturbed RECQ1-depleted cells, labeling schemes for iPOND experiments and cell cycle effects of RAD51 depletion.** (A) Immunoblot for ATR (pCHK1) and ATM (pATM and pKAP1) activation and total DDR proteins (ATM, CHK1, and KAP1) in U2OS cells stably transduced (shRNA) for Luciferase (shLuc) or RECQ1 depletion (shRECQ1). RPA32 (RPA) phosphorylation at S4/S8 indicates ATM/DNA-PK activation and is typically used as DSB marker. Total RPA32 levels (and phosphorylation-associated mobility shift) are also displayed. 1 μM CPT treatment is used as positive control for full DDR activation. TFIIH is used as a loading control. (B) Frequency of molecules containing no ssDNA gaps, one ssDNA gap, or more than one ssDNA gap along replicated duplexes (Fig. 2 C, white arrow) in U2OS cells stably transfected (shRNA) for Luciferase or RECQ1 depletion. In brackets, the total number of analyzed molecules is given. Similar results were obtained in at least one independent experiment. (C) Labeling scheme for the iPOND experiment in Fig. 6 B. HEK293T cells were labeled with EdU for 7 or 15 min followed by a chase into thymidine (Thy), 0.5 mM HU, 25 nM CPT, 200 nM MMC, or 1 mM CPT for the indicated times before performing iPOND. Red/pink tracks indicate continued EdU incorporation in the absence or presence of genotoxic stress, respectively. Blue tracks identify replication time without EdU incorporation. (D) FACS analysis of DNA synthesis (EdU) and DNA content (DAPI) after mock (siRNA Luciferase [siLuc]) or RAD51 (siRAD51) depletion at the indicated time points in U2OS cells. U2OS cells were transfected with two different siRNAs against RAD51. (E) Immunoblot of U2OS cells transfected with Luciferase or RAD51 siRNA at the indicated time points. U2OS cells were transfected with two different siRNAs against RAD51. β-Tubulin is used as a loading control. (F) Frequency of reversed forks detected by EM in U2OS cells stably transduced (shRNA) for RECQ1 depletion and transfected with Luciferase or RAD51 siRNA 24 h before DNA extraction. In brackets, the total number of analyzed molecules is given. Above each column, the percentage of reversed forks is indicated. RECQ1 and RAD51 levels after shRNA- or siRNA-mediated depletion were detected by immunoblotting. GAPDH was used as a loading control.

Reference

Neelsen, K.J., A.R. Chaudhuri, C. Follonier, R. Herrador, and M. Lopes. 2014. Visualization and interpretation of eukaryotic DNA replication intermediates in vivo by electron microscopy. *Methods Mol. Biol.* 1094:177–208. http://dx.doi.org/10.1007/978-1-62703-706-8_15

Replication Fork Slowing and Reversal upon DNA Damage Require PCNA Polyubiquitination and ZRANB3 DNA Translocase Activity

This publication showed that the annealing helicase ZRANB3 is necessary for efficient replication fork reversal upon genotoxic stress. The project revealed that upon genotoxic treatments ZRANB3 is recruited to replication forks via UBC13 dependent K63-linked poly-ubiquitination of PCNA, where it mediates fork reversal through its translocase activity. These findings provide the first in vivo evidence for a mechanistic link between error-free post -replicative repair and replication fork reversal in human cells.

To this manuscript, I personally contributed the DNA fiber spreading experiment in figure 2A showing that K63-linked ubiquitin chains are necessary for efficient fork slowing upon genotoxic treatments in human cells. I also conducted the FACS based cell cycle analysis of Ub^{r}-WT and Ub^{r}-K63R upon tetracycline treatment in figure S2B and prepared the cells used for the immunoblot analysis in figure S2A.

Short Article

Molecular Cell

Replication Fork Slowing and Reversal upon DNA Damage Require PCNA Polyubiquitination and ZRANB3 DNA Translocase Activity

Graphical Abstract

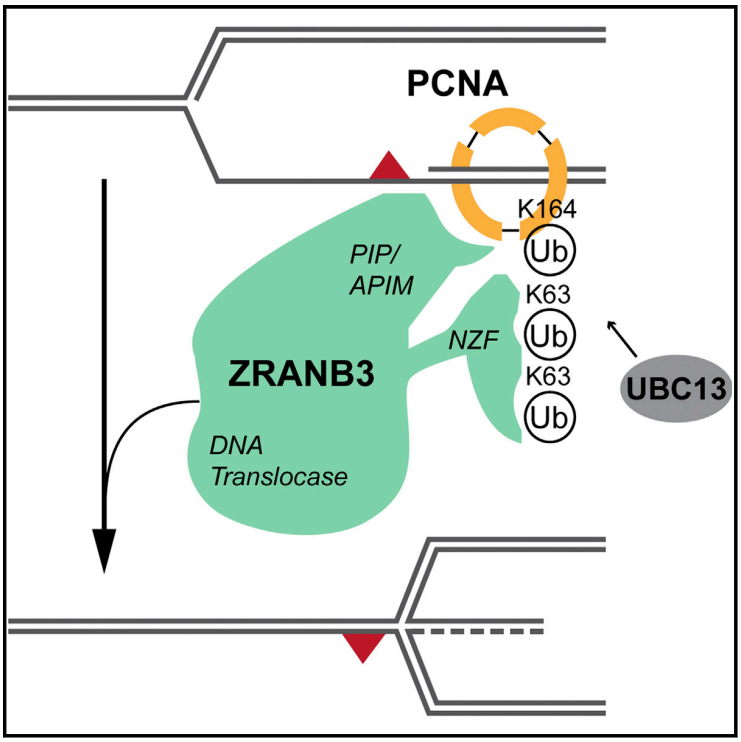

Authors

Marko Vujanovic, Jana Krietsch, Maria Chiara Raso, ..., Alberto Ciccia, Lorenza Penengo, Massimo Lopes

Correspondence

lopes@imcr.uzh.ch

In Brief

Vujanovic et al. show that UBC13-mediated, K63-linked PCNA polyubiquitination mediates DNA damage-induced replication fork slowing and reversal, via recruitment to forks of ZRANB3 DNA translocase. These data link the postreplication repair pathway, yet elusive in mammals, to the regulation of fork progression and remodeling.

Highlights

- Fork slowing and reversal upon damage require K63-linked PCNA polyubiquitination
- ZRANB3 mediates fork slowing/reversal *in vivo* via binding to polyubiquitinated PCNA
- ZRANB3 DNA translocase—not nuclease—activity mediates fork slowing and reversal
- Mammalian error-free postreplication repair entails global fork slowing and reversal

Vujanovic et al., 2017, Molecular Cell *67*, 882–890
September 7, 2017
http://dx.doi.org/10.1016/j.molcel.2017.08.010

CellPress

CellPress

Molecular Cell
Short Article

Replication Fork Slowing and Reversal upon DNA Damage Require PCNA Polyubiquitination and ZRANB3 DNA Translocase Activity

Marko Vujanovic,[1] Jana Krietsch,[1] Maria Chiara Raso,[1] Nastassja Terraneo,[1,5] Ralph Zellweger,[1] Jonas A. Schmid,[1] Angelo Taglialatela,[2] Jen-Wei Huang,[2] Cory L. Holland,[3] Katharina Zwicky,[1] Raquel Herrador,[1] Heinz Jacobs,[4] David Cortez,[3] Alberto Ciccia,[2] Lorenza Penengo,[1] and Massimo Lopes[1,6,*]

[1]Institute of Molecular Cancer Research, University of Zurich, 8057 Zurich, Switzerland
[2]Department of Genetics and Development, Columbia University Irving Medical Center, Irving Cancer Research Center, New York, NY 10032, USA
[3]Department of Biochemistry, Vanderbilt University School of Medicine, Nashville, TN 37205-0146, USA
[4]Division of Tumor Biology and Immunology, the Netherlands Cancer Institute, 1066 CX, Amsterdam, the Netherlands
[5]Present address: Center for Radiopharmaceutical Sciences ETH-PSI-USZ, Paul Scherrer Institut, Villigen-PSI, Switzerland
[6]Lead Contact
*Correspondence: lopes@imcr.uzh.ch
http://dx.doi.org/10.1016/j.molcel.2017.08.010

SUMMARY

DNA damage tolerance during eukaryotic replication is orchestrated by PCNA ubiquitination. While mono-ubiquitination activates mutagenic translesion synthesis, polyubiquitination activates an error-free pathway, elusive in mammals, enabling damage bypass by template switching. Fork reversal is driven *in vitro* by multiple enzymes, including the DNA translocase ZRANB3, shown to bind polyubiquitinated PCNA. However, whether this interaction promotes fork remodeling and template switching *in vivo* was unknown. Here we show that damage-induced fork reversal in mammalian cells requires PCNA ubiquitination, UBC13, and K63-linked polyubiquitin chains, previously involved in error-free damage tolerance. Fork reversal *in vivo* also requires ZRANB3 translocase activity and its interaction with polyubiquitinated PCNA, pinpointing ZRANB3 as a key effector of error-free DNA damage tolerance. Mutations affecting fork reversal also induced unrestrained fork progression and chromosomal breakage, suggesting fork remodeling as a global fork slowing and protection mechanism. Targeting these fork protection systems represents a promising strategy to potentiate cancer chemotherapy.

INTRODUCTION

Replicating cells react to genotoxic stress activating different molecular pathways, devoted to regulate origin firing and to protect the stability of ongoing replication forks (Berti and Vindigni, 2016). Replication completion in the presence of DNA lesions is assisted by the activation of the so-called "post-replication repair" (PRR) pathway, which is modulated in eukaryotic cells by controlled ubiquitination of the DNA polymerase clamp, i.e., proliferating cellular nuclear antigen (PCNA) (Branzei and Psakhye, 2016; García-Rodríguez et al., 2016). Accumulation of single-stranded DNA (ssDNA) at replication forks facing DNA lesions triggers recruitment of the E2-E3 pair RAD6-RAD18, mediating PCNA mono-ubiquitination on the K164 residue (Hoege et al., 2002; Niimi et al., 2008). This modification has been linked to the recruitment of translesion synthesis (TLS) polymerases, promoting error-prone DNA damage bypass at the expense of increased mutations rates (Bienko et al., 2005; Plosky et al., 2006). In yeast, further modification of the same PCNA residue via K63-linked polyubiquitination—which requires the dimeric E2 MMS2/UBC13 and the Rad5 E3 ligase (Hoege et al., 2002)—promotes error-free PRR, an alternative DNA damage tolerance pathway that fills postreplicative ssDNA gaps via template-switching (TS) and recombinational mechanisms, involving sister chromatid junctions (Branzei and Psakhye, 2016; Giannattasio et al., 2014). Alternative models for error-free PRR and TS entail remodeling of the replication fork in a four-way junction—a process known as replication fork reversal—to allow TS to occur directly at the elongating fork (Higgins et al., 1976). However, replication fork reversal in yeast cells has only been observed upon fork stalling in replication or checkpoint mutants (Fumasoni et al., 2015; Sogo et al., 2002) or upon topological stress induced by Topoisomerase I (Top1) poisons (Ray Chaudhuri et al., 2012), questioning the physiological role of fork reversal in this organism.

In mammals, detection of PCNA polyubiquitination proved more difficult and has so far required acute genotoxic treatments and/or overexpression of the responsible enzymes (Brun et al., 2010; Motegi et al., 2008). Rad5 has two related proteins in human cells—HLTF and SHPRH—both contributing to PCNA polyubiquitination (Motegi et al., 2008; Unk et al., 2010), possibly assisting the response to different types of DNA damage (Lin et al., 2011). A third E3 ligase has also been invoked (Krijger et al., 2011). Whether PCNA polyubiquitination directly promotes TS and/or regulates TLS has long been controversial (García-Rodríguez et al., 2016). Also, no direct data are currently available on

whether error-free PRR in higher eukaryotes mostly entails post-replicative junctions or fork reversal. Intriguingly, besides their E3 ligase activity, both Rad5 in yeast and HLTF in human cells possess specific domains capable of reversing replication forks *in vitro* (Blastyák et al., 2007; Kile et al., 2015), although their contribution to fork reversal *in vivo* is currently uncertain.

Recent visual inspection of mammalian replication intermediates *in vivo* has uncovered replication fork reversal as a global and genetically controlled response to various challenges to the replication process. These include oncogene activation, unstable repetitive sequences, and treatments with various genotoxins (Follonier et al., 2013; Neelsen et al., 2013; Ray Chaudhuri et al., 2012; Zellweger et al., 2015). These transient structures were proposed to exert a protective role upon replication stress, but to date only a few factors have been directly implicated in their formation, stabilization, and restart (Neelsen and Lopes, 2015). Importantly, genetic defects in reversed fork formation or stabilization upon genotoxic treatments were also shown to impair active replication fork slowing, thus linking controlled fork progression and fork remodeling upon replication stress (Ray Chaudhuri et al., 2012; Zellweger et al., 2015). PCNA ubiquitination was shown to be dispensable for continued fork progression upon UV damage in DT40 cells (Edmunds et al., 2008), but its potential contribution to actively remodel and slow down replication forks in mammalian cells has not been thoroughly investigated.

A number of proteins, mostly belonging to RECQ helicase or SWI/SNF protein families, are able to reverse forks in biochemical assays (Neelsen and Lopes, 2015). HARP/SMARCAL1 and AH2/ZRANB3 DNA translocases can re-anneal RPA-coated DNA strands (Yusufzai and Kadonaga, 2008, 2010) and reverse synthetic replication forks (Bétous et al., 2012, 2013; Ciccia et al., 2012), but their contribution to fork reversal *in vivo* is elusive. ZRANB3 was shown to associate with replication factories, to assist restart of stalled forks and to mildly contribute to genotoxin resistance (Ciccia et al., 2012; Yuan et al., 2012). These functions require the DNA translocase activity of ZRANB3, as well as its binding to PCNA—via PIP and APIM domains—and to polyubiquitinated PCNA—via its NZF domain (Ciccia et al., 2012; Yuan et al., 2012). ZRANB3 carries also a structure-specific endonuclease activity in the HNH domain (Weston et al., 2012), but its functional relevance is currently unclear.

Here, combining DNA fiber analysis and electron microscopy (EM) visualization of replication intermediates *in vivo*, we provide evidence that PCNA polyubiquitination mediates active fork slowing and reversal upon genotoxic treatments. Moreover, we report that a known "reader" of this modification—the translocase ZRANB3—regulates fork speed, fork remodeling, and chromosome integrity *in vivo*, via its DNA translocase activity and its ability to interact with polyubiquitinated PCNA.

RESULTS

PCNA Ubiquitination Mediates Active Fork Slowing and Reversal upon Genotoxic Stress

In order to assess whether PCNA ubiquitination is required to actively reduce replication fork speed upon replication stress, we investigated by DNA fiber spreading replication fork progression in PCNA-K164R mouse embryonic fibroblasts (MEFs) and their wild-type counterparts (Langerak et al., 2007). We combined incorporation of halogenated nucleotides and optional treatments with nanomolar doses of the Top1 inhibitor camptothecin (CPT) or the DNA crosslinking agent mitomycin C (MMC) (Zellweger et al., 2015). Both treatments induced a significant slowdown of replication fork progression, but this response was abolished by the K164R PCNA mutation (Figures 1A and 1B). Thus, PCNA ubiquitination is strictly required to mediate active fork slowing upon these genotoxic treatments.

We next used psoralen crosslinking coupled to EM (Zellweger and Lopes, 2017) to investigate *in vivo* replication fork architecture and to reveal the possible conversion of standard replication forks into four-way junctions—known as reversed forks (Figure 1C)—previously associated with a variety of genotoxic treatments (Ray Chaudhuri et al., 2012; Zellweger et al., 2015). As expected, reversed fork frequency in wild-type MEFs was markedly increased by CPT and MMC treatments. Remarkably, PCNA-K164R MEFs did not significantly increase reversed fork levels upon both genotoxic treatments (Figure 1D, Table S1A), showing that PCNA ubiquitination is required for effective replication fork reversal. Similar DNA fiber and EM results were obtained upon CPT treatment in independent lines of wild-type and PCNA-K164R MEFs (Figures S1A and S1B, Table S1B).

In order to visualize endogenous PCNA modifications occurring upon different genotoxic treatments, we performed cell fractionation to enrich for polyubiquitinated species of PCNA (Figure S1C). This approach enabled us to detect endogenous levels of polyubiquitinated PCNA, which were induced upon acute UV irradiation (Figure S1D), as previously reported (Motegi et al., 2008). Albeit technically challenging, using this protocol we detected low levels of polyubiquitinated PCNA also upon nanomolar doses of CPT or MMC, as those typically used for our DNA fiber and EM experiments (Figure S1D).

K63-Linked, UBC13-Dependent Polyubiquitination Is Required for Fork Slowing and Reversal upon Genotoxic Stress

In order to distinguish whether PCNA mono- or poly-ubiquitination mediates the observed fork slowing and reversal upon genotoxic stress, we took advantage of a previously characterized ubiquitin replacement system in U2OS cells (Xu et al., 2009). Doxycycline addition allows the replacement of endogenous ubiquitin with similar levels of exogenous wild-type or K63R mutant ubiquitin and does not impair overall cell-cycle progression (Figures S2A and S2B). DNA fiber experiments revealed that impairing K63-linked ubiquitin chain formation by the K63R mutation significantly affects CPT-induced replication fork slowing (Figure 2A). Moreover, replacement of endogenous ubiquitin with the K63R mutant markedly reduced the frequency of fork reversal upon CPT and MMC treatment (Figure 2B, Table S2A). Thus, K63-linked polyubiquitination is essential for efficient fork remodeling upon genotoxic stress.

In light of the reported redundancy of different E3 ligases mediating PCNA polyubiquitination (Krijger et al., 2011; Motegi et al., 2008), we next assessed the relevance of PCNA polyubiquitination by inactivation of the E2 enzyme required for

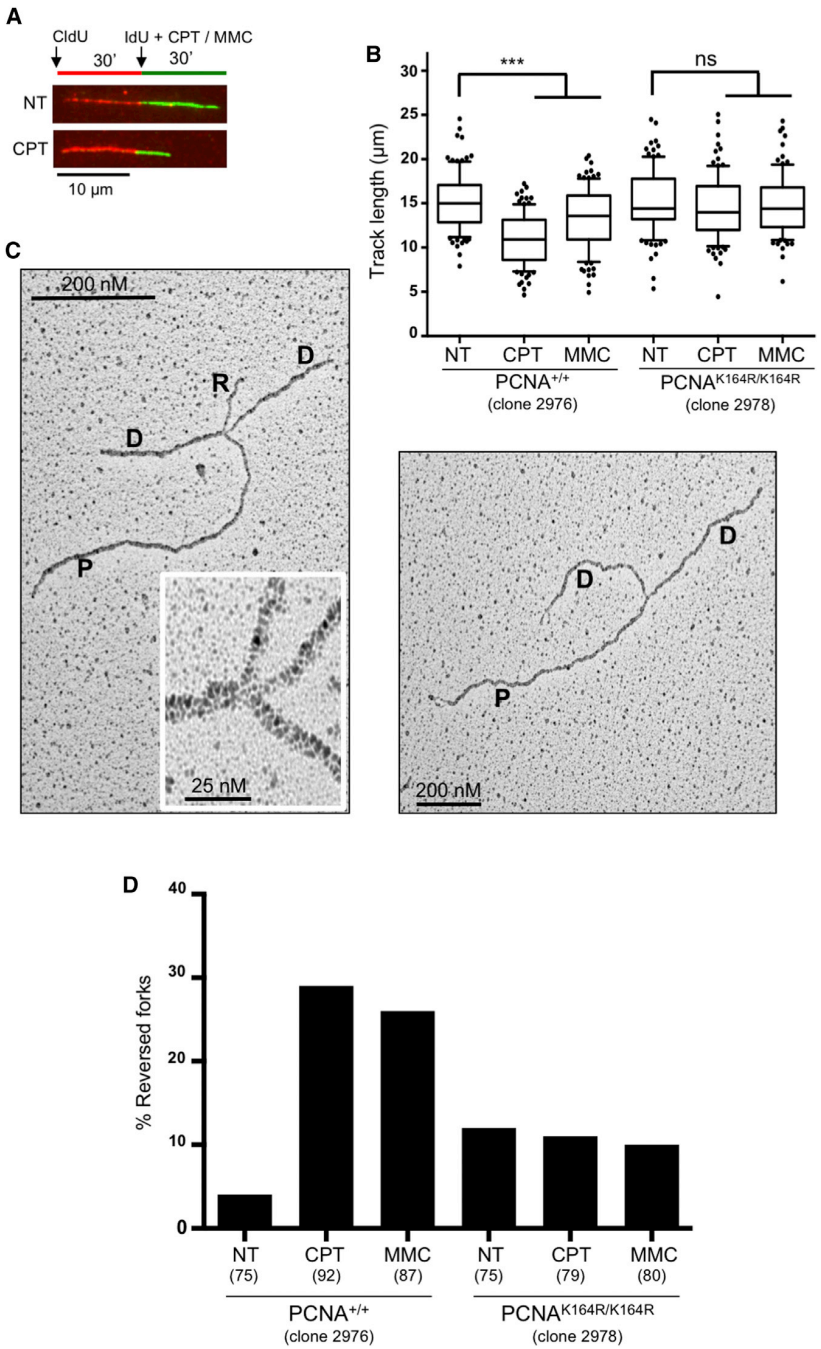

Figure 1. PCNA Ubiquitination Is Required for Replication Fork Slowing and Reversal upon Genotoxic Stress

(A) Labeling scheme of DNA fiber experiments: cells were provided with chlorodeoxyuridine (CldU, red). 30 min later, cells were washed and supplemented with iododeoxyuridine (IdU, green) and optionally treated with camptothecin (CPT) 50 nM and/or mitomycin C (MMC) 200 nM for 30 min. Green tracks were measured to assess fork speed.

(B) Control and PCNA-K164R mouse embryonic fibroblasts (MEFs) were subjected to the DNA fiber protocol described in (A). At least one hundred tracts were scored per sample. Whiskers: 10^{th}–90^{th} percentile (***$p < 0.001$; ns, non-significant; Mann-Whitney test). Similar results were obtained in at least two biological replicates.

(C) Representative electron microscopy images of reversed (left) or normal (right) replication forks. P, parental strand; D, daughter strand; R, regressed arm.

(D) Frequency of reversed forks in the indicated MEFs, upon optional 1 hr treatment with CPT 50 nM or MMC 200 nM, assessed by EM visualization. Similar results were obtained in two biological replicates and in independent MEF clones (Tables S1A and S1B).

this modification, i.e., UBC13 (García-Rodríguez et al., 2016). UBC13 knockout (KO) in HCT116 cells did not affect cell-cycle progression (Figure S2C) but abolished the reduction in replication fork speed upon CPT, MMC, and UV-C treatments (Figures 2C and 2D). Moreover, UBC13-KO cells failed to appreciably induce replication fork reversal, monitored by EM, upon all tested genotoxic treatments (Figure 2E; Table S2B). Similar results were obtained by siRNA-mediated downregulation of UBC13 in CPT- or MMC-treated U2OS cells (Figures S2D–S2F, Table S2C). Taken together, the data presented so far strongly suggest that PCNA polyubiquitination is required to mediate active fork slowing and fork reversal upon different genotoxic treatments.

The ZRANB3 Translocase Is Required for Fork Slowing and Reversal upon Different Genotoxic Treatments

As the DNA translocase ZRANB3 was reported as a specific interactor of polyubiquitinated PCNA and was shown to mediate replication fork reversal in biochemical assays (Ciccia et al., 2012), we directly tested its requirement for replication fork slowing and reversal *in vivo*. Therefore, a ZRANB3 knockout U2OS cell line generated by CRISPR/Cas9 technology—which did not display altered cell-cycle progression (Figure S3A)—was compared to its wild-type counterpart for replication fork slowing by DNA fiber assays and for fork reversal by EM, upon treatment with CPT, MMC, and UV-C. As observed upon impairment of UBC13-dependent K63-linked polyubiquitination (Figure 2), ZRANB3-KO cells displayed unrestrained fork progression in response to all tested treatments, with fork slowing being completely abolished upon CPT, MMC, and UV treatments (Figures 3A and 3B). Moreover, ZRANB3-KO cells displayed unaffected frequencies of fork reversal in

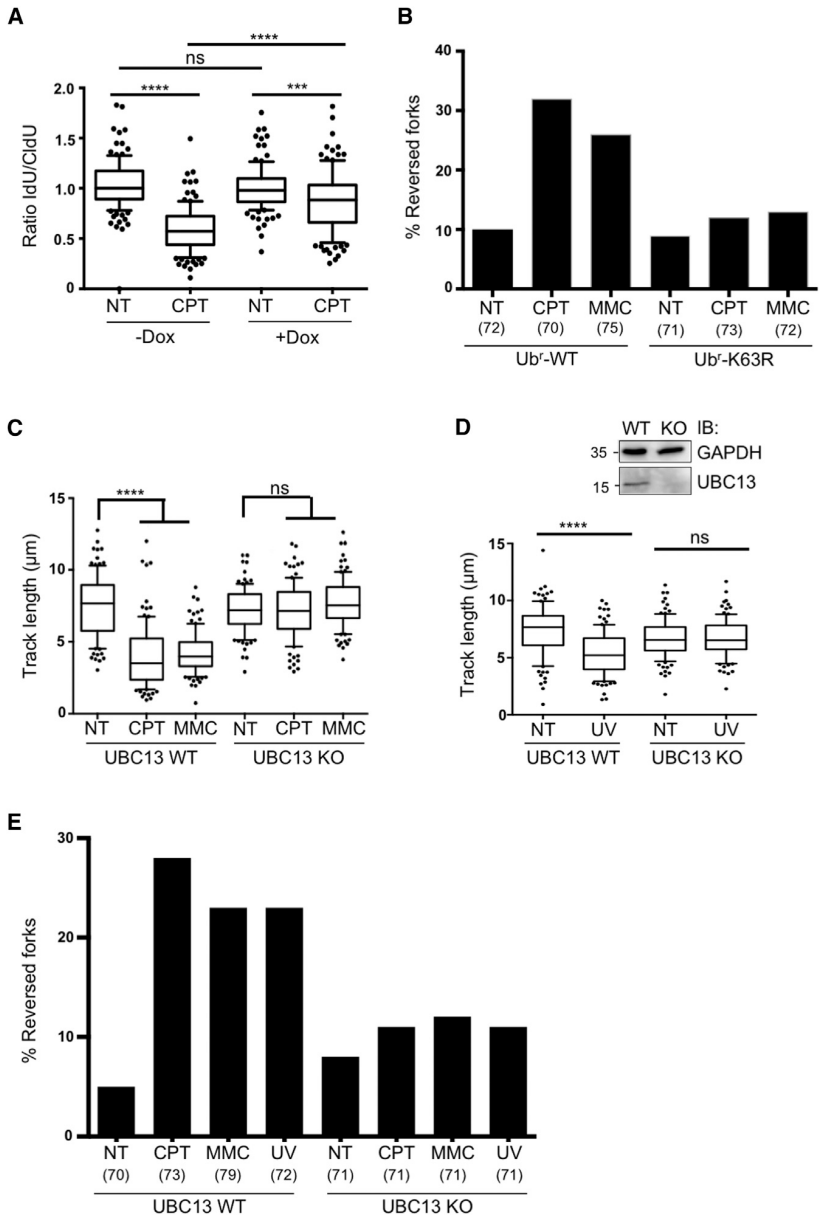

Figure 2. K63-Linked, UBC13-Dependent Polyubiquitination Is Required for Drug-Induced Fork Slowing and Reversal

(A) Cells conditionally (+Dox) replacing endogenous ubiquitin with a K63R ubiquitin mutant were subjected to the DNA fiber protocol as in Figure 1A. The ratio between green and red tracts is plotted, to display drug-induced fork slowing.

(B) Frequency of replication fork reversal in cells replacing endogenous ubiquitin with WT or K63R-ubiquitin, upon optional 1 hr treatment with CPT 50 nM or MMC 200 nM, assessed by EM visualization. In brackets, the number of analyzed molecules. Similar results were obtained in two biological replicates (Table S2A).

(C) Wild-type (WT) or UBC13-knockout (UBC13-KO) HCT116 cells were subjected to the DNA fiber protocol in Figure 1A.

(D) The same cell lines as in (C) were used for DNA fiber analysis, upon optional 5 J/m^2 UV-C irradiation in between the two labeling periods. Top right: the western blot shows the absence of UBC13 in UBC13-KO HCT116 cells. GAPDH, loading control. In (A), (C), and (D) at least one hundred tracts were scored per sample. Whiskers: 10th–90th percentile (****p < 0.0001; ***p < 0.001; ns, non-significant; Mann-Whitney test). Similar results were obtained in at least two biological replicates.

(E) Frequency of replication fork reversal in WT and UBC13-KO HCT116 cells, assessed by EM visualization, upon optional 1 hr treatment with CPT 50 nM or MMC 200 nM, or 1 hr after 5 J/m^2 UV-C irradiation. In brackets, the number of analyzed molecules. Similar results were obtained in two biological replicates (Table S2B).

unperturbed conditions but were unable to efficiently promote replication fork reversal upon all tested genotoxic treatments (Figure 3C, Table S3A). Similar effects were observed by DNA fiber spreading and EM analysis of another ZRANB3-KO clone and upon siRNA-mediated downregulation of ZRANB3 in U2OS cells (Figures S3A–S3F, Tables S3B and S3C).

Damage-Induced Fork Slowing and Reversal Protect Chromosome Integrity and Require ZRANB3-PCNA Interaction and ZRANB3 DNA Translocase Activity

ZRANB3 contains multiple domains and motifs, which mediate its enzymatic activities or the interaction with PCNA and its ubiquitinated forms (Ciccia et al., 2012; Weston et al., 2012; Yuan et al., 2012). To assess the relevance of these activities and interactions in replication fork slowing and reversal *in vivo*, we analyzed specific point mutations in ZRANB3 (Figure 4A), affecting respectively its interaction with PCNA (PIP+APIM domains), its interaction with polyubiquitinated PCNA (NZF-zinc finger), its DNA translocase activity (DEXDc domain; helicase dead [HD]) (Ciccia et al., 2012), or a crucial residue of the HNH domain, which was shown to provide ZRANB3 nuclease activity (Weston et al., 2012). We obtained stable cell lines by viral transduction of ZRANB3-KO U2OS cells, re-expressing FLAG/HA-tagged wild-type ZRANB3 or one of these mutant forms. We ensured that all tagged proteins were expressed at approximately the level of endogenous ZRANB3 in the original U2OS cell line (Figure 4A) and that none of the mutant cell lines had marked delays in cell-cycle progression (Figure S4A). Using these cell lines, we assessed whether wild-type and mutant forms of ZRANB3 could complement the defects in fork slowing and reversal observed in ZRANB3-KO cells (Figure 3), focusing on CPT treatments. Expression of WT ZRANB3 in ZRANB3-KO cells restored effective CPT-induced

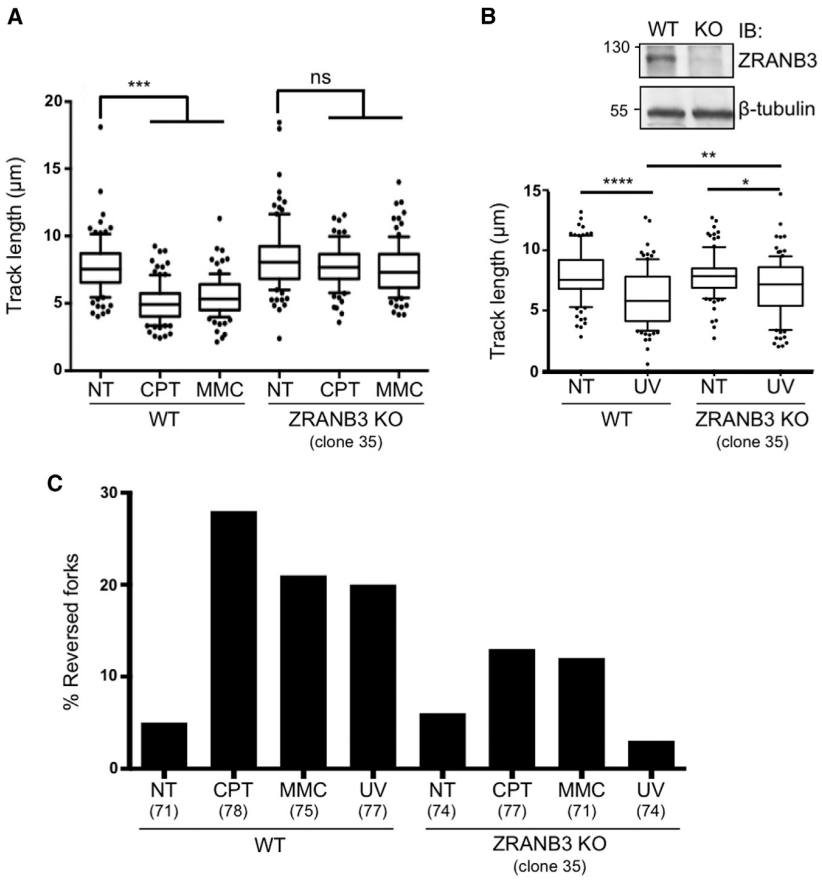

Figure 3. ZRANB3 Is Required for Efficient Replication Fork Slowdown and Fork Reversal upon Different Genotoxic Treatments

(A) Wild-type (WT) or ZRANB3-knockout (ZRANB3-KO) U2OS cells were subjected to the DNA fiber protocol as in Figure 1A.

(B) The same cell lines as in (A) were used for DNA fiber analysis, upon optional 5 J/m^2 UV-C irradiation in between the two labelings. Top right: the western blot shows the absence of ZRANB3 in ZRANB3-KO U2OS cells. β tubulin, loading control. In (A) and (B), at least one hundred tracts were scored per sample. Whiskers: 10th–90th percentile (****$p < 0.0001$; ***$p < 0.001$; **$p < 0.01$; *$p < 0.1$; ns, non-significant; Mann-Whitney test). Similar results were obtained in at least two biological replicates.

(C) Frequency of replication fork reversal in WT and ZRANB3-KO U2OS cells, assessed by EM visualization, upon optional 1 hr treatment with CPT 50 nM or MMC 200 nM, or 1 hr after 5 J/m^2 UV-C irradiation irradiation. In brackets, the number of analyzed molecules are shown. Similar results were obtained in two biological replicates and in two independent ZRANB3-KO clones (Tables S3A and S3B).

fork slowing and reversal (Figures 4B and 4C, Table S4), showing that the tagged protein is functional upon genotoxic treatment. Expression of the PIP+APIM mutant failed to restore fork slowing and reversal, suggesting that ZRANB3-PCNA interaction is essential to regulate fork progression and remodeling upon damage. Similarly, mutations destabilizing the NZF zinc finger impaired CPT-induced fork slowing and reversal (Figures 4B and 4C, Table S4). A complete defect in fork slowing and reversal was also observed upon expression of the helicase dead (HD) mutant that impairs ZRANB3 DNA translocation activity, while a mutant that inactivates the HNH nuclease motif restored efficient control of fork progression and remodeling (Figures 4B and 4C, Table S4). Thus, effective interaction of ZRANB3 with both unmodified and polyubiquitinated PCNA and its DNA translocase activity, but not an intact HNH nuclease domain, are required for replication fork slowing and reversal upon genotoxic stress. In order to test whether ZRANB3-mediated fork slowing and reversal limit DNA damage-induced chromosomal instability, we assessed chromosomal abnormalities by metaphase spreads after CPT treatment. To exclude selection of compensatory mutations in ZRANB3-KO cells, we chose to transiently inactivate ZRANB3 by siRNA in cell lines stably expressing siRNA-resistant HA-tagged ZRANB3 variants that retain (WT, HNH) or impair (PIP-APIM) fork slowing and reversal activities (Figures 4A–4C; Figure S4B). ZRANB3 downregulation led to increased chromosomal abnormalities upon CPT treatment (Figure 4D). Notably, this increase was suppressed by the presence of WT and HNH mutant forms of ZRANB3, while the PIP-APIM ZRANB3 mutant—specifically defective in fork slowing and reversal—failed to restore chromosome integrity after CPT treatment. These data strongly suggest that ZRANB3-mediated fork slowing and reversal prevent chromosomal instability upon genotoxic treatments.

DISCUSSION

Our data establish the genetic dependency of replication fork slowing and reversal on PCNA ubiquitination, UBC13, and K63-linked polyubiquitination—all of which are known to mediate the error-free PRR pathway in mammalian cells (García-Rodríguez et al., 2016)—thus showing that activation of this pathway entails global fork slowing and reversal in response to a variety of genotoxic treatments. In agreement with the prevalent occurrence of error-free PRR at replication forks in higher eukaryotes, in human cells we failed to detect significant accumulation of postreplicative junctions—under similar experimental conditions that were previously successfully used to visualize and characterize TS postreplicative intermediates in *S. cerevisiae* cells (Giannattasio et al., 2014)—even upon acute treatments and genetic stabilization of these structures (Figures S4C–S4E). We thus propose that—differently from yeast cells—activation of the error-free PRR pathway in human cells leads to extensive fork remodeling, transiently limiting fork progression on the damaged template.

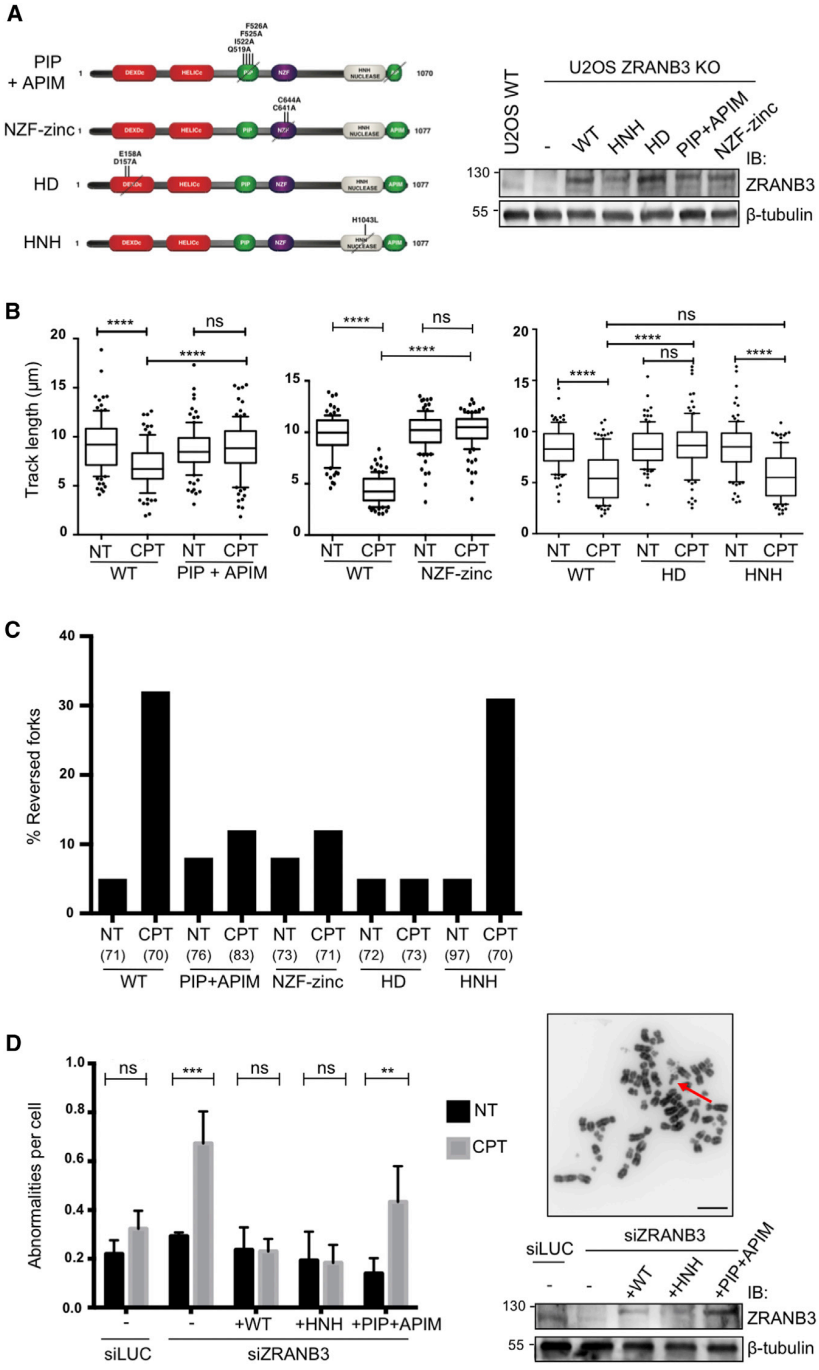

Figure 4. Fork Progression, Fork Remodeling and Chromosomal Integrity Defects upon Inactivation of Different ZRANB3 Domains

(A) Left: schematic representation of ZRANB3 domain organization and of mutations analyzed in this study. Right: western blot analysis of ZRANB3 in the indicated cell lines.

(B) The indicated stable cell lines, expressing WT or mutant ZRANB3, were used for DNA fiber analysis as in Figure 1A, upon optional CPT 50 nM treatment. At least one hundred tracts were scored per sample. Whiskers: 10th–90th percentile (****p < 0.0001; ns, non-significant; Mann-Whitney test). Similar results were obtained in at least two biological replicates.

(C) Frequency of replication fork reversal in the indicated cell lines, assessed by EM visualization, upon optional 1 hr treatment with CPT 50 nM. In brackets, the number of analyzed molecules. Similar results were obtained in two biological replicates (Table S4).

(D) Left: number of chromosomal abnormalities per indicated cell line, as determined by metaphase spreading upon optional 8 hr CPT treatment (50 nM) and 16 hr nocodazole treatment (200 ng/mL). Error bars, standard deviations. Right: representative DAPI stained metaphase; the arrow points to a chromosome break. Scale bar, 5 μm. Western blot analysis of ZRANB3 protein levels in U2OS cell lines used in (D, left). In (A) and (D), the expression level of HA-tagged ZRANB3 WT and mutant proteins (retarded mobility) is close to endogenous ZRANB3 levels in U2OS cells. β tubulin, loading control.

In turn, genetic inactivation of fork remodeling in error-free PRR mutants causes unrestrained fork progression, occasionally leading to chromosomal breaks, visible in the next mitosis. The choice between fork reversal and postreplicative error-free PRR likely reflects differences in the efficiency of re-priming in higher versus lower eukaryotes, the abundance of repetitive DNA in human cells and the different control of several key players in these pathways (Branzei and Psakhye, 2016; Sale, 2012).

By cell fractionation, we were able to enrich and detect endogenous levels of polyubiquitinated PCNA upon acute UV treatment, as previously reported (Motegi et al., 2008). Albeit technically challenging (Niimi et al., 2008), in the same experimental conditions PCNA polyubiquitination could also be detected upon sublethal (nanomolar) MMC and CPT treatments. Importantly, while extensive TS is expected at UV-induced lesions, CPT- and MMC-induced DNA lesions are expected to delay template unwinding and should not extensively involve DNA damage bypass by TS. We propose that activation of this branch of the PRR likely results from a common molecular feature detected at replication forks upon all tested genotoxic treatments—i.e., ssDNA accumulation (Zellweger et al., 2015)—which reportedly promotes the recruitment of the E3 ligases for PCNA ubiquitination (Niimi et al., 2008) and may thus mediate replication fork remodeling even in the absence of a DNA lesion specifically requiring TS. This scenario is in agreement with the

surprising evidence that reversed fork frequency in human cells is not significantly dependent on the type and dose of genotoxic treatments (Ray Chaudhuri et al., 2012; Zellweger et al., 2015). In this context, fork reversal should be considered as a general fork protection mechanism, which actively delays global fork progression and promotes DNA damage tolerance when required. The mechanisms underlying the global remodeling of replication forks from local DNA damage at a subset of forks certainly deserve further investigation.

In addition, our data uncover the key role in active fork slowing and reversal of a known interaction partner of polyubiquitinated PCNA, i.e., the DNA translocase ZRANB3. This protein was shown to contribute in human cells to genome maintenance upon genotoxic treatments and to the restart of stalled replication forks, via its DNA translocase activity and its multiple interactions with unmodified and polyubiquitinated PCNA (Ciccia et al., 2012; Yuan et al., 2012). Our data reveal the dependency on the same activity and domains for DNA damage-induced replication fork slowing and reversal, strongly suggesting that the key role of ZRANB3 in the replication stress response entails recruitment to replication forks to assist fork remodeling, in keeping with its known biochemical properties (Ciccia et al., 2012). Besides formation of reversed forks, ZRANB3 may also mediate reversed fork accumulation by controlling their stability, preventing unscheduled restart or processing. Interestingly, binding to polyubiquitinated PCNA is not required for ZRANB3 recruitment, but rather for its retention at replication factories (Ciccia et al., 2012), which may suggest its involvement in modulating fork restart. Our DNA fiber, EM, and chromosomal analyses of different ZRANB3 mutants reinforce the tight association between fork reversal, active fork slowing, and chromosome stability in human cells. Inactivation of the ZRANB3 nuclease domain (HNH) had no visible impact on fork slowing or reversal and, in keeping with our model, did not increase chromosomal breakage upon CPT treatment. Alternative mechanistic roles for ZRANB3 nuclease activity in response to replication stress will require further investigation.

We noted that the low levels of replication fork reversal consistently observed in unperturbed cells were not significantly affected by ZRANB3 depletion or inactivation, possibly suggesting that endogenous impediments to fork progression lead to fork remodeling via ZRANB3-independent mechanisms. However, this may also reflect the functional redundancy of other members of the same family—such as SMARCAL1 or RAD54—possibly providing fork reversal activities when ZRANB3 is inactive. Similarly, despite the marked reduction in fork reversal that we observed in ZRANB3-defective cells upon all tested genotoxic treatments, it is well possible that other translocases play a role in fork remodeling in response to specific types of replication interference, as suggested by additive contributions to cell survival and fork restart upon genotoxic treatments (Ciccia et al., 2012; Yuan et al., 2012). The functional analysis of this redundancy and/or damage specificity would require extensive EM analysis, upon simultaneous inactivation of several members of this protein family.

As the E3 ligases responsible for PCNA polyubiquitination—Rad5 in yeast and HLTF, among others, in human cells—were shown to possess fork reversal activities in biochemical assays (Blastyák et al., 2007; Kile et al., 2015), it will be important to clarify whether these activities stimulate fork reversal *in vivo* and how they are possibly coordinated with additional enzymatic activities recruited to replication forks via binding to polyubiquitinated PCNA (i.e., ZRANB3). Similarly, the central recombinase RAD51 was shown to mediate fork reversal *in vivo* (Zellweger et al., 2015). Understanding the mechanistic cross-talk between translocase and strand exchange activities in driving fork reversal will require complex biochemical reconstitution of this transaction, possibly including chromatinized substrates. Moreover, as additional factors have been proposed to bind polyubiquitinated PCNA in yeast and human cells (Saugar et al., 2012), it will be important to test their potential contribution to fork slowing and reversal upon different genotoxic treatments.

Overall, this study contributes to our mechanistic understanding of active fork slowing and remodeling upon genotoxic treatments. As these fork protection mechanisms are expected to provide resistance to cancer chemotherapeutic treatments acting via DNA damage, further elucidation of the underlying mechanisms will be required to identify promising targets to potentiate cancer chemotherapy.

STAR★METHODS

Detailed methods are provided in the online version of this paper and include the following:

- KEY RESOURCES TABLE
- CONTACT FOR REAGENT AND RESOURCE SHARING
- EXPERIMENTAL MODEL AND SUBJECT DETAILS
- METHOD DETAILS
  - Cell culture and cell lines
  - Generation of stable cell lines expressing exogenous ZRANB3
  - Transfections
  - Drugs and reagents
  - Western blotting
  - Chromatin fractionation to detection endogenous ubiquitinated PCNA
  - Antibodies
  - FACS analysis of cell cycle progression
  - Replication fork progression by DNA fiber analysis
  - Electron microscopic analysis of genomic DNA
  - Chromosomal breakage and abnormalities by metaphase spreading
- QUANTIFICATION AND STATISTICAL ANALYSIS
- DATA AND SOFTWARE AVAILABILITY

SUPPLEMENTAL INFORMATION

Supplemental Information includes four figures and four tables and can be found with this article online at http://dx.doi.org/10.1016/j.molcel.2017.08.010.

AUTHOR CONTRIBUTIONS

M.V. performed and analyzed all EM, DNA fibers, western blot, and FACS experiments, with technical assistance of J.K., R.Z., and R.H. N.T. generated important preliminary data. M.C.R. produced the PCNA ubiquitination data

and assisted J.K. for the metaphase spreads. J.A.S. performed DNA fiber experiments and FACS analyses in the ubiquitin replacement systems. K.Z. performed all 2D gel experiments on postreplicative junctions. H.J. produced and provided PCNA-K164R MEFs. C.L.H and D.C. produced and provided the ZRANB3-KO U2OS cells. A.T., J.-W.H., and A.C. designed, produced, and characterized biochemically the ZRANB3 mutants. L.P. supervised the detection of ubiquitinated PCNA. M.L. designed and supervised the project and wrote the manuscript, assisted by L.P.

ACKNOWLEDGMENTS

We thank the Center for Microscopy and Image Analysis of the University of Zurich for technical assistance with electron microscopy. We are grateful to Z.J. Chen for sharing the ubiquitin replacement system, to M. Gatti and K. Mutreja for technical assistance, and to all members of the Lopes group for discussions. This work was supported by the SNF grants 31003A_146924 and 31003A_169959 and the ERC Consolidator Grant 617102 to M.L., by the SNF grant 31003A_166370 and the Helmut Horten grant to L.P., by the NIH grant R01CA197774 to A.C., by the NIH grant GM116616 to D.C. and by the KWF grant NKI-2012-5243 and the ZonMW Top grant 91213018 to H.J.

Received: December 1, 2016
Revised: May 24, 2017
Accepted: August 16, 2017
Published: September 7, 2017

SUPPORTING CITATIONS

The following references appear in the Supplemental Information: Follonier and Lopes, 2014; Wu and Hickson, 2003.

REFERENCES

Berti, M., and Vindigni, A. (2016). Replication stress: getting back on track. Nat. Struct. Mol. Biol. *23*, 103–109.

Bétous, R., Mason, A.C., Rambo, R.P., Bansbach, C.E., Badu-Nkansah, A., Sirbu, B.M., Eichman, B.F., and Cortez, D. (2012). SMARCAL1 catalyzes fork regression and Holliday junction migration to maintain genome stability during DNA replication. Genes Dev. *26*, 151–162.

Bétous, R., Couch, F.B., Mason, A.C., Eichman, B.F., Manosas, M., and Cortez, D. (2013). Substrate-selective repair and restart of replication forks by DNA translocases. Cell Rep. *3*, 1958–1969.

Bienko, M., Green, C.M., Crosetto, N., Rudolf, F., Zapart, G., Coull, B., Kannouche, P., Wider, G., Peter, M., Lehmann, A.R., et al. (2005). Ubiquitin-binding domains in Y-family polymerases regulate translesion synthesis. Science *310*, 1821–1824.

Blastyák, A., Pintér, L., Unk, I., Prakash, L., Prakash, S., and Haracska, L. (2007). Yeast Rad5 protein required for postreplication repair has a DNA helicase activity specific for replication fork regression. Mol. Cell *28*, 167–175.

Branzei, D., and Psakhye, I. (2016). DNA damage tolerance. Curr. Opin. Cell Biol. *40*, 137–144.

Brun, J., Chiu, R.K., Wouters, B.G., and Gray, D.A. (2010). Regulation of PCNA polyubiquitination in human cells. BMC Res. Notes *3*, 85.

Ciccia, A., Nimonkar, A.V., Hu, Y., Hajdu, I., Achar, Y.J., Izhar, L., Petit, S.A., Adamson, B., Yoon, J.C., Kowalczykowski, S.C., et al. (2012). Polyubiquitinated PCNA recruits the ZRANB3 translocase to maintain genomic integrity after replication stress. Mol. Cell *47*, 396–409.

Edmunds, C.E., Simpson, L.J., and Sale, J.E. (2008). PCNA ubiquitination and REV1 define temporally distinct mechanisms for controlling translesion synthesis in the avian cell line DT40. Mol. Cell *30*, 519–529.

Follonier, C., and Lopes, M. (2014). Combined bidimensional electrophoresis and electron microscopy to study specific plasmid DNA replication intermediates in human cells. Methods Mol. Biol. *1094*, 209–219.

Follonier, C., Oehler, J., Herrador, R., and Lopes, M. (2013). Friedreich's ataxia-associated GAA repeats induce replication-fork reversal and unusual molecular junctions. Nat. Struct. Mol. Biol. *20*, 486–494.

Fumasoni, M., Zwicky, K., Vanoli, F., Lopes, M., and Branzei, D. (2015). Error-free DNA damage tolerance and sister chromatid proximity during DNA replication rely on the Polα/Primase/Ctf4 Complex. Mol. Cell *57*, 812–823.

García-Rodríguez, N., Wong, R.P., and Ulrich, H.D. (2016). Functions of Ubiquitin and SUMO in DNA Replication and Replication Stress. Front. Genet. *7*, 87.

Giannattasio, M., Zwicky, K., Follonier, C., Foiani, M., Lopes, M., and Branzei, D. (2014). Visualization of recombination-mediated damage bypass by template switching. Nat. Struct. Mol. Biol. *21*, 884–892.

Higgins, N.P., Kato, K., and Strauss, B. (1976). A model for replication repair in mammalian cells. J. Mol. Biol. *101*, 417–425.

Hoege, C., Pfander, B., Moldovan, G.L., Pyrowolakis, G., and Jentsch, S. (2002). RAD6-dependent DNA repair is linked to modification of PCNA by ubiquitin and SUMO. Nature *419*, 135–141.

Kile, A.C., Chavez, D.A., Bacal, J., Eldirany, S., Korzhnev, D.M., Bezsonova, I., Eichman, B.F., and Cimprich, K.A. (2015). HLTF's Ancient HIRAN Domain Binds 3′ DNA Ends to Drive Replication Fork Reversal. Mol. Cell *58*, 1090–1100.

Krijger, P.H.L., Lee, K.-Y., Wit, N., van den Berk, P.C.M., Wu, X., Roest, H.P., Maas, A., Ding, H., Hoeijmakers, J.H.J., Myung, K., and Jacobs, H. (2011). HLTF and SHPRH are not essential for PCNA polyubiquitination, survival and somatic hypermutation: existence of an alternative E3 ligase. DNA Repair (Amst.) *10*, 438–444.

Langerak, P., Nygren, A.O.H., Krijger, P.H.L., van den Berk, P.C.M., and Jacobs, H. (2007). A/T mutagenesis in hypermutated immunoglobulin genes strongly depends on PCNAK164 modification. J. Exp. Med. *204*, 1989–1998.

Lin, J.R., Zeman, M.K., Chen, J.Y., Yee, M.C., and Cimprich, K.A. (2011). SHPRH and HLTF act in a damage-specific manner to coordinate different forms of postreplication repair and prevent mutagenesis. Mol. Cell *42*, 237–249.

Motegi, A., Liaw, H.-J., Lee, K.-Y., Roest, H.P., Maas, A., Wu, X., Moinova, H., Markowitz, S.D., Ding, H., Hoeijmakers, J.H.J., and Myung, K. (2008). Polyubiquitination of proliferating cell nuclear antigen by HLTF and SHPRH prevents genomic instability from stalled replication forks. Proc. Natl. Acad. Sci. USA *105*, 12411–12416.

Neelsen, K.J., and Lopes, M. (2015). Replication fork reversal in eukaryotes: from dead end to dynamic response. Nat. Rev. Mol. Cell Biol. *16*, 207–220.

Neelsen, K.J., Zanini, I.M.Y., Herrador, R., and Lopes, M. (2013). Oncogenes induce genotoxic stress by mitotic processing of unusual replication intermediates. J. Cell Biol. *200*, 699–708.

Niimi, A., Brown, S., Sabbioneda, S., Kannouche, P.L., Scott, A., Yasui, A., Green, C.M., and Lehmann, A.R. (2008). Regulation of proliferating cell nuclear antigen ubiquitination in mammalian cells. Proc. Natl. Acad. Sci. USA *105*, 16125–16130.

Plosky, B.S., Vidal, A.E., Fernández de Henestrosa, A.R., McLenigan, M.P., McDonald, J.P., Mead, S., and Woodgate, R. (2006). Controlling the subcellular localization of DNA polymerases iota and eta via interactions with ubiquitin. EMBO J. *25*, 2847–2855.

Ray Chaudhuri, A., Hashimoto, Y., Herrador, R., Neelsen, K.J., Fachinetti, D., Bermejo, R., Cocito, A., Costanzo, V., and Lopes, M. (2012). Topoisomerase I poisoning results in PARP-mediated replication fork reversal. Nat. Struct. Mol. Biol. *19*, 417–423.

Sale, J.E. (2012). Competition, collaboration and coordination–determining how cells bypass DNA damage. J. Cell Sci. *125*, 1633–1643.

Saugar, I., Parker, J.L., Zhao, S., and Ulrich, H.D. (2012). The genome maintenance factor Mgs1 is targeted to sites of replication stress by ubiquitylated PCNA. Nucleic Acids Res. *40*, 245–257.

Sogo, J.M., Lopes, M., and Foiani, M. (2002). Fork reversal and ssDNA accumulation at stalled replication forks owing to checkpoint defects. Science *297*, 599–602.

Thorslund, T., Ripplinger, A., Hoffmann, S., Wild, T., Uckelmann, M., Villumsen, B., Narita, T., Sixma, T.K., Choudhary, C., Bekker-Jensen, S., and Mailand, N. (2015). Histone H1 couples initiation and amplification of ubiquitin signalling after DNA damage. Nature *527*, 389–393.

Unk, I., Hajdú, I., Blastyák, A., and Haracska, L. (2010). Role of yeast Rad5 and its human orthologs, HLTF and SHPRH in DNA damage tolerance. DNA Repair (Amst.) *9*, 257–267.

Weston, R., Peeters, H., and Ahel, D. (2012). ZRANB3 is a structure-specific ATP-dependent endonuclease involved in replication stress response. Genes Dev. *26*, 1558–1572.

Wu, L., and Hickson, I.D. (2003). The Bloom's syndrome helicase suppresses crossing over during homologous recombination. Nature *426*, 870–874.

Xu, M., Skaug, B., Zeng, W., and Chen, Z.J. (2009). A ubiquitin replacement strategy in human cells reveals distinct mechanisms of IKK activation by TNFalpha and IL-1beta. Mol. Cell *36*, 302–314.

Yuan, J., Ghosal, G., and Chen, J. (2012). The HARP-like domain-containing protein AH2/ZRANB3 binds to PCNA and participates in cellular response to replication stress. Mol. Cell *47*, 410–421.

Yusufzai, T., and Kadonaga, J.T. (2008). HARP is an ATP-driven annealing helicase. Science *322*, 748–750.

Yusufzai, T., and Kadonaga, J.T. (2010). Annealing helicase 2 (AH2), a DNA-rewinding motor with an HNH motif. Proc. Natl. Acad. Sci. USA *107*, 20970–20973.

Zellweger, R., and Lopes, M. (2017). Dynamic architecture of eukaryotic DNA replication forks *in vivo*, visualized by electron microscopy. In Genome Instability: Methods and Protocols, M. Muzi-Falconi and G. Brown, eds. (Springer Science+Business Media). http://dx.doi.org/10.1007/978-1-4939-7306-4_19.

Zellweger, R., Dalcher, D., Mutreja, K., Berti, M., Schmid, J.A., Herrador, R., Vindigni, A., and Lopes, M. (2015). Rad51-mediated replication fork reversal is a global response to genotoxic treatments in human cells. J. Cell Biol. *208*, 563–579.

Molecular Cell, Volume 67

Supplemental Information

Replication Fork Slowing and Reversal upon DNA Damage Require PCNA Polyubiquitination and ZRANB3 DNA Translocase Activity

Marko Vujanovic, Jana Krietsch, Maria Chiara Raso, Nastassja Terraneo, Ralph Zellweger, Jonas A. Schmid, Angelo Taglialatela, Jen-Wei Huang, Cory L. Holland, Katharina Zwicky, Raquel Herrador, Heinz Jacobs, David Cortez, Alberto Ciccia, Lorenza Penengo, and Massimo Lopes

Replication fork slowing and reversal upon DNA damage require PCNA polyubiquitination and ZRANB3 DNA translocase activity

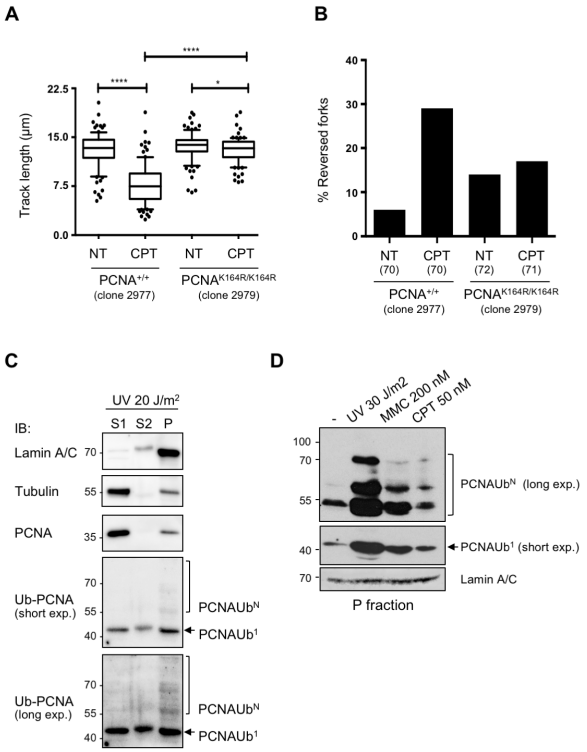

Figure S1, related to Figure 1. A cell fractionation procedure reveals PCNA polyubiquitination in response to acute UV treatment and upon mild CPT or MMC treatments. (A) Control and PCNA-K164R mouse embryonic fibroblasts (MEFs) were subjected to the DNA fiber protocol described in Figure 1A. At least one hundred tracks were scored per sample. Whiskers: 10-90th percentile (***, $P < 0.001$; ns, non-significant, Mann – Whitney test. Similar results were obtained in at least two biological replicates. (B) Frequency of replication fork reversal in the indicated MEFs, upon optional 1h treatment with CPT 50 nM, assessed by *in vivo* psoralen-crosslinking and EM visualization (Zellweger and Lopes, 2017). Similar results were obtained in two biological replicates and in independent MEF clones (Tables S1A-B). (C) Cell fractionation experiment showing the enrichment of ubiquitinated PCNA in fraction P. HCT116 cells were treated with UV irradiation (20 J/m^2) and then subjected to the fractionation protocol detailed in STAR methods. 20 µg of each fraction were loaded onto an SDS-PAGE and analyzed using the indicated antibodies. (D) HCT116 cells were treated with genotoxic treatments (UV 30 J/m^2, MMC 200 nM for 1 h and 50 nM CPT for 1 h). Upon cell fractionation (as in Figure S1C), 70 µg of fraction P were analyzed by immuno-blotting using anti-UbK164PCNA. Lamin A/C is used as loading control. To improve detection of rare PCNA poly-ubiquitinated forms (PCNAUb^N) by UbK164PCNA antibody, the membrane was cut to incubate separately mono-ubiquitinated PCNA (PCNAUb^1, 43 kDa) and the higher molecular weight bands corresponding to the poly-ubiquitinated forms (PCNAUb^N). Two different exposures are shown.

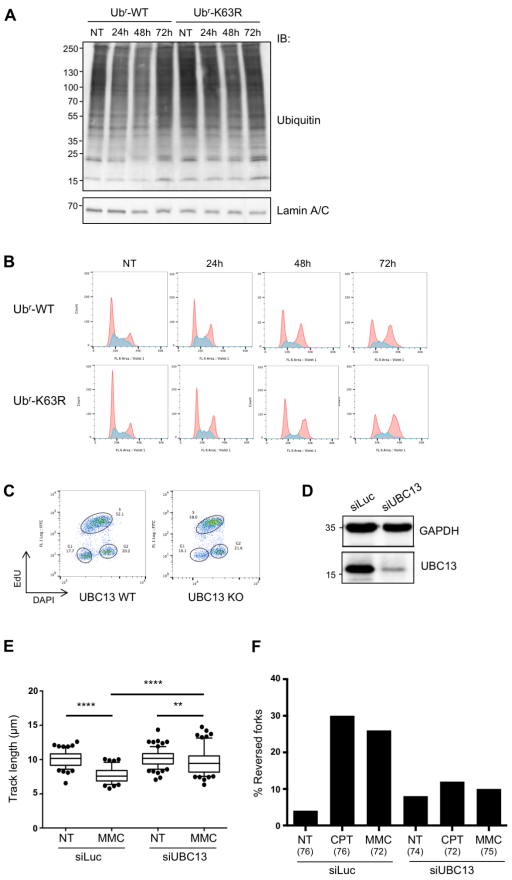

Figure S2, related to Figure 2. UBC13 downregulation in U2OS cells leads to unrestrained replication fork progression and reduced reversed fork frequency upon genotoxic treatments. (A) U2OS cell lines stably carrying either the wild type (Ubr-WT) or the K63R (Ubr-K63R) ubiquitin replacement system (Xu et al, 2009) were treated with doxycycline for different time points to induce the simultaneous knockdown of endogenous ubiquitin and expression of ectopic version. Anti-ubiquitin immunoblotting reveals that - 72h after induction of knowckdown/expression (conditions used in Figure 2A-B) - comparable levels of ubiquitin conjugates are present in Ubr-WT and Ubr-K63R expressing cells. Lamin A/C is used as loading control. (B) Cell cycle distribution analysis by FACS using DAPI for the same cells as in Figure S2A. (C) EdU-DAPI FACS experiment showing marginal differences in cell cycle distribution, between wild type (WT) or UBC13 knock out (KO) HCT116 cells (see Figure 2). (D) Western Blot showing efficiency of siRNA-mediated UBC13 downregulation in U2OS cells. GAPDH, loading control. (E) Control (siLuc) or UBC13-depleted (siUBC13) U2OS cells were subjected to the DNA fiber protocol as in Figure 1A upon optional mitomycin C (200 nM) treatment. At least one hundred tracks were scored per sample. Whiskers: 10-90th percentile (****, P < 0.0001; **, P < 0.05; Mann – Whitney test). Very similar results were obtained in at least two biological replicates. (F) Frequency of replication fork reversal in control (siLuc) or UBC13-depleted (siUBC13) U2OS cells, assessed by in vivo psoralen-crosslinking and EM visualization, upon optional 1h treatment with CPT 50 nM or MMC 200 nM. In brackets, the number of analyzed molecules. Very similar results were obtained in two biological replicates (Table S2C).

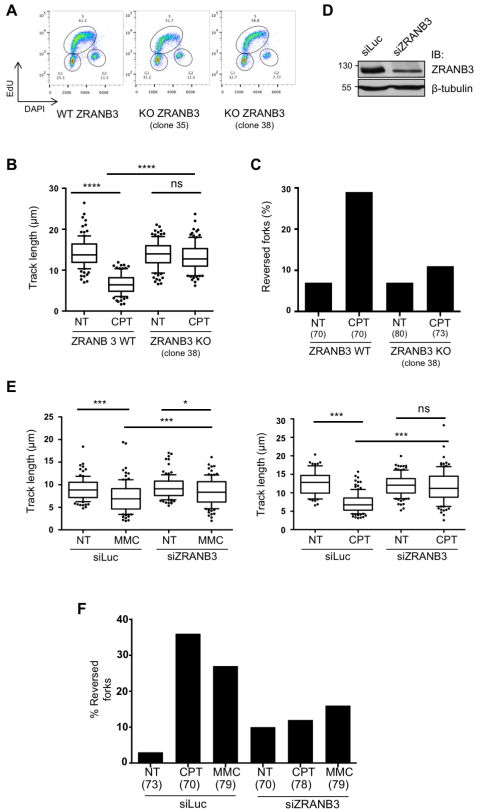

Figure S3, related to Figure 3. ZRANB3 downregulation in U2OS cells leads to unrestrained replication fork progression and reduced reversed fork frequency upon genotoxic treatments. (A) EdU-DAPI FACS experiment showing marginal differences in cell cycle distribution, between wild type (WT) or ZRANB3 knock out (KO) U2OS clones (see Figure 3 and Figure S3B-S3C). (B) Wild type (WT) or ZRANB3-knock-out (ZRANB3-KO) U2OS cells were subjected to the DNA fiber protocol in Figure 1A. At least one hundred tracks were scored per sample. Whiskers: 10-90th percentile (****, P < 0.0001; ns, non-significant, Mann – Whitney test). Similar results were obtained in at least two biological replicates. (C) Frequency of replication fork reversal in WT and ZRANB3-KO U2OS cells, assessed by in vivo psoralen-crosslinking and EM visualization, upon optional 1h treatment with CPT 50 nM. In brackets, the number of analyzed molecules. Similar results were obtained in two biological replicates and in two independent ZRANB3-KO clones (Tables S3A-B). (D) Western Blot showing efficiency of siRNA-mediated ZRANB3 downregulation in U2OS cells. β tubulin, loading control. (E) Control (siLuc) or ZRANB3-depleted (siZRANB3) U2OS cells were subjected to the DNA fiber protocol as in Figure 1A, upon optional treatments with MMC 200 nM (left) or CPT 50 nM (right). At least one hundred tracks were scored per sample. Whiskers: 10-90th percentile (****, P < 0.0001; *, P < 0.5; Mann – Whitney test). Very similar results were obtained in at least two biological replicates. (F) Frequency of replication fork reversal in control (siLuc) or ZRANB3-depleted (siZRANB3) U2OS cells, assessed by in vivo psoralen-crosslinking and EM visualization, upon optional 1h treatment with CPT 50 nM or MMC 200 nM. In brackets, the number of analyzed molecules. Very similar results were obtained in two biological replicates (Table S3C).

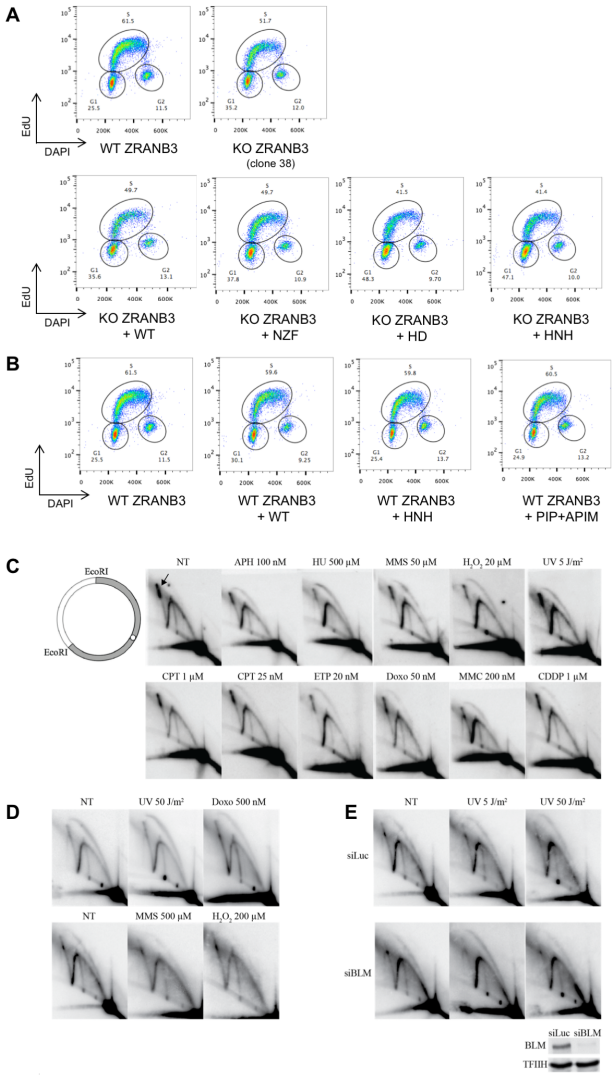

Figure S4, related to Figure 4. See next page.

Figure S4, related to Figure 4. (A-B) EdU-DAPI FACS analysis of cell lines stably expressing HA-ZRANB3 WT or mutant protein. FACS analysis of EdU-incorporation and DAPI illustrating marginal differences in cell cycle distribution among stable cell lines derived from U2OS ZRANB3 KO cell lines (A) and ZRANB3 WT cell lines (B), upon complementation with WT or mutant HA-ZRANB3 (see Figure 4). (C-E) Acute genotoxic treatments and genetic impairment of joint-molecule dissolution do not lead to detectable accumulation of post-replicative sister-chromatid junctions in human cells. Rationale: Depending on repair/replication kinetics and lesion type, cells can tolerate DNA impediments at or behind the replication fork. Lesion bypass at the fork is achieved by switching to a translesion synthesis polymerase (TLS) or by template switching through fork reversal. Single strand gaps behind the fork can be sealed by TLS or by template switching via post-replicative junctions. In Saccharomyces cerevisiae, post-replicative template switching has been extensively studied. X-shaped structures representing post-replicative junctions accumulate in specific genetic conditions, in particular upon impairment of their dissolution by deletion of the yeast RecQ helicase Sgs1 (Branzei et al., 2006; Liberi et al., 2005). Using high-copy number linear minichromosomes, these X-shaped structures were selectively isolated from 2D gels and studied by TEM (Giannattasio et al., 2014). Data: To visualize post-replicative junctions in human cells, we took advantage of an SV40-based episomal system that replicates with very high efficiency and allows isolation of in vivo replication intermediates (Follonier and Lopes, 2014; Follonier et al., 2013). However, neither low (C) nor high (D) dose of various genotoxic treatments did induce detectable accumulation of X-shaped structures, over levels usually detected in untreated cells (arrow). (E) Furthermore, X-shaped structures did not accumulate after downregulation of the human Sgs1 homolog Bloom syndrome protein (BLM), which has been shown to dissolve sister chromatid junctions in human cells (Wu and Hickson, 2003). These data strongly suggest that, contrary to yeast, template switching in human cells occurs primarily at the replication for via fork reversal, which is indeed very abundantly detected and dependent upon error-free PRR factors (see main text). Method: Neutral-neutral 2D-gel analysis of plasmid pML113 transfected into untreated (NT) HEK-293T cells and upon 1 h treatment with the indicated dose of genotoxic drugs. Plasmid was recovered after 40 h and digested by EcoRI as indicated. 2D gel analysis was performed as described (Follonier and Lopes, 2014); the probe reveals replication intermediates in the gray fragment (top left scheme; circle, SV40 replication origin). APH=Aphidicolin, HU=Hydroxyurea, MMS=Methyl Methanesulfonate, H2O2=Hydrogen Peroxide, UV=UV-C irradiation, CPT=Camptothecin, ETP=Etoposide, Doxo=Doxorubicin, MMC=Mitomycin C, CDDP=Cisplatin. Bloom (BLM) levels after siRNA-mediated depletion were detected by immunoblotting. TFIIH, loading control.

A

MEF	WT (clone 2976)	WT (clone 2976)	WT (clone 2976)	PCNA^{K164R} (clone 2978)	PCNA^{K164R} (clone 2978)	PCNA^{K164R} (clone 2978)
CPT	-	+	-	-	+	-
MMC	-	-	+	-	-	+
% RF Exp #1	4 (75)	29 (92)	26 (87)	12 (75)	11 (79)	10 (80)
% RF Exp #2	9 (79)	30 (79)	23 (92)	11 (85)	13 (80)	16 (106)

B

MEF	WT (clone 2977)	WT (clone 2977)	PCNA^{K164R} (clone 2979)	PCNA^{K164R} (clone 2979)
CPT	-	+	-	+
% RF Exp #1	6 (70)	29 (70)	14 (72)	17 (71)
% RF Exp #2	6 (70)	30 (73)	12 (73)	19 (74)

Table S1, related to Figure 1. Electron microscopy data for experiments in Figures 1D and S1B.
(A) Percentage of observed reversed forks (% RF) in two independent EM experiments for samples in Figure 1D.
(B) Percentage of observed reversed forks (% RF) in two independent EM experiments for samples in Figure S1B.
Number of analyzed molecules in brackets.

A

U2OS Ub^{r}-system	WT	WT	WT	K63R	K63R	K63R
CPT	-	+	-	-	+	-
MMC	-	-	+	-	-	+
% RF Exp #1	10 (72)	32 (70)	26 (75)	9 (71)	12 (73)	13 (72)
% RF Exp #2	8 (82)	29 (74)	25 (77)	9 (70)	17 (73)	13 (70)

B

HCT116 UBC13 WT/KO	WT	WT	WT	WT	KO	KO	KO	KO
CPT	-	+	-	-	-	+	-	-
MMC	-	-	+	-	-	-	+	-
UV	-	-	-	+	-	-	-	+
% RF Exp #1	5 (70)	28 (73)	23 (79)	23 (72)	8 (71)	11 (71)	12 (71)	11 (71)
% RF Exp #2	5 (71)	27 (87)	21 (91)	21 (75)	8 (74)	11 (81)	11 (71)	11 (72)

C

U2OS	siluc	siluc	siluc	siUBC13	siUBC13	siUBC13
CPT	-	+	-	-	+	-
MMC	-	-	+	-	-	+
% RF Exp #1	4 (76)	30 (76)	26 (72)	8 (74)	12 (72)	10 (75)
% RF Exp #2	4 (75)	29 (92)	26 (86)	12 (75)	11 (79)	10 (80)

Table S2, related to Figure 2. Electron microscopy data for experiments in Figures 2B, 2E and S2F.
(A) Percentage of observed reversed forks (% RF) in two independent EM experiments for samples in Figure 2B.
(B) Percentage of observed reversed forks (% RF) in two independent EM experiments for samples in Figure 2E.
(C) Percentage of observed reversed forks (% RF) in two independent EM experiments for samples in Figure S2F.
Number of analyzed molecules in brackets.

A

U2OS ZRANB3 WT/KO	WT	WT	WT	WT	KO (clone 35)	KO (clone 35)	KO (clone 35)	KO (clone 35)
CPT	-	+	-	-	-	+	-	-
MMC	-	-	+	-	-	-	+	-
UV	-	-	-	+	-	-	-	+
% RF Exp #1	5 (71)	28 (78)	21 (75)	20 (77)	6 (74)	13 (77)	12 (71)	3 (74)
% RF Exp #2	6 (74)	30 (71)	22 (70)	20 (71)	7 (70)	15 (73)	11 (74)	9 (72)

B

U2OS ZRANB3 WT/KO	WT	WT	KO (clone 38)	KO (clone 38)
CPT	-	+	-	+
% RF Exp #1	7(70)	29 (70)	7 (80)	11 (73)
% RF Exp #2	7(75)	27 (76)	7 (71)	11 (70)

C

U2OS	siluc	siluc	siluc	siZRANB3	siZRANB3	siZRANB3
CPT	-	+	-	-	+	-
MMC	-	-	+	-	-	+
% RF Exp #1	4 (73)	35 (70)	26 (79)	10 (70)	12 (78)	14 (79)
% RF Exp #2	6 (71)	31 (79)	25 (76)	9 (81)	14 (71)	12 (70)

Table S3, related to Figure 3. Electron microscopy data for experiments in Figures 3C, S3C and S3F.
(A) Percentage of observed reversed forks (% RF) in two independent EM experiments for samples in Figure 3C.
(B) Percentage of observed reversed forks (% RF) in two independent EM experiments for samples in Figure S3C.
(C) Percentage of observed reversed forks (% RF) in two independent EM experiments for samples in Figure S3F.
Number of analyzed molecules in brackets.

U2OS ZRANB3 KO (clone 35) - complementation	WT	WT	PIP/APIM	PIP/APIM	NZF-zinc	NZF-zinc
CPT	-	+	-	+	-	+
% RF Exp #1	5 (71)	32 (70)	8 (76)	12 (83)	8 (73)	12 (71)
% RF Exp #2	6 (76)	30 (72)	9 (72)	12 (74)	10 (73)	12 (73)

U2OS ZRANB3 KO (clone 35) - complementation	WT	WT	HD	HD	HNH	HNH
CPT	-	+	-	+	-	+
% RF Exp #1	5 (72)	29 (73)	5 (72)	5 (73)	5 (97)	31 (70)
% RF Exp #2	4 (75)	28 (70)	5 (94)	5 (70)	6 (70)	26 (86)

Table S4, related to Figure 4. Electron microscopy data for experiments in Figure 4C.
Percentage of observed reversed forks (% RF) in two independent EM experiments for samples in Figure 4C.
Number of analyzed molecules in brackets.

Selective loss of PARG restores PARylation and counteracts PARP inhibitor mediated synthetic lethality

This publication establishes that the loss of poly(ADP-ribose) glycohydrolase (PARG) is an important mechanism conferring PARP inhibitor (PARPi) resistance in BRCA2 negative breast cancer. It demonstrates that PARG loss restores normal PARylation levels, rescues controlled replication fork progression and promotes recruitment of downstream DNA repair factors upon PARPi treatment. However, PARG depletion also causes increased cellular radiosensitivity, pointing towards an opportunity for new therapeutic approaches in PARPi resistant breast cancer. Furthermore, the project establishes that PARG-negative cellular clones are present in a subset of human triple-negative breast and serous ovarian cancers, highlighting the potential relevance of PARG loss for PARPi resistance in human malignancies.

My contributions to this project are the fiber spreading analysis in figure 5A and the comet Tail moment values in figure 5B, demonstrating that PARG inhibition rescues controlled fork progression in olaparib and low dose CPT/MMS treated cells and thereby alleviates replication fork breakage. Moreover, I conducted the experiment depicted in figure S5I showing that PARG inhibition also rescues controlled fork progression in cells treated with the PARP inhibitor AZD2461 and low dose CPT. For figure S5J, I provided the Olive moment values extracted from the same comet experiment as presented in figure 5B.

Article

Cancer Cell

Selective Loss of PARG Restores PARylation and Counteracts PARP Inhibitor-Mediated Synthetic Lethality

Graphical Abstract

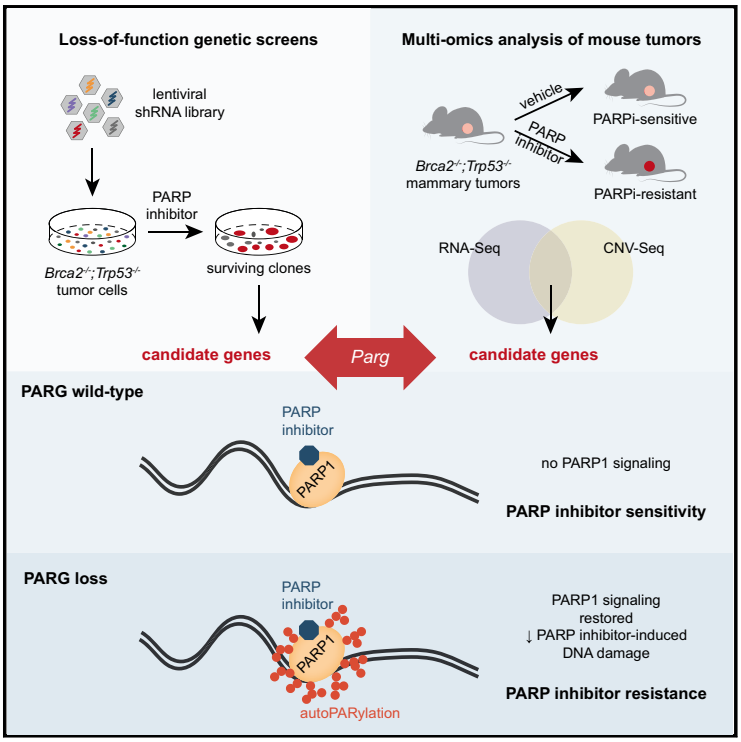

Highlights

- Endogenous PARG activity is crucial for the success of PARP inhibition therapy
- PARG suppression restores downstream PARP1 signaling upon PARP inhibitor treatment
- PARG depletion results in new vulnerabilities that can be exploited therapeutically
- PARG-negative clones are pre-existing in cancers relevant for PARPi therapy

Authors

Ewa Gogola, Alexandra A. Duarte, Julian R. de Ruiter, ..., Piet Borst, Jos Jonkers, Sven Rottenberg

Correspondence

j.jonkers@nki.nl (J.J.), sven.rottenberg@vetsuisse.unibe.ch (S.R.)

In Brief

Gogola et al. show loss of poly(ADP-ribose) glycohydrolase (PARG) confers resistance of BRCA2-deficient tumor cells to PARP inhibition by restoring PAR formation, controlled DNA replication fork progression, and the recruitment of downstream DNA repair factors while sensitizing them to ionizing radiation and temozolomide.

Gogola et al., 2018, Cancer Cell *33*, 1078–1093
June 11, 2018
https://doi.org/10.1016/j.ccell.2018.05.008

CellPress

CellPress

Cancer Cell
Article

Selective Loss of PARG Restores PARylation and Counteracts PARP Inhibitor-Mediated Synthetic Lethality

Ewa Gogola,[1,14] Alexandra A. Duarte,[1,14,16] Julian R. de Ruiter,[1,2,14,16] Wouter W. Wiegant,[6] Jonas A. Schmid,[7] Roebi de Bruijn,[1,2,14] Dominic I. James,[8] Sergi Guerrero Llobet,[9] Daniel J. Vis,[2,14] Stefano Annunziato,[1,14] Bram van den Broek,[3] Marco Barazas,[1,14] Ariena Kersbergen,[5] Marieke van de Ven,[4] Madalena Tarsounas,[10] Donald J. Ogilvie,[8] Marcel van Vugt,[9] Lodewyk F.A. Wessels,[2,14] Jirina Bartkova,[11,12] Irina Gromova,[11] Miguel Andújar-Sánchez,[13] Jiri Bartek,[11,12] Massimo Lopes,[7] Haico van Attikum,[6] Piet Borst,[5] Jos Jonkers,[1,14,*] and Sven Rottenberg[1,15,17,*]

[1]Division of Molecular Pathology, The Netherlands Cancer Institute, Amsterdam 1066CX, the Netherlands
[2]Division of Molecular Carcinogenesis, The Netherlands Cancer Institute, Amsterdam 1066CX, the Netherlands
[3]Division of Cell Biology and BioImaging Facility, The Netherlands Cancer Institute, Amsterdam 1066CX, the Netherlands
[4]Mouse Clinic for Cancer and Aging (MCCA), Preclinical Intervention Unit, The Netherlands Cancer Institute, Amsterdam 1066CX, the Netherlands
[5]Division of Molecular Oncology, The Netherlands Cancer Institute, Amsterdam 1066CX, the Netherlands
[6]Department of Human Genetics, Leiden University Medical Center, Leiden 2333 ZC, the Netherlands
[7]Institute of Molecular Cancer Research, University of Zurich, Zurich CH-8057, Switzerland
[8]Drug Discovery Unit, Cancer Research UK Manchester Institute, University of Manchester, Manchester M20 4BX, UK
[9]Department of Medical Oncology, University Medical Center Groningen, University of Groningen, Groningen 9723GZ, the Netherlands
[10]CRUK/MRC Oxford Institute for Radiation Oncology, University of Oxford, Oxford OX3 7DQ, UK
[11]Danish Cancer Society Research Center, Copenhagen 2100, Denmark
[12]Karolinska Institute, Department of Medical Biochemistry and Biophysics, Division of Genome Biology, Science for Life Laboratory, Stockholm 171 77, Sweden
[13]Pathology Department, Complejo Hospt. Univ. Insular Materno Infantil, Las Palmas, Gran Canaria, Spain
[14]Cancer Genomics Netherlands, Oncode Institute, Amsterdam 1066CX, the Netherlands
[15]Institute of Animal Pathology, Vetsuisse Faculty, University of Bern, Bern 3012, Switzerland
[16]These authors contributed equally
[17]Lead Contact
*Correspondence: j.jonkers@nki.nl (J.J.), sven.rottenberg@vetsuisse.unibe.ch (S.R.)
https://doi.org/10.1016/j.ccell.2018.05.008

SUMMARY

Inhibitors of poly(ADP-ribose) (PAR) polymerase (PARPi) have recently entered the clinic for the treatment of homologous recombination (HR)-deficient cancers. Despite the success of this approach, drug resistance is a clinical hurdle, and we poorly understand how cancer cells escape the deadly effects of PARPi without restoring the HR pathway. By combining genetic screens with multi-omics analysis of matched PARPi-sensitive and -resistant *Brca2*-mutated mouse mammary tumors, we identified loss of PAR glycohydrolase (PARG) as a major resistance mechanism. We also found the presence of PARG-negative clones in a subset of human serous ovarian and triple-negative breast cancers. PARG depletion restores PAR formation and partially rescues PARP1 signaling. Importantly, PARG inactivation exposes vulnerabilities that can be exploited therapeutically.

Significance

To explore defects in the DNA damage response in cancer therapy, exciting opportunities have been achieved using the "synthetic lethal" approach. A successful example is the development of PARP inhibitors to kill cancer cells that are defective in HR; e.g., due to lack of function of BRCA1 or BRCA2. Thus, there is a real opportunity to cure patients with HR-deficient cancers if we overcome the hurdle of drug resistance. At present, it is largely unknown how tumor cells escape PARP inhibition without restoring BRCA2-mediated HR. Here, we show that loss of PARG governs PARPi resistance in HR-deficient tumors by restoring PARP1 signaling. Importantly, inactivation of PARG results in vulnerabilities that can be exploited to combat resistance.

INTRODUCTION

Defects in the DNA damage response (DDR) result in genomic instability and are implicated in many types of cancer (Dietlein et al., 2014). DDR alterations are responsible for the accumulation of mutations that result in tumorigenesis, and they can be specifically exploited for targeted cancer therapy. A prime example of such a tailored approach is the application of poly (ADP-ribose) polymerase (PARP) inhibitors (PARPi) in the treatment of tumors defective in homology-directed DNA repair due to BRCA1 or BRCA2 inactivation (Bryant et al., 2005; Farmer et al., 2005). PARP1, a founding member of the PARP family, is a nuclear protein functioning in various cellular processes, including chromatin remodeling and DNA damage repair (Gibson and Kraus, 2012). Upon DNA damage, PARP1 is rapidly recruited to DNA nicks where it induces the synthesis of protein-conjugated polymers of ADP-ribose (poly(ADP-ribose) [PAR]). PARP1 itself is a prime target of PARylation and the resulting PAR chains serve as a platform for the recruitment of downstream repair factors. PARylation is a transient and reversible modification, as it is counteracted by the activity of PAR glycohydrolase (PARG), which degrades PAR (Pascal and Ellenberger, 2015). Inhibition of PARP1 leads to the accumulation of unresolved single-strand breaks (SSBs) (Xu et al., 2015a). Moreover, several PARPi trap PARP1 onto chromatin (Murai et al., 2012, 2014a), resulting in the collapse of replication forks (RF) that hit trapped PARP1. This leads to DNA double-strand breaks (DSBs) and cells depend on BRCA1/2-mediated repair to resolve these DSBs in an error-free way. Hence, PARP1 inhibition causes synthetic lethality in tumors with defects in homologous recombination (HR) (Bryant et al., 2005; Farmer et al., 2005). Indeed, this lethality was also observed in mouse models for *BRCA1/2*-mutated breast cancer (Evers et al., 2008; Rottenberg et al., 2008) as well as in patients with *BRCA1/2* mutations who developed breast or ovarian cancer (Audeh et al., 2010; Fong et al., 2009; Tutt et al., 2010). On the basis of these positive clinical results, three different PARPi were recently approved as a monotherapy for the treatment of *BRCA1/2*-mutated ovarian cancers (Ohmoto and Yachida, 2017).

Drug resistance often follows the introduction of therapeutics in the clinic, and unfortunately PARPi are no exception (Audeh et al., 2010; Fong et al., 2009). Using cell lines and mouse models, several mechanisms of PARPi resistance have been identified, including upregulation of the P-glycoprotein (P-gp; also known as ABCB1) drug efflux transporter (Evers et al., 2008; Rottenberg et al., 2008) and restoration of HR activity (reviewed in Annunziato et al., 2016). While the clinical significance of P-gp-driven resistance remains controversial, HR restoration has been observed in human tumors that re-established BRCA1/2 function (Edwards et al., 2008; Swisher et al., 2008). Nevertheless, secondary *BRCA1/2* mutations explain only some of the cases of PARPi resistance (Ang et al., 2013). The requirement of BRCA1 for HR activity can be bypassed by the loss of the 53BP1-RIF1-REV7 pathway, as shown by various studies (Annunziato et al., 2016). In contrast, there is no evidence that HR can be rescued in the absence of BRCA2, suggesting that BRCA2-deficient tumors employ distinct, HR-independent pathways to overcome PARPi toxicity.

Little is known thus far about HR-independent resistance to PARPi. Loss of the drug target PARP1 has been described as a mechanism of resistance in HR-proficient cells (Pettitt et al., 2013), but this cannot explain resistance in the PARPi target group, since PARP1 loss causes synthetic lethality of BRCA1/2-mutated cells (Bryant et al., 2005; Farmer et al., 2005). In this study, we set out to determine how cells with an irreversible and complete defect in the HR pathway develop PARPi resistance.

RESULTS

Functional Genetic Screens Identify Loss of PARG as a PARPi Resistance Factor

To identify HR-independent mechanisms of PARPi resistance, we carried out functional genetic screens in two types of *in vitro* cultures that we derived from *Brca2*$^{-/-}$;*Trp53*$^{-/-}$ mouse mammary tumors from *K14cre;Trp53*$^{F/F}$;*Brca2*$^{F/F}$ (KB2P) mice: two-dimensional (2D) tumor cell lines (KB2P1.21, KB2P3.4) and three-dimensional (3D) cancer organoids (ORG-KB2P26S.1) (Jonkers et al., 2001; Evers et al., 2008; Duarte et al., 2018). In these cells we introduced a library of 1,976 short hairpin RNA (shRNA) constructs targeting 391 DDR-related genes (on average five shRNAs/gene) (Xu et al., 2015b). The cells were then selected for 3 weeks with the PARPi olaparib or AZD2461 (Figure 1A) at a concentration lethal to the parental cells (data not shown). Sequencing of PARPi-surviving populations revealed a reproducible enrichment of multiple hairpins targeting PARG. The strong effect of PARG depletion is reflected by the overall top score of *Parg* among all positively selected genes, as determined by the MAGeCK (Model-based Analysis of Genome-wide CRISPR-Cas9 Knockout) algorithm (Li et al., 2014) (Figures 1B and 1C; Table S1). We applied the same screening approach to a cell line isolated from BRCA-proficient mouse mammary tumors from *K14cre;Trp53*$^{F/F}$ (KP) mice (Evers et al., 2008) and also identified *Parg* among the top outliers. In fact, *Parg* was the only common hit in both BRCA-deficient and -proficient screens (Figures 1D and 1E). In contrast, shRNAs targeting PARP1 were only enriched in the BRCA-proficient KP3.33 cells (Figures 1C–1E), providing functional evidence that PARP1 loss confers PARPi resistance in BRCA-proficient cells, presumably by preventing PARP1 trapping, but not in BRCA2-deficient cells that depend on PARP1 for survival.

PARG Is Frequently Lost in PARPi-Resistant KB2P Mouse Mammary Tumors

Although high-throughput genetic screens are powerful tools for the identification of gene candidates, *in vitro* conditions do not fully recapitulate the complexity of drug response observed in real tumors. We therefore generated a panel of KB2P mouse mammary tumors that had acquired PARPi resistance *in vivo*. For this purpose, 21 individual spontaneous KB2P carcinomas were orthotopically transplanted into multiple syngeneic mice to allow differential treatment of the original donor tumor. Upon outgrowth, the tumors were either treated with vehicle control or with the PARPi AZD2461 (Figure 2A). As expected, KB2P tumors were initially highly sensitive to PARPi treatment but eventually developed drug resistance (Figures 2B and 2C). The observed resistance cannot be explained by BRCA2 restoration,

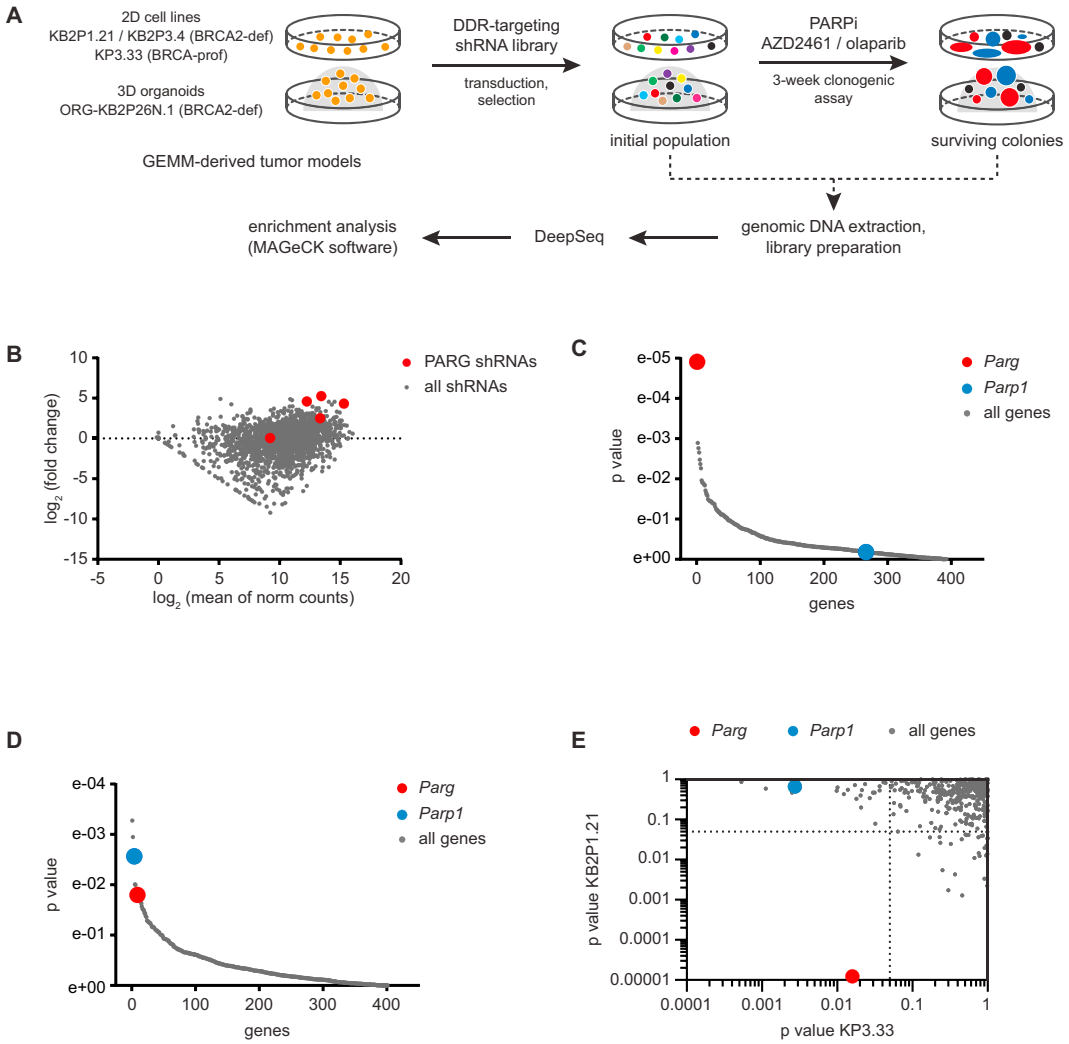

Figure 1. Functional shRNA-Based Screens in BRCA2-Deficient and -Proficient Cells Identify PARG as PARPi Resistance Factor

(A) Outline of the functional shRNA screen.

(B) Log ratio (fold change) versus abundance (mean of norm counts) plot representing the screening outcome in KB2P1.21 cells treated with AZD2461.

(C and D) Distribution of the one-sided p value (gene enrichment) for all 391 genes targeted by the shRNA-based library in KB2P1.21 cells (C) and KP3.33 (D) cells upon PARPi treatment.

(E) Comparison of the screening outcome between indicated cell lines; dotted grid line indicates p value = 0.05. All p values were generated per gene with MAGeCK software; each screen was performed and analyzed in triplicate.

See also Table S1.

which is prevented by the irreversible intragenic deletion in *Brca2*, nor by upregulation of P-gp (Figure S1A), because of the low affinity of AZD4261 to this transporter (Jaspers et al., 2013; Oplustil O'Connor et al., 2016).

Our extensive *in vivo* studies yielded a unique collection of matched PARPi-naive (n = 21) and PARPi-resistant tumors (n = 34; for some of the donors more than one resistant tumor was generated). We have recently shown that the resistance phenotype is stable upon transplantation into allografts (Duarte et al., 2018; Ray Chaudhuri et al., 2016). We now used this collection of tumors to identify genetic factors contributing to PARPi resistance. For this purpose, we generated transcriptome (RNA sequencing [RNA-seq]) and DNA copy-number variation (CNV) sequencing (CNV-seq) data for all tumors and carried out an integrative analysis of naive versus resistant samples (Figures 2D and 2E). First, we identified differentially expressed genes using the DIDS (detection of imbalanced differential signal) algorithm (cutoff $p < 0.05$), which is specifically designed for the detection of subgroup markers in heterogeneous populations (de Ronde et al., 2013). In parallel, we selected acquired copy-number events, present only in resistant, but not in naive, samples. Since KB2P tumors exhibit high levels of genomic instability and

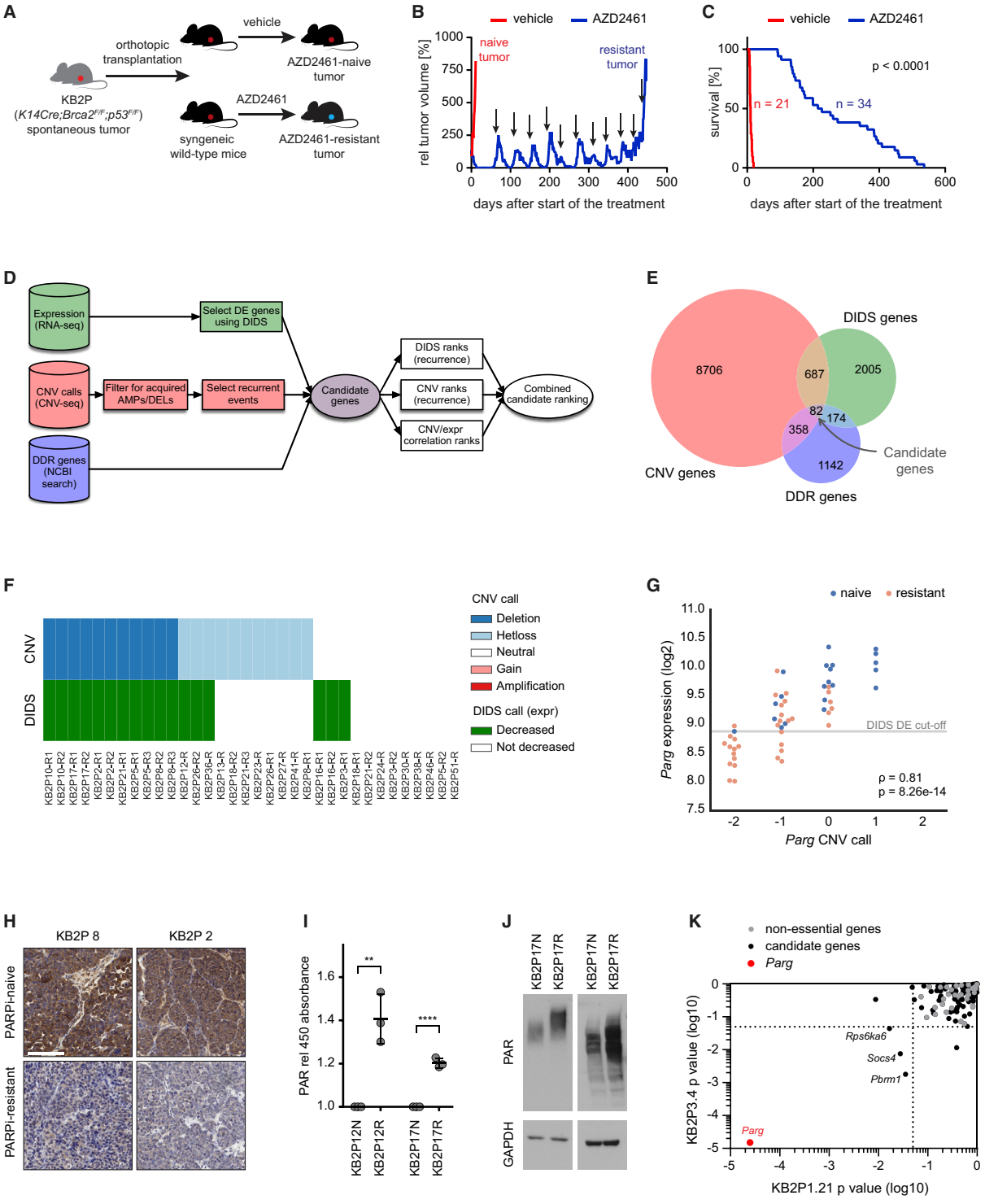

Figure 2. PARG Is Frequently Lost in KB2P Tumors That Acquired PARPi Resistance *In Vivo*

(A) Generation of matched PARPi-naive and -resistant KB2P tumors.

(B) Treatment response of individual KB2P tumor treated with either vehicle or AZD2461, orally for 28 consecutive days. Treatment was resumed when the tumors reached a size of 100% (initial volume at the start of the treatment) and the treatment cycles were repeated until acquired resistance (black arrows mark the beginning of repeated cycles). Graph shows relative tumor volume as a function of time.

(legend continued on next page)

accumulate many genetic alterations, we decided to focus on DDR-related genes, as their contribution to the PARPi response is most plausible. We generated a list of approximately 1,800 genes that have been implicated in DDR processes (Table S2) and combined it with the significant hits from the DIDS and CNV analyses. The 82 genes that survived these selection criteria were ranked based on their recurrence or correlation between expression and CNV data. To integrate these rankings, we used three different aggregation statistics: mean aggregation, Stuart aggregation, and robust rank aggregation (RRA) (Kolde et al., 2012). Consistent with our *in vitro* screens, all three algorithms placed *Parg* at the top of the list of gene candidates (Table S3). *Parg* also ranked among the top outliers in a non-curated, genome-wide comparison (Table S3). In our panel of 34 PARPi-resistant tumors, we observed decreased expression of *Parg* in 17 tumors, and acquired copy-number loss of the *Parg* locus in 22 tumors (11 deletions, 11 heterozygous loss events), with a substantial overlap between both datasets (Figures 2F, 2G, and S1B). The difference in PARG levels between PARPi-naive and -resistant tumors was also confirmed by immunohistochemistry (IHC) (Figure 2H). Blinded semi-quantitative analysis of the PARG staining revealed a significant difference between resistant versus naive samples ($p < 0.015$, Mann-Whitney U test). This was further validated using an ELISA assay in which we monitored the loss of biotinylated PAR from immobilized histones and thereby directly measured the relative activity of endogenous PARG in 3D cancer organoids derived from PARG-deficient PARPi-resistant tumors and PARPi-sensitive controls (Figure 2I). As expected, PARPi-resistant organoids showed reduced ability to degrade synthetic PAR (Figure 2I) and overall exhibited elevated levels of endogenous PAR (Figure 2J).

To investigate the contribution of the other candidate genes to PARPi resistance, we performed a secondary genetic loss-of-function screen using an shRNA library targeting the identified candidates and 32 non-essential genes as internal controls (Table S4). *Parg* was again identified as a top outlier by the enrichment analysis in both KB2P cell lines (Figure 2K and Table S1), suggesting that loss of PARG is one of the strongest mechanisms involved in PARPi resistance in our model.

To test whether PARPi-induced loss of PARG is specific to KB2P tumors, we also studied genetic alterations in *Parg* in our previously described collection of PARPi-naive and -resistant BRCA1-deficient mammary tumors from *K14cre;Brca1*$^{F/F}$*;Trp53*$^{F/F}$ (KB1P) mice (Jaspers et al., 2013). Also in this cohort, combined RNA-seq and CNV-seq analysis identified several PARPi-resistant tumors with significantly lower expression and acquired copy-number loss of *Parg* (Figure S1C). Taken together, our *in vivo* data confirm and extend the results from the *in vitro* screens and suggest that PARG depletion alleviates PARPi toxicity.

PARG Downregulation Causes PARPi Resistance *In Vitro*

To validate the role of PARG depletion in PARPi resistance, we introduced two individual shRNAs against PARG (PARG sh1, PARG sh4) in KB2P1.21 and KB2P3.4 cells, resulting in substantial decrease of *Parg* mRNA levels (Figures 3A and S2A) and reduced PARG activity (Figures 3B and S2B) Consistently, genetic depletion of PARG in KB2P cells led to the accumulation of PAR under genotoxic stress induced by the alkylating agent methyl methanesulfonate (MMS) (Figures S2C and S2D) but did not affect *Parp1* expression levels (Figure S2E).

The shRNA-mediated loss of PARG resulted in increased resistance to the PARPi olaparib and AZD2461 in long-term clonogenic survival assays. This effect was observed in cell lines derived from both KB2P and KB1P tumor models, in which PARPi-induced loss of PARG was observed *in vivo* (Figures 3C and S3A–S3C). To exclude off-target effects of the shRNAs, we also targeted the *Parg* locus in KB2P cells using CRISPR-Cas9 technology (Figures 3D and S3D–S3F). In contrast to the control cells, *Parg*-targeted cells formed many resistant colonies after 14 days of PARPi selection. This effect was specific to *Parg* inactivation, as shown by the TIDE (Tracking of Indels by Decomposition) analysis (Brinkman et al., 2014). In the initial tumor cell population, roughly half of the alleles carried frameshift mutations, and vehicle (DMSO) treatment did not significantly affect allele composition. In contrast, PARPi selection resulted in a substantial increase in frameshift disruptions (>90%), showing that the surviving populations are predominantly PARG deficient (Figures 3D and S3D–S3F, Table S5).

We obtained further evidence for the role of PARG in PARPi resistance with a recently developed small-molecule PARG inhibitor (PARGi) PDDX-004 (PDD00017272), which is very active against mouse PARG (James et al., 2016a). In line with this, PDDX-004 caused a dose-dependent accumulation of nuclear PAR upon MMS-induced DNA damage in our cell lines (Figures S3G and S3H). Consistent with our genetic inhibition experiments, the clonogenic assays in KB2P cells also showed an increased PARPi survival upon chemical inhibition of PARG (Figures 3E and S3I). Moreover, the viability of cells exposed to the

(C) Kaplan-Meier curve showing overall survival of mice bearing KB2P tumors treated with either vehicle or AZD2461. Log rank (Mantel-Cox) p value is indicated.
(D) Flowchart illustrating the steps of multi-omics approach used for the discovery of resistance factors in a panel of KB2P tumors.
(E and F) (E) Venn diagram showing overlap of potential gene candidates identified within indicated datasets. (F) Overview of genomic alterations in *Parg* acquired by a panel of 34 KB2P PARPi-resistant tumors (KB2Px-Ry: x, original donor identification [ID] number; y, ID of individual resistant tumors derived from the same donor tumor).
(G) Correlation between *Parg* expression and copy-number estimation for the whole panel of KB2P tumors. Spearman correlation coefficient (ρ), p value, and expression threshold generated by DIDS algorithm (gray line) are indicated.
(H) Representative images of PARG IHC staining in KB2P tumors; scale bar, 100 μm.
(I) ELISA-based PARG activity assay in tumor organoids (N, naive; R, resistant); $^{**}p < 0.01$, $^{****}p < 0.0001$ (two-tailed t test); experiment repeated three times, data presented as mean ± SD of replicates.
(J) Western blot analysis of PAR in tumor-derived organoids; data representative of two independent experiments.
(K) Enrichment analysis of the secondary genetic screen in KB2P cells: comparison of the p values for all genes targeted, shown for the cell lines indicated; one-sided p value was determined by the MAGeCK algorithm; the screen was performed in triplicate.
See also Figure S1 and Tables S1–S4).

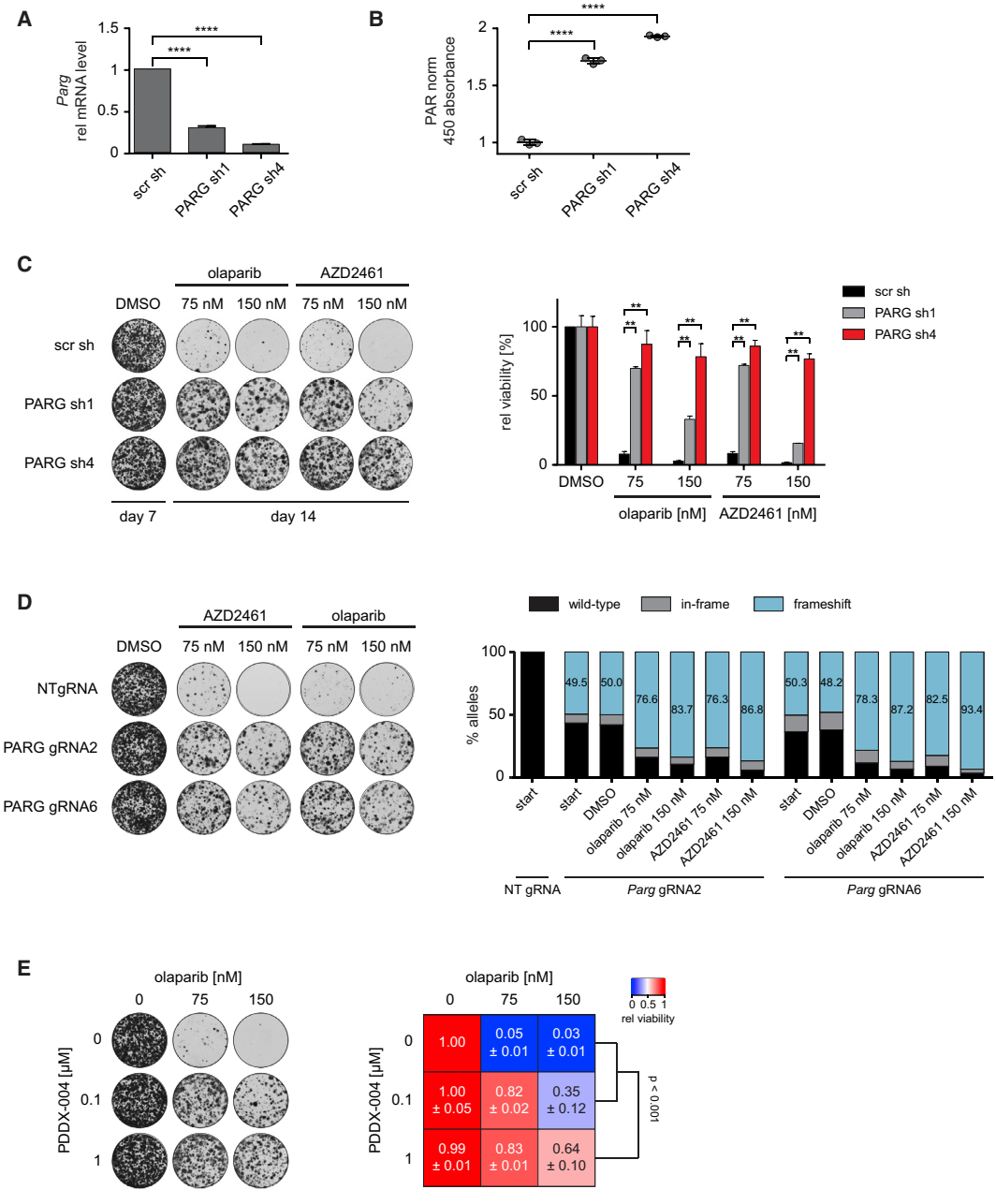

Figure 3. Downregulation of PARG Causes PARPi Resistance in BRCA2-Deficient Cells *In Vitro*

(A and B) (A) RT-qPCR analysis of *Parg* expression levels in KB2P1.21 cell lines expressing indicated shRNAs; data represent mean ± SD of triplicate; ****$p < 0.001$ (two-tailed t test). (B) PAR ELISA assay in KB2P1.21 cells; data shown as mean ± SD of triplicate, ****$p < 0.001$ (two-tailed t test).

(C) Representative images (left) and quantification (right) of long-term clonogenic assay with KB2P1.21 cells, treated with PARPi or untreated (DMSO). Data represent mean ± SD of three independent repeats; **$p < 0.01$ (t test).

(D) Representative images (left) and TIDE quantification (right) of long-term clonogenic assay with KB2P1.21 cells expressing indicated guide RNAs.

(E) Representative images (left) and quantification (right) of long-term clonogenic assay with KB2P1.21 cells treated as indicated. The experiment was repeated three times; data plotted as mean ± SD; $p < 0.001$ (ANOVA).

See also Figures S2 and S3 and Table S5.

combination of PARPi and PARGi correlated with the degree of PARG inhibition, while PDDX-004 alone did not affect cell growth nor PARPi response of PARG-depleted cells (Figure S3J). In conclusion, both genetic depletion or inactivation and chemical inhibition of PARG lead to PARPi resistance in KB2P cells, confirming an important functional role of PARG in mediating PARPi toxicity.

PARG-Depleted KB2P Cells Remain HR Deficient and Fail to Protect Stalled RF

The sequence of events that leads to PARPi-induced death of BRCA-deficient cells includes the inhibition of PAR synthesis, RF collapse, and the formation of DSBs. In collaboration with the Nussenzweig laboratory, we have recently shown that RF protection can explain resistance in some of the PARPi-resistant KB2P mouse mammary tumors (Ray Chaudhuri et al., 2016). Given its role in PAR catabolism, however, we did not expect that the tumors in which we find PARG downregulation would correct the BRCA2 defect by protecting stalled RFs or by BRCA2-independent restoration of HR. To verify this, we measured the capacity of PARG-depleted KB2P cells to protect stalled RF using DNA fiber assays. In both control and PARG knockdown KB2P cells, the induction of replication stress resulted in the degradation of nascent tracts (Figure S4A), suggesting that PARG loss cannot bypass the requirement of BRCA2 for RF stabilization. Next, we assessed the capability of KB2P cells to form RAD51 ionizing radiation (IR)-induced foci (IRIF), a hallmark of HR activity. As expected, we did not detect any RAD51 IRIF in KB2P cells, regardless of *Parg* expression levels (Figures S4B and S4C). Moreover, the same phenotype was observed in PARPi-resistant KB2P tumors, in which PARG loss was confirmed at the genomic level (Figure S4D). These results demonstrate that loss of PARG causes PARPi resistance independently of BRCA2 and that resistance cannot be explained by HR restoration or RF protection.

PARG Downregulation Rescues PARylation upon PARPi Treatment

To assess how PARG depletion causes PARPi resistance, we studied its effect on PARylation. Upon PARPi treatment, inhibition of PARP enzymes serves as the major barrier to PAR formation, but this is reinforced by the PARG-mediated degradation of PAR, which acts in the same direction as PARPi. We therefore hypothesized that PARPi alone do not fully inhibit PARP and loss of PARG would allow sufficient PAR formation in the presence of PARPi. We tested this hypothesis by measuring endogenous PAR levels in KB2P cells treated with the PARPi olaparib and the PARGi PDDX-004 (Figure 4A). To discriminate between stabilization of pre-existing and *de novo* synthesized PAR, we first incubated cells with the inhibitors for 1 hr and then exposed them to MMS to stimulate PARP activity. As predicted, olaparib treatment resulted in a strong reduction of PAR, already at nanomolar doses. Inhibition of PARG overcame this reduction, and MMS treatment led to a further increase of the PAR signal. These data indicate that olaparib concentrations sufficient to kill cells do not completely inhibit PARP and that this residual activity is sufficient for PAR formation if PARG activity is suppressed. We conclude that endogenous PARG activity is required for efficient inhibition of PAR signaling by PARPi.

We next investigated the effect of different PARP family members on the PARPi response using BRCA-proficient KP3.33 cells, in which CRISPR/Cas9-mediated disruption of *Parp1*, *Parp2*, or *Parp3* was well tolerated (Figures S5A–S5C). While the PARPi sensitivity of *Parp2*$^{-/-}$ and *Parp3*$^{-/-}$ KP3.33 cells was significantly reduced by PARG inhibition, *Parp1* depletion resulted in partial resistance to olaparib (consistent with Murai et al., 2012), which was not further increased by PARGi treatment (Figure S5D). This result is in line with a previous report suggesting that up to 90% of cellular PAR results from PARP1 activity (Kim et al., 2005) and shows that PARG-related PARPi resistance is mainly mediated by PARP1 signaling.

PARG Inhibition Reduces PARP1-DNA Complexes Induced by PARPi Treatment

It has been shown that PARP1 association to and dissociation from chromatin is regulated by its PARylation (Pascal and Ellenberger, 2015) and persistent PARP1-DNA complexes, induced by clinical PARPi, are toxic to cells (Murai et al., 2012). We therefore measured the levels of chromatin-bound PARP1 in KB2P cells using a previously described trapping assay (Murai et al., 2012). Immunoblot analysis showed olaparib-dependent accumulation of PARP1 in chromatin fractions, which was reduced in cells expressing PARG-targeting shRNAs (Figure 4B). Since stable PARG depletion could result in a substantial proportion of free PARP1 in a PARylated state, and therefore lower its affinity to chromatin, we repeated the PARP1 trapping assay in cells exposed to short-time inhibition of PARG (Figure 4C). Although single treatment with PDDX-004 led to decreased levels of chromatin-associated PARP1, simultaneous inhibition of both PARP1 and PARG resulted in PARP1 trapping comparable with olaparib alone. We further corroborated this finding by measuring PARP1 association kinetics at multiphoton laser-induced DNA damage sites in U2OS cells (Figures 4D and 4E). Cells were exposed to 0.5 μM olaparib and/or the PARGi PDDX-001/PDD00017273 (1 μM) (James et al., 2016a), which alone efficiently inhibited downstream signaling of both proteins (Figures S5E–S5G). We utilized U2OS GFP-PARP1 cells and quantified the intensities of laser tracks; first, 1 min post irradiation, when under native conditions PARP1 accumulation reached a maximum, and then 15 min after the induction of DNA damage, when most of the chromatin evicted PARP1 (Figure S5H). Both olaparib treatment alone and the combination with PDDX-001 resulted in a slight increase of chromatin-associated PARP1 15 min post irradiation (Figures 4D and 4E). Of note, even more PARP1 protein remained associated with damaged sites in cells exposed to PARGi only. The results, however, do not show any evidence that PARG depletion results in more rapid release of chromatin-bound PARP1. Taken together, our data demonstrate that PARG depletion does not enhance PARP1 dissociation from chromatin and therefore do not diminish PARP1 trapping *per se*. Instead, long-term suppression of PARG prevents excessive PARP1 binding and thus reduces PARPi-dependent accumulation of toxic PARP1-DNA complexes. The relevance of this finding is further supported by the fact that PARG depletion also results in resistance to talazoparib, a highly potent PARP1-DNA trapping agent in clinical use (Figure 4F).

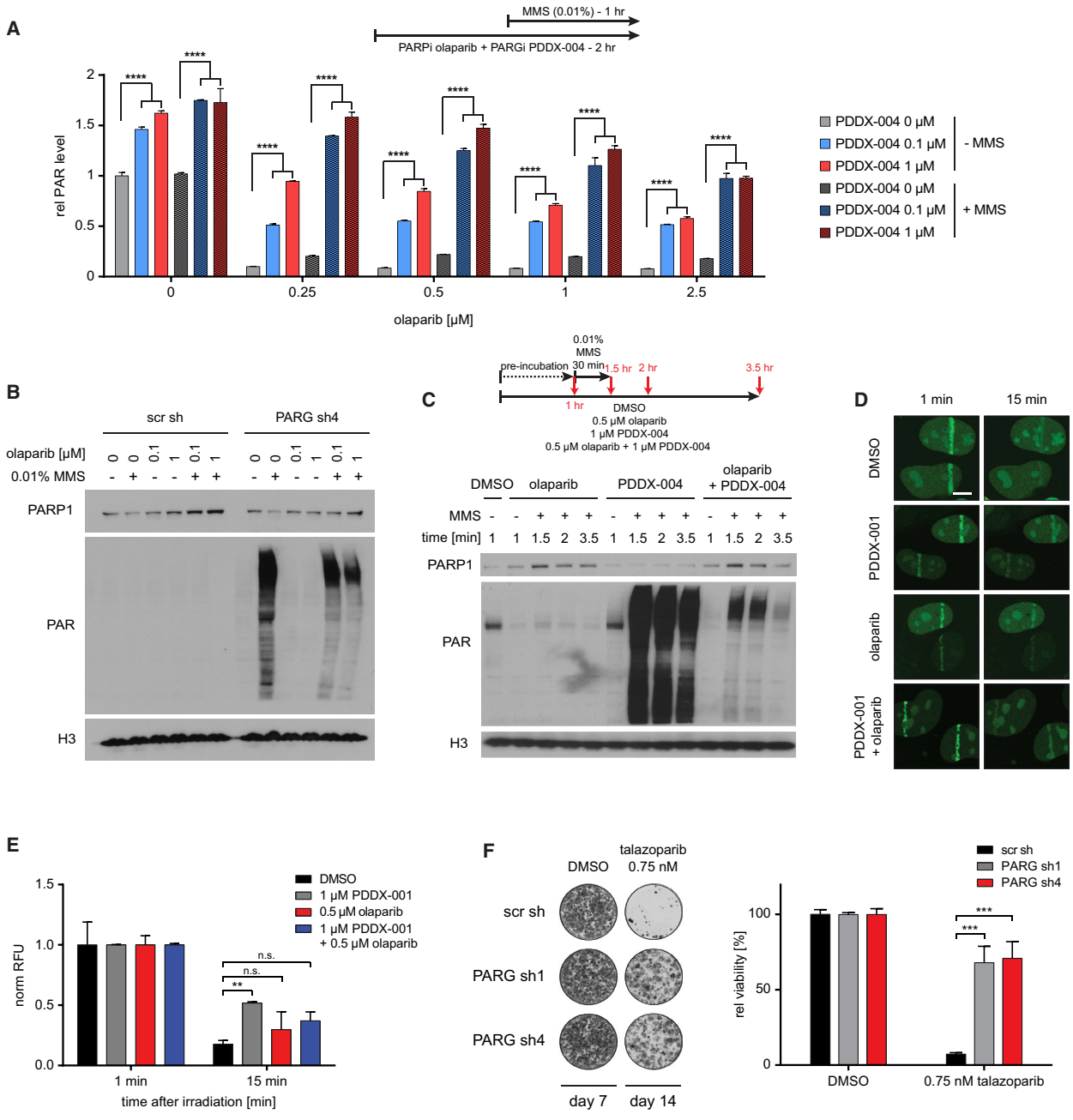

Figure 4. PARG Deficiency Partially Rescues PARylation and Reduces the Accumulation of PARP1-DNA Complexes

(A) ELISA PAR assay in KB2P3.4 cells treated as indicated; data shown as mean ± SD of triplicate (t test). ****p < 0.0001

(B and C) Immunoblot analysis of PARP1 in chromatin-bound fractions upon genetic (B) and chemical (C) inhibition of PARG in KB2P cells, treated as indicated; data representative for two independent experiments.

(D and E) Representative images (left) and quantification (right) of analysis of PARP1 recruitment kinetics to multiphoton tracks in U2OS PARP1-GFP cells, following the indicated treatments. **p < 0.01; n.s., not significant; two-tailed t test, data represented as mean ± SEM. Scale bar, 10 μm.

(F) Representative images of stained wells (right) and quantification (left) of clonogenic assay in KB2P cells expressing the indicated shRNAs and treated with talazoparib; data presented as mean ± SD of two experiments; ***p < 0.001 (two-tailed t test).

See also Figures S4 and S5.

PARG Depletion Alleviates PARPi-Induced DNA Damage

Following different forms of genotoxic stress, PARP1 activity has recently been shown to limit the rate of RF progression (Sugimura et al., 2008; Ray Chaudhuri et al., 2012) by modulating fork reversal and preventing premature restart of reversed RF (Berti et al., 2013; Zellweger et al., 2015). Deregulated RF remodeling by PARP inhibition was suggested to contribute to the synthetic lethality of PARPi with HR defects, as it increases the fraction of SSBs being processed into DSBs (Neelsen and Lopes, 2015). As shown in Figure 5A, we confirmed that PARPi treatment increases the DNA fiber track length upon induction of DNA damage with MMS or camptothecin (CPT). When PARG was also inhibited in these cells, the track length was significantly decreased, suggesting that PARG depletion prevents unrestrained RF progression in PARPi-treated cells (Figures 5A and S5I). Concomitantly, PARG inhibition reduced the formation of DSBs in these cells, as measured by the neutral comet assay (Figures 5B and S5J).

Given the role of PARP1 in DNA repair, we next investigated the PARP1-mediated recruitment of the scaffold protein XRCC1, a PAR interactor and a key player in the BER pathway (Nazarkina et al., 2007). To study the effects of PARPi and/or PARGi on XRCC1 recruitment, we applied the laser micro-irradiation assay to U2OS cells expressing a XRCC1-GFP fusion protein. We found that under drug-free conditions XRCC1-GFP was rapidly recruited to sites of laser-induced DNA damage (Figures 5C and 5D). Although a large proportion of the protein dissociated from chromatin within 60 min after irradiation, a substantial amount of XRCC1-GFP remained at the sites of DNA damage. In line with previous reports (Kim et al., 2015), treatment of cells with the PARPi olaparib abrogated XRCC1-GFP localization to laser-inflicted damage (Figures 5C and 5D). Inhibition of PARG mitigated the inhibitory effect of olaparib, however, and partially rescued XRCC1-GFP recruitment. Importantly, the quantitative analysis of laser track intensities showed that the restored accumulation, although delayed in time, resulted in a similar retention of XRCC1-GFP at 1 hr post irradiation as in the control cells (Figures 5C and 5D). This effect of PARGi is specific to PARylation-induced recruitment of DNA repair factors, as we did not observe any differences in chromatin association of MDC1, which localizes to damaged sites in a PARP1-independent manner (Yan et al., 2013) (Figure 5E). As a readout for PARP1 function in the repair of SSBs, we employed the previously described Fast Micromethod SSB assay (Schröder et al., 2006). Consistent with our previous results, *Parg*-depleted cells exhibited increased capacity to repair SSBs in comparison with control cells (Figure 5F). This was further confirmed in cells exposed to olaparib for 24 hr. Immunofluorescence (IF) analysis of γH2AX foci revealed that *Parg*-depleted cells accumulated less olaparib-induced DNA damage (Figure 5G).

Based on our data, we conclude that PARG suppression not only reduces PARP1-DNA complexes but also rescues controlled RF progression and promotes the recruitment of DNA repair enzymes to sites of damage in cells exposed to PARPi. Altogether, this leads to a reduction of PARPi-induced DNA damage and improved PARPi survival (Figure 5H).

PARG Deficiency Overcomes PARPi Toxicity in Human Cancer Cells

The anticancer efficacy of PARPi has been validated in various clinical studies and several PARPi were recently approved for the treatment of patients with *BRCA1/2*-mutated tumors. We therefore determined whether PARG depletion confers PARPi resistance in human cancer cells by introducing two individual shRNAs targeting PARG in *BRCA1*-mutated SUM149PT (carrying a protein-truncating 2288delT mutation) and BRCA2-deficient DLD-1 cells. Both shRNAs efficiently suppressed PARG expression and conferred resistance to olaparib (Figures 6A, 6B, and S6A). Similarly, chemical inhibition of PARG led to increased survival of both cell lines in the presence of PARPi (Figures S6B and S6C).

Given that PARG loss causes PARPi resistance independently of BRCA1/2, we extended our analysis to a recently published pharmacogenomics dataset of 1,001 human cancer cell lines (Iorio et al., 2016). In particular, we assessed the correlation between half maximal inhibitory concentration (IC_{50}) values of PARPi and gene expression levels of 1,800 DDR-related factors (Table S2). Gene expression data and drug responses to four different PARPi (olaparib, veliparib, rucaparib, and talazoparib) were available for 935 cell lines from this panel. Statistical analysis revealed a significant negative association between *PARG* expression and IC_{50} values of all four PARPi (Figures 6C and S6D); i.e., higher *PARG* RNA levels were related to increased sensitivity to these drugs. A similar negative association was also observed for *PARP1* gene expression, in agreement with the concept that more PARP1 leads to more trapping of PARP1 onto DNA in the presence of PARPi.

PARG Depletion Occurs in Triple-Negative Breast and Serous Ovarian Cancer

To further assess the clinical relevance of PARG depletion, we measured the heterogeneity of PARG expression in large sections of 56 treatment-naive triple-negative human breast cancer (TNBC) biopsies from high-risk women eligible for PARPi treatment (Cabezón et al., 2013; Gromova et al., 2015). IHC analysis (Figures 6D, 6E, and S6E) revealed that, although PARG protein was expressed in a vast majority of the biopsies, PARG-negative areas were found in a sizable proportion of samples. Specifically, 29 (52%) and 14 (25%) out of 56 cancers showed lack of PARG in areas corresponding to >10% and >20% of the tumor, respectively. Moreover, PARG-negative cells were positive for PAR, and in some of the samples PAR levels were substantially increased (Figure 6E). Of note, the variable degree of PAR could also reflect the degree of the endogenous DNA damage among the cases, as PARP enzymes are activated by DNA damage and these patients did not receive any genotoxic therapy. A similar PARG expression spectrum was also found in a cohort of serous ovarian carcinomas (Moudry et al., 2016), a cancer type that has been recently approved for PARPi treatment (Figures 6D and S6F). Taken together, our data show that PARG-depleted cells pre-exist in a substantial proportion of clinically relevant tumors and could potentially be selected by PARPi treatment.

PARG Suppression Results in Acquired Vulnerabilities

Molecular alterations that render cells resistant to targeted therapies may also cause synthetic dependencies, which in turn

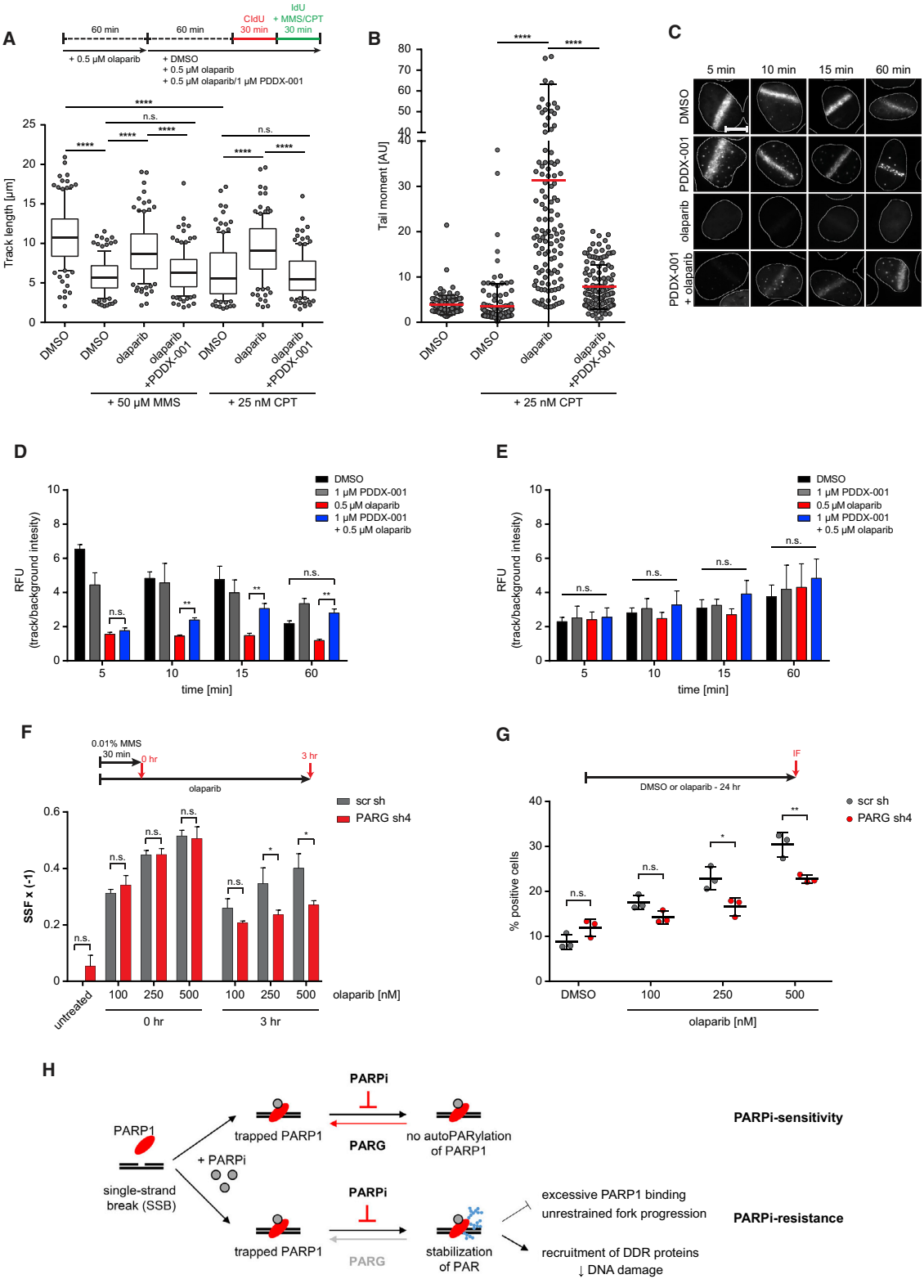

(legend on next page)

could be exploited therapeutically to prevent cancer progression. Perturbed PAR signaling due to downregulation of PARG has been shown to increase the sensitivity to IR (Amé et al., 2009). Susceptibility to IR is also one of the characteristics of cells with dysfunctional BRCA1/2 proteins (Kan and Zhang, 2015). We therefore set out to determine whether PARG suppression could potentiate IR toxicity in *BRCA1/2*-mutated cells. For this purpose, SUM149PT cells with shRNA-mediated PARG knockdown were exposed to a range of IR doses and grown for another 7 days. Viability measures showed increased IR sensitivity of PARG-depleted cells in comparison with control populations (Figure 6F). Furthermore, dose-dependent sensitization was also achieved by chemical inhibition of PARG in SUM149PT, BRCA2-deficient DLD-1, and KB2P cells (Figures 6G, 6H, and S6G). Notably, we also observed synergistic effects between PARG inhibition and treatment with temozolomide (Figures 6I and S6H), an alkylating agent that has been previously shown to potentiate PARPi toxicity (Murai et al., 2014b).

Together, these results illustrate that PARG suppression, although detrimental to PARPi efficacy, provides therapeutic vulnerabilities that could be used to target resistant tumors.

DISCUSSION

In this study, we show that loss of PARG is a frequent mechanism of PARPi resistance in *Brca2*-mutated tumors. Our data provide an HR-independent mechanism for tumor cells to adapt their DDR in order to escape the lethal effects of PARPi. PARG is the main enzyme responsible for degrading nuclear PAR and thereby counteracting the action of PARP enzymes. Hence, PARG works in the same direction as PARPi and prevents PAR accumulation. Our finding that PARG depletion causes PARPi resistance in BRCA2-deficient tumors highlights an important aspect of PARPi therapy: the endogenous PARG activity in tumor cells is crucial for therapy success. As PARPi do not fully block PARP activity, loss of PARG activity is sufficient to restore PAR formation and rescue downstream signaling of PARP1.

Within the PARP family of ADP-ribosyltransferases, three family members, PARP1, PARP2, and PARP3, have been linked to DNA repair (Sousa et al., 2012). PARP1 is the most abundant of these and has been shown to play critical roles in the DDR (De Lorenzo et al., 2013). Upon DNA damage, RFs are rapidly and globally reversed and are maintained in the reversed state by transient PARP-mediated inhibitory ADP ribosylation of RECQ1 helicase, the enzymatic activity specifically required for restart of reversed RFs (Berti et al., 2013; Zellweger et al., 2015). In this way, PARP1 represents a molecular switch to control transient fork reversal and RF restart following genotoxic stress (Zellweger et al., 2015). Neelsen and Lopes (2015) therefore suggested that the synthetic lethality of PARPi with HR defects results not only from an increasing load of SSBs but also from a greater fraction of these lesions being processed into DSBs. Whereas untreated cells gain extra time to repair DNA damage through RF reversal, PARPi-treated cells are unable to reverse forks efficiently, resulting in increased DNA breakage and the requirement for HR-mediated DSB repair. In line with this hypothesis, we found that PARG depletion restores controlled RF progression in the presence of PARPi and reduces subsequent DNA damage. We also found a mechanism at the level of DNA repair that contributes to PARPi resistance induced by PARG loss: PAR stabilization rescues the recruitment of the downstream scaffolding protein XRCC1, which is known to bring together a variety of components required for efficient SSB repair (Horton et al., 2008).

In BRCA-proficient tumors, the toxic effect of PARPi can also be counteracted by the loss of the drug target PARP1. Consistent with the data of Pettitt et al. (2013), we found a significant enrichment for *Parp1*-targeting shRNAs in our drug resistance screen in BRCA-proficient mammary tumor cells. In accordance with the concept of synthetic lethality, however, this hit did not show up when we screened BRCA2-deficient mammary tumor cells. Previous screens in BRCA1-deficient tumor cells also did not yield *Parp1* as a hit (Xu et al., 2015b).

Most PARPi do not only block the catalytic activity of PARP1 but also induce toxic PARP1-DNA complexes. Our study shows that PARG inhibition reduces the amount of trapped PARP1 by preventing its excessive binding. This result underscores the delicate balance between enzymatic PARP1 activity and its toxicity when trapped on DNA.

Since PAR synthesis and degradation go hand in hand in orchestrating the DNA damage response, the use of PARGi has been put forward for the treatment of cancers with DDR defects (Fauzee et al., 2010), and the possibility of a synthetic lethal interaction between PARG and BRCA proteins has received considerable interest. However, several studies that addressed this question have produced contradictory results (Fathers et al., 2012; Noll et al., 2016; Gravells et al., 2017), which suggest that sensitivity to PARG depletion may depend on the cell line

Figure 5. PARG Inhibition Alleviates PARPi-Induced DNA Damage

(A) RF progression assay in U2OS cells exposed to indicated treatments; the experiment was repeated twice; box extends from 25th to 75th percentile, with a middle line representing the median and whiskers drawn down to the 10th percentile and up to the 90th; Mann-Whitney U test; ****$p < 0.001$; n.s., not significant.

(B) Neutral comet assay in U2OS cells treated as in (A); Mann-Whitney U test, ****$p < 0.001$, data shown as mean ± SD of a replicate; the experiment was repeated twice.

(C and D) Representative images (C) and quantification (D) of time course analysis of GFP-XRCC1 recruitment in U2OS cells treated as indicated; **$p < 0.01$; n.s., not significant; two-tailed unpaired t test; data represent mean ± SEM of three independent experiments. Scale bar, 10 μm.

(E) Quantification of MDC1 tracks following immunostaining; statistical analysis as in (D).

(F) SSB assay in KB2P cells, treated as indicated; SSF, strand scission factor; data representative for two independent experiments, shown as mean ± SD of a replicate; two-tailed unpaired t test; *$p < 0.05$; n.s., not significant.

(G) IF analysis of γH2AX foci in KB2P cells, treated as indicated; statistical analysis as in (F); **$p < 0.01$; *$p < 0.05$.

(H) Proposed model: in the presence of PARPi, PARP1 maintains residual activity but is counteracted by PARG. Loss of PARG leads to stabilization of PAR chains and, consequently, limits accumulation of toxic PARP-DNA complexes, prevents unrestrained RF progression, and promotes the recruitment of the downstream factors. Together, this results in reduced PARPi-induced DNA damage and improves PARPi survival.

See also Figure S5.

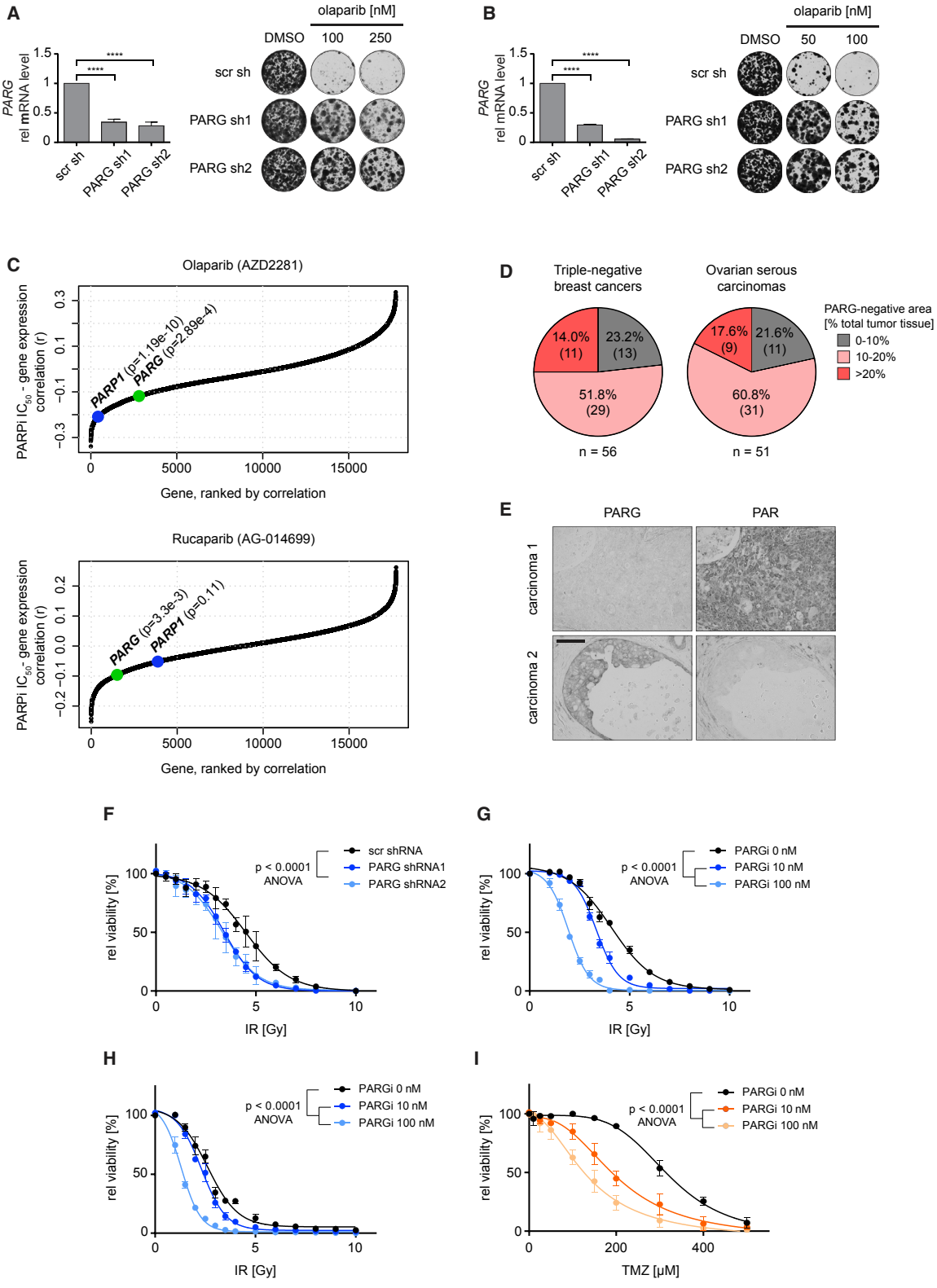

(legend on next page)

and the degree of PARG suppression. Importantly, Koh et al. (2004) showed that PARG depletion, although embryonically lethal, can be tolerated in embryonic stem cells cultured in the presence of PARPi. In our cell lines, both genetic depletion and chemical inhibition of PARG were well tolerated and did not affect cellular viability. Moreover, homozygous loss of *Parg* was acquired *in vivo* in a substantial fraction of KB2P tumors. PARG-negative clones were also found in a sizable proportion of human high-risk TNBCs or serous ovarian cancers, potential target groups for PARPi treatment due to the increased presence of HR-deficient cancers. Taken together, these data suggest that PARG-negative clones can be specifically selected by PARPi treatment and modulate therapy response.

While the clinical application of PARPi has initially focused on *BRCA1/2*-mutated tumors, the therapeutic scope of these drugs is now being extended to other molecular defects (reviewed in Lord and Ashworth, 2017). Since PARG acts directly at PAR structures and independently of the HR pathway, stabilization of PARylation via PARG suppression might represent a generic mechanism of PARPi resistance, relevant for a broad spectrum of cancers. Although this is bad news for the clinical use of PARPi, loss of PARG can also be exploited as a potential Achilles' heel for cancer treatment, as it confers sensitivity to IR (Amé et al., 2009). Our data indeed show that PARG suppression potentiates the toxicity of radiation therapy in BRCA-deficient cells. Additionally, we show that PARG inhibition synergizes with temozolomide, a chemotherapeutic agent that is now being evaluated in the clinic in combination with PARPi (Dréan et al., 2016).

Our research has yielded a collection of matched PARPi-naive and -resistant *Brca2*$^{-/-}$ mouse mammary tumors, which can be further utilized in a search for additional resistance mechanisms. Although PARG loss was observed in the majority of the PARPi-resistant KB2P tumors, it cannot explain resistance in all cases. Three other candidates, *Rps6ka6*, *Socs4*, and *Pbrm1*, were validated as additional significant hits in a secondary screen. Since all three of these genes are connected to chromatin, it will be interesting to understand the underlying mechanism of how they affect PARPi response in a follow-up study.

In collaboration with the Durocher and Lord laboratories, we have recently identified that PARPi resistance can also be caused by loss of the Shieldin (SHLD) complex, which acts downstream of 53BP1 in blocking DNA end resection (Noordermeer et al., manuscript submitted). Importantly, loss of the SHLD complex is not a generic PARPi resistance mechanism, since it causes PARPi resistance specifically in BRCA1- but not in BRCA2-deficient cells. In contrast, loss of PARG explains PARPi resistance in both BRCA1- and BRCA2-mutated tumors, as it operates independently of the HR pathway.

Taken together, our findings suggest that PARG is an important mediator of PARPi response. The presence of PARG-negative cells in treatment-naive tumors from the clinically relevant groups of high-risk women suggests that PARG loss should be assessed as a potential cause of clinical PARPi resistance. In this case, measurement of PARG activity should further improve clinical decision making for patients with tumors that lack homology-directed DNA repair.

STAR★METHODS

Detailed methods are provided in the online version of this paper and include the following:

- KEY RESOURCES TABLE
- CONTACT FOR REAGENT AND RESOURCE SHARING
- EXPERIMENTAL MODEL AND SUBJECT DETAILS
  - Mice
  - Human Samples of Triple-Negative Breast and Serous Ovarian Cancer
  - Cell Lines
  - Tumor-Derived Organoids
- METHOD DETAILS
  - Generation of PARPi-Naive and -Resistant KB2P Tumors
  - Generation of Deep Sequencing Data and Analysis
  - Immunohistochemistry Analysis
  - PARG/PAR Analysis in TNBC and Serous Ovarian Carcinomas Cohorts
  - Constructs, Lentiviral Transductions and Genome Editing
  - Functional Genetic Screens
  - Long-Term Clonogenic Assays
  - RT-qPCR
  - PAR Immunoblotting
  - PARP1 Trapping Assay
  - PARG Activity Assay
  - PAR ELISA Assay
  - PAR Immunofluorescence Analysis
  - RAD51/53BP1 IRIF Analysis
  - *In Situ* Analysis of GEMM Tumors
  - Immunofluorescent Staining of Olaparib-Induced γH2AX Foci
  - DNA Fiber Assay
  - Neutral Comet Assay
  - Fast Micromethod DNA Single-Strand Break Assay

Figure 6. *PARG* Depletion in Human Cancer Cells Leads to PARPi Resistance but Results in Acquired Vulnerabilities

(A and B) Long-term clonogenic assay with SUM149PT (A) and DLD-1 BRCA2-deficient (B) cells expressing indicated shRNAs and treated with olaparib; *PARG* expression levels were determined by qRT-PCR (left; mean ± SD of triplicate, ****$p < 0.001$, t test) and representative images of stained wells (right) are shown.

(C) Correlation between IC_{50} of olaparib or rucaparib and expression of DDR genes; *PARP1* and *PARG* are highlighted; p values were determined using the relation between estimated coefficient and Student's t distribution.

(D) Summary of IHC analysis of PARG expression in TNBCs and ovarian serous carcinomas.

(E) Representative images of PARG and PAR IHC of TNBC biopsies. Scale bar, 100 μm.

(F and G) Response to irradiation of SUM149PT cells, expressing indicated shRNAs (F) or treated with PARGi (G).

(H) Response to irradiation of DLD-1 BRCA2-deficient cells treated as indicated.

(I) Response to temozolomide of SUM149PT cells treated as indicated. In (F)–(I) data are presented as mean ± SD of triplicates.

See also Figure S6.

SUPPLEMENTAL INFORMATION

Supplemental Information includes six figures and six tables and can be found with this article online at https://doi.org/10.1016/j.ccell.2018.05.008.

ACKNOWLEDGMENTS

We thank the members of the Preclinical Intervention Unit of the Mouse Clinic for Cancer and Ageing (MCCA) at the NKI, Wendy Sol, and Guotai Xu for their technical support with the animal studies, and we thank the NKI core facilities: Animal Pathology facility, Digital Microscopy facility, Genomics Core facility, and Animal facility for their excellent service. We are also grateful to Peter Bouwman (NKI) and Thanos Halazonetis (Geneve University) for help in generating the list of DDR-associated genes, to SurfSara for allowing us to use their HPC Cloud service for the computational analyses, and to Chief Pathologist Vera Timmermans Wielenga (Department of Pathology, Copenhagen University Hospital, Denmark) and the technician Maria Grønvig Nielsen (Danish Cancer Society Research Center) for their contribution to IHC analysis of TNBC biopsies. Financial support came from the Dutch Cancer Society (KWF 2011-5220 and 2014-6532), the Netherlands Organisation for Scientific Research (VICI 91814643 and a National Roadmap grant for Large-Scale Research Facilities), the Netherlands Genomics Initiative (93512009), Cancer Research UK (C480/A1141 and C5759/A17098), the Danish Cancer Society, Swedish Research Council, Cancerfonden and Danish National Research Foundation (project CARD), the Swiss National Science Foundation (310030_156869), the Swiss Cancer League (KLS-4282-08-2017), and the European Research Council (CoG-617485, CoG-681572, SyG-319661).

AUTHOR CONTRIBUTIONS

Conceptualization, E.G., P.B., J.J., and S.R.; Methodology, E.G., A.A.D., W.W.W., D.I.J., and B.v.d.B.; Investigation, E.G., A.A.D., J.R.d.R., W.W.W., J.A.S., S.G.L., J. Bartkova, I.G., M.A.S., R.d.B., S.A., M.B., and A.K.; Software and Formal Analysis, E.G., J.R.d.R., R.d.B., and D.J.V.; Resources, D.I.J, D.J.O., and M.T.; Writing – Original Draft, Review & Editing – E.G., P.B., J.J., and S.R.; Supervision, M.v.d.V., M.v.V., L.F.A.W., J. Bartek., M.L., H.v.A., P.B., J.J., and S.R.; Funding Acquisition, D.J.O., J. Bartek., H.v.A., J.J., and S.R.

DECLARATION OF INTERESTS

The authors declare no potential conflicts of interest.

Received: May 8, 2017
Revised: March 27, 2018
Accepted: May 14, 2018
Published: June 11, 2018

REFERENCES

Amé, J.-C., Fouquerel, E., Gauthier, L.R., Biard, D., Boussin, F.D., Dantzer, F., de Murcia, G., and Schreiber, V. (2009). Radiation-induced mitotic catastrophe in PARG-deficient cells. J. Cell Sci. *122*, 1990–2002.

Anders, S., and Huber, W. (2010). Differential expression analysis for sequence count data. Genome Biol. *11*, R106.

Ang, J.E., Gourley, C., Powell, C.B., High, H., Shapira-Frommer, R., Castonguay, V., De Greve, J., Atkinson, T., Yap, T.A., Sandhu, S., et al. (2013). Efficacy of chemotherapy in BRCA1/2 mutation carrier ovarian cancer in the setting of PARP inhibitor resistance: a multi-institutional study. Clin. Cancer Res. *19*, 5485–5493.

Annunziato, S., Barazas, M., Rottenberg, S., and Jonkers, J. (2016). Genetic dissection of cancer development, therapy response, and resistance in mouse models of breast cancer. Cold Spring Harb. Symp. Quant. Biol. *81*, 141–150.

Audeh, M.W., Carmichael, J., Penson, R.T., Friedlander, M., Powell, B., Bell-McGuinn, K.M., Scott, C., Weitzel, J.N., Oaknin, A., Loman, N., et al. (2010). Oral poly(ADP-ribose) polymerase inhibitor olaparib in patients with BRCA1 or BRCA2 mutations and recurrent ovarian cancer: a proof-of-concept trial. Lancet *376*, 245–251.

Barazas, M., Annunziato, S., Pettitt, S.J., de Krijger, I., Ghezraoui, H., Roobol, S.J., Lutz, C., Frankum, J., Song, F.F., Brough, R., et al. (2018). The CST complex mediates end-protection at double-strand breaks and promotes PARP inhibitor sensitivity in BRCA1-deficient cells. Cell Rep. https://doi.org/10.1016/j.celrep.2018.04.046.

Bartkova, J., Horejsí, Z., Koed, K., Krämer, A., Tort, F., Zieger, K., Guldberg, P., Sehested, M., Nesland, J.M., Lukas, C., et al. (2005). DNA damage response as a candidate anti-cancer barrier in early human tumorigenesis. Nature *434*, 864–870.

Berti, M., Ray Chaudhuri, A., Thangavel, S., Gomathinayagam, S., Kenig, S., Vujanovic, M., Odreman, F., Glatter, T., Graziano, S., Mendoza-Maldonado, R., et al. (2013). Human RECQ1 promotes restart of replication forks reversed by DNA topoisomerase I inhibition. Nat. Struct. Mol. Biol. *20*, 347–354.

Brinkman, E.K., Chen, T., Amendola, M., and van Steensel, B. (2014). Easy quantitative assessment of genome editing by sequence trace decomposition. Nucleic Acids Res. *42*, e168.

Bryant, H.E., Schultz, N., Thomas, H.D., Parker, K.M., Flower, D., Lopez, E., Kyle, S., Meuth, M., Curtin, N.J., and Helleday, T. (2005). Specific killing of BRCA2-deficient tumours with inhibitors of poly(ADP-ribose) polymerase. Nature *434*, 913–917.

Cabezón, T., Gromova, I., Gromov, P., Serizawa, R., Timmermans Wielenga, V., Kroman, N., Celis, J.E., and Moreira, J.M.A. (2013). Proteomic profiling of triple-negative breast carcinomas in combination with a three-tier orthogonal technology approach identifies Mage-A4 as potential therapeutic target in estrogen receptor negative breast cancer. Mol. Cell. Proteomics *12*, 381–394.

Costantino, L., Sotiriou, S.K., Rantala, J.K., Magin, S., Mladenov, E., Helleday, T., Haber, J.E., Iliakis, G., Kallioniemi, O.P., and Halazonetis, T.D. (2014). Break-induced replication repair of damaged forks induces genomic duplications in human cells. Science *343*, 88–91.

Dietlein, F., Thelen, L., and Reinhardt, H.C. (2014). Cancer-specific defects in DNA repair pathways as targets for personalized therapeutic approaches. Trends Genet. *30*, 326–339.

Dobin, A., Davis, C.A., Schlesinger, F., Drenkow, J., Zaleski, C., Jha, S., Batut, P., Chaisson, M., and Gingeras, T.R. (2013). STAR: ultrafast universal RNA-seq aligner. Bioinformatics *29*, 15–21.

Dréan, A., Lord, C.J., and Ashworth, A. (2016). PARP inhibitor combination therapy. Crit. Rev. Oncol. Hematol. *108*, 73–85.

Duarte, A.A., Gogola, E., Sachs, N., Barazas, M., Annunziato, S., R de Ruiter, J., Velds, A., Blatter, S., Houthuijzen, J.M., van de Ven, M., et al. (2018).

BRCA-deficient mouse mammary tumor organoids to study cancer-drug resistance. Nat. Methods *15*, 134–140.

Edwards, S.L., Brough, R., Lord, C.J., Natrajan, R., Vatcheva, R., Levine, D.A., Boyd, J., Reis-Filho, J.S., and Ashworth, A. (2008). Resistance to therapy caused by intragenic deletion in BRCA2. Nature *451*, 1111–1115.

Evers, B., Drost, R., Schut, E., de Bruin, M., van der Burg, E., Derksen, P.W.B., Holstege, H., Liu, X., van Drunen, E., Beverloo, H.B., et al. (2008). Selective inhibition of BRCA2-deficient mammary tumor cell growth by AZD2281 and cisplatin. Clin. Cancer Res. *14*, 3916–3925.

Ewels, P., Magnusson, M., Lundin, S., and Käller, M. (2016). MultiQC: summarize analysis results for multiple tools and samples in a single report. Bioinformatics *32*, 3047–3048.

Farmer, H., McCabe, N., Lord, C.J., Tutt, A.N.J., Johnson, D.A., Richardson, T.B., Santarosa, M., Dillon, K.J., Hickson, I., Knights, C., et al. (2005). Targeting the DNA repair defect in BRCA mutant cells as a therapeutic strategy. Nature *434*, 917–921.

Fathers, C., Drayton, R.M., Solovieva, S., and Bryant, H.E. (2012). Inhibition of poly(ADP-ribose) glycohydrolase (PARG) specifically kills BRCA2-deficient tumor cells. Cell Cycle *11*, 990–997.

Fauzee, N.J.S., Pan, J., and Wang, Y. (2010). PARP and PARG inhibitors–new therapeutic targets in cancer treatment. Pathol. Oncol. Res. *16*, 469–478.

Follenzi, A., Ailles, L.E., Bakovic, S., Geuna, M., and Naldini, L. (2000). Gene transfer by lentiviral vectors is limited by nuclear translocation and rescued by HIV-1 pol sequences. Nat. Genet. *25*, 217–222.

Fong, P.C., Boss, D.S., Yap, T.A., Tutt, A., Wu, P., Mergui-Roelvink, M., Mortimer, P., Swaisland, H., Lau, A., O'Connor, M.J., et al. (2009). Inhibition of poly(ADP-ribose) polymerase in tumors from BRCA mutation carriers. N. Engl. J. Med. *361*, 123–134.

Gibson, B.A., and Kraus, W.L. (2012). New insights into the molecular and cellular functions of poly(ADP-ribose) and PARPs. Nat. Rev. Mol. Cell Biol. *13*, 411–424.

Gravells, P., Grant, E., Smith, K.M., James, D.I., and Bryant, H.E. (2017). Specific killing of DNA damage-response deficient cells with inhibitors of poly(ADP-ribose) glycohydrolase. DNA Repair *52*, 81–91.

Gromova, I., Gromov, P., Honma, N., Kumar, S., Rimm, D., Talman, M.-L.M., Wielenga, V.T., and Moreira, J.M.A. (2015). High level PHGDH expression in breast is predominantly associated with keratin 5-positive cell lineage independently of malignancy. Mol. Oncol. *9*, 1636–1654.

Hart, T., Brown, K.R., Sircoulomb, F., Rottapel, R., and Moffat, J. (2014). Measuring error rates in genomic perturbation screens: gold standards for human functional genomics. Mol. Syst. Biol. *10*, 733.

Horton, J.K., Watson, M., Stefanick, D.F., Shaughnessy, D.T., Taylor, J.A., and Wilson, S.H. (2008). XRCC1 and DNA polymerase beta in cellular protection against cytotoxic DNA single-strand breaks. Cell Res. *18*, 48–63.

Iorio, F., Knijnenburg, T.A., Vis, D.J., Bignell, G.R., Menden, M.P., Schubert, M., Aben, N., Gonçalves, E., Barthorpe, S., Lightfoot, H., et al. (2016). A landscape of pharmacogenomic interactions in cancer. Cell *166*, 740–754.

James, D.I., Smith, K.M., Jordan, A.M., Fairweather, E.E., Griffiths, L.A., Hamilton, N.S., Hitchin, J.R., Hutton, C.P., Jones, S., Kelly, P., et al. (2016a). First-in-class chemical probes against poly(ADP-ribose) glycohydrolase (PARG) inhibit DNA repair with differential pharmacology to olaparib. ACS Chem. Biol. *11*, 3179–3190.

James, D.I., Durant, S., Eckersley, K., Fairweather, E., Griffiths, L.A., Hamilton, N., Kelly, P., O'Connor, M., Shea, K., Waddell, I.D., et al. (2016b). An assay to measure poly(ADP ribose) glycohydrolase (PARG) activity in cells. F1000Res. *5*, 736.

Jaspers, J.E., Kersbergen, A., Boon, U., Sol, W., van Deemter, L., Zander, S.A., Drost, R., Wientjens, E., Ji, J., Aly, A., et al. (2013). Loss of 53BP1 causes PARP inhibitor resistance in Brca1-mutated mouse mammary tumors. Cancer Discov. *3*, 68–81.

Jonkers, J., Meuwissen, R., van der Gulden, H., Peterse, H., van der Valk, M., and Berns, A. (2001). Synergistic tumor suppressor activity of BRCA2 and p53 in a conditional mouse model for breast cancer. Nat. Genet. *29*, 418–425.

Kan, C., and Zhang, J. (2015). BRCA1 mutation: a predictive marker for radiation therapy? Int. J. Radiat. Oncol. Biol. Phys. *93*, 281–293.

Kim, M.Y., Zhang, T., and Kraus, W.L. (2005). Poly(ADP-ribosyl)ation by PARP-1: 'PAR-laying' NAD+ into a nuclear signal. Genes Dev. *19*, 1951–1967.

Kim, I.-K., Stegeman, R.A., Brosey, C.A., and Ellenberger, T. (2015). A quantitative assay reveals ligand specificity of the DNA scaffold repair protein XRCC1 and efficient disassembly of complexes of XRCC1 and the poly(ADP-ribose) polymerase 1 by poly(ADP-ribose) glycohydrolase. J. Biol. Chem. *290*, 3775–3783.

Koh, D.W., Lawler, A.M., Poitras, M.F., Sasaki, M., Wattler, S., Nehls, M.C., Stöger, T., Poirier, G.G., Dawson, V.L., and Dawson, T.M. (2004). Failure to degrade poly(ADP-ribose) causes increased sensitivity to cytotoxicity and early embryonic lethality. Proc. Natl. Acad. Sci. USA *101*, 17699–17704.

Kolde, R., Laur, S., Adler, P., and Vilo, J. (2012). Robust rank aggregation for gene list integration and meta-analysis. Bioinformatics *28*, 573–580.

Li, H., and Durbin, R. (2010). Fast and accurate long-read alignment with Burrows-Wheeler transform. Bioinformatics *26*, 589–595.

Li, H., Handsaker, B., Wysoker, A., Fennell, T., Ruan, J., Homer, N., Marth, G., Abecasis, G., and Durbin, R.; 1000 Genome Project Data Processing Subgroup (2009). The sequence alignment/map format and SAMtools. Bioinformatics *25*, 2078–2079.

Li, W., Xu, H., Xiao, T., Cong, L., Love, M.I., Zhang, F., Irizarry, R.A., Liu, J.S., Brown, M., and Liu, X.S. (2014). MAGeCK enables robust identification of essential genes from genome-scale CRISPR/Cas9 knockout screens. Genome Biol. *15*, 554.

Liao, Y., Smyth, G.K., and Shi, W. (2014). featureCounts: an efficient general purpose program for assigning sequence reads to genomic features. Bioinformatics *30*, 923–930.

Lord, C.J., and Ashworth, A. (2017). PARP inhibitors: synthetic lethality in the clinic. Science *355*, 1152–1158.

De Lorenzo, S.B., Patel, A.G., Hurley, R.M., and Kaufmann, S.H. (2013). The elephant and the blind men: making sense of PARP inhibitors in homologous recombination deficient tumor cells. Front. Oncol. *3*, 228.

Luijsterburg, M.S., de Krijger, I., Wiegant, W.W., Shah, R.G., Smeenk, G., de Groot, A.J.L., Pines, A., Vertegaal, A.C.O., Jacobs, J.J.L., Shah, G.M., et al. (2016). PARP1 links CHD2-mediated chromatin expansion and H3.3 deposition to DNA repair by non-homologous end-joining. Mol. Cell *61*, 547–562.

Martin, M. (2011). Cutadapt removes adapter sequences from high-throughput sequencing reads. EMBnet.Journal *17*, 10–12.

Moudry, P., Watanabe, K., Wolanin, K.M., Bartkova, J., Wassing, I.E., Watanabe, S., Strauss, R., Troelsgaard Pedersen, R., Oestergaard, V.H., Lisby, M., et al. (2016). TOPBP1 regulates RAD51 phosphorylation and chromatin loading and determines PARP inhibitor sensitivity. J. Cell Biol. *212*, 281–288.

Murai, J., Huang, S.N., Das, B.B., Renaud, A., Zhang, Y., Doroshow, J.H., Ji, J., Takeda, S., and Pommier, Y. (2012). Trapping of PARP1 and PARP2 by clinical PARP inhibitors. Cancer Res. *72*, 5588–5599.

Murai, J., Huang, S.-Y.N., Renaud, A., Zhang, Y., Ji, J., Takeda, S., Morris, J., Teicher, B., Doroshow, J.H., and Pommier, Y. (2014a). Stereospecific PARP trapping by BMN 673 and comparison with olaparib and rucaparib. Mol. Cancer Ther. *13*, 433–443.

Murai, J., Zhang, Y., Morris, J., Ji, J., Takeda, S., Doroshow, J.H., and Pommier, Y. (2014b). Rationale for poly(ADP-ribose) polymerase (PARP) inhibitors in combination therapy with camptothecins or temozolomide based on PARP trapping versus catalytic inhibition. J. Pharmacol. Exp. Ther. *349*, 408–416.

Nazarkina, Z.K., Khodyreva, S.N., Marsin, S., Lavrik, O.I., and Radicella, J.P. (2007). XRCC1 interactions with base excision repair DNA intermediates. DNA Repair *6*, 254–264.

Neelsen, K.J., and Lopes, M. (2015). Replication fork reversal in eukaryotes: from dead end to dynamic response. Nat. Rev. Mol. Cell Biol. *16*, 207–220.

Noll, A., Illuzzi, G., Amé, J.-C., Dantzer, F., and Schreiber, V. (2016). PARG deficiency is neither synthetic lethal with BRCA1 nor PTEN deficiency. Cancer Cell Int. *16*, 53.

Ohmoto, A., and Yachida, S. (2017). Current status of poly(ADP-ribose) polymerase inhibitors and future directions. Onco Targets Ther. *10*, 5195–5208.

Oplustil O'Connor, L., Rulten, S.L., Cranston, A.N., Odedra, R., Brown, H., Jaspers, J.E., Jones, L., Knights, C., Evers, B., Ting, A., et al. (2016). The PARP inhibitor AZD2461 provides insights into the role of PARP3 inhibition for both synthetic lethality and tolerability with chemotherapy in preclinical models. Cancer Res. *76*, 6084–6094.

Pascal, J.M., and Ellenberger, T. (2015). The rise and fall of poly(ADP-ribose): an enzymatic perspective. DNA Repair *32*, 10–16.

Pettitt, S.J., Rehman, F.L., Bajrami, I., Brough, R., Wallberg, F., Kozarewa, I., Fenwick, K., Assiotis, I., Chen, L., Campbell, J., et al. (2013). A genetic screen using the PiggyBac transposon in haploid cells identifies Parp1 as a mediator of olaparib toxicity. PLoS One *8*, e61520.

Prahallad, A., Heynen, G.J.J.E., Germano, G., Willems, S.M., Evers, B., Vecchione, L., Gambino, V., Lieftink, C., Beijersbergen, R.L., Di Nicolantonio, F., et al. (2015). PTPN11 is a central node in intrinsic and acquired resistance to targeted cancer drugs. Cell Rep *12*, 1978–1985.

Ray Chaudhuri, A., Hashimoto, Y., Herrador, R., Neelsen, K.J., Fachinetti, D., Bermejo, R., Cocito, A., Costanzo, V., and Lopes, M. (2012). Topoisomerase I poisoning results in PARP-mediated replication fork reversal. Nat. Struct. Mol. Biol. *19*, 417–423.

Ray Chaudhuri, A., Callen, E., Ding, X., Gogola, E., Duarte, A.A., Lee, J.-E., Wong, N., Lafarga, V., Calvo, J.A., Panzarino, N.J., et al. (2016). Replication fork stability confers chemoresistance in BRCA-deficient cells. Nature *535*, 382–387.

de Ronde, J.J., Rigaill, G., Rottenberg, S., Rodenhuis, S., and Wessels, L.F.A. (2013). Identifying subgroup markers in heterogeneous populations. Nucleic Acids Res. *41*, e200.

Rottenberg, S., Nygren, A.O.H., Pajic, M., van Leeuwen, F.W.B., van der Heijden, I., van de Wetering, K., Liu, X., de Visser, K.E., Gilhuijs, K.G., van Tellingen, O., et al. (2007). Selective induction of chemotherapy resistance of mammary tumors in a conditional mouse model for hereditary breast cancer. Proc. Natl. Acad. Sci. USA *104*, 12117–12122.

Rottenberg, S., Jaspers, J.E., Kersbergen, A., van der Burg, E., Nygren, A.O.H., Zander, S.A.L., Derksen, P.W.B., de Bruin, M., Zevenhoven, J., Lau, A., et al. (2008). High sensitivity of BRCA1-deficient mammary tumors to the PARP inhibitor AZD2281 alone and in combination with platinum drugs. Proc. Natl. Acad. Sci. USA *105*, 17079–17084.

Sanjana, N.E., Shalem, O., and Zhang, F. (2014). Improved vectors and genome-wide libraries for CRISPR screening. Nat. Methods *11*, 783–784.

Sato, T., Vries, R.G., Snippert, H.J., van de Wetering, M., Barker, N., Stange, D.E., van Es, J.H., Abo, A., Kujala, P., Peters, P.J., et al. (2009). Single Lgr5 stem cells build crypt-villus structures in vitro without a mesenchymal niche. Nature *459*, 262–265.

Scheinin, I., Sie, D., Bengtsson, H., van de Wiel, M.A., Olshen, A.B., van Thuijl, H.F., van Essen, H.F., Eijk, P.P., Rustenburg, F., Meijer, G.A., et al. (2014). DNA copy number analysis of fresh and formalin-fixed specimens by shallow whole-genome sequencing with identification and exclusion of problematic regions in the genome assembly. Genome Res. *24*, 2022–2032.

Schröder, H.C., Batel, R., Schwertner, H., Boreiko, O., and Müller, W.E.G. (2006). Fast micromethod DNA single-strand-break assay. Methods Mol. Biol. *314*, 287–305.

Sousa, F.G., Matuo, R., Soares, D.G., Escargueil, A.E., Henriques, J.A.P., Larsen, A.K., and Saffi, J. (2012). PARPs and the DNA damage response. Carcinogenesis *33*, 1433–1440.

Sugimura, K., Takebayashi, S., Taguchi, H., Takeda, S., and Okumura, K. (2008). PARP-1 ensures regulation of replication fork progression by homologous recombination on damaged DNA. J. Cell Biol. *183*, 1203–1212.

Swisher, E.M., Sakai, W., Karlan, B.Y., Wurz, K., Urban, N., and Taniguchi, T. (2008). Secondary BRCA1 mutations in BRCA1-mutated ovarian carcinomas with platinum resistance. Cancer Res. *68*, 2581–2586.

Tutt, A., Robson, M., Garber, J.E., Domchek, S.M., Audeh, M.W., Weitzel, J.N., Friedlander, M., Arun, B., Loman, N., Schmutzler, R.K., et al. (2010). Oral poly(ADP-ribose) polymerase inhibitor olaparib in patients with BRCA1 or BRCA2 mutations and advanced breast cancer: a proof-of-concept trial. Lancet *376*, 235–244.

Xu, G., Jonkers, J., and Rottenberg, S. (2015a). PARP inhibitor resistance—what is beyond BRCA1 or BRCA2 restoration? In PARP Inhibitors for Cancer Therapy, N.J. Curtin and R.A. Sharma, eds. (Springer International Publishing), pp. 453–471.

Xu, G., Chapman, J.R., Brandsma, I., Yuan, J., Mistrik, M., Bouwman, P., Bartkova, J., Gogola, E., Warmerdam, D., Barazas, M., et al. (2015b). REV7 counteracts DNA double-strand break resection and affects PARP inhibition. Nature *521*, 541–544.

Yan, Q., Xu, R., Zhu, L., Cheng, X., Wang, Z., Manis, J., and Shipp, M.A. (2013). BAL1 and its partner E3 ligase, BBAP, link poly(ADP-ribose) activation, ubiquitylation, and double-strand DNA repair independent of ATM, MDC1, and RNF8. Mol. Cell. Biol. *33*, 845–857.

Zellweger, R., Dalcher, D., Mutreja, K., Berti, M., Schmid, J.A., Herrador, R., Vindigni, A., and Lopes, M. (2015). Rad51-mediated replication fork reversal is a global response to genotoxic treatments in human cells. J. Cell Biol. *208*, 563–579.

Cancer Cell, Volume *33*

Supplemental Information

Selective Loss of PARG Restores PARylation and Counteracts PARP Inhibitor-Mediated Synthetic Lethality

Ewa Gogola, Alexandra A. Duarte, Julian R. de Ruiter, Wouter W. Wiegant, Jonas A. Schmid, Roebi de Bruijn, Dominic I. James, Sergi Guerrero Llobet, Daniel J. Vis, Stefano Annunziato, Bram van den Broek, Marco Barazas, Ariena Kersbergen, Marieke van de Ven, Madalena Tarsounas, Donald J. Ogilvie, Marcel van Vugt, Lodewyk F.A. Wessels, Jirina Bartkova, Irina Gromova, Miguel Andújar-Sánchez, Jiri Bartek, Massimo Lopes, Haico van Attikum, Piet Borst, Jos Jonkers, and Sven Rottenberg

Table S1. Genetic screens identify *Parg* as a PARPi-resistance factor. Related to Figures 1 and 2.

Primary screen – DDR library						
***in vitro* model**	**PARP inhibitor**	**replicates**	***Parg* gene rank**	**p value**	**RRA score**	**hairpins enriched/total**
KB2P1.21 cell line	AZD2461	3	1	1.23e-5	3.59e-7	4/5
KB2P1.21 cell line	AZD2281 (olaparib)	3	1	1.23e-5	7.79e-8	5/5
KB2P3.4 cell line	AZD2461	3	1	3.70e-5	1.47e-5	5/5
KB2P3.4 cell line	AZD2281 (olaparib)	3	1	7.28e-4	1.63e-4	5/5
KP3.33 cell line	AZD2281 (olaparib)	3	9	1.59e-2	4.54e-3	4/5
ORG-KB2P26S.1 organoids	AZD2461	3	4	7.73e-3	2.39e-3	4/5
Secondary screen – *in vivo* PARPi-resistance candidates library						
***in vitro* model**	**PARP inhibitor**	**replicates**	***Parg* gene rank**	**p value**	**RRA score**	**hairpins enriched/total**
KB2P1.21 cell line	AZD2461	3	1	4.99e-6	3.76e-6	5
KB2P1.21 cell line	AZD2281 (olaparib)	3	1	2.49e-5	5.39e-6	5
KB2P3.4 cell line	AZD2461	3	1	1.50e-5	3.59e-5	5
KB2P3.4 cell line	AZD2281 (olaparib)	3	1	4.99e-6	1.02e-6	5

p value and RRA score (Robust Rank Aggregation) determined by MAGeCK.

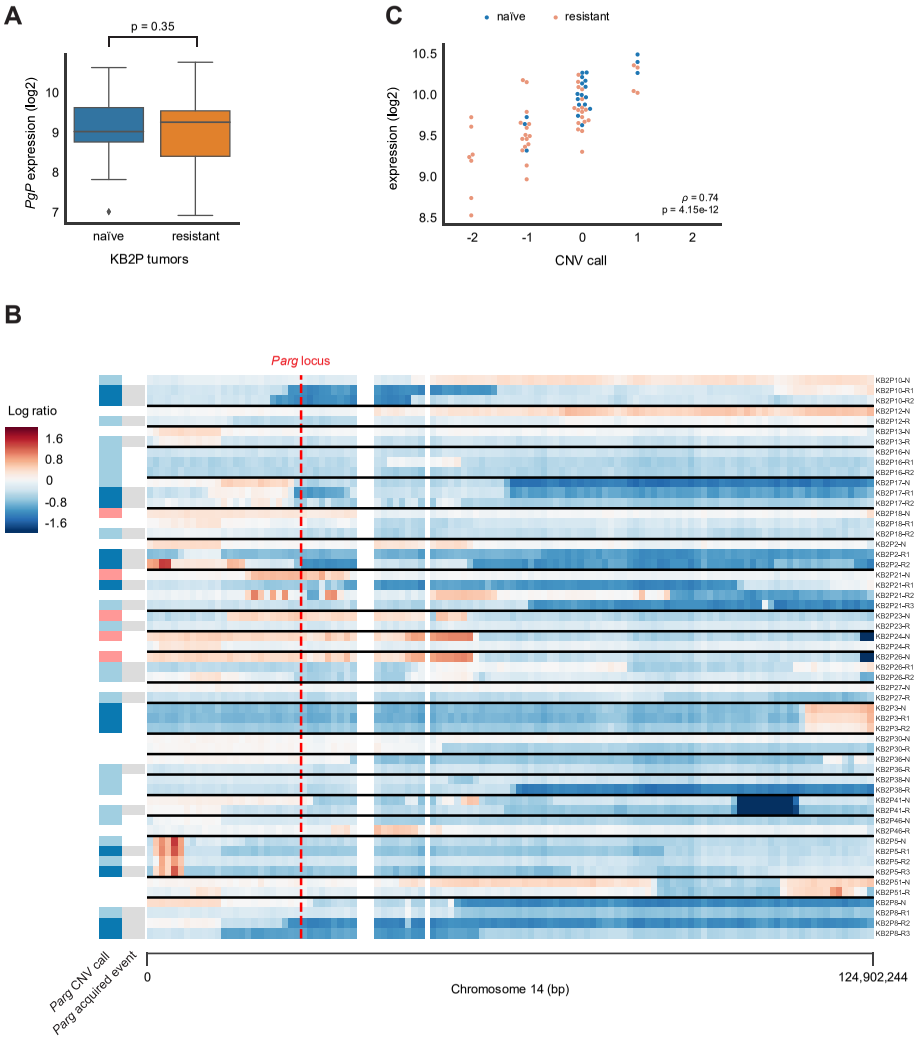

Figure S1. Multi-omics analysis of PARPi-resistant mouse mammary tumors. Related to Figure 2. (A) Expression (RNA-seq) of P-gp drug efflux transporter in KB2P PARPi-naïve and resistant tumors; p value: two-tailed t-test. The box extends from the lower to upper quartile values of the data, with a line at the median; whiskers (whis) are a function of the inner quartile range, they extend to the most extreme data point within (whis*(75%-25%)) data range. (B) Copy number log2 ratios of chromosome 14 shown for all KB2P tumors; the *Parg* locus is indicated by the red dashed line. KB2Px-R/Ny: x – original donor ID number, y – ID of individual resistant tumors derived from the same donor tumor, R – resistant, N – naive. (C) Correlation between *Parg* expression and copy-number estimation for a panel of KB1P tumors. Spearman correlation coefficient (ρ) and p value (DIDS algorithm) are indicated.

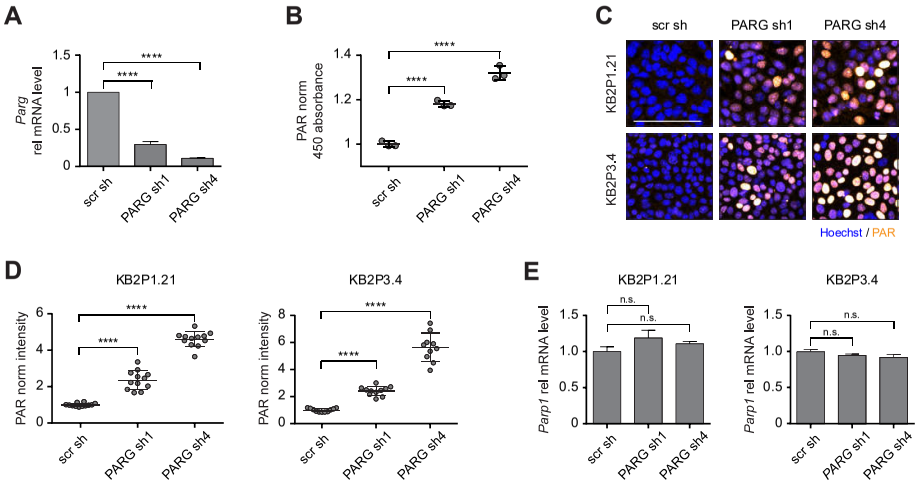

Figure S2. Suppression of PARG in KB2P cells. Related to Figure 3. (A) RT-qPCR analysis of *Parg* expression in KB2P3.4 cells expressing indicated shRNAs; ****p < 0.001 (two-tailed t-test), data shown as mean ± SD of triplicate. (B) ELISA-based PARG activity assay in the cell lines indicated; data represent mean ± SD of triplicate, ****p < 0.001 (two-tailed t-test). (C-D) Immunofluorescence-based PAR detection in the indicated cell lines upon MMS (0.01%) treatment. Representative microscopic images (C) and quantification of the assay (D) are shown; ****p < 0.001 (two-tailed t-test), data are presented as mean ± SD of single areas imaged (experiment repeated three times, four areas/experiment, average 300 cells/area); scale bar, 100 μm. (E) RT-qPCR analysis of *Parp1* gene expression in KB2P PARG kd cells; n.s. – not significant (two tailed t-test), data are shown as mean ± SD of triplicate experiments.

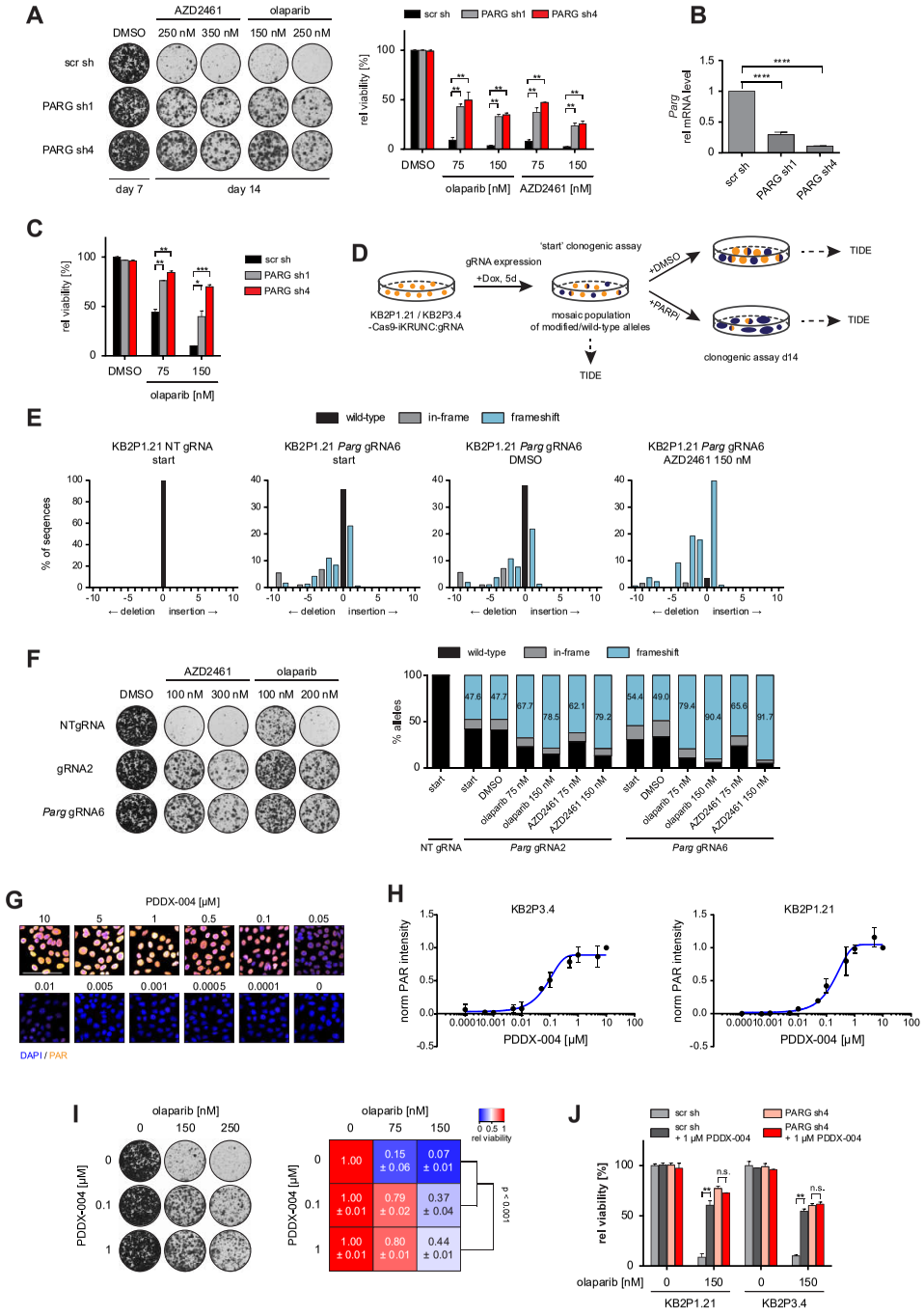

Figure S3. Downregulation of PARG drives PARPi resistance in KB2P cell lines. Related to Figure 3. (A) Long-term clonogenic assay using KB2P3.4-scr sh (scramble shRNA, control), -PARG sh1 and -PARG sh4 cells and the PARPi AZD2461 or olaparib. Representative images of stained wells (left) and quantification of the assay (right; mean ± SD of three repeats) are shown; **p < 0.01 (two-tailed t-test). (B) qRT-PCR analysis of *Parg* expression in KB1P-G3 cells expressing the hairpins indicated; ****p < 0.001 (two-tailed t-test), data shown as mean ± SD of triplicate. (C) Clonogenic assay in KB1P-G3 cells expressing the hairpins indicated and treated with olaparib; *p < 0.05, **p < 0.01, ***p < 0.001 (two-tailed t-test); data represents mean ± SD of two repeats. (D) Outline of the long-term clonogenic assays in KB2P cells expressing control (NT) or gRNAs targeting *Parg*. (E) Example of the TIDE analysis: spectrum of alleles identified by the algorithm in the samples indicated. (F) Long-term clonogenic assay using KB2P3.4 cells expressing the indicated gRNAs. Representative images (left) and TIDE quantification of allele composition (right) are shown. (G-H) Chemical inhibition of PARG using PDDX-004 in the cell lines indicated. Representative images of PAR immunofluorescent staining (G) and quantification (H) are shown; data represent mean ± SD of three repeats; scale bar, 100 µm. (I) Long-term clonogenic assay using KB2P3.4 cells treated with the PARPi olaparib and PARGi PDDX-004 alone or in combination. Representative images of stained cells (left) and quantification of the assay (right) are shown. Data on the graph represent experiments repeated three times (mean ± SD); p value (ANOVA) is indicated. (J) Clonogenic assay in KB2P cells expressing the shRNAs indicated, and treated with olaparib; **p < 0.01, n.s. – not significant (two-tailed t-test); data shown as mean ± SD of triplicate.

Table S5. TIDE analysis of clonogenic assays using KB2P cells expressing gRNAs targeting *Parg*. Related to Figure 3.

cell line	gRNA	condition	wild-type [%]	in-frame [%]	frameshift [%]
KB2P1.21	NT	start	99.80	0	0.20
	Parg gRNA2	start	43.40	7.06	49.54
		DMSO	41.94	8.06	50.00
		AZD2461 75nM	16.43	7.24	76.33
		AZD2461 150nM	6.00	7.25	86.75
		olaparib 75nM	16.08	7.37	76.55
		olaparib 150nM	10.56	5.74	83.70
	Parg gRNA6	start	36.50	13.18	50.32
		DMSO	38.04	13.80	48.16
		AZD2461 75nM	9.04	8.50	82.46
		AZD2461 150nM	3.38	3.27	93.35
		olaparib 75nM	11.55	10.13	78.32
		olaparib 150nM	6.77	6.00	87.23
KB2P3.4	NT	start	99.90	0	0.10
	Parg gRNA2	start	41.87	10.49	47.64
		DMSO	40.99	11.33	47.68
		AZD2461 100nM	28.18	9.71	62.11
		AZD2461 300nM	13.30	7.53	79.17
		olaparib 100nM	22.93	9.42	67.65
		olaparib 200nM	14.69	6.77	78.54
	Parg gRNA6	start	30.65	15.00	54.35
		DMSO	33.37	17.61	49.02
		AZD2461 100nM	23.76	10.69	65.55
		AZD2461 300nM	5.09	3.21	91.70
		olaparib 100nM	10.47	10.13	79.40
		olaparib 200nM	5.95	3.68	90.37

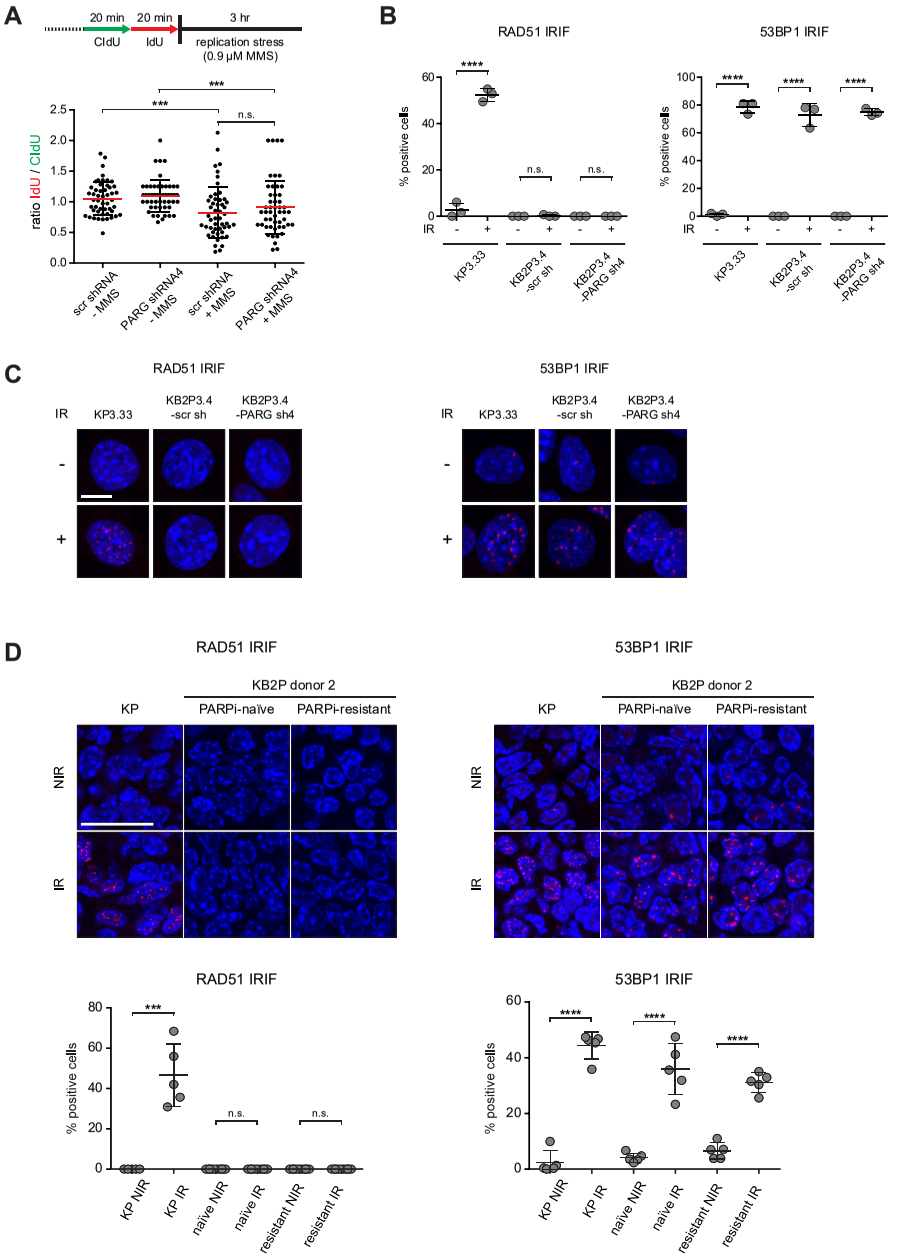

Figure S4. PARG loss causes PARPi resistance independently of HR and RF protection. Related to Figure 4. (A) DNA fiber assay using KB2P3.4 cells treated with MMS (0.9 μM); ***p < 0.001, n.s. – not significant (Mann-Whitney U). Error bars represent SD and red lines represent mean values. (B-C) RAD51/53BP1 IRIF formation assay in the given cell lines; KP3.33 (*p53*$^{-/-}$) cells were used as HR-proficient control in this assay; 53BP1 served as DNA damage marker. Quantification (B) and representative images (C) are shown. A cell was considered positive when: RAD51 ≥ 5 foci/nuclei, 53BP1 ≥ 10 foci/nuclei. Data represent mean ± SD; ****p < 0.0001, n.s. – not significant (two-tailed t-test); scale bar, 10 μm. (D) Example of RAD51 foci formation analysis in a KB2P2 tumor pair, representative for all PARPi-resistant tumors for which alterations in the *Parg* gene were identified by DeepSeq analysis. Matched naïve samples, as well as KP (*p53*$^{-/-}$) tumor (positive control) were taken along for the analysis. Microscopy images (upper panels) and foci quantification (lower panels) are shown. For quantification, a fraction of positive cells (≥5 foci/nuclei for RAD51 and ≥10 foci/nuclei for 53BP1) was calculated for five different areas of each tumor (shown as single data point on the graph, error bars represent SD). ***p < 0.0001, ****p < 0.0001, n.s. – not significant (two-tailed t-test). 53BP1 was used as a marker of DNA damage. Scale bar, 25 μm.

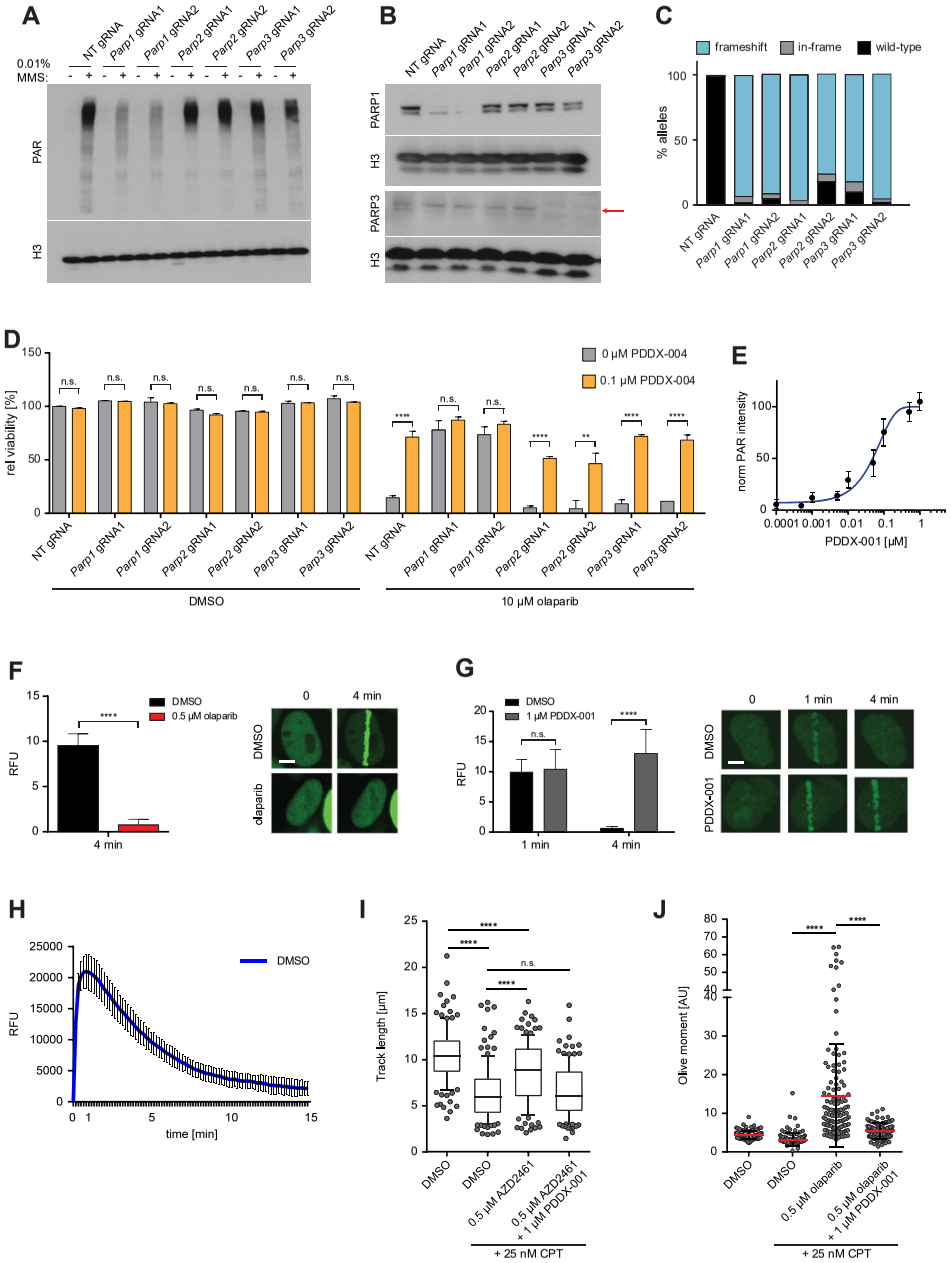

Figure S5. PARG depletion partially restores downstream signaling of PARP1. Related to Figures 4 and 5. (A-B) Immunoblot analysis of PAR (A), PARP1 and PARP3 (B) cellular levels in KP3.33 expressing the gRNAs indicated. Red arrow (B) indicates band specific for PARP3. Histone 3 (H3) was used as a loading control. Data representative of experiments repeated twice. (C) TIDE analysis of allele modification rates in KP3.33 cells expressing the gRNAs indicated; data representative for experiment repeated twice. (D) Clonogenic assay with KP3.33 cells expressing the gRNAs indicated, treated with olaparib; **p < 0.01, ****p < 0.0001, n.s. – not significant; data shown as mean ± SD of two repeats. (E) PARG inhibition in U2OS cells by PDDX-001; data presented as mean ± SD of two repeats. (F) GFP-XRCC1 recruitment analysis in DMSO (control) or olaparib-treated GFP-XRCC1 U2OS cells; representative images (right) and quantification (left) are shown. XRCC1 recruitment was used as a readout for PARP1 inhibition. (G) GFP-CHD2 binding to the site of DNA damage in GFP-CHD2 U2OS cells treated with DMSO (control) or PDDX-001; representative images (right) and quantification (left panel) are shown. CHD2 association to chromatin was used as a positive control for PARG inhibition. (H) Time-course recruitment analysis of GFP-PARP1 to laser tracks in control cells (DMSO). For experiments shown in (F-H) data are represented as mean ± SEM of two independent repeats; ****p < 0.0001 (t-test); in all images scale bar, 10µm. (I) Fork progression assay in U2OS cells exposed to the treatments indicated. Box extends from 25th to 75th percentile, with a middle line representing the median and whiskers drawn down to the 10th percentile and up to the 90th. (J) Neutral comet assay in U2OS cells treated as indicated. Data shown as mean ± SD of a replicate. Experiments shown in (I-J) were repeated twice; ****p < 0.001, n.s. – not significant, Mann-Whitney U test.

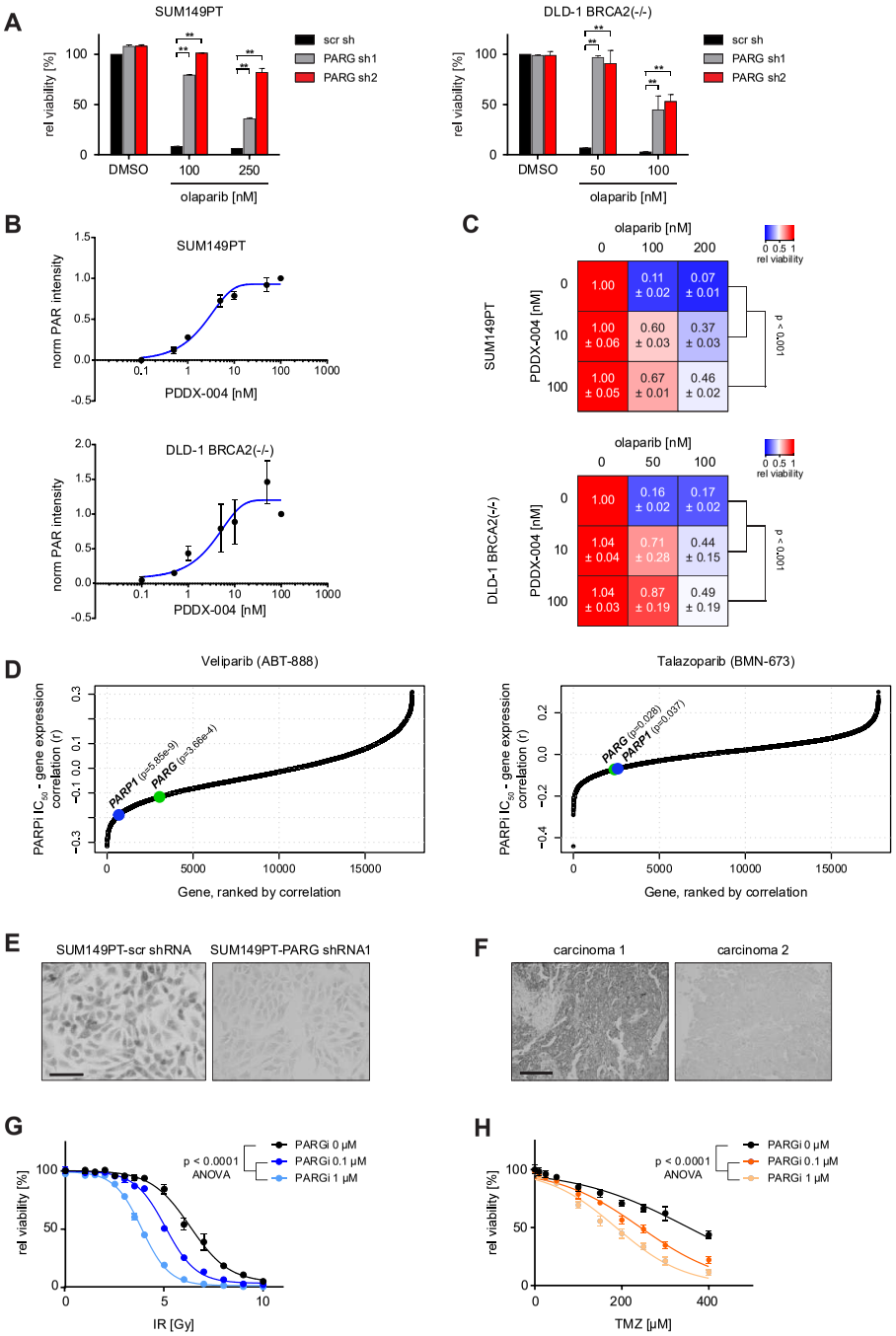

Figure S6. PARPi response of PARG-depleted human cancer cells. Related to Figure 6. (A) Quantification of long-term clonogenic assays shown in Figure 6A. Graph represents mean ± SD values of triplicates; **p < 0.01 (two-tailed t-test). (B) Chemical inhibition of PARG with PDDX-004 in indicated cells. Data represent mean ± SD of three repeats. (C) Quantification of a long-term clonogenic assay in SUM149PT (upper panel) and DLD-1 BRCA2(-/-) (lower panel) cells treated with the PARPi olaparib and the PARGi PDDX-004 alone or in combination. Data presented as mean ± SD values of three repeats. (D) Correlation analysis between IC_{50} values of PARPi (veliparib and talazoparib) and expression of DDR genes in a panel of 935 human cancer cell lines; *PARP1* and *PARG* are highlighted; Pearson correlation was computed and p values were determined using the relation between estimated coefficient and the student-t distribution. (E) Validation of PARG antibody used in IHC analyses; representative images of SUM149PT cells expressing indicated shRNAs are shown; scale bar, 100 µm. (F) Example of PARG IHC staining in two ovarian serous carcinomas; scale bar, 100 µm. (G-H) Response of KB2P1.21 cells to ionizing radiation (IR) and temozolomide (TMZ), treated with PARGi PDDX-004. Data is presented as mean ± SD.

Table S6. Related to STAR methods. Oligonucleotides used in this study.

oligonucleotide	experiment	sequence
scr (scrambled) shRNA	shRNA-mediated knockdown	CCTAAGGTTAAGTCGCCCTCG
mouse *Parg* shRNA1	shRNA-mediated knockdown	CCTCTCAAAGAGACATCCTAT
mouse *Parg* shRNA4	shRNA-mediated knockdown	GCAGTTTCTTACACCTATAAA
human *PARG* shRNA1	shRNA-mediated knockdown	GCTAAGATGAAATCGGAGTAT
human *PARG* shRNA2	shRNA-mediated knockdown	GCTGAGCGAGATGTGGTTTAT
mouse *Parg* forward primer	RT-qPCR	CTGTTCACTGAGGTGCTGGA
mouse *Parg* reverse primer	RT-qPCR	TCTCAGGCACAAACTGATCG
human *PARG* forward primer	RT-qPCR	GCAATCGTGTCAAGGGTTTT
human *PARG* reverse primer	RT-qPCR	CATCAAGGAAACCGGAGAAA
mouse *Hprt* forward primer	RT-qPCR	CTGGTGAAAAGGACCTCTCG
mouse *Hprt* reverse primer	RT-qPCR	TGAAGTACTCATTATAGTCAAGGGCA
human *HPRT* forward primer	RT-qPCR	GAAGAGCTATTGTAATGACC
human *HPRT* reverse primer	RT-qPCR	GCGACCTTGACCATCTTTG
mouse *Parp1* forward primer	RT-qPCR	GCAGCGAGAGTATTCCCAAG
mouse *Parp1* reverse primer	RT-qPCR	CCGTCTTCTTGACCTTCTGC
NT (non-targeting) gRNA	CRISPR/Cas9 genome editing	TGATTGGGGGTCGTTCGCCA
Parg gRNA2	CRISPR/Cas9 genome editing	CTTGTACCCTGTGGAAGATG
Parg gRNA6	CRISPR/Cas9 genome editing	CAGCTTAGTAATGCTAACAT
Parp1 gRNA1	CRISPR/Cas9 genome editing	CGAGTGGAGTACGCGAAGAG
Parp1 gRNA2	CRISPR/Cas9 genome editing	CTCAACATCAGGCTGCCGGA
Parp2 gRNA1	CRISPR/Cas9 genome editing	GGGACTTTCCCATCGAACAT
Parp2 gRNA2	CRISPR/Cas9 genome editing	GTGCAGTCACCCATGTTCGA
Parp3 gRNA1	CRISPR/Cas9 genome editing	AGCCGGAACCCCGGGATAC
Parp3 gRNA2	CRISPR/Cas9 genome editing	GATAATCGGGTCATCCGTG
Parg gRNA2 forward primer	TIDE PCR1, TIDE PCR2	CACAAGACGTGGTGATTGCTAAA
Parg gRNA2 reverse primer	TIDE PCR1	GAGCCTTCATAAGTGACAGGACA
Parg gRNA6 forward primer	TIDE PCR1, TIDE PCR2	TCACAGGGCAAACGTCTCAC
Parg gRNA6 reverse primer	TIDE PCR1	TCCAGTTCCAATGTCCTCGG
Parp1 gRNA1 forward primer	TIDE PCR1, TIDE PCR2	AACCGACAAAAGGGGTGGCG
Parp1 gRNA1 reverse primer	TIDE PCR1	GCAGGGTAAGCGCAATGTCC
Parp1 gRNA2 forward primer	TIDE PCR1, TIDE PCR2	TCAAGTGCTGCTTCCTGGCT
Parp1 gRNA2 reverse primer	TIDE PCR1	ACATACACACACATACACCCACAA
Parp2 gRNA1 forward primer	TIDE PCR1, TIDE PCR2	GAGGGAGCACTAGCAAGTCAGG
Parp2 gRNA1 reverse primer	TIDE PCR1	GACAGCACAACCTTACCCAAAGT
Parp2 gRNA2 forward primer	TIDE PCR1, TIDE PCR2	TCAGACTCTGTGCAGCCCCT
Parp2 gRNA2 reverse primer	TIDE PCR1	TTGAGATAGAGTTAAAGCTGGCCTC
Parp3 gRNA1 forward primer	TIDE PCR1, TIDE PCR2	CTCGGGGAACACCTCGAGCC
Parp3 gRNA1 reverse primer	TIDE PCR1	CAGAAGACAGGTACGCAATCCCT
Parp3 gRNA2 forward primer	TIDE PCR1, TIDE PCR2	CTCGGGGAACACCTCGAGCC
Parp3 gRNA2 reverse primer	TIDE PCR1	CAGAAGACAGGTACGCAATCCCT

Curriculum Vitae

Personal Information

Name	Jonas Andreas Schmid
Address:	Haldenstrasse 23 3014 Bern, Switzerland
Cell Phone:	+41 79 818 77 22
Email	jonas.schmid@imcr.uzh.ch
Date of Birth	05.02.1988
Citizenship:	Canadian/ Swiss
LinkedIn	https://www.linkedin.com/in/jonas-andreas-schmid/

Education

Since 07.2014	Fast track PhD Student (Master & PhD combined) in cancer biology at the Institute of Molecular Cancer Research, University of Zürich
07.2014-02.2016	Master studies in Cancer Biology at the University of Zürich, final grade 6.0
09.2011-08.2013	Bachelor studies in Biology at the University of Zürich, final grade 5.8
09.2008-11.2011	Bachelor studies in Economics at the University of Bern, final grade 5.7
02.2011-07.2011	Exchange semester at the University of Vienna
02.2008-01.2018	Supported by the Swiss Study Foundation for excellent students
2004 – 2007	Higher education at Gymnasium Bern Kirchenfeld

Professional experience

15.07.2013 – 01.02.2014	Research assistant in human genetic diagnostics for Prof. Sabina Galatti, University Hospital Bern (Inselspital)
11.07.2011 – 02.09.2011	Research assistant in molecular plant physiology for Prof. Enrico Martinoia at the Botanical Institute of the University of Zürich
04.2008 – 09.2010	Assistant in accounting and quality management for the CSD engineers and geologists in Bern
18.08.2007 – 20.12.2007	Research assistant in behavioral ecology at the Department of Biological Science for Prof. Kathreen Ruckstuhl at the University of Calgary in Alberta, Canada

Extra-curricular activities

Since 2016	Chief financial officer of CVI Technologies (Startup company)
04.04.- 06.04.2016	Participation at the GapSummit 2016 (A global biotech leadership summit, at the University of Cambridge, UK)
Since 2014	Teaching assistant at the Life Science Learning Center (LSLC Zürich)

Since 2014	Organizer and instructor of the yearly intellectual tool in life sciences for the Swiss Study Foundation
2014-2015	Member of the college of life sciences of the German study foundation
02.-03.2014	Volunteer in different projects of the Missionaries of Charity in Kolkata, India
25.08.- 28.08.2013	Participation in the 2013 Novartis International Biotechnology Leadership camp.
02.2009	Participation at the first Swiss Talent Forum, organized by the Swiss Youth in Science.

Awards

04.2016	Winner of the Voices of Tomorrow Global Bio-Innovation Competition.
08.2013	Winner of the team competition at the Novartis International Biotechnology Leadership camp

Language skills

German	First language
English	C1
French	B2
Spanish	A2
Slovene	A2

Publications

Schmid, JA., Berti, M., Pfistner, F., Raso, MC., Schmid, F., Krietsch, J., Zwicky, K., Stoy, H., Ursich, S., Freire, R., Lopes, M.,& Penengo, L. (2018). Histone-ubiquitination by the DNA damage response is required for efficient DNA replication in unperturbed S-Phase. Molecular Cell, in press

Gogola, E., Duarte, AA., de Ruiter, JR., Wiegant, WW., **Schmid, JA.**, James, DI., Guerrero Llobet, S., Vis, DJ., Annunziato, S., van den Broek, B., Barazas, M., Kersbergen, A., de Brujin, R., van de Ven, M., Tarsounas, M., Ogilvie, DJ., van Vugt, M., Wessels, LFA., Bartkova, J., Gromova, I., Andujar Sanchez, M., Bartek, J., Lopes, M., van Attikum, H., Borst, P., Jonkers, J.,& Rottenberg, S. (2018). Selective loss of PARG restores PARylation and counteracts PARP inhibitor-mediated synthetic lethality. Cancer Cell, in press

Vujanovic, M., Krietsch, J., Raso, CR., Terraneo N., Zellweger, R., **Schmid, JA**., Taglialatela, A. Hunag, JW., Holland, CL., Zwicky, K., Herrador, R., Jacobs, H., Cortez, D., Ciccia, A., Penengo, L.,& Lopes, M. (2017). Replication Fork Slowing and Reversal upon DNA Damage Require PCNA Polyubiquitination and ZRANB3 DNA Translocase Activity. Molecular Cell, 67(5), 882–889

Zellweger, R., Dalcher, D., Muteja, K., Berti, M., **Schmid, JA**., Herrador, R., Vindigni, A.,& Lopes, M. (2015). Rad51-mediated replication fork reversal is a global response to genotoxic treatments in human cells. JCB, 208(5), 563–579.